David John McGovern, BSc. (Hons).

The Interaction of Tidal Currents with Offshore Wind Turbine Monopiles: An Experimental Study of Flow, Turbulence, Scour and the Reduction of Scour around the Monopile.

This thesis is submitted in partial fulfilment of the requirements for the degree of

Doctor of Philosophy

November, 2010.

Lancaster University

I. Abstract

The installation of offshore wind turbines involves the driving of a cylindrical steel monopile into the sea bed. The presence of the monopile in the water column causes changes in the local flow and turbulence field resulting in increased flow velocity, turbulence and bed shear stress. This causes a scour hole to develop around the base of the monopile, adversely affecting its stability. An extensive laboratory campaign was run to study how tidal currents may change the flow, turbulence, bed shear stress amplification, scour time development and scour depth around a scaled cylinder representing the monopile. The experiments yielded detailed results showing a highly three-dimensional flow field whose characteristics vary significantly with changes in velocity and water depth. The scour hole resulting from reversing time/depth-varying currents was symmetrical in shape and its time development was slower than in unidirectional currents. The results implied this scour depth to be lower than unidirectional current scour depth. The possibility of reducing scour by attaching collars and helical strakes to the cylinder was investigated. The flow and turbulence field around was found to be markedly different to that around the regular cylinders, exhibiting large horizontal-axis rotation in the downstream wake. For the collared cylinder, these differences translated to a lower scour depth during the early stages of the reversing time/depth-varying current in comparison to that of a steady unidirectional current. However, the scour depth at the end of the test was the same for both the smooth and collared cylinders. From the presentation and discussion of the model results, it is suggested that prototype tidal variation in flow depth and velocity does not simplify to unidirectional currents and that the continued use of

unidirectional current based prediction methods may overestimate scour in tidal

conditions and lead to unnecessary scour protection and resource expenditure.

II. Acknowledgements

The four years that it has taken to produce this thesis are filled with people who deserve my thanks. First and foremost are my supervisors Dr Suzana Ilic and Dr Andy Folkard. Both have provided essential guidance, support and encouragement without which this thesis would not have been completed.

In Hull, I am very grateful for the help in all aspects of the experimental design, commission and the completion of data collection campaign from Dr Stuart McLelland and Mr Brendan Murphy. On top of this, the games of lab cricket, the daily lesson in 'great' music from the '80s and visits to Hitchock's 'all-you-can-eat' veggie restaurant ensured that it was indeed, 'never dull in Hull'.

My friends both in the PhD office and elsewhere also deserve much credit for providing support, encouragement and R & R. A special mention goes to Rachael Haywood.

This thesis is dedicated to my parents. No child can ever repay the debt they owe to their parents for the love, care and guidance they give. However, that should not stop them from trying, though I admit that a 50k+ word thesis on fluid dynamics and sediment transport may not be as high up the wish list as the new plasma TV. Therefore its dedication to them is to convey the following sentiment: any success that I may achieve in my life, past, present and future is shared in equal measure with both of you, and I am both immensely proud and lucky to be your son.

III. List of Symbols

A	Surface area of sediment grain	[m^2]
Al	Monopile/cylinder alignment factor	[-]
D^*	Dimensionless grain size	[-]
D	Monopile/cylinder diameter	[m]
d	Grain diameter	[m]
d_{50}	Median grain diameter	[m]
d_{sc}	Depth of scour	[m]
f	Dimensionless coefficient	[-]
F_D	Horizontal drag force	[N m^{-2}]
Fr_c	Critical Froude number	[-]
Fr_D	Monopile/cylinder Froude number	[-]
f_v	Vortex shedding frequency	[s^{-1}]
G	Effect of lateral shear in the approaching flow	[-]
g	Acceleration due to gravity	[m s^{-2}]
h	Water depth	[m]
$h_{upstream}$	Water depth upstream of the cylinder	[m]

$h_{downstream}$	Water depth downstream of the cylinder	[m]
K	Empirical dimensionless scour depth correction factor	[-]
K_{AL}	Pier alignment factor	[-]
K_d	Sediment size factor	[-]
K_G	Channel Geometry factor	[-]
K_{hD}	Flow depth to monopile/cylinder diameter ratio factor	[-]
K_I	Flow intensity factor	[-]
K_s	Monopile/cylinder shape factor	[-]
K_t	Time factor	[-]
K_1	Correction factor for pier nose shape	[-]
K_2	Correction factor for angle of attack flow	[-]
K_3	Correction factor for bed condition	[-]
L	Length scale	[m]
l	Wave length	[m]
N_g	Ration of Acceleration due to gravity	[-]
N_L	Length scale ratio	[-]
N_λ	Time scale ratio	[-]
q_b	Sediment transport rate	[m^3 s^{-1}]

Re_h	Flow Reynolds Number	[-]
Re^*	Grain Reynolds number	[-]
Re_D	Monopile/cylinder Reynolds Number	[-]
s	Relative density of sediment	[-]
Sh	Monopile/cylinder shape Factor	[-]
St_D	Strouhal number	[-]
T	Time scale of scour	[s]
T^*	Normalised time scale of scour	[-]
t	Time	[s]
t_e	Time to equilibrium scour depth	[s]
$t_{e(days)}$	Time to equilibrium scour depth	[days]
U	Velocity	[m s^{-1}]
$\bar{U}$	Depth averaged velocity	[m s^{-1}]
U_∞	Undisturbed velocity	[m s^{-1}]
U_{cr}	Critical velocity for sediment motion	[m s^{-1}]
u	Streamwise velocity	[m s^{-1}]
$\bar{u}$	Mean Streamwise velocity	[m s^{-1}]

u^+	u turbulence intensity	$[\text{m s}^{-1}]$
u'	Normalised streamwise velocity	$[-]$
u''	u velocity fluctuation	$[\text{m s}^{-1}]$
u^*	Friction velocity	$[\text{m s}^{-1}]$
V_∞	Undisturbed lateral velocity	$[\text{m s}^{-1}]$
v	Lateral velocity	$[\text{m s}^{-1}]$
$\bar{v}$	Mean lateral velocity	$[\text{m s}^{-1}]$
v^+	v turbulence intensity	$[\text{m s}^{-1}]$
v'	Normalised lateral velocity	$[-]$
v''	v velocity fluctuation	$[\text{m s}^{-1}]$
w	Vertical velocity	$[\text{m s}^{-1}]$
$\bar{w}$	Mean vertical velocity	$[\text{m s}^{-1}]$
W_∞	Undisturbed vertical velocity	$[\text{m s}^{-1}]$
w^+	w turbulence intensity	$[\text{m s}^{-1}]$
w'	Normalised vertical velocity	$[-]$
w''	w velocity fluctuation	$[\text{m s}^{-1}]$
w_t	Sediment particle weight	$[\text{kg}]$
X_s	Position of horseshoe vortex separation	$[\text{m}]$

x	Streamwise coordinate	[m]
x'	Normalised streamwise coordinate	[-]
y	Lateral coordinate	[m]
y'	Normalised lateral coordinate	[-]
z	Vertical coordinate	[m]
z'	Normalised vertical coordinate	[-]
z_0	Roughness length	[m]
α	Bed shear stress amplification factor	[-]
$\alpha_{downstream}$	Downstream scour hole slope angle	[°]
$\alpha_{upstream}$	Upstream scour hole slope angle	[°]
δ	Boundary layer thickness	[m]
κ	von Karman constant	[-]
θ	Shields parameter	[-]
θ_{cr}	Critical Shields parameter	[-]
λ	Normalised Time scale	[-]
λ_m	Time scale in model	[s]
λ_p	Time scale in prototype	[s]
μ	Dynamic viscosity of water	[kg m^{-1} s^{-1}]

ν	Kinematic viscosity of water	$[\text{m}^2 \text{ s}^{-1}]$
ρ_s	Density of sediment	$[\text{kg m}^{-3}]$
ρ_w	Density of water	$[\text{kg m}^{-3}]$
$\sigma_{dsc/D}$	Standard deviation of normalised scour depth	$[\text{m}]$
σ_g	Standard deviation of the sediment grain size distribution	$[\text{m}]$
τ_b	Bed shear stress	$[\text{N m}^{-2}]$
τ_c	Critical bed shear stress	$[\text{N m}^{-2}]$
τ_{uv}	uv Reynolds stress	$[\text{m}^2 \text{ s}^{-2}]$
τ_{uw}	uw Reynolds stress	$[\text{m}^2 \text{ s}^{-2}]$
τ_{vw}	vw Reynolds stress	$[\text{m}^2 \text{ s}^{-2}]$
τ_∞	Undisturbed bed shear stress	$[\text{N m}^{-2}]$
Φ	Angle of static sediment repose	$[°]$
ω	Vorticity	$[\text{s}^{-1}]$

IV. Contents

Chapter 1: Introduction, Background, Aims and Objectives

Chapter 2: Experiment Design and Methodology

Chapter 3: Rigid-bed Experiments on the Flow, Turbulence and Bed Shear Stress around the Cylinder in Tidal Flow

4. Time Development of Scour around an Offshore Wind Turbine in Variable and Reversing Currents

Chapter 5: Flow Field Alteration and Reduction of Scour through the use of Collared and Helical Strake Cylinders

6. Conclusions

7. References

8. Appendices

Chapter 1: Introduction, Background, Aims and Objectives

1.1 Introduction

Offshore wind energy generation is a fast growing sector of the renewable energy market in the U.K. This recent and rapid growth has been in response to growing socio-economic and environmental demands for renewable energy sources. Wind energy is harnessed by these systems via an electricity generating turbine driven by large rotating blades that are placed on top of a long cylindrical monopile, which is driven into the sea-bed. Considerable numbers of offshore wind farms exist in the shallow continental shelf seas around the U.K. and its North West European neighbours, with many more in the planning stages (Table 1-1). Offshore wind turbines are popular due to their larger size, consistently higher wind speed environment and lower visual impact in comparison to their onshore counterparts. However, their construction and maintenance requires solutions to many problematic issues. Shelf seas are dynamic environments subject to numerous cyclical and transient forcing agents such as tides and waves. This makes the construction and maintenance of offshore wind turbines inherently challenging, and as a result they require sophisticated engineering and planning. Among the significant issues associated with their construction is the problem of scour of the sediment on the sea bed at its interface with the base of the monopile structure. Scour is a consequence of flow modification by the monopile which causes an increase in velocity and turbulence of the flow around it. The resulting amplification of bed shear stress may induce scour of the

sediment around the base of the monopile which is manifested as a large, steep-sided hole around the monopile. Scour can reduce the stability of the structure and consequentially affect its longevity (e.g., Melville and Coleman, 2000 and Breusers and Raudkivi, 1991). While the knowledge of scour at bridge piers, which are subject to relatively steady unidirectional current flows and water depths is expansive, knowledge of the process of scour in tidal currents where flow direction, depth and speed is variable is very limited. Here there may be differences in the scour depth, scour hole shape and time-development due to the different characteristics of tidal flow as opposed to unidirectional flow.

Wind farm	Location	Region	Number of Turbines	Turbine Type (MW)	Total Capacity MW	Water Depth	Pile Diameter	Status
Barrow	7km off Walney Island	North West England	30	3	90	15 - 20	4.75	Operational
Beatrice	Beatrice Oilfield, Moray Firth	Scotland	2	5	10	45	\	Operational
Blyth Offshore	1km off Blyth Harbour	North West England	2	2	4	6 - 11	3.5	Operational
Burbo Bank	5.2km off Crosby	North West England	25	3.6	90	1 - 8	4.7	Operational
Cirrus Array (Shell Flats)	7km off Cleveleys	North West England	90	0	270	\	\	Submitted
Greater Gabbard	26km off Orford, Norfolk	Thames Estuary	140	3.6	504	\	\	Under construction
Gunfleet Sands I	7km off Clacton-on-Sea	East of England	30	3.6	108	\	\	Under construction
Gunfleet Sands II	8.5km off Clacton-On-Sea	East of England	18	3.6	64	\	\	Under construction
Gwynt y Mor	13-15km off North Wales Coast	North Wales	200	0	750	\	\	Submitted
Humber Gateway	Withernsea	Yorkshire & Humber	70	3	300	\	\	Submitted
Inner Dowsing	5.2km off Ingoldmells	East Midlands	27	3.6	90	\	\	Under construction
Kentish Flats	8.5 km offshore from Whitstable	South East	30	3	90	\	\	Operational
Lincs	8km off Skegness	Greater Wash	0	0	250	\	\	Submitted
London Array	24km off Clacton-on-Sea	Thames Estuary	271	0	1000	\	\	Approved
Lynn	5.2km off Skegness	East Midlands	54	3.6	194	\	\	Under construction
North Hoyle	7.5km off Prestatyn & Rhyl	North Wales	30	2	60	4 - 12	4	Operational
Ormonde	off Walney Island	North West England	30	5	150	\	\	Approved
Rhyl Flats	8km off Abergele	North Wales	25	3.6	90	\	\	Under construction
Robin Rigg	Maryport	North West England	30	3	90	\	\	Operational
Scarweather Sands	5.5km Sker off Point (nr Porthcawl)	South Wales	30	3.6	108	\	\	Approved
Scroby Sands	3km off NE Great Yarmouth	East of England	30	2	60	<21	4.2	Operational
Sheringham Shoal	Sheringham, Greater Wash	East of England	0	0	315	\	\	Approved
Solway Firth/Robin Rigg A	9.5km Maryport/8.5km off Rock Cliffe	Scotland	30	3	90	\	\	Under construction
Solway Firth/Robin Rigg B	9.5km off Maryport/8.5km off Rock Cliffe	Scotland	30	3	90	\	\	Under construction
Teeside / Redcar	1.5km off NE Teesmouth	Yorkshire & Humber	30	0	90	\	\	Approved
Thanet	11-13km off Foreness Point, Margate	Thames Estuary	0	0	300	\	\	Approved
Walney	14km off Walney Island, Irish Sea	North West England	42	3.6	450	\	\	Approved
West of Duddon Sands	N. Irish Sea	North West England	0	0	500	\	\	Approved

Table 1-1. List of U.K. offshore wind farms that are operational, under construction and approved.

This chapter presents an overview of the subject to which this thesis is related to; sediment transport and fluid dynamics. §1.2 provides an overview of sediment transport, including boundary layer flow, bed shear stress, the threshold of sediment motion and sediment transport rate. §1.3 introduces the local flow field around a vertical cylinder, which is derived from the most recent literature. This includes the nature of the downflow, horseshoe vortex, lateral boundary layer separation and vortex formation and shedding, flow constriction, sediment transport in the wake and the surface roller. §1.4 introduces the influence of individual non-dimensional parameters, sediment characteristics and cylinder shape on scour around the cylinder. In §1.5 a detailed review of scour predictor equations is given. §1.7 reviews the literature of the current state of knowledge on the flow field and mechanism of scour, the process, evolution and estimation of scour, and the reduction of scour around a single vertical cylinder. In §1.8 the aims and objectives of the thesis are presented and in §1.9 the omission of waves is discussed.

1.2 Introduction to Sediment Transport

When a vertical cylindrical structure (such as a bridge pier or a wind turbine monopile) is placed in a flow of water its presence affects the flow and turbulence field around it. The flow around the monopile becomes more three-dimensional, faster and more turbulent. These changes in the flow field may encourage sediment transport in the structure's locality by increasing the bed shear stress around it. It is this local monopile flow field which causes scour. This chapter will provide a comprehensive summary of the current

knowledge of the local monopile flow field and the mechanisms of scour. It will also address the mechanisms of scour, its evolution in time, the various different parameter influences on scour and summarise some of the equations used for its prediction. As befitting a thesis in the field of sediment transport, the basic processes of sediment transport by water are described first.

1.2.1 Sediment Transport

The term 'sediment transport' is used in different ways in the literature, and thus is somewhat ambiguous, but is defined here as any movement of sediment caused by the disturbing forces applied by the water flow (e.g. lift, drag) outweighing the resisting forces acting on a particle (e.g. gravity). The subject is tackled in numerous textbooks including for example (Brown et al., 2005 and Soulsby, 1997).

Sediment transport can be divided into the processes of entrainment, transportation and deposition. Entrainment is the result of friction exerted by the fluid on the bed; this can cause grains to move into suspension, or undergo bedload transport. Once particles are entrained, they can be transported by bed-load such as rolling or saltation or suspended load within the water column (Figure 1-2). Bed-load transport is usually associated with slower flow velocities and/or heavier grains, whereas suspended load transport is found in faster flow conditions and/or smaller particle sizes. Deposition takes place when grains fall out of suspension or are no longer transported in bed load and come to rest on the bed, usually due to a decrease in flow velocity.

The rate of sediment transport can be classified as the amount of sediment that passes through a plane normal to the flow per unit time. If the transport rate differs between planes bounding a region of flow at its upstream and downstream ends, the implication is that erosion (loss of sediment) or accretion (gain of sediment) is occurring within that region. Bed shear stress is the most commonly invoked parameter in the description of sediment transport. It describes the frictional shearing force applied by the fluid to the sediment grains and its value determines whether sediment transport occurs.
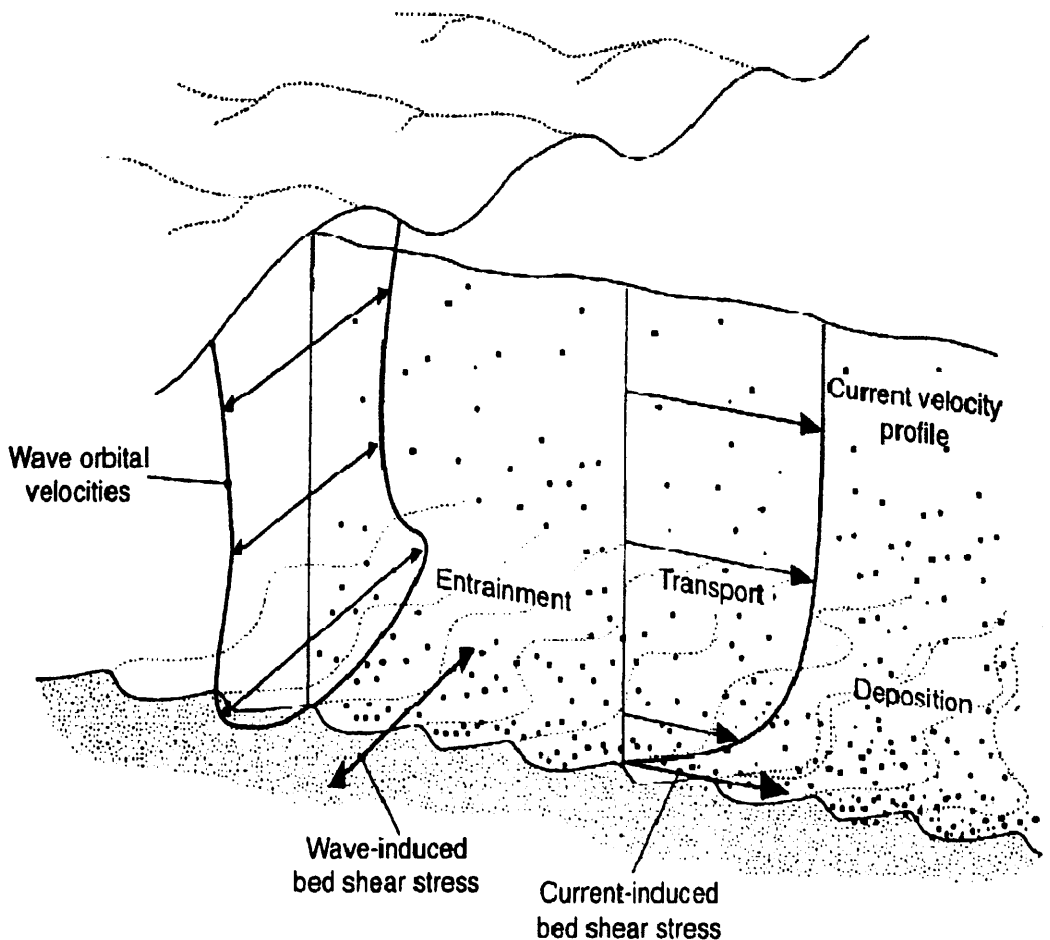
Figure 1-2. Schematic diagram of the main transport processes in the Marine environment, (after Soulsby, 1997)

1.2.2 Boundary Layer Flow

As mentioned above, sediment transport occurs due to the bed shear stress applied to the bed by the flow above it. The most important area of this flow in terms of sediment transport is therefore that which is immediately above the bed, the boundary layer. A boundary layer of a fluid flow is formed in the region of contact between different media. In the marine environment, it can be described as the layer of flow that is influenced significantly by the bed (Nielsen, 1994). The boundary layer forms due to the friction applied to the flow by the seabed. Such friction causes shear in the flow. A typical boundary layer current profile is given in Figure 1-3.
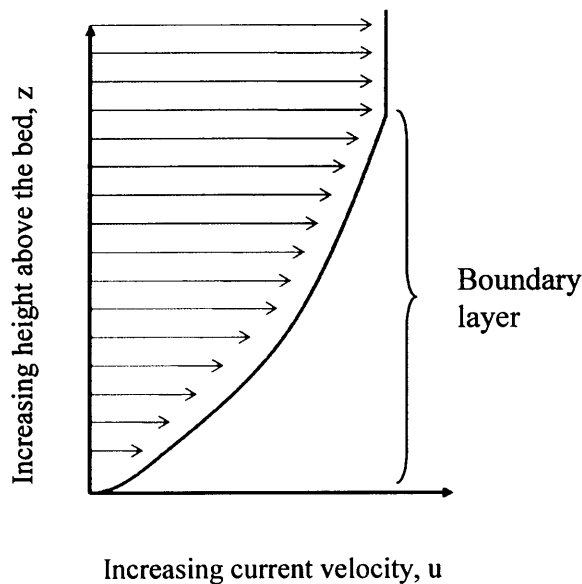
Figure 1-3. Schematic diagram of a typical boundary layer flow velocity profile

In the absence of sediment motion, the current speed at the interface between the flow and the surface is, theoretically, zero. Above this, the water is in motion; the water layer

immediately above the bed slides slowly over the bed, the layer above slides over this lowest layer at a slightly greater speed, and so on. These shear layers create a velocity gradient as seen in Figure 1-3. The rate of increase decreases with height from the bed until it reaches a relatively constant value at the top of the boundary layer.

Boundary layer thickness has several derivations, (Fredsoe and Deigaard, 1992), however, a generally accepted definition is the distance between the boundary surface and the point at which velocity reaches 0.99 of the free-stream velocity U_∞. It can span the entire depth of water in the shallow sea environment (Brown et al., 2005).

The majority of boundary layer flows in nature are turbulent. Laminar boundary layer flow will be present very close to the water-bed interface but is not often significant in sediment transport, which relies on shear flow and turbulent diffusions to take place. Measurements of velocity profiles in a steady, uniform and turbulent boundary layer, that can be analogous to an instantaneous point in the tidal cycle (i.e., a period of time where current and depth remains the same), correspond well to the semi-logarithmic von Karman-Prandtl profile, (Soulsby, 1997, Nielsen, 1994 and Equation 1-1).

$$U(z) = \frac{u_*}{\kappa} \ln \left(\frac{z}{z_0} \right) \qquad (1\text{-}1)$$

where $U(z)$ is the current velocity at height z, u_* is the shear velocity, κ is the von Karman constant, and z_0 is the height of the bed.

1.2.3 Bed Shear Stress

The amount of sediment transport that may take place is dictated by the amount of current shear and turbulence present in the boundary layer. Both of these phenomena dictate the amount of shear stress applied to the bed. The shear stress τ is proportional to the square of the velocity of the flow (Brown et al., 2005).

Bed shear stress τ_b [N m^{-2}] is the force per unit area exerted on the bed by the flow and describes the frictional force which is exerted on the bed by the flow. It can be expressed as the shear velocity u_* [m s^{-1}] which is described as:

$$u_* = \sqrt{\frac{\tau_b}{\rho_w}} \qquad (1\text{-}2)$$

where τ_b is the shear stress at the bed and ρ_w is the density of water.

Shear velocity is not a real velocity but has dimensions of velocity, and can be used to calculate τ_b:

$$\tau_b = \rho_w u_*{}^2 \qquad (1\text{-}3)$$

Shields, (1936) defined a dimensionless parameter θ.

$$\theta = \frac{\tau_b}{(\rho_s / \rho_w)gd} = \frac{u_*^2}{(s-1)gd} \qquad (1-4)$$

where ρ_s = density of sediment, $s = \rho_s / \rho_w$ (relative density of the sediment), d = grain diameter, g = acceleration due to gravity (9.81 m s^{-2}).

Equation 1-4 shows that θ is dependent on the ratio between the disturbing force (bed shear stress) and the stabilizing force (gravity). Equation 1-4 is commonly used to express shear stress; when $\theta > \theta_c$ sediment motion will occur, where θ_c is the critical value of Shields parameter for sediment motion.

1.2.4 Threshold of Motion

Where the local value of bed shear stress τ_b is greater or equal to the critical bed shear stress τ_c, the frictional force exerted by the boundary layer flow on the bed will be high enough to cause sediment transport. The point at which shear stress is large enough for sediment transport to take place is known as the 'threshold of motion'. A graded sediment size will have several different thresholds of motion, with the smaller particles being moved first.

A particle in a fluid flow is subject to various body and contact forces. It is the instantaneous values of these forces that will determine the mobility of the particle. A single grain lying freely on the bed under uniform flow is subject to lift forces and drag forces, (Figure 1-4).
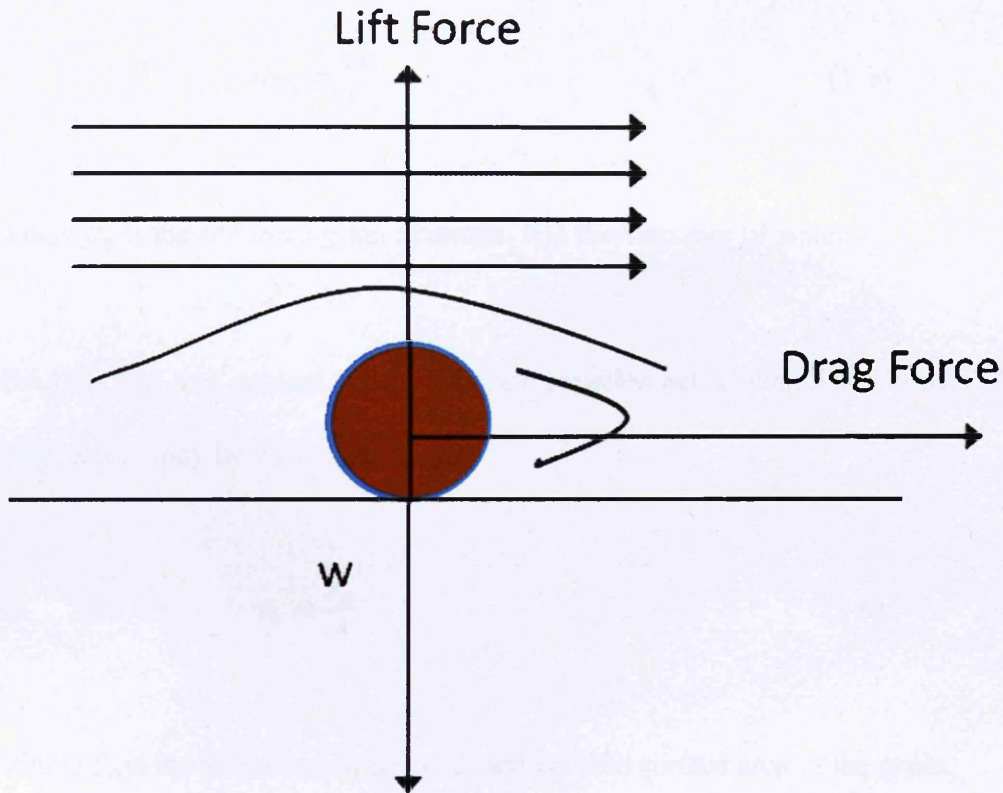
Figure 1-4. Forces acting on a single particle grain in a steady uniform flow, where w_t is the

particle weight.

When other particles are present there are also inter-granular forces to be considered. These forces and the forces between the particle and the fluid are known as contact forces, whereas gravity is a body force. The horizontal drag force F_D is the primary force, and is the sum of friction drag, and form drag. Form drag results from the pressure differences created by the flow over bed forms while skin friction is caused by the shear between the flow and the grains' surfaces. The nature of the bed itself including its roughness and sediment type, density, grain geometry and the density and viscosity of the water also effect the conditions under which the sediment transport may occur. The amount of drag is also dependent on the grain Reynolds number Re_* (Equation 1-5).

$$Re_* = \frac{Ud}{v} \qquad\qquad (1\text{-}5)$$

where d_s is the sediment grain diameter, v is the viscosity of water.

Gravity, and any contact forces between particles act as stabilising forces. The bottom shear stress may be written as:

$$\tau_b = \frac{F_D}{A} \qquad\qquad (1\text{-}6)$$

Where F_D is the horizontal drag force, and A is the surface area of the grain.

The seminal work by Shields, (1936) defined the dimensionless form of bed shear stress θ (Equation 1-4), and from this the critical Shields parameter for sediment motion θ_{cr}, which defines the threshold value of sediment motion (i.e., the critical bed shear stress). Shields plotted θ as a function of Re_* giving the Shields curve (Figure 1-5).

The figure shows a graph with y-axis labeled "Critical Shields Stress $\theta_c = \dfrac{\tau_o}{(\rho_s - \rho)gD}$" and x-axis labeled "Boundary Reynolds Number $R_{e^*} = \dfrac{\mu_* D}{v}$".

Y-axis values: 1.0, 0.8, 0.6, 0.5, 0.4, 0.3, 0.1, 0.08, 0.06, 0.05, 0.04, 0.03, 0.02. X-axis values: 0.2, 0.4, 0.6, 1, 2, 4, 6, 8, 10, 20, 40, 100, 200, 500, 1000.

Inside the plot: $\dfrac{D}{v}\sqrt{0.1\left(\dfrac{\rho_s}{\rho} - 1\right)gD}$

Upper diagonal scale: 2, 4, 6, 8, 10, 20, 40, 60, 100, 200, 400, 1000

Label: Shields curve
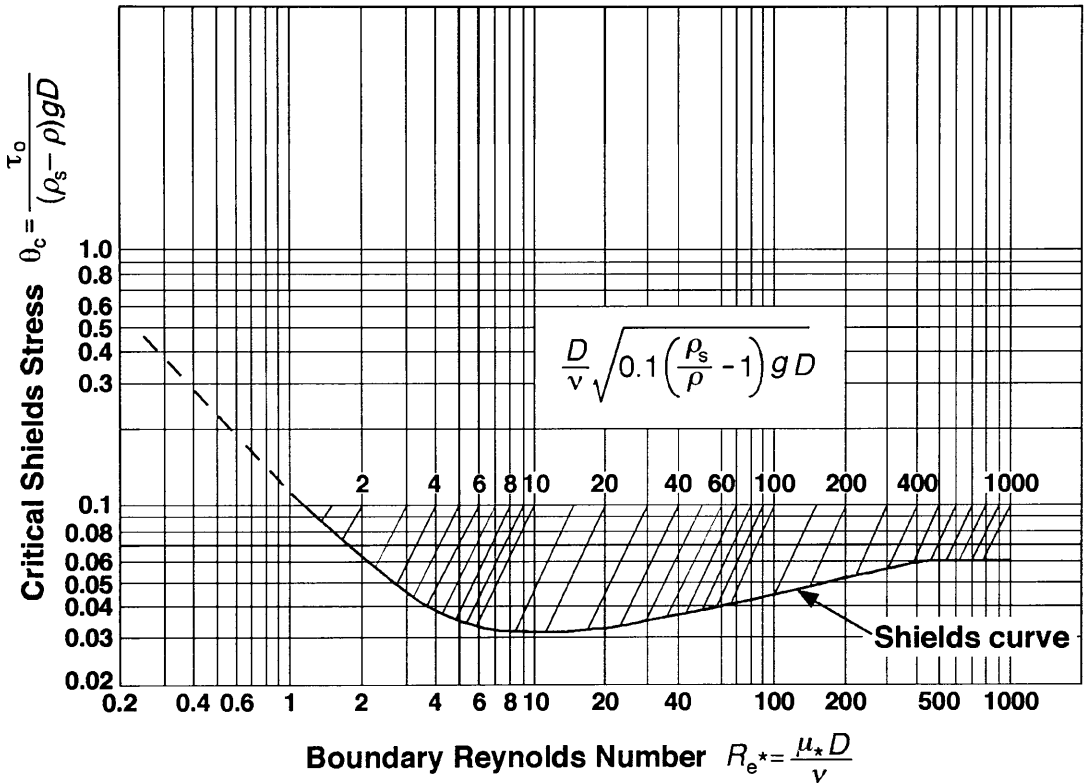
Figure 1-5 Shields curve showing θ plotted against Re_*, after Shields, (1936)

Soulsby, (1997) adapted the shields curve to plot θ_{cr} against the dimensionless grain size D_* (Equation 1-7) in Figure 1-6.

$$D_* = \left[\frac{g(s-1)}{v^2}\right]^{\frac{1}{3}} d \qquad\qquad (1\text{-}7)$$

where D_* is the dimensionless grain size.

Equation (1-7) can be used to obtain the value of critical Shields parameter value for sediment motion on an initially flat bed, (Soulsby, 1997). Soulsby and Whitehouse,

(1997) developed the following improved expression for the threshold shields parameter in Equation 1-8.

$$\theta_{(cr)} = \left[\frac{0.3}{1+1.2D_*}\right] + 0.055^*[1 - \exp(0.020D_*)] \qquad (1\text{-}8)$$
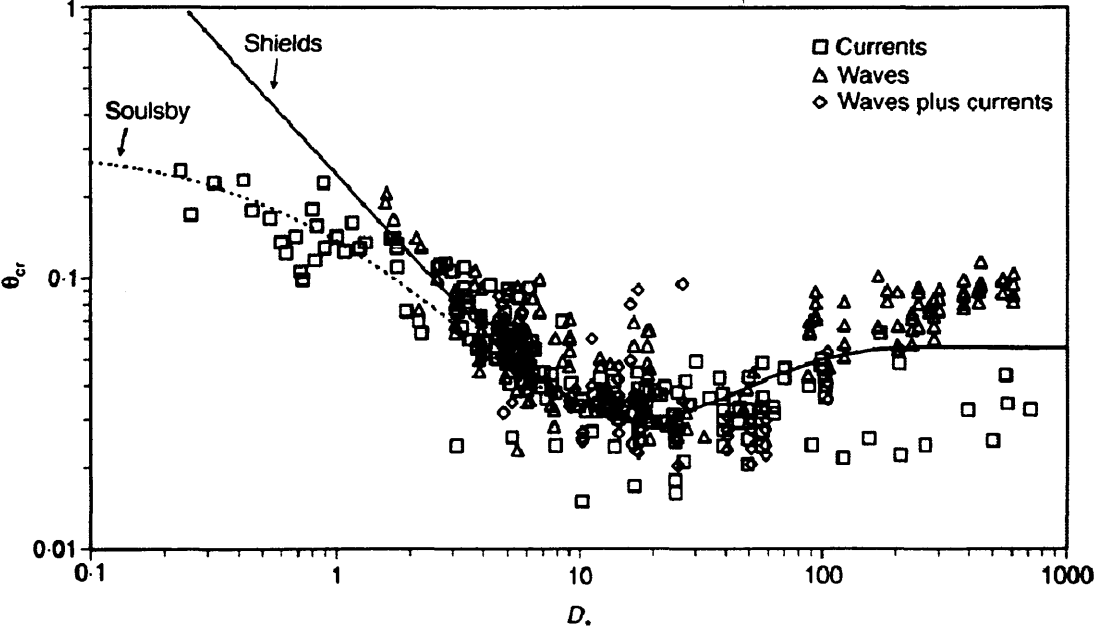
Figure 1-6. Adapted shields curve from experimental data. Here θ_{cr} is plot against the dimensionless grain size D*. Soulsby, (1997).

By combining Equation 1-8 with the friction law given in Equation 1-9, the Soulsby formula for threshold current speed is given in Equation 1-10, (Soulsby, 1997).

$$\frac{u_*}{\overline{U}} = \frac{1}{7}\left(\frac{d_{50}}{h}\right)^{\frac{1}{7}} \qquad (1\text{-}9)$$

where h is water depth and $\overline{U}$ is the depth-averaged velocity.

$$\bar{U}_{cr} = 7 \left(\frac{h}{d_{50}}\right)^{\frac{1}{7}} [g(s-1)d_{50}(D_*)]^{\frac{1}{2}}, \text{ for } D_* > 0.1 \qquad (1\text{-}10)$$

For sediments on a sloping bed, such as that of a scour hole, the force of gravity becomes important. Gravity may act to increase or decrease the threshold of motion depending on whether the flow of water is up or down the slope.

1.2.5 Sediment Transport Rate

For scour to occur, the entrained sediment must be transported away from the site for the hole to develop. The sediment transport rate q_b, though difficult predict in the field, is through experimental data and theory, proportional to the cube of the shear velocity, (Brown et al., 2005).

$$q_b \propto u_*^3 \qquad\qquad\qquad (1\text{-}11)$$

1.3 The Local Flow Field around a Vertical Monopile

Scour is the result of the increased velocity and turbulence in the local flow field around a vertical monopile. In the case of a single monopile whose height spans the entire depth of the flow and is subject to a unidirectional and steady current, the structure of the flow field are shown in Figure 1-7. Flow around monopiles in the marine environment is more

complex than in unidirectional flow, because of the presence of waves and tidal currents, (Sumer et al., 2001).
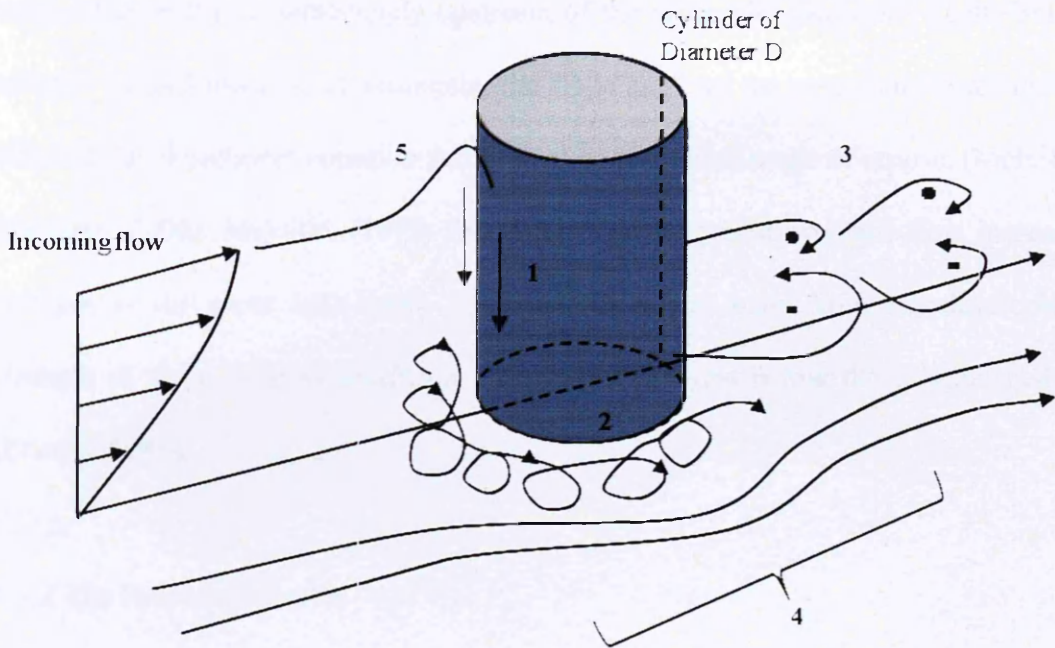
Figure 1-7. A schematic diagram of the flow field around a monopile in a current where [1] is the downflow, [2] is the horse-shoe vortex, [3] are the wake vortices, [4] is the constriction of flow and [5] is the surface roller. After Ettema et al., (1998).

The main features of the flow field are given in Figure 1-7. Each of the main features of the flow field illustrated in Figure 1-7 will now be discussed individually.

1.3.1 The Downflow

Incoming flow approaching the monopile is forced to stagnate at its front surface. Due to the logarithmic structure of the velocity profile the stagnation pressure

decreases with depth creating a downward pressure gradient, (Whitehouse, 1998). This drives the downflow towards the bed ([1] in Figure 1-7). The downflow acts to erode a hole in the sediment immediately upstream of the monopile. The walls of the hole then collapse inward towards the monopile; the slope angle of the scour hole is related to the fully saturated sediment cohesion and limited by its natural angle of repose, (Melville and Coleman, 2000). Melville, (1975) found that this vertical downward flow increased in strength as the scour hole depth increased. Once the scour hole has developed, the strength of the downflow reaches a maximum value just below the original bed level, (Ettema, 1980).

1.3.2 The Horseshoe Vortex

A circular or 'blunt' nosed monopile will form an adverse pressure field in front of the monopile; the pressure increases towards the monopile due to its presence slowing the flow. It is termed 'adverse' as pressure increases against the direction of flow. If the gradient in pressure is strong enough, (which is dependent on the flow properties and the monopile geometry) the approaching flow bed boundary layer will be forced into full three-dimensional separation. Once separated, the boundary layer rolls into a 'horseshoe' shaped vortex ([2] in Figure 1-7) both ahead and along the sides of the monopile, (Melville, 1975). Raudkivi and Sutherland, (1981) described the horseshoe vortex as analogous to a '...thick rope caught by the pier *[i.e. monopile]* with its ends trailing downstream...' The horseshoe vortex is a lee eddy and is an effective mechanism for removing sediment from the scour hole, (Breusers and Raudkivi, 1991). To form, the horseshoe vortex requires separation of the boundary layer. Before the scour hole starts to

develop, the point of separation is provided by the adverse pressure gradient at the front face of the monopile. On a mobile bed, the separation point is shifted upstream to the lip of the scour hole, (Chiew, 1984). The horseshoe vortex, therefore, does not initiate scour but becomes a primary mechanism in entrainment and removal of sediment once the initial scour hole has developed, (Breusers and Raudkivi, 1991). The size of the horseshoe vortex grows as the scour hole deepens, (Melville, 1975). The translation of the horseshoe vortex downstream is due to the mean current flow; the vortex can extend for several monopile diameters depending on flow and monopile conditions until it loses its structure and becomes part of the general turbulence in the wake region.

In steady currents there has been extensive investigation of the horseshoe vortex such as investigations by Hjorth, (1975), Baker, (1979), Dargahi, (1989), Sumer et al., (2002b), and Dey and Raikar, (2007). Baker, (1979) suggests that the characteristics of the horseshoe vortex are dependent on the thickness of the boundary layer, δ/D (where δ is the thickness of the boundary layer and D is monopile diameter) and the monopile Reynolds number, Re_D (Equation 1-12).

$$Re_D = \frac{UD}{v} \qquad\qquad (1\text{-}12)$$

Smaller values of Re_D result in a smaller size of horseshoe vortex, and there is no vortex formation for very small values of Re_D. This is due to larger viscosity and more resistance to separation at low Re_D. Sumer and Fredsoe, (2002b) suggests that in the case of a turbulent boundary layer, the size of the horseshoe vortex may well *decrease* with

increasing Re_D due to increased turbulent momentum exchange between fluid layers. Such exchange may delay boundary layer separation.

Like with Re_D, the smaller the ratio δ/D, the smaller the horseshoe vortex. As the boundary layer is essential for separation to take place, (Sumer and Fredsoe, 2002b), if the ratio of δ/D is too small, there may not be any separation at all as a smaller boundary layer has a more uniform velocity distribution and the lack of sufficient gradient will inhibit separation.

Figure 1-8 shows the mean amplification of bed shear stress α (Equation 1-13) due the presence of the horseshoe vortex in a steady current along the centreline axis of the monopile with three different combinations of δ/D and Re_D, (Sumer and Fredsoe, 2002b). Maximum absolute values of α reach up to 7.

$$\alpha = \frac{\tau_b}{\tau_\infty} \qquad (1\text{-}13)$$

where α = bed shear stress amplification and τ_∞ = undisturbed (free-stream) bed shear stress, (e.g, Graf and Yulistianto, 1999).

Figure 1.9 shows bed shear stress amplification around the circumference of half of the monopile dissected along the centreline axis. Here the bed shear amplification reaches as high as 11 at the midpoint between the front and side edge of the monopile. It is apparent here that the combination of flow constriction (§1.3.5) and the horseshow vortex raises α

more so than the horseshoe vortex alone (Hjorth, 1975). Work by Niedoroda and Dalton, (1982) on the dynamics of shear stress around a monopile in a steady flow built on the measurements made by Hjorth, (1975). They detected an increase in bed shear stress under the horseshoe vortex of up to 12 times that of the surrounding bed. Closer analysis of the data from Hjorth, (1975) by Whitehouse, (1998) at a given h/D indicates maximum α varies slightly with flow speed U and an overall increase with Re_D. Baker, (1979) demonstrated amplification in local bed shear stress due to the horseshoe vortex by a factor of 7 to 11.
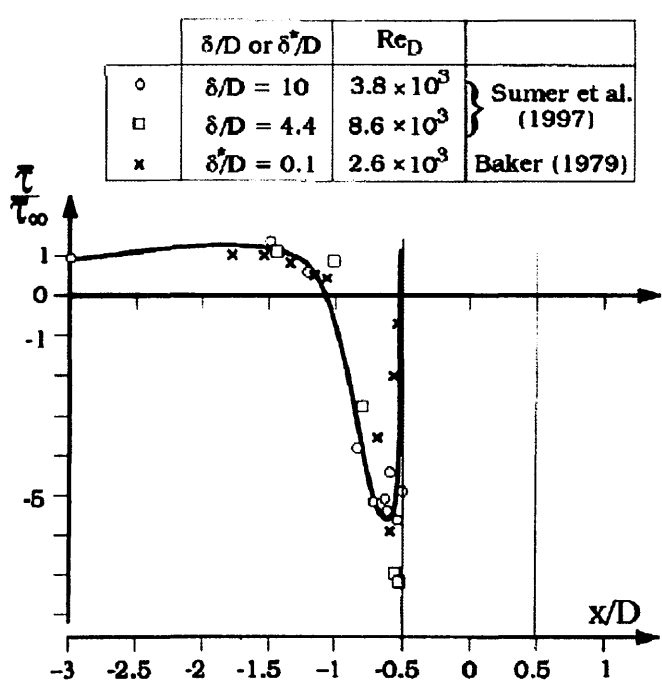
Figure 1-8. Bed shear stress amplification α on the upstream centreline approach to the monopile due to the horseshoe vortex; after Sumer and Fredsoe, (2002b).
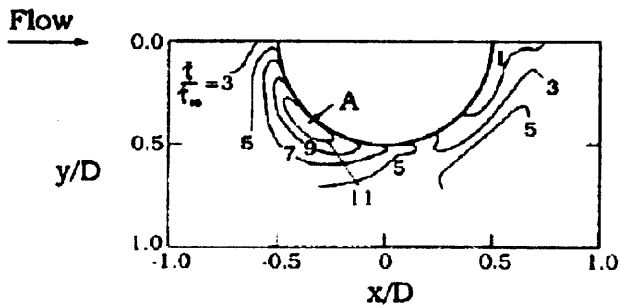
Figure 1-9. Bed shear stress amplification around the vertical monopile viewed from above where $D = 7.5$ cm, $U = 0.3$ m s^{-1}, $\delta/D = 2.7$, $Re_D = 2.3 \times 10^4$; Hjorth, (1975).

1.3.3 Lateral Boundary Layer Separation

Vortex formation and shedding in the wake of a vertical monopile is well researched (e.g. Hung, 1968, Gerrard, 1978, Williamson, 1989, Breusers and Raudkivi, 1991, Sumer et al., 1997, Sumer and Fredsoe, 2002a and Sumer and Fredsoe, 2002b). Vortex formation in the wake is a consequence of separation of the boundary layer that is attached to the surface of the monopile (Figure 1-10a-c). This separation happens due to the increase in flow velocity as it is deflected around the monopile. Separation occurs due to the adverse pressure gradient created by the changing velocity around the obstacle: if the adverse pressure gradient is strong enough, the boundary layer flow will stagnate and eventually reverse to form a large, slow eddy. Separation in laminar boundary layer flow occurs more readily than in turbulent boundary layer flow as in turbulent flow the free flow above the layer is more able to add momentum to the boundary layer helping it to overcome the adverse pressure gradient. A streamlined object also reduces the tendency for boundary layer separation by increasing the momentum of the flow. As the flow in the boundary layer passes around the surface of the monopile it will stagnate at the front face

1-21

where pressure will be high (Figure 1-10c). It will then increase in velocity and as a result decrease in pressure as it passes round the outline of the monopile to a maximum at the side edge, after which it will begin to decrease in velocity while pressure increases (Figure 1-10c).

If the adverse pressure gradient set up by the flow constriction (§1.3.5) at the rear of the monopile is strong enough, the highly-sheared boundary layer will be unable to push through the increase in pressure and will be forced to separate (Figure 1-10b). It is the vorticity in this sheared boundary layer that creates the separated eddies, as will be discussed in §1.3.4.

a)

b)

Boundary layer

Shear layer
(Wake region)

Vorticity

c)

Minimum
pressure

Steeply rising
pressure

Falling
pressure

Separation

Stagnation
point
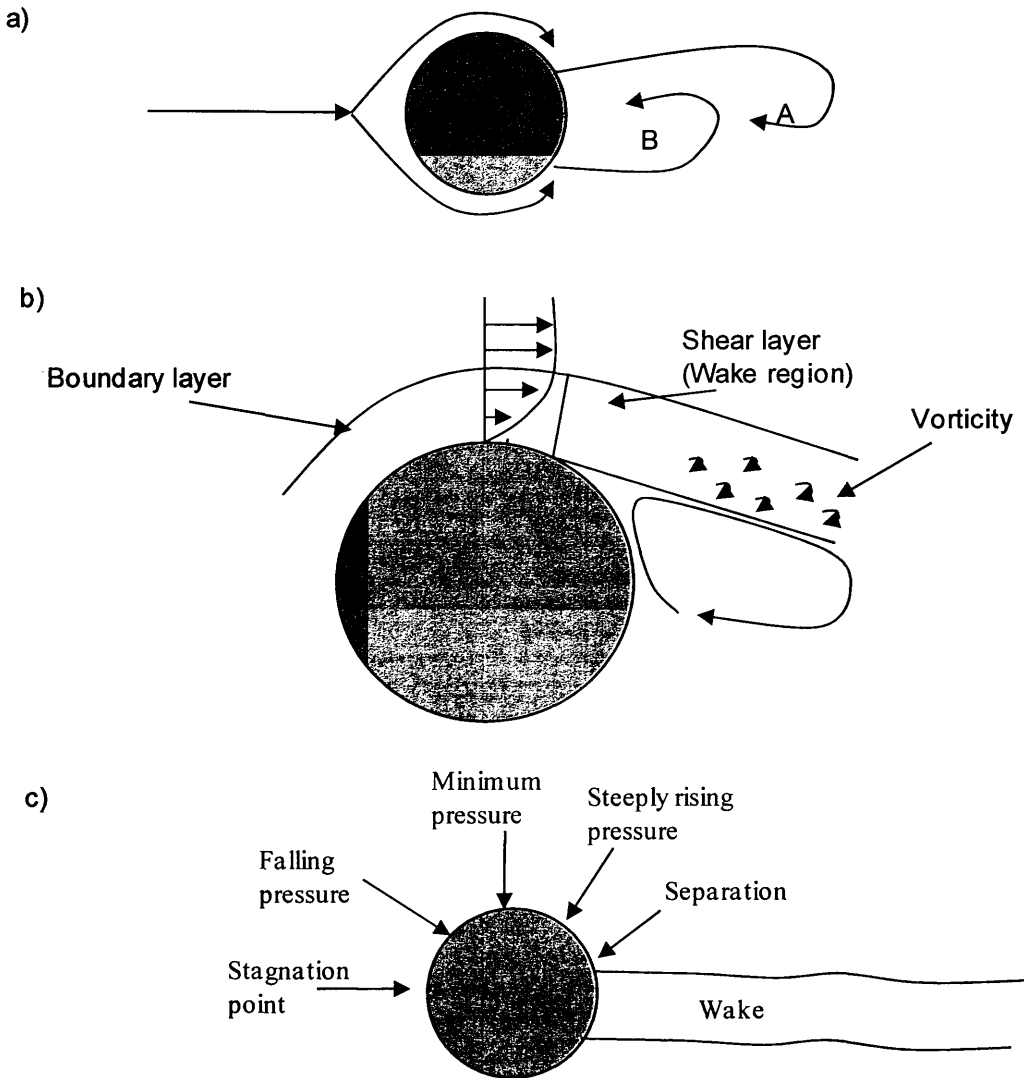
Wake

Figure 1-10a-c. Schematic top view diagram showing: a), vortex separation in the monopile wake, b) lateral boundary layer shear, and c) the changes in pressure of the fluid in the boundary layer as it travels around a typical cylindrical monopile to the point of separation. After Gerrard, (1966).

The pressure field around a typical blunt monopile was measured in detail by Hung, (1968). The nature of the flow separation regime around the monopile is dependent on

Re_D. Figure 1-11 shows the different regimes of flow around a smooth monopile under steady currents.

a)	No separation. Creeping flow	$Re_D < 5$
b)	A fixed pair of symmetric vortices	$5 < Re_D < 40$
c)	Laminar vortex street	$40 < Re_D < 200$
d)	Transition to turbulence in the wake	$200 < Re_D < 300$
e)	Wake completely turbulent A: Laminar boundary layer separation	$300 < Re_D < 3 \times 10^5$ Subcritical
f)	A: Laminar boundary layer separation B: Turbulent boundary layer separation: but boundary layer turbulent	$3 \times 10^5 < Re_D < 3.5 \times 10^5$ Critical (Lower transition)
g)	B: Turbulent boundary layer separation: boundary layer partly laminar partly turbulent	$3.5 \times 10^5 < Re_D < 1.5 \times 10^6$ Supercritical
h)	C: boundary layer completely turbulent at one side	$1.5 \times 10^6 < Re_D < 4 \times 10^6$ Upper transition
i)	C: boundary layer completely turbulent at two sides	$4 \times 10^6 < Re_D$ Transcritical
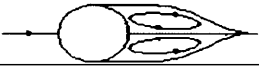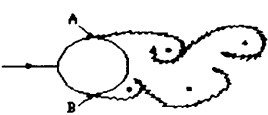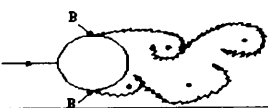
Figure 1-11a-i. Schematic diagrams of the various regimes of flow for a range of monopile Reynolds number. After Sumer, (2002a).

1.3.4 Formation and Shedding of Vortices

Vortex formation is a consequence of separation (section 1.3.3); where there is no separation (Re_D < 5 Figure 1-11a) there are no vortices. Figure 1-11 implies that vortex shedding will only occur at Re_D > 40. As Figure 1-12 demonstrates, the boundary layer formed along the monopile sides contains significant vorticity ω. Vorticity in the boundary layer upstream of the separation point is fed into the shear layer downstream of the separation point (Figure 1.10b). This causes the shear layer to roll into a vortex of the same sign of rotation as the incoming vorticity, with a vortex of opposite sign being formed on the opposite side (vortices A and B respectively in Figure 1-10a). Shedding occurs due to disturbances to the pair of vortices at Re > 40. Gerrard, (1966) gives a detailed description of vortex shedding, the main features of which will be described here.
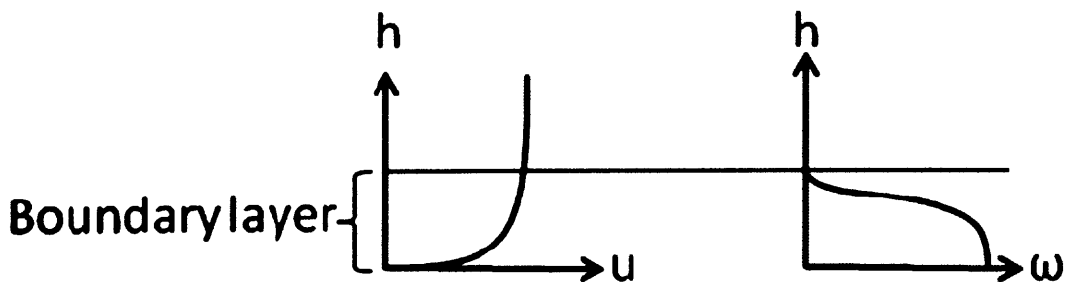
Figure 1-12. Schematic diagrams of velocity and vorticity within the boundary layer where $\omega = 1/2 \, \delta_u/\delta_h$. From Sumer and Fredsoe, (2002a).

As shown in Figure 1-10a, as vortex A grows larger it draws vortex B across the wake towards it. The opposite rotation sign of vortex B will cut off vortex A from its feed of

vorticity from the boundary layer. Vortex A is therefore shed and advected downstream by the general flow. Once Vortex A is shed, a vortex forms in its place as vortex C, (Figure 1-13a). Vortex C then is drawn towards vortex B which is then cut off and shed, and this process continues for as long as there is sufficient vorticity supply from the boundary layers at either sides of the monopile, (Figure 1-13b).
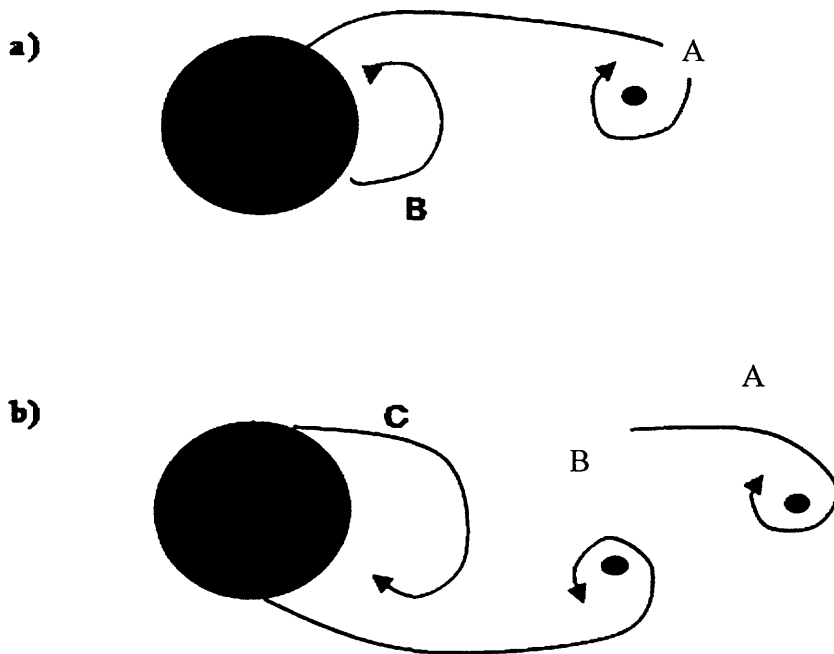
Figure 1-13. a) Vortex B is drawn across the wake towards vortex A, eventually causing vortex A to shed. b) Vortex C is drawn across the wake towards vortex A, eventually causing vortex B to shed. After Gerrard, (1966).

Vortex shedding frequency is represented by the dimensionless Strouhal number St:

$$St_D = \frac{f_v D}{U} \qquad (1\text{-}14)$$

where f_v is the vortex shedding frequency.

Figure 1-14 shows the relationship between St_D and Re_D for a smooth monopile surface. Shedding first occurs at $Re_D = 40$ at a Strouhal number just above 0.1. St_D increases to approximately 0.2 at $Re_D \approx 300$ and remains approximately constant until the critical boundary layer range is reached ($Re_D > 3 \times 10^5$, Figure 1-11e). St_D then jumps from 0.2 to approximately 0.45 when Re_D becomes critical (Figure 1-14). The increase in St_D in the supercritical flow regime is due to fully turbulent boundary layers at the separation points at both sides of the monopile (Figure1-11g). Separation of the boundary layer is delayed while the separation points move closer to the rear of the monopile resulting in quicker interaction between the now closer together vortices, resulting in faster rates of shedding. St_D remains high (decreasing slowly with Re_D) across the super-critical range until the upper transition range is reached. The drop in St_D in the upper transition range relates to the fact that the boundary layer on one side of the monopile has become fully turbulent (Figure 1-11h). This results in asymmetric vortex formation, which partly inhibits the shedding, resulting in the lower value of St_D. In the transcritical range (Figure 1-11i) the regular shedding is re-established.
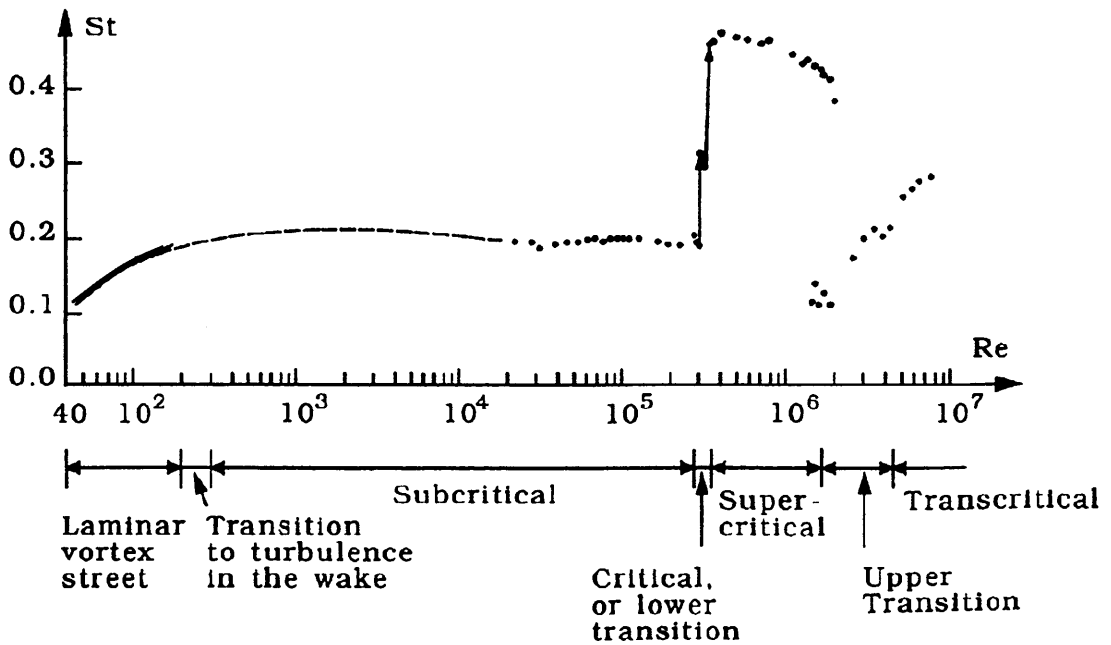
Figure 1-14. The Strouhal number of a smooth monopile as a function of Re_D from Sumer,

(2002a). This figure contains experimental data from: Williamson, (1989, solid line); Roshko,

(1961, dashed line) and; Schewe, (1983, dots).

1.3.5 Constriction of Flow

Flow constriction occurs because as the flow comes into the vicinity of the monopile its velocity is forced to increase in order to conserve continuity (Whitehouse, 2004, and [4] in Figure 1-7). This flow constriction can result in scour due to increased bed shear stress, particularly in conjunction with the strong presence of the horseshoe vortex, (Figure 1-9).

1.3.6 Sediment Transport in the Wake

Numerous investigators including Shen et al., (1966) have observed a general up-flow downstream of the monopile. This is related to the wake vortices which act as 'vacuum cleaners' in lifting particles off the downstream bed. The scouring effect of the wake vortices is generally less than the horseshoe vortex, (Melville, 1975). Their effect is manifest as a shallow scouring pattern downstream of the monopile. They are, however, effective at transporting sediment away from the monopile. The velocity profile downstream of the monopile causes the vortices to bend. The bottoms of the vortices interact with the shedding horseshoe vortex and cause it to oscillate laterally and vertically with the wake-vortex shedding frequency, (Breusers and Raudkivi, 1991).

The main non-dimensional parameter describing the wake vortex flow is the monopile Reynolds number Re_D, which dictates the point of separation, and the regime of separation (i.e., the classification of the monopile boundary layer - broadly as turbulent, intermediate or laminar, Tritton, 1990). The wake vortices act as a sediment removal mechanism, carrying scoured sediment downstream of the monopile, (Sumer and Fredsoe, 1999).

1.3.7 The Surface Roller

The surface roller [5] is created at the surface, similar to the bow wave of a ship travelling through water. In large flow depths, the surface roller is of little significance to scour at the base of the monopile. At small values of flow depths in comparison to monopile

diameter, the roller may act to interfere and ultimately weaken the downflow, (Ettema et al, 1998a and Melville and Coleman, 2000). The surface roller has an opposite sign of rotation to the horseshoe vortex at the bottom of the monopile. In the depths generally associated with those of offshore wind turbines the surface roller should not be significant. As such, it is not considered significant in this thesis.

1.4 Scour around a Single Vertical Monopile

The flow field described above and in Figure 1-7 will, if velocities and turbulence are high enough, increase the local sediment transport around the monopile and create a scour hole. Figure 1-15 shows the typical shape such a scour hole may assume. Scour around a monopile can be divided into three different types: local scour, global scour and general scour. Local scour forms as a steep sided depression in the immediate vicinity around the monopile, (Figure 1-15), global scour is a depression around the structure that is much wider than the local scour hole but also much shallower. General scour is a term given to the general sediment erosion occurring in the vicinity of the monopile but not induced by the structure.

Knowledge of local scour and its maximum depth in a given set of conditions is of paramount importance in the design configuration of the monopile. Local scour over time will reduce the depth of sediment that the monopile is driven into and thus adversely affect its stability. This section summarises the present knowledge of scour and its

development around a monopile, as this is important background information before identifying the areas which this thesis will address.
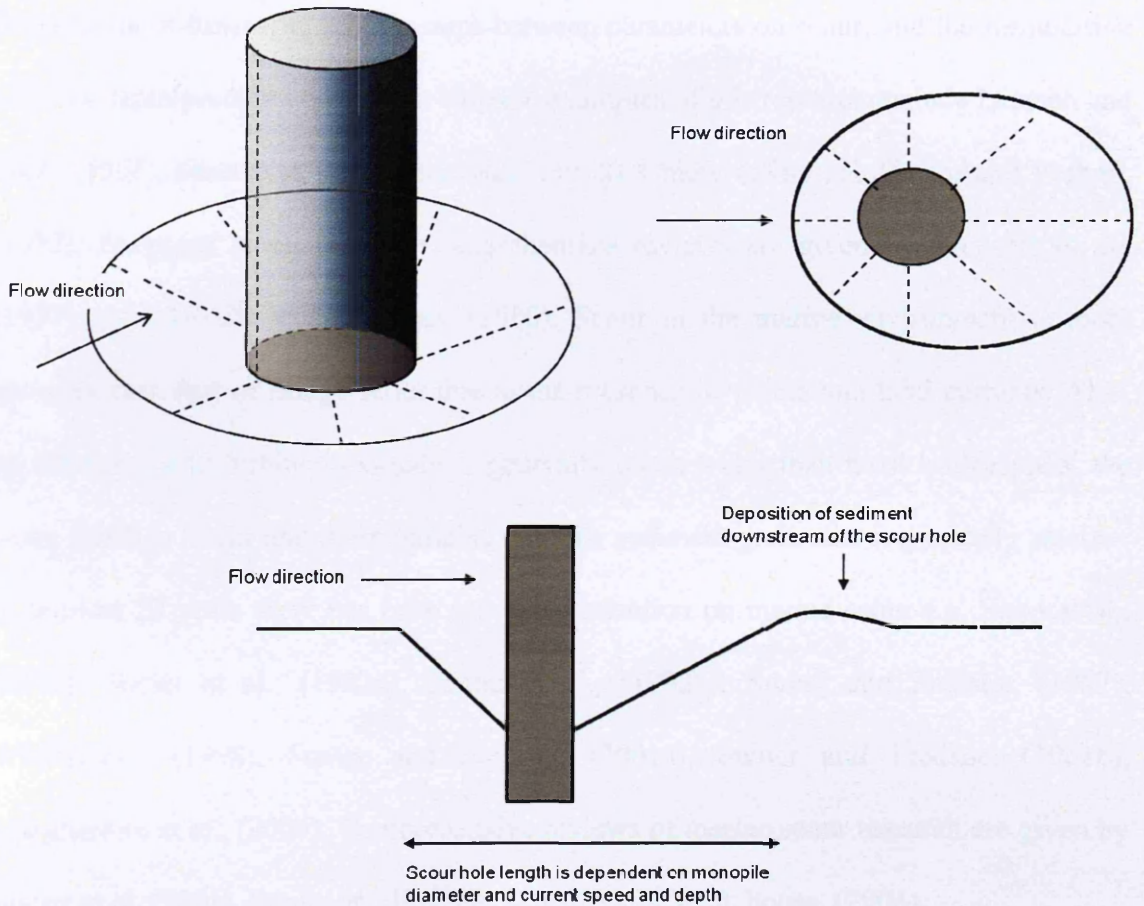
Figure 1-15. Schematic diagrams of the typical shape of the scour hole that may form at the base of a vertical monopile subject to a unidirectional current (e.g., Melville and Coleman, 2000). Note the elongated shape downstream and the depositional mound of sediment on the downstream lip of the scour hole.

Local scour around a single vertical circular monopile in steady unidirectional currents is quite well understood. Many studies exist that look at the problem of scour around the

foundations of bridge piers as it is one of the main causes of bridge failure. The bridge

scour phenomenon is studied primarily by laboratory scale models which look at a variety

of issues including; the time development of scour, the spatial characteristics of scour, the

formulation of functional relationships between parameters on scour, and the formulation

of scour depth predictor equations. Notable examples of this research include Laursen and

Toch, (1956), Shen et al, (1969), Melville, (1975), Chiew, (1984), Hoffmans and Verheij,

(1997), Sheppard et al, (2004). Comprehensive reviews are given by Breusers et al.,

(1977) and Melville and Coleman, (2000). Scour in the marine environment is more

complex than that of bridge scour due to the presence of waves and tidal currents. Also,

an offshore wind turbine monopile is generally much wider than most bridge piers, the

water depth is larger and more variable, and the sediment grain size is generally smaller.

In the last 20 years there has been increased attention on marine scour e.g. Saito et al.,

(1990), Sumer et al., (1992a), Sumer et al., (1992b), Sumer and Fredsoe, (1997),

Whitehouse, (1998), Sumer and Fredsoe, (2001a), Sumer and Fredsoe, (2001b),

Margheritini et al., (2006). Comprehensive reviews of marine scour research are given by

Sumer et al, (2001), Sumer and Fredsoe, (2002b) and Whitehouse, (2004).

1.4.1. Parameter Influence on Local Scour

A great deal of the research of scour at a vertical monopile has been directed towards the

determination of equilibrium scour depth, d_{sc} for a given set of conditions and the

analysis of functional relationships between individual parameters affecting scour and

d_{sc}. d_{sc} is the most important quantitative measure of scour for the design of foundations.

d_{sc} indicates the maximum expected depth of scour under normal flow conditions, though

storm events may increase scour depth beyond d_{sc}. Studies of d_{sc} are often carried out via laboratory-based scale models which use dimensional analysis to determine the key parameters that affect scour. The following functional relationship between the dimensionless scour depth, d_{sc}/D and the major influencing non-dimensional variables is commonly referred to in the literature (e.g. Breusers et al, 1997 and Melville and Coleman, 2000):

$$\frac{d_{sc}}{D} = f\left(\frac{U}{U_c}, \frac{U^2}{gD}, \frac{h}{D}, \frac{D}{d}, \frac{\rho U D}{\mu}, \frac{\rho_s}{\rho}, \Phi, \sigma_g, G, Sh, Al\right) \tag{1-15}$$

where ρ = fluid density; μ = fluid dynamic viscosity; U = mean velocity of approach flow; U_c = the critical velocity associated with sediment mobility; h = flow depth; D = monopile diameter; g = gravitational acceleration; d = particle diameter; ρ_s = sediment density; ρ = density of water; Φ = angle of static sediment repose; σ_g = standard deviation of the sediment grain size distribution; G describes the effect of lateral shear in the approaching flow; Sh describes influence of the shape of the monopile and Al describes the alignment of the monopile to the approaching flow. For circular monopiles, Sh and Al are not important.

U/U_c is the flow intensity, which is the ratio of free-stream velocity U to the critical velocity for the initiation of sediment motion U_c. U^2/gD is the Froude number, which describes the ratio of inertial forces to gravitational forces acting on a fluid particle. h/D is ratio of water depth to the monopile diameter. D/d is the relative grain size. $\rho U D / \mu$. Is the monopile Reynolds number ρ_s / ρ is the relative sediment density.

1.4.2 The Effect of U/U_c

U/U_c is the flow intensity and its value determines whether 'clear-water' or 'live-bed' conditions prevail. Live-bed conditions are those where the velocity of the approaching undisturbed flow is high enough to generate sediment motion on the bed. Clear-water conditions are those where the undisturbed flow velocity is less than that needed to move sediment on the bed. When $U/U_c < 1$ clear-water scour conditions exist and $U/U_c > 1$ live-bed scour conditions prevail, where U_c is the threshold current velocity for the motion of sediment. This is true if $\sigma_g < 1.3$, where the sediment behaves as if it were of uniform grain size.

The scouring process is asymptotic under clear-water conditions (Figure 1-16a) and equilibrium scour depth d_{sc} is achieved at a slower rate than for live-bed conditions. Once achieved, however, clear-water d_{sc} is more stable than the live-bed d_{sc}. Live-bed d_{sc}, though reached faster than clear-water d_{sc}, is subject to depth fluctuations due to passing bed-forms and variations in sediment influx and outflow within the scour hole, (Melville and Coleman, 2000, and Figure 1-16a). Figure 1-16b shows the relationship between d_{sc} and Shields parameter θ. Clear-water scour has a strong relationship with θ; for small values of θ there is not enough amplification of bed shear stress near the monopile to create scour at all, but as θ increases scour depth increases rapidly to a maximum at the critical Shields parameter θ_{cr}. Here sediment transport occurs over the entire bed, including the area that is un-affected by the monopile. Live-bed scour has a much weaker dependency on θ as, in these conditions, changes in θ affect the whole bed,

both in and outside the scour area. Breusers and Raudkivi, (1991) suggests that the maximum equilibrium scour depth in clear-water conditions can be as much as 10% higher than equilibrium in live-bed conditions.
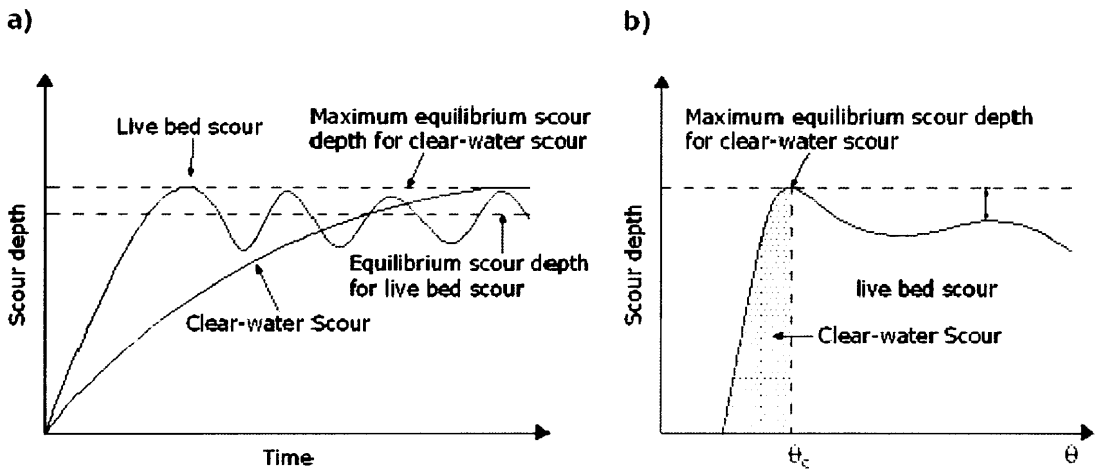
Figure 1-16a-b. a) Comparison of the time development of clear-water and live-bed scour. b) equilibrium scour depth against shields parameter θ, After Breusers, (1991).

In non-uniform sediments where $\sigma_g > 1.3$, the bed may 'armour'. Bed armouring occurs in non-uniform sediments where an increase in velocity can cause grains to rearrange themselves in to more stable configurations. If $\sigma_g > 1.3$, $U/U_c > 1$ but $U < U_a$ (where U_a = the critical velocity for bed armouring) then the bed sediment will act to armour itself as scouring takes place, (Henderson, 1966). In this situation clear-water scour may still exist even though $U/U_c > 1$. If $U/U_a < 1$ then there is no armouring, thus the bed is free to move and live-bed scour pertains. U/U_a is the flow intensity ratio for non-uniform sediment, (Raudkivi, 1986) and U_a is the equivalent to U_c in non-uniform sediment.

Under clear-water conditions in uniform sediments, local scour depth increases with U to a maximum at U_c. This maximum scour depth is the 'threshold peak' in uniform sediment. After this is reached, the local scour depth decreases initially before again increasing to the 'live-bed peak'. The threshold peak does not describe the transition between clear-water and live-bed scour if the sediment is non-uniform, (Melville, 2000): in such a case it is the armour peak that describes the transition, as described in Figure 1-17. These trends have been observed in the laboratory, (e.g., Shen et al, 1966; Ettema, 1980; Raudkivi and Ettema, 1983; Chiew, 1984 and Baker, 1986).
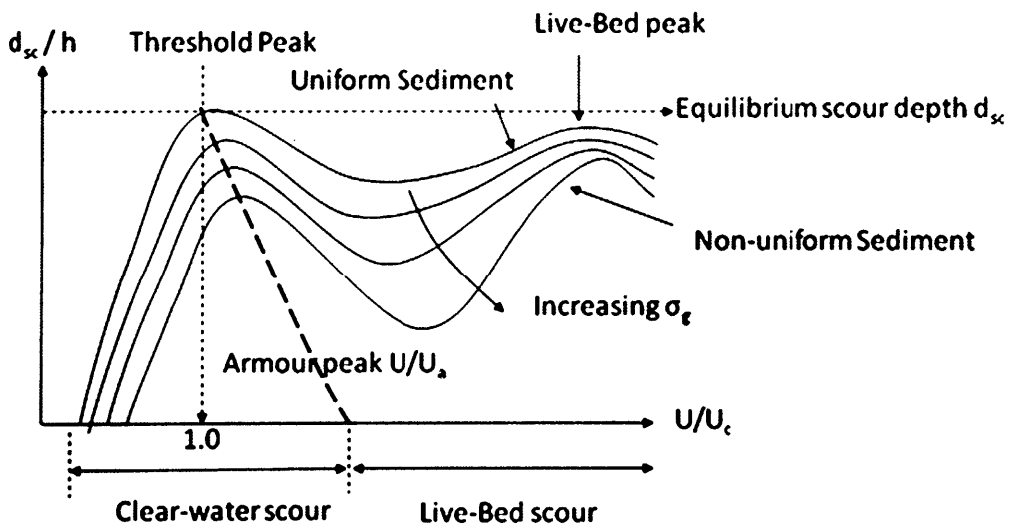
Figure 1-17. Variation of scour depth with U/U_c and σ_g. After Melville, (2000).

1.4.3 The effect of h/D

The parameter h/D represents the ratio of the depth of the approaching flow to the diameter of the monopile. Scour depth increases as h/D increases up to a limiting value after which scour depth becomes independent of the ratio (for example, Ettema, 1980, Chiew, 1984 and Melville and Coleman, 2000). Chiew, (1984) suggests a limiting ratio value of h/D between approximately 1 and 3 for both clear-water and live-bed scour. Deeper flows show scour depth to be almost independent of h, (Breusers and Raudkivi, 1991). They cite that many authors state that for $h/D > 1$ or 2 in constant flow over uniform sediment, the effect of depth may be neglected. However, they argue that this characteristic is not clearly separated from experimental phenomena and conclude that $h/D > 3$ is a safer limit. Discussion by Breusers et al., (1977) on the influence of h/D do not distinguish between clear-water and live-bed scour.

In shallower flow, the surface roller may interact with and weaken the downflow and at very shallow flows it would interfere with the horseshoe vortex acting to weaken its effect, thus reducing the scouring ability of these phenomena, (Melville and Coleman, 2000).

1.4.4 The Effect of D/d

The parameter D/d is the ratio of monopile diameter to sediment grain size (usually the median grain size d_{50}). Clear-water experimental data obtained by Ettema, (1980) over

six piers with D from 28.5 - 240 mm and $d_{50} = 0.24 - 7.80$ mm showed that the maximum value of d_{sc}/D was unaffected by sediment size when $D/d_{50} > 25$. For smaller values of D/d_{50} the grains are larger relative to the size of the groove excavated by the downflow. The contribution of the downflow is lessened due to the increased porosity of the bed absorbing much of the energy of the downflow. Ettema, (1980) found that initial scour developed similarly for most values of D/d_{50}. The development of the scour hole and the equilibrium phase are, however, affected by D/d_{50}. When $D/d_{50} < 8$ Ettema, (1980) showed that because the individual grains were relatively large compared to the pier, scour is mainly confined to the sides of the pier and d_{sc}/D is reduced further. Ettema, (1980) also found that for $d_{50} < 0.7$ mm scour depth was limited due to the sediment's tendency to ripple even where $U < U_c$. Chiew, (1984) investigating the live-bed case, found that d_{sc} was influenced by grain size for $D/d_{50} < 50$.

1.4.5 The Effect of Monopile Froude Number Fr_D and Monopile Reynolds Number Re_D

The monopile Froude number can be thought of as the ratio of stagnation pressure head $U^2/2g$ to D. Data from Ettema et al., (1998) suggests that d_{sc}/D increases with increasing monopile Froude number. Their data, however, are too limited to quantify the influence of Fr_D on d_{sc}.

Fr_D is usually considered more important than Re_D, particularly if the flow is turbulent (for example, Ettema et al., 1998a). An increase in Froude number may result in an increase in d_{sc}/D according to data from Ettema et al., (1998) though Melville and

Coleman, (2000) suggests that this observation cannot be confirmed as that particular data set was too small. Johnson and Ting, (2003) found that Froude number relates to the relative water depth around the monopile, however they also produced data to suggest Re_D was more influential on the flow field and depth of scour than the Froude number. Clearly, the role of Re_D and Fr_D are not fully understood, and this is one of the areas that this thesis aims to elucidate.

1.4.6 Sediment Characteristics

Grain size is the most influential sediment property on scour (e.g., Melville and Coleman, 2000). For uniform sediments, the grain size is the same for all grains. Non-uniform sediments require description by geometric standard deviation σ_g of the grain-size distribution. The effects of sediment non-uniformity on scour depth for the live-bed case have been studied by Ettema, (1980), Chiew, (1984) and Baker, (1986).

Heterogeneity in the bed sediment, particularly in the field, is important as different layers of sediment may have different resistances to erosion. For example, a resistant material above a more erodible material may result in large scour depths when the first layer is broken through. Heterogeneity is often a three dimensional characteristic in sediments and the depth to bed rock may also be a limiting factor in maximum or equilibrium scour depth.

1.4.7 Monopile Shape

Wind turbine monopiles are uniform circular cylinders, and span the whole water depth. Circular monopiles produce lower scour depths that non-circular monopiles. For example, a square monopile will generate a larger horseshoe vortex across its larger leading surface, and also generate a larger separation zone.

1.4.8 Scour Hole Shape

In unidirectional currents, the shape of the scour hole can be approximated by truncated cone (Figure 1-18a and b). It is asymmetrical with a smaller diameter and steeper slope at the upstream side, and a larger diameter and shallower slope at the downstream side. The dimensions of a scour hole can be described by the angles that the slopes of the scour hole upstream ($\alpha_{upstream}$), and downstream ($\alpha_{downstream}$) make with the original flat bed. $\alpha_{upstream}$ is, once d_{sc} is reached, approximately equal to the angle of repose for the sediment grain size and properties (Hoffmans and Verheij, 1997). $\alpha_{downstream}$ is approximately equal to 25° according to Sumer and Fredsoe, (2002b) though Hoffmans and Verheij, (1997) suggest that $\alpha_{downstream}$ is approximately equal to $1/2\, \alpha_{upstream}$. The sides of the scour hole perpendicular to the flow direction are similar in slope angle to $\alpha_{upstream}$, (De Vos, 2008).
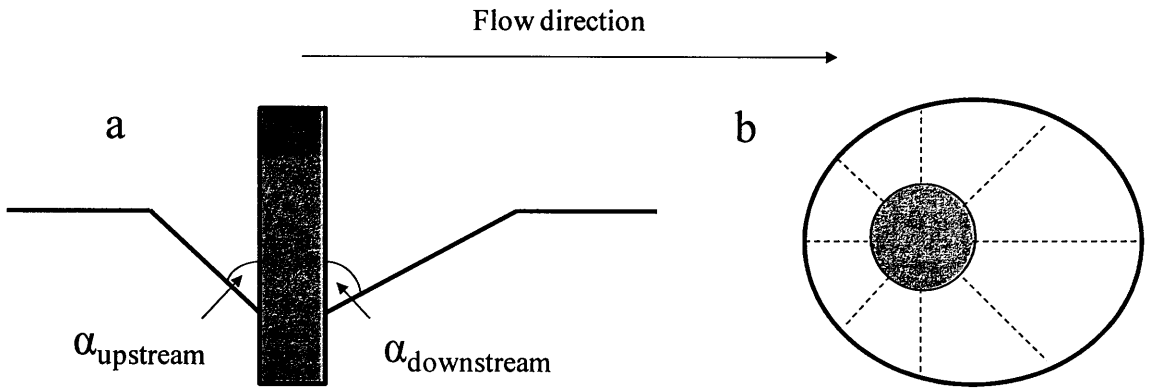
Figure 1-18a and b. Cross-sectional (a) and plan view (b) of the asymmetrical scour hole around a monopile or bridge pier in unidirectional flow.

Under tidal currents the scour hole assumes a more symmetrical shape due to the alternating direction of flow (Margheritini et al, 2006), with a slope angle that tends towards the shallower slope of α_{down} (Frigaard and De Vos, 2006).

1.5 Estimation of Scour Depth

There are numerous studies that look to determine accurate estimations of d_{sc} via formulation of predictor equations from extensive laboratory tests. These studies use the understanding of the flow dynamics around the pier/monopile which was outlined in §1.2, and the parameter influence on scour depth as outlined in §1.3, to derive empirical formulae that will predict d_{sc} for a given set of input parameters. Reviews of the many of these equations are found in Breusers et al., (1977) and Melville and Coleman, (2000) for

the case of bridge piers in unidirectional steady currents. Some of the most well used

equations for unidirectional current scour for non-cohesive soils will be summarised here.

In scour depth estimation, a common design approach is based upon the relation of the

main parameters to scour depth given in Equation 1-16. Thus, d_{sc} is a function of

empirical expressions (K) of the main scour influencing parameters (Melville, 1997 and

Melville and Coleman, 2000):

$$d_{sc} = K_{hD,}\, K_I,\, K_d,\, K_s,\, K_{AL},\, K_G,\, K_t \qquad (1\text{-}16)$$

Where K_{hD} = depth – size ratio; K_I = flow intensity; K_d = sediment size; K_s = pier shape;

K_{AL} = pier alignment; K_G = channel geometry and K_t = time.

The K's represent an empirical function or multiplying factor for each variable, the value

of which depends on the prototype. Melville, (1997) gives the following K_{hD} factors for

circular piers:

$$K_{hD} = 2.4D \qquad \text{for } h/D < 0.7 \qquad (1\text{-}17)$$

$$K_{hD} = 2\sqrt{hD} \qquad \text{for } 0.7 < h/D < 5 \qquad (1\text{-}18)$$

$$K_{hD} = 4.5h \qquad \text{for } h/D > 5 \qquad (1\text{-}19)$$

K_I, the flow intensity factor is given by:

$$K_I = U/U_c \qquad \text{for } U/U_c < 1 \qquad (1\text{-}20)$$

$$K_I = 1 \qquad \text{for } U/U_c > 1 \qquad (1\text{-}21)$$

K_d, the sediment size factor is given by:

$$K_d = 0.57 log \left(2.24 \frac{D}{d} \right) \qquad \text{for } \frac{D}{d} \leq 5 \qquad (1\text{-}22)$$

$$K_d = 1.0 \qquad \text{for } \frac{D}{d} > 5 \qquad (1\text{-}23)$$

K_t, is the time factor defined as the ratio of d_{sc} at a particular time t to the time to equilibrium d_{sc} at t_e (where t_e is the time to reach equilibrium scour depth):

$$K_t = 1.0 \qquad \text{for } U/U_c \geq 1 \qquad (1\text{-}24)$$

The Colorado State University (CSU) equation, (HEC 18, 1993) is one of the most widely used versions of this type of equation (e.g., Johnson, 1995). The equation (Equation 1-25) which was developed from laboratory data, can be used in both live-bed and clear-water situations, and may be written:

$$d_{sc} = 2.0hK_1K_2K_3 \left(\frac{D}{y}\right)^{0.65} Fr^{0.43} \geq 1 \qquad (1\text{-}25)$$

where K_1 = correction factor for pier nose shape; K_2 = correction factor for angle of attack flow; K_3 = correction factor for bed condition. These correction factors are given in tables in HEC 18, 1993.

Melville and Sutherland, (1988) developed the following scour formula with extensive laboratory testing, with the K factor values obtained from equations or graphs:

$$d_{sc} = K_I K_d K_h K_{AL} K_s D \qquad (1\text{-}26)$$

Breusers et al., (1977), through experimental data and comparison with data in the literature developed the following formula:

$$d_{sc} = DfK_1K_2(2\tanh[h/D]) \qquad (1\text{-}27)$$

where $f = 0$ for $U/U_c \geq 0.5$; $f = 2U/U_c - 1$ for $0.5 < U/U_c \leq 1$; $f = 1$ for $U/U_c > 1$.

Jain and Fischer, (1979) equation is based on laboratory experiments:

$$d_{sc} = 2.0D(Fr - Fr_c)^{0.25} \left(\frac{y}{D}\right)^{0.5} \qquad (1\text{-}28)$$

when $Fr - Fr_c > 0.2$, where Fr_c is the critical Froude number, and:

$$d_{sc} = 1.85D(Fr_c)^{0.25}\left(\frac{y}{D}\right)^{0.5}$$ (1-29)

when $0 < Fr - Fr_c < 0.2$ the larger of the two scour depths computed from equations 1-28 and 1-29 is used.

Sumer et al., (1992a) gives the following equation for the live-bed scour developed from laboratory data:

$$\frac{d_{sc}}{D} = 1.3$$ (1-30)

Whitehouse, (1998) developed the following clear-water scour equation:

$$\frac{d_{sc}}{D} = 1.3\left(2\sqrt{\frac{\theta}{\theta_c}} - 1\right)$$ (1-31)

where θ_c is the critical shields parameter for sediment motion.

Using design curves developed by Laursen and Toch, (1956), Neill, (1964) produced the following equation:

$$d_{sc} = 1.35D^{0.7}h^{0.3}$$ (1-32)

In a review paper by Johnson, (1995), seven commonly used equations' performances were compared using a large set of field data, including Equations 1-25, 1-26, 1-27, 1-28 and 1-32. Results showed Equation 1-27 to be the most reliable for general applications. Some equations were found to under predict scour, which is very undesirable for obvious safety reasons.

Mohamed et al., (2005) completed a comparison of the performance of Equations 1-25, 1-26, 1-28, 1-29 and 1-32 against experimental and field data. Statistical tests were used to evaluate predicted scour depths obtained from the application of the equations using field and model data. 1-25 and 1-32 appeared to give the best predictions with 1-26 and 1-28-1-29 over-predicting d_{sc}. The Melville and Sutherland, (1988) Equation 1-26 appeared to over-predict scour depth the most.

Both Johnson, (1995) and Mohamed et al., (2005) suggest the inaccuracies of the predictions given by these equations indicate that current understanding of the scour process is inadequate. As mentioned above, the equations described in this section were developed from unidirectional steady currents, and as such, their ability to accurately predict scour in tidal currents is uncertain.

1.6 Summary

Sediment transport will occur if the frictional force applied by the flow to the bed, known as shear stress τ_b [N m^2], is large enough to dislodge grains from their resting position. τ_b is proportional to the square of the flow velocity U. The quantification of τ_b and the identification of the threshold of motion have been discussed in this chapter.

The presence of the monopile in a flow causes distinct changes to the flow field which raise the value of bed shear stress around it. The main features of the monopile flow field have been described including; the downflow at the leading face of the monopile; the horseshoe vortex at the base and sides of the monopile; the contraction of flow at the monopile sides; and the wake vortex formation and shedding. These phenomena act to amplify bed shear stress up to 12 times that of the undisturbed value at certain areas around the monopile. It is this increase in τ_b that causes the scour at the base of the monopile, and the flow field encourages the removal of suspended sediment from the locality of the monopile. The result is the formation of a scour hole.

Many laboratory experiments have been conducted to determine the relationship of scour with the dimensionless parameters of flow, monopile geometry and sediment characteristics. Their influence on the maximum equilibrium depth of scour, which is of interest in terms of design of the monopile and mitigation of the scour around it, is discussed. A selection of the most common empirical formulae used for the estimation of scour depth is given. These formulae, which are based on laboratory measurements of

scour often over-predict scour at best, or worse under-predict it. Predicted scour depths range from 1 - 2.5 times the diameter of the monopile.

1.7 Literature Review

In this section an overview of the available monopile scour literature will be given. Following from this analysis of the literature, gaps in the current understanding will be identified and the aims and objectives of the thesis will be outlined.

Monopile scour in the field is well documented, with examples of marine scour given in Sybert, (1963), Dahlberg, (1983), ESS, (2003), Louwersheimer et al., (2006) and NPower, and of bridge pier scour in Melville, (2000). Understanding the mechanism of scour is vital for accurate prediction of its depth, time-development and effective mitigation (e.g., Melville and Raudkivi, 1977, Niedoroda and Dalton, 1982, Dargahi, 1987, Ettema et al, 1998b and Johnson and Ting, 2003). This chapter outlines three broad research themes concerned with scour at monopiles, reviews the work within each of these themes, and identifies further opportunities for research. The themes are 1) the flow field and mechanism of scour; 2) the evolution and equilibrium depth of scour; and 3) methods of reduction of scour by flow modification.

1.7.1 Flow Field and Mechanism of Scour

Scour is caused by the complex, three-dimensional modification of flow in the monopile's

vicinity due to its presence. The details of the current state of knowledge of the flow field and mechanism of scour were outlined in §1.3. To date, the study of local scour at a monopile has been primarily by the use of laboratory scale models under unidirectional flow; the large majority of these studies were motivated by a desire to understand bridge pier scour in rivers. There is a substantial amount of literature in this field and comprehensive reviews of this are given by Breusers et al., (1977) and Melville and Coleman, (2000). More recently interest in scour in the marine environment, where waves and tidal currents are important, has increased. Reviews of earlier works are found in Sumer et al., (2001) and Sumer and Fredsoe, (2002b) and more recent examinations include Whitehouse, (2004), Gothel and Zielke, (2006), Jensen et al., (2006), Louwersheimer et al., (2006), and Margheritini et al., (2006). Much of this research focuses on the formulation of equilibrium scour-depth predictor equations (as discussed in §1.5), parameter influence on scour through dimensional analysis (§1.4), and the time development of scour (§1.4). The equations that result from these experiments, however, can give scattered and sometimes contradictory results (e.g., Johnson, 1995 and Mohamed et al., 2005) which often over-estimate the equilibrium scour depth compared to field studies, (Ettema et al., 1998a). Such over-estimation of scour depth can lead to increased design and installation costs for the monopile and unnecessary scour protection measures. Limited knowledge of the flow field is a contributing factor to the inaccuracies in these equations (for example, Ettema et al., 1998a and Johnson and Ting, 2003). Further uncertainty in applying these equations to estimate marine scour depths arises due to the different flow and monopile parameters involved. Therefore, in order to increase understanding of the mechanism of scour in the marine environment and accurately predict its development around the monopile, a greater understanding of the flow field is

required. Such an increased understanding of the flow field should lead to better design equations, and aid the calibration of numerical models.

The structure of the flow field around a bridge pier has been studied in numerous investigations (e.g. Hjorth, 1975, Shen et al., 1966, Melville and Raudkivi, 1977, Niedoroda and Dalton, 1982, Dargahi, 1987, Dargahi, 1989, Kobayashi, 1994, Sarker, 1998, Ahmed and Rajaratman, 1998, Graf and Yulistiyanto, 1999, Graf and Istiarto, 2002, Johnson and Ting, 2003, Roulund et al., 2005 and Dey and Raikar, 2007), with a comprehensive review given by Sumer and Fredsoe, (2002a). Though numerous, these investigations still give an incomplete picture of the flow field, a consequence of its complexity. Since these investigations are focused on the flow and scour around bridge piers, the geometric and flow parameters are not easily scaled to typical marine prototypes: current velocities and Froude numbers are often larger in rivers while bridge pier diameters are generally smaller than typical offshore wind farm monopile parameters. There have been several investigations of the role of waves, steady currents, and the combination of the two on scour around offshore structures (for example Sumer et al., 1992, Sumer and Fredsoe, 2001b, with a review given by Sumer and Fredsoe, 2002b). However, there has been, to the authors' knowledge, no previous investigation of the dynamics of how the tidal changes in water depth and current speed may change the spatial characteristics and magnitude of flow and turbulence around the monopile during a tidal cycle. Whitehouse, (1998) suggests that the instantaneous flow field due to tides and waves is analogous to that of the bridge pier flow field, and to date studies of tidal current-induced scour at the monopile simplify the tide to an equal and opposite unidirectional current (see Escarameia, 1998, Jensen et al., 2006, and Margheritini et al.,

1-50

2006). However, in a typical tidal cycle the period of time that both current velocity and flow depth may be reasonably treated as constant can only last approximately ten minutes before both parameters begin to change, (Soulsby, 1997). The time-varying nature of the flow velocity, depth and direction add further complexity to the flow field and mechanism of scour in a tidal current.

Most monopile flow studies to date are concerned with the horseshoe vortex and rarely with the wake flow behind the monopile. Often data collection is concentrated on either the axis of symmetry of the monopile (e.g., Sarker, 1998 and Ahmed and Rajaratnam, 1998), or at polar coordinates around a half circumference of the monopile (e.g., Graf and Yulistiyanto, 1999, Graf and Istiarto, 2002 and Dey and Raikar, 2007). The horseshoe vortex is a primary mechanism of scour (§1.3.2), but the wake flow also plays a key role in transporting suspended sediment away from the monopile along with its small contribution to scour (e.g, Breusers and Raudkivi, 1991, Melville and Coleman, 2000 and §1.3.4), and is also worthy of study. Many of the velocity measurement techniques employed in these studies are intrusive point measurements: equipment such as yaw probes (Ahmed and Rajaratnam, 1998) and anemometers (Melville, 1977), are becoming less desirable with the advent of less intrusive instruments.

One such less intrusive instrument is the Acoustic Doppler Velocimeter (ADV). The advent of ADV technology in the past two decades has allowed high frequency time series point measurements of three dimensional velocities and turbulence. Their deployment is quasi non-intrusive, straightforward and self calibrating, and low in error (Appendix 2). Doppler Velocimetry in various forms has been used to good effect by

researchers recently such as Sarker, (1998), Ahmed and Rajaratnam, (1998), Graf and Yulistiyanto, (1999), Graf and Istiarto, (2002), and Dey and Raikar, (2007). These investigations have greatly moved forward the understanding of the spatial and temporal characteristics of the flow and turbulence field around the monopile. More recently truly non-intrusive methods of velocity measurement have become readily available including Particle Image Velocimetry (PIV). 3D PIV was used by Johnson and Ting, (2003) for measurements in the horizontal plane to assess the effect of relative water depth and Froude number on the water surface elevation and velocity field. De Vos, (2008) employed PIV in studies of wave run-up on offshore wind turbines and Sahin and Ozturk, (2009) showed the detailed spatial time-series and time-averaged data that can be gained from PIV in cylinder-flow studies at Reynolds numbers between 1500 and 9600.

1.7.1.1 Identification of Areas for Further Research

From the literature reviewed above, there are a number of specific areas of research opportunity in this field, which are based upon the general need for a further understanding of the flow structure and mechanism of scour. There is a requirement for research into the temporal changes in the flow field around the monopile under tidal currents where water depth and velocity have transient values. Such research needs to be scaled to the conditions found in prototype offshore wind turbine farm locations rather than to unidirectional river flow around bridge piers. There is also a general need for detailed spatial data on the flow and turbulence field around the monopile.

The focus in particular is on the flow field over a smooth, rigid immoveable bed. The

reasoning for this is as follows: at the start of the scour process, which will begin immediately at the point at which monopile insertion into the bed begins, the bed is assumed to be flat (e.g., Melville and Coleman, 2000 and Jensen et al., 2006). In practice this is rarely the case, the seabed in particular is usually subject to rippling and other naturally occurring dynamic morphology, but can be reasonably approximated to being flat. At the start of the scour process, therefore, the flow field around the monopile would be over a flat bed. How this may change during the progression of the tide is of interest. By focussing on the bed as a smooth surface relative to the prototype, the influence of the monopile on the flow and not bed roughness can be defined.

1.7.2 Process, Evolution and Estimation of Scour

A key aim of the majority of scour research is the derivation of empirical predictor equations of scour equilibrium depth, (for example, Laursen and Toch, 1956, Roshko, 1961, Neill, 1964, Shen et al., 1969, Hjorth, 1975, Melville, 1975, Jain and Fischer, 1979, Ettema, 1980, Raudkivi and Sutherland, 1981, Raudkivi and Ettema, 1983, Raudkivi, 1986, Chiew, 1984, Baker, 1986, Melville and Sutherland, 1988, Oliveto and Hager, 2002, Sheppard et al., 2004 and Whitehouse, 2004, with comprehensive reviews given by Breusers et al., 1977, Hoffmans and Verheij, 1997 and Melville and Coleman, 2000). Equilibrium scour depth describes the scour depth that will be achieved once the system reaches equilibrium, i.e., the point at which scour depth does not increase under the prevailing current velocity, depth and pier and sediment parameters. It is an important parameter as it will determine the design of bridge piers, particularly their shape and size and the extent of the required protection against scour.

Scour depth in the marine environment is generally predicted using these uni-directional flow equations, even though the flow in this environment is periodic (at both tide and wave scales) and there are significantly different monopile parameters involved. The action of waves, which generate only short lived currents (Sumer and Fredsoe, 1992) is reasonably well researched (for example, Saito et al., 1990, Sumer et al., 1992, Sumer et al., 1992a, Sumer et al., 1997, Whitehouse, 1998, Sumer and Fredsoe, 1999, Sumer and Fredsoe, 2001a, Sumer and Fredsoe, 2001b, Whitehouse, 2004, Jensen et al., 2006, Louwersheimer et al., 2006, Gothel and Zielke, 2006, and De Vos, 2008). Reviews of earlier works are found in Sumer et al., (2001) and Sumer and Fredsoe, (2002b). Some of this research also looks at the effect of steady currents superimposed on waves, (e.g., Sumer and Fredsoe, 2001b) but the effect of tidal flow direction, velocity and depth changes, and the temporal changes of parameter ratios (Equation 1-16) that this causes is much less well understood. While there is some research on tidal current scour (e.g., Escarameia, 1998, Jensen et al., 2006 and Margheritini et al., 2006), this does not explicitly address the cyclical variation of tidal flow depth and velocity in unison.

Escarameia, (1998) conducted a study of the scour depth and time-development in estuaries under reversing currents. Because she was unable to simulate concurrent changes in velocity and water depth, the two parameters were varied independently thereby giving some indication of their individual effects on scour depth. She observed that the maximum scour depth achieved under tidal flows tended to be lower than the equilibrium depth under equivalent unidirectional currents, due to infilling on current reversal. She also found evidence that the maximum scour depth in tidal currents may be

reached under live bed ($U/U_c > 1$) conditions rather that at threshold conditions ($U/U_c =$ 1) as observed in unidirectional steady currents, because the effect of infilling of the scour hole when the current reversed appeared to be lower under live-bed conditions. Her data is too limited to draw general conclusions but suggests that the generation of bed forms alters the velocity field when the current reverses. In the offshore environment, Jensen et al., (2006) and Margheritini et al., (2006) conducted a series of experiments to investigate tidal scour. Jensen et al., (2006) found the equilibrium scour depth to be the same as those under unidirectional currents and recommended the use of the Breusers et al, (1977) equation with a factor of 1.25 to predict equilibrium scour depth in tidal currents where $h/D > 1$:

$$d_{sc}/D = 1.25\tanh{(h/D\,)}, \quad (\sigma_{dsc/D} = 0.2) \qquad \text{Equation (1-33)}$$

Where $\sigma_{dsc/D}$ is the standard deviation of the scour depth.

Margheritini et al., (2006) studied the scour development over two full tidal cycles (four changes of current direction). Both Jensen et al, (2006) and Margheritini et al., (2006) approximated tidal flow to a square tide (i.e., an equal and opposite constant tidal maximum velocity and constant depth is used, thus ignoring the sinusoidal tidal variation of flow velocity and depth, Figure 1-19 and Brown et al., 2005). The tests were exclusively under live-bed conditions thus do not asses the changes in flow intensity during the tidal cycle. Margheritini et al, (2006) found that the tidal scour hole was symmetrical in shape resulting in a larger eroded volume than the asymmetrical

unidirectional scour hole. Scour depth, as in Jensen et al, (2006), was found to be the same as the unidirectional case. Both Jensen et al., (2006) and Margheritini et al, (2006)'s findings are somewhat at odds to those of Escarameia, (1998) who suggested lower scour depths in tidal currents. It is argued here that this may be due to the dominance of live-bed conditions in these tests, which may have nullified the effect of infilling, artificially increased the scour rate and, due to the lack of infilling increased the equilibrium scour depth achieved.
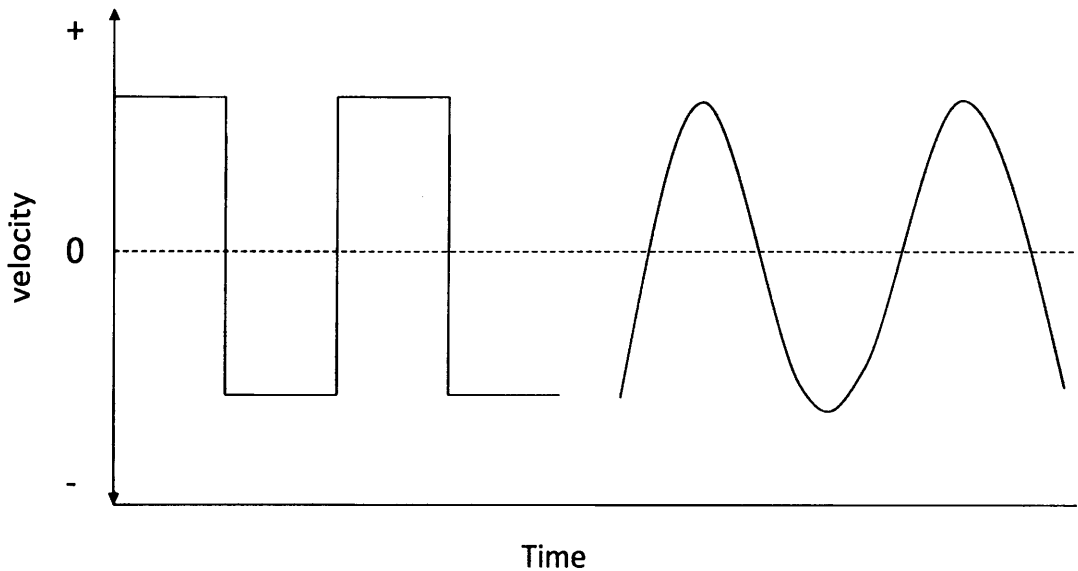
Figure 1-19. Square tide (left) where velocity and depth is equal for each half-cycle and a sinusoidal tide (right) where velocity and depth is variable.

Knowledge of the time-development of scour (i.e., the time taken to reach equilibrium from the onset of scour), is important in certain situations. For example, the knowledge of the depth and size of the scour hole at a certain time after monopile instillation is important as certain scour protection methods, such as infilling the scour hole with rip-rap

boulders, require the scour hole to have sufficiently developed before the insertion of a protection. The time-development of scour is less well researched than equilibrium scour depth; some of the few examinations include Melville and Chiew, (1999), Sumer et al., (1992a) and for offshore wind turbines in tidal currents, Harris et al., (2010). All three of these investigations resulted in an empirically derived prediction method for the time-scale of scour. Melville and Chiew, (1999) found the time-development of scour to be a function of the flow intensity $/U_c$, relative water depth h/D and sediment coarseness d_{50}/D. Sumer et al., (1992a) relates the live-bed time-scale of scour with the Shields parameter θ and the δ/D (where δ is the boundary layer depth) and formulate the following relationship between normalised time-scale T^*, θ and δ/D (Equation 1-34).

$$T^* = \frac{1}{2000} \frac{\delta}{D} \theta^{-2.2} \qquad \text{(Equation 1-34)}$$

where

$$T^* = \frac{[g(s-1)d^3]^{\frac{2}{3}}}{D^2} T \qquad \text{(Equation 1-35)}$$

Where T is the time scale.

This implies that the time scale of scour increases with increasing δ/D and decreases with decreasing θ in live-bed conditions. The data presented in these two studies relate the time-development of scour to sediment mobility (u/U_c and θ) and h/D and δ/D

implying that the tidal changes to these parameters will change the time development during the tidal cycle (with d_{50}/D remaining constant).

1.7.2.1 Identification of Areas for Further Research

This literature review demonstrates that there is a clear lack of experimental data and research on scour depth and its time-development in tidal currents. These are important to assess as the currently-used predictions based on unidirectional current experiments in the river environment may not accurately estimate scour depths and time-development at offshore monopiles. Such research needs to assess the effect of changes in water depth, velocity and direction in a manner that is appropriately scaled to prototype tidal conditions at typical locations of offshore wind farms.

Drawing on the literature discussed above, the following hypothesis can be outlined. As during the tidal cycle the flow intensity moves through clear-water ($u/U_c < 1$), threshold ($u/U_c = 1$) and live-bed ($u/U_c > 1$) scour periods, the time development of scour will not follow a smooth asymptotic curve to equilibrium depth (or threshold peak for live-bed scour) as it would for a constant flow intensity (Figure 1-16). The rate of scour will change as each instantaneous tidal flow velocity and depth will follow different asymptotic time-development curves based on instantaneous values of u/U_c, θ and h/D or δ/D. A combination of time-development curves based on these instantaneous parameter values may constitute the tidal time-development curve. The result will likely be a less smooth curve and a longer time to equilibrium. The shape of the scour hole will

be a superposition of two opposite unidirectional asymmetrical scour holes leading to a symmetrical shaped scour hole, as observed by Margheritini et al., (2006) for a square tide (Figure 1-19). The process of erosion will not be the same as for unidirectional currents when flow reverses due to the different 'reversed' bed morphology encountered around the monopile.

1.7.3 Reduction of Scour

The understanding of the process of scour and its effective mitigation is the ultimate aim of the research discussed above in §1.7.1 and §1.7.2. There are two forms of scour reduction that can be applied to the monopile or pier scour phenomena. The modification of the flow field to reduce its scouring potential, or the mitigation of scour during and after it occurs. Flow modification can be by the addition of collars, slots and helical strakes to the monopile, or by installing smaller sacrificial monopiles around the monopile requiring protection. The mitigation of scour by protection of the bed using 'scour protection' layers usually consists of a layer or layers of material whose weight is heavy enough that the bed shear stress required to move it exceeds the expected bed shear stress amplification at that point. The remainder of this section will assess the need for scour mitigation, review the scour mitigation options presently available and examine the relevant literature.

With the basis for scour prediction often being the interaction of unidirectional steady flows with the monopile (e.g., Sumer and Fredsoe, 2001b and 2002b, Whitehouse, 2004, and Jensen et al., 2006) the result may be a false estimation of scour depth and lateral

extent leading to over or (worse) underestimation of required mitigation measures.

1.7.3.1 Effect of Scour on the Monopile

At bridges, pier scour is a major cause of bridge failure, which has serious economic and safety consequences (e.g., Melville and Coleman, 2000). Scour reduces the depth to which the pier is buried into the river bed and can eventually undermine the foundation resulting in loss of structural support from the surrounding sediment, which can cause the pier and hence the bridge to fail. There are many examples of this in the field such as those cited by Melville and Coleman, (2000) and Breusers and Raudkivi, (1991). In the marine environment, scour is a problem that affects under sea pipelines, breakwaters and coastal defences, gravity structures as well as vertical piles, such as the offshore wind turbine monopile. Field examples of marine scour can be found in Sybert, (1963), Watson, (1979), Dijk., (1980), Dahlberg, (1983), ESS, (2003), Louwersheimer et al., (2006) and NPower (2008). The consequence of scour at a wind turbine monopile is similar to that of the bridge pier: a loss of structural stability, though a complete failure may not be as significant a problem as the piled depth of the monopile is much greater. Loss of stability may affect performance and longevity of the turbine (Whitehouse, 1998, Whitehouse, 2004, Zaaijer and Van Der Tempel, 2004, Margheritini et al., 2006, Louwersheimer et al., 2006 and De Vos, 2008). Specifically, the presence of a scour hole at the base of the monopile can (as described in Figure 1-20):

1. Increase the bending moment experienced by the monopile due to the effective increase in its length.

2. Cause variation (often a decrease) in the natural oscillation frequency of the monopile which in turn must be accounted for in its design.

3. Changes to the lateral bearing capacity of the monopile, which will dictate the required piling depth of the monopile. The monopile is loaded laterally by the action of wind, current and wave forcing as well as the rotation of the turbine blades. The presence of the scour hole reduces the lateral bearing capacity, thus requiring a greater piled depth.

4. Cable and J-tube free-spanning. Power and control cabling is generally situated on the outside of the monopile and is transferred to the sea-bed via a J-tube (N-POWER, 2008, Appendix A1 and Figure 1-20). Scour can expose the J-tube and cables from their original buried position, which leaves them unprotected from wave and current forcing.

A detailed discussion of these effects can be found in De Vos, (2008) and Zaaijer and Van Der Tempel, (2004). Figure 1-20 describes schematically the affect of the scour hole on the monopile.
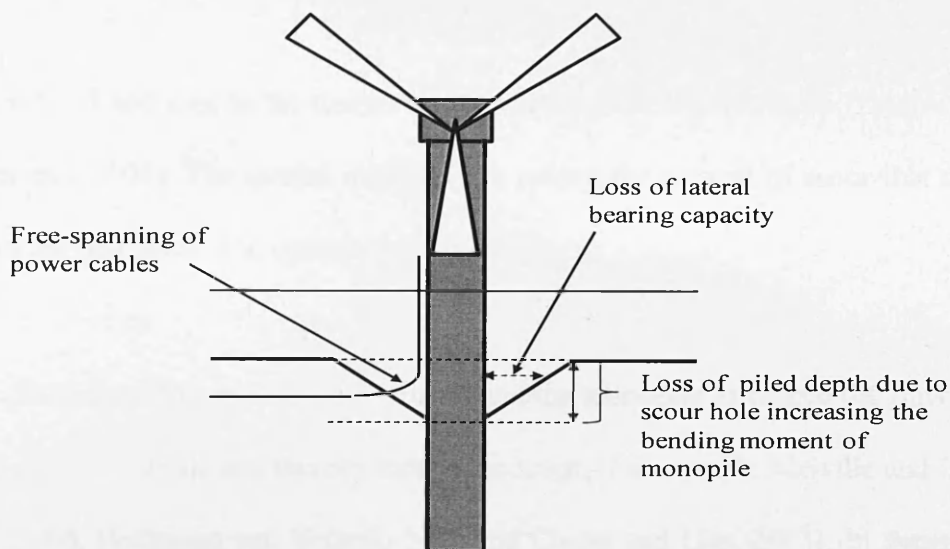
Figure 1-20, Schematic diagram of the issues associated with scour around the monopile (after De Vos, 2008).

1.7.3.2 Scour Mitigation Options and Potential Research Areas

There are three different ways that scour can be mitigated. Firstly, the structural design capabilities of the monopile are increased to allow it to compensate against any scour that occurs. This may include the following:

1. Increasing the depth at which the monopile is driven into the bed, thereby increasing the amount of scour required before structural stability reduces below preferred design limits.

2. Increasing the wall thickness of the monopile to increase the bending moment that the monopile can withstand.

3. Providing extra support for cables to allow them to withstand free-spanning (e.g. Zaaijer and Van Der Tempel, 2004).

Options 1 – 3 add cost to the design and construction of the monopile (Zaaijer and Van Der Tempel, 2004). The second method is to reduce the amount of scour that may take place in the first place. The options to do this include:

4. Placing sacrificial piles and sills around the monopile to reduce the flow velocity at the monopile and thereby reduce the scour, (for example Melville and Coleman, 2000, Hoffmans and Verheij, 1997 and Chiew and Lim, 2003). In doing so they sacrifice themselves to scour in order to protect the monopile. The knowledge required for their use is largely based on bridge pier scour where current direction is known. Placing sacrificial structures around the entire circumference of a turbine monopile for tidal flow may lead to greater costs, impact on the benthic environment and the layout of the turbine farm as a whole and hence is not considered hereinafter.

5. Using a fixed splitter plate to inhibit vortex formation and shedding, such as in Dey et al., (2006), a slot through the cylinder such as in Odgaard and Wang, (1987) and Kumar et al., (1999) or a junction flow modifier (Gupta, 1987). Though suitable for certain applications in bridge scour, this option is not suitable for the marine environment as it requires constant flow direction. This also excludes the streamlining of the cylinder, as is commonly employed for bridge piers (e.g., Melville and Coleman, 2000).

6. Employing helical stakes and collars around the circumference of the monopile to inhibit the downflow and reduce vortex shedding, The attachment of a collar around the monopile has proved effective in reducing scour (Ettema, 1980 and

Kumar et al., 1999) as have helical strakes (Dey et al., 2006) in clear-water steady currents and waves. Such an option is not dependent on the direction of flow.

Options 4 and 5 are clearly unsuitable for marine applications, with 4 requiring more research before its application, and 5 not suitable for variable current directions. 6 could be applied to the marine environment, but again will add cost to the design and construction of the monopile so its application must be cost-effective. Helical strakes are attached to sub-aerial smoke stacks in order to inhibit eddy formation in their wakes and reduce vortex induced vibrations (VIV) of the stack. While the effect of VIV on an offshore monopile is not known, vortex formation and shedding is also an important phenomenon in the case of scour, which acts to remove sediment from the bed and deliver it down stream in the wake (§1.3.6). However the main role of helical strakes is the disruption of the downflow and formation and strength of horseshoe vortex. Collars are specifically designed to disrupt the downflow, thereby reducing the strength of the horseshoe vortex. Through research in clear-water unidirectional flow, the deployment of collars varies in number, spacing between each collar, and spacing from the bed depending on flow and sediment parameters and pier size (Kumar et al., 1999). The angle and number of helical strakes is also variable depending on flow and sediment parameters and pier size, (e.g. Dey et al., 2006). In the tidal environment the variation of water depth presents variability that renders such protocols less useful and the offshore environment generally presents much more challenging engineering and logistical obstacles than rivers. In particular, there is uncertainty in how such deployments may react to the live bed nature of the marine environment where passing bed forms may raise and lower the bed level significantly. With this in mind, the collar and helical strake fittings tested in the

experiments below are designed to be easy to retrofit on the monopile after it has been installed into the seabed. There is little investigation into the flow field around collared and helical strake monopiles, and further knowledge would enable a greater understanding of how these may reduce scour leading to more efficient designs. Furthermore, there is to the author's knowledge no investigation of these monopile designs in either live-bed conditions, or tidal flow of variable water velocity and depth.

The third method is to employ a static scour protection, and is the most widely used option for wind turbine monopiles. Static protection against scour involves bed armouring techniques which raise the bed shear stress required for sediment motion above that which the flow around the monopile is capable of generating. The various options include:

7. Rip-rap scour protection involves the placement of material whose weight is greater than that which the expected velocities can move and is a common choice for bridge piers (for example Breusers et al., 1977, Breusers, and Raudkivi, 1991 and Melville and Coleman, 2000). It is also used in the marine environment (for example, Sumer and Fredsoe, 2002b, Hoffmans and Verheij, 1997, Van Der Tempel, 2004 and De Vos, 2008).

8. A caisson foundation, which involves placing a wider foundation to the monopile below the bed surface (Hoffmans and Verheij, 1997 and Whitehouse, 2004). Or a tetrapod foundation (Lagasse et al., 2001).

Rip-rap is commonly employed at offshore wind turbine monopiles as it is often more

cost-effective than allowing scour to develop (Zaaijer and Van Der Tempel, 2004). It is, however subject to damage over time and can itself fail due to scour (De Vos, 2008). Damaged static scour protection can exacerbate scour and cause further problems to the monopile (Zaaijer and Van Der Tempel, 2004). If the rip-rap does not sufficiently prevent scour, it may form beneath the rip-rap layer causing the rip-rap to fall into the scour hole and potentially damage the monopile and any attached cabling.

In §1.7.3.2 items 1-3 require accurate predictions of scour depth. As discussed in §1.7.1, predictor equations are subject to inaccuracies, and the majority are designed for unidirectional scour around bridge piers. The accurate extrapolation of unidirectional bridge scour equations - and any laboratory-derived empirical equation - to the geometric and flow parameters associated with offshore wind turbines raises uncertainty. Scale effects between the model and prototype, and the effects of marine tidal and wave forcing are not fully understood.

The choice between scour protection and increasing structural design parameters (for example, thicker steel walls and greater driven depth) to tackle scour often leads to the former as being the most economically viable, particularly for larger turbine Mega Watt (MW) capacities Ballast Nedam and Oud, (2002). General costs, however, are not small and can be in the region of ~ €350,000 per turbine depending on depth and size requirements (for example, Van Oord, 2003 and Zaaijer and Van Der Tempel, 2004). For large wind farms this can add up to tens of millions of Euros for rip-rap scour protection. Clearly, therefore, an investigation into the potential of passive scour reducing monopile designs is worthwhile as it may reduce scour related costs.

Along with active scour protection, passive scour reduction techniques which are widely used at bridge piers, may well have a role to play in reducing the amount, cost and maintenance of scour protection. From the literature reviewed above, there is a clearly an opportunity for further research in passive scour reduction, particularly collars and helical strakes. This research will need to assess the potential reduction of scour in the offshore wind turbine environment, with a particular emphasis on tidal currents. The research will also be needed provide an insight into how the collars and helical strakes may alter the flow field, hopefully leading to a greater understanding and more efficient designs.

1.8 Thesis Research Outline, Aims and Objectives

The above review of the literature in §1.7 highlights three broad areas of research opportunity; a further understanding of the flow field and mechanism of scour, and its changes in tidal currents (theme 1); the evolution of scour under tidal variations in velocity, direction and depth, particularly in comparison to unidirectional currents (theme 2); and the potential of passive flow field modification in reducing the amount of scour that may occur (theme 3).

1.8.1 Thesis Aim

The aim of this thesis is to; increase the understanding of the complex monopile flow field characteristics, describe the evolution of scour, and determine the effectiveness of

passive flow modification monopile designs in reducing scour under tidal current conditions around an offshore wind turbine monopile.

1.8.2 Objectives

In order to achieve the aim set out above series of extensive laboratory scaled experiments were completed. The experiments consisted of rigid and mobile bed tests around a scaled circular cylinder. The cylinder, sediment and test conditions were scaled from typical prototype monopile diameter, sediment and flow conditions. The scaling is detailed in §2.2. The experiments were designed to achieve the following objectives:

1. To complete a detailed study of the variation in the lee and wake velocity field around the monopile through tidal currents.

2. To analyse the variation of turbulence characteristics in the lee and wake of the monopile in tidal currents.

3. To indentify the dynamics of bed shear stress around the monopile in tidal currents.

4. To determine the spatio-temporal characteristics of the formation of scour under tidal currents.

5. To assess and understand the differences in the flow and turbulence fields around a collared and helical strake monopile in comparison to a smooth monopile and how these may reduce scour.

6. To analyse the effectiveness of a collared and strake monopile in modifying the local flow field and reduce scour.

1.8.3 Outline and Structure of Study

This thesis reports three related studies: a set of rigid bed experiments, via which the flow dynamics around monopiles in tidal currents are elucidated; a series of mobile bed experiments, which are used to analyse the time-development of scour under tidal currents; and a set of experiments used to assess the effects of flow modification retro-fits on the flow field and scour development. The thesis will attempt to draw all three themes together to give a comprehensive view of the process of scour, its mechanics and its time development under tidal currents and give an assessment of flow field modification techniques.

1.9 Omission of Wind Generated Waves

Wind generated waves are to be neglected in this thesis for the following reasons. In the shallow shelf sea environment only larger waves will generate orbital motions that will reach the bed and generate shear stresses. The diameter of wave orbital motions reduces exponentially with depth until a depth of approximately half the wavelength at the surface, where orbital motion is negligible (Brown et al., 2005). For wave oscillatory motion to reach the bed the water depth must be small compared to the wavelength; $h/l <$ 1/2. The wave boundary layer is much thinner than that of a steady current boundary layer due to the short-lived currents that waves generate limiting vertical growth before the current reverses. This results in larger bed shear stresses for wave boundary layers due to the steeper gradient in the shear layer than for the same current velocities. Therefore,

wave induced sediment entrainment is greater than current induced sediment entrainment. However, in the shallow sea environment only larger waves will generate orbital motions that will reach the bed and generate shear stresses, and furthermore, the back and forth motion of the currents they generate are not as efficient as steady currents in transporting entrained sediment away (Nielsen, 1994).

Sumer and Fredsoe, (2001b) conducted a series of experiments with currents superimposed with waves propagating both with, and perpendicular to the current. They found that the scour depth under waves was greatly increased when even a small current was added. The reason for this is the transient nature of wave induced currents created the downflow and horseshoe vortex phenomena for only the same amount of time as the wave period, before reversing as the orbital motion changes direction. The current induced flow field remains longer and therefore can develop stronger downflow and horseshoe vortex and the results from Sumer and Fredsoe, (2001b) indicate that scour depth is dictated by the current component when there is combined wave and current action. This is further demonstrated due to the fact that the direction of wave propagation in relation to the current had negligible effect on the scour depth. Furthermore, the back and forth motion of wave generated currents are not nearly as capable as steady currents in transporting entrained sediment away; that is, the consistent presence of vortex formation and shedding in the wake is an important sediment removal process (Nielsen, 1994 and Sumer and Fredsoe, 2001b).

Though it is acknowledged that waves are an important part of the marine environment in which the monopile is sited, for the reasons listed above, and for the purpose of this thesis

which is to concentrate on the less well researched role of tidal currents in scour around the wind turbine monopile, waves are omitted from the study.

Furthermore, the impact of a tsunami the monopile is an important consideration not covered by this thesis. A tsunami wave train may have a multitude of impacts on an offshore wind farm including wave loading onto the structure, impact damage, and scour. Further research is required to determine the impact of tsunami on the monopile.

Chapter 2: Experiment Design and Methodology

In order to achieve the aims and objectives set out in §1.8, an extensive series of laboratory experiments was conducted on a scaled turbine cylinder. These experiments were split into two separate campaigns; a rigid bed experimental programme, and a mobile bed experimental programme (§1.8.3). The design and methodology of these experimental programmes will be discussed in this chapter.

2.1 Rigid Bed Experimental Set-up

To achieve objectives one, two, three, and five (as set out in §1.8) an extensive series of rigid bed experiments was conducted at The Total Environment Simulator Tank situated in The Deep, Hull, U.K over the period from March to May 2008 (Figure 2-1). Within the 11 m long, 6 m wide re-circulating tank a 1.2 m wide by 11 m in long channel was constructed. The width of this channel was confirmed using a laser distance measurer and a tape measure. The channel was constructed with a raised bed formed from marine plywood drilled onto blocks of concrete (Figure 2-2). The flow dividers were securely clamped together to adjacent and opposite dividers and all joins between them and the marine ply-wood were flush and sealed using Duck tape. Unidirectional flow was provided by an electric pump housed under the flume. A lattice screen at the inlet calmed the flow on entry to the flume. A layer of pebbles were glued to the upstream end of the channel in order to encourage boundary layer formation (Figure 2-1 top right and 2-4 bottom right). Appendix A5 and A6 provides details of the control tests in which the various flow parameter combinations were run

with no cylinder in the flume. Figure 2-3 is a schematic diagram of the experimental set-up. The centre of a 0.2 m diameter black circular PVC cylindrical cylinder was positioned at the mid-point of the flume length and width into a groove cut out of the marine plywood (Figure 2-4). The cylinder was tapered on its bottom end in order to ensure a flush fit to the bed and was secured vertically by two pieces of wood clamped to the flow dividers on either side of it. All surfaces and distances were checked throughout the construction process using spirit levels, tape measure and the laser distance measurer.

Figure 2-1. Images of The Deep with flume constructed in the centre.

Figure 2-2. Images of the construction of the raised bed.
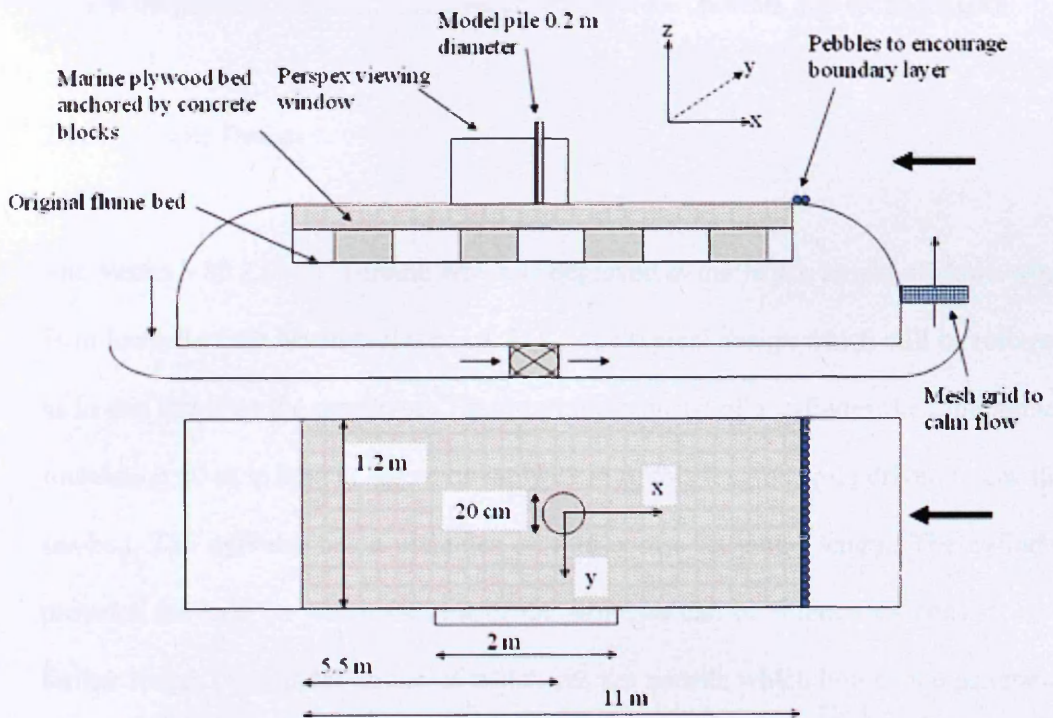
Figure 2-3. Schematic diagram of the experimental set-up.

Figure 2-4. Images of the marine plywood board with hole for the cylinder (top row), cylinder in the flume (bottom left), and layer of pebbles at the upstream inlet (bottom right).

2.1.1 Cylinder Design

The Vestas V80 2.0MW Turbine which is deployed at the North Hoyle offshore wind farm located of the North Wales coast, U.K., is a typical design which will be referred to in this thesis as the prototype. These turbines consist of a cylinder (i.e., monopile) foundation 50 m in length. Approximately 25 m of this length is pile-driven below the sea-bed. The cylinder has a diameter of 4 m across its entire length. The cylinder provides the base on which the rest of the structure can be fitted. This consists of a further length of cylinder on top of which sits the nacelle which houses the generator and onto which is fixed the hub and blades. The hub height is approximately 70 m above mean sea level. The blade length is approximately 40 m giving a maximum height of 110 m above sea level, and a minimum of 30 m.

The model of the prototype was cut from a smooth circular cylindrical length of 0.2 m outside diameter PVC piping with 6 mm wall thickness, a readily available piping used for a variety of plumbing applications. The pipe was sprayed with black waterproof paint in order to reduce the reflection of the PIV laser from its surface. The model cylinder had a smooth surface. The prototype is likely to experience erosion through abrasion by sediment (for example Zaaijer and Van der Tempel, 2004) and corrosion by sea water over longer periods. Roughness would affect the vortex shedding and may influence the behaviour of the wake. Roughness is not taken into account in these experiments, partly because fouling of the cylinder may take a longer period of time to develop than the time to equilibrium scour, and partly because it is difficult to quantify in the field.

2.1.2 Data acquisition

The flume was divided into three sections related to the measurements taken which are 'upstream region' of the cylinder, the 'near-cylinder region', and the 'downstream region' of the cylinder, (Figure 2-5).
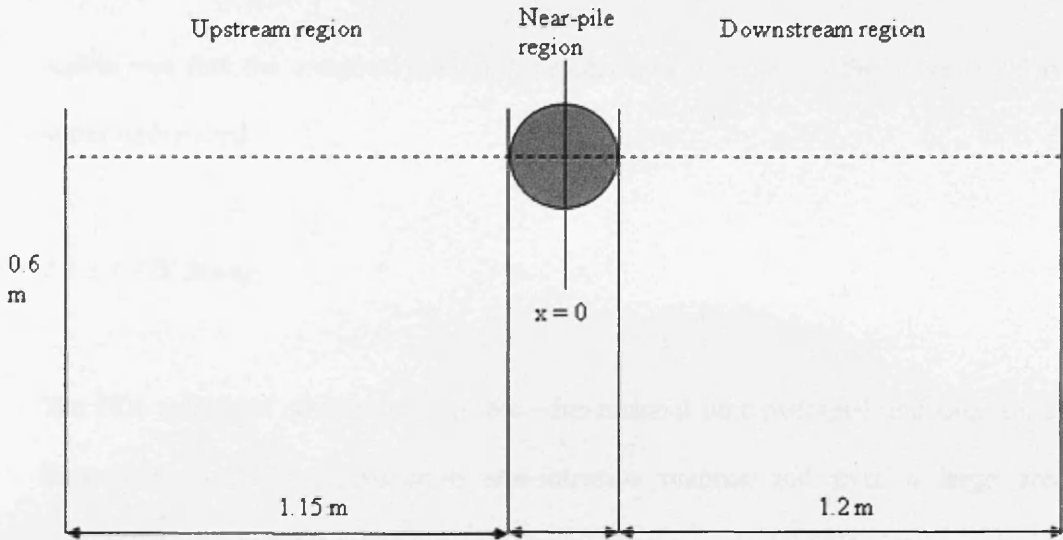
Figure 2-5. Schematic diagram showing the upstream, near-pile and downstream regions of

data collection.

The Cartesian coordinate system is set in the flume with the origin set at the cylinder

centre, with   denoting longitudinal position (positive downstream of origin), y

denoting lateral position (positive to the right when looking upstream) and z denoting

the vertical position with the flat rigid bed lying in the   = 0 plane, (Figure 2-4). The

data collection campaign provides a dense coverage in hitherto less well covered areas

of the flow field. Two methods of data collection were used; in the upstream and near-

pile regions a set of four Nortek 3D 50 Hz Acoustic Doppler Velocimeters (ADVs)

were employed, in the downstream region, a Dantec Stereoscopic 3D Particle Image

Velocimetry (PIV) system was employed. PIV provides a comprehensive and detailed

analysis of the flow which has superior spatial coverage to ADV, but is far more

complex and time-intensive to set-up. Due to time constraints, it was therefore chosen

to be used only in the downstream region which as discussed in §2.1, is more

turbulent, three-dimensional and has to date not been subject to a detailed analyses

with these parameters and method. The intention of employing PIV in the downstream

region was that the complex flow and turbulence that occurs in the wake could be better understood.

2.1.2.1 PIV Set-up

The PIV technique allows detailed three-dimensional time-averaged and time-series flow maps to be captured in a non-intrusive manner and over a large area simultaneously. In these experiments a Dantec Stereoscopic 3D PIV system was used to capture vertical flow velocity profiles over large areas of the wake flow simultaneously (Figures 2-6 and 2-8). A detailed description of the PIV technique and its application to fluid dynamics is given in Adrian, (1991). PIV is relatively new technology that has grown in popularity in the last ten years. Recent examples of its use in laboratory studies of cylinder flow include Johnson and Ting, (2003) and Sahin and Ozturk, (2009). The particular set-up an operation of the PIV system for this experiment is described here.

A section ('slice') of the flow field approximately 0.25 x 0.25 m x 0.01 m is illuminated by a Nd:Yag 120mJ double pulse laser light-sheet with a 15 Hz repetition rate. Two Charged Couple Device (CCD) Kodak/Roper 1k x 1k pixels cameras with 8 bit resolution and 15 Hz cross-correlation (dual frame) frame rate were used to capture two consecutive images of the seeded flow at different angles. The seeding material used was timoron particles of $d_{50} = 21$ μm. The laser light-sheet double pulses at a rate 15 Hz for two minutes allowing each CCD camera to capture a total of 3600 images of the flow field. The individual images captured by each camera at the same instant are paired together. Each pair at a particular instant in time is compared with

the next pair at the instant immediately afterwards using the computer software 'Dantec Flow Manager'. This software compares the position of thousands of individual seeding particles in the first pair with their position in the second pair. From each comparison of two pairs the components of velocity u, v and w are derived and a 3D vector map is constructed, giving a time-series of 1800 vector maps. An time-averaged vector map is calculated from these 1800 vector maps. The PIV was calibrated at the start of the experiment, and re-calibrated near the end of the experiment to cater for any offset brought about by movements in the structure of the flume.

In the downstream region, the PIV was set-up to capture vertical slices of the flow field downstream of the cylinder in four parrallel planes (Figure, 2-6 and 2-8). In the y = 0 and y = 0.15 m planes, four slices were captured which together covered the region from the cylinder to approximately x = 1.2 m. Along the y = 0.05 m and y = 0.10 m planes, only the region between x = 0 and 0.6 m was sampled. Figure 2-9 shows a selection of images of the PIV system in the flume.

2.1.2.2 ADV Set-up

In the upstream region an array of four ADV (three down-looking and one side-looking) were fixed vertically on a sliding mount (Figure 2-10a). This allowed the x position of the sampling volume to be varied from -0.013m to -1.150m upstream of the cylinder, and vertically from the bed up to 5cm below the surface, (the highest sampling point allowed by the operation of the ADVs as the sample volume is located ~ 5 cm below the transducer head which must be submerged, Figure 2-10b). Laterally,

the ADVs sampled in planes at $y = 0$, 0.12 m, 0.17 m and 0.22 m. In the near-cylinder region, the ADVs sampled along the $y = 0.06$, 0.18, 0.25 and 0.3 at $x = -0.12$ to 0.13. The upstream and near-cylinder ADV sampling locations are shown schematically in Figure 2-6 and 2-7 respectively.

From hereon, the x and y positions are normalised with cylinder diameter D, where $x/D = x'$ and $y/D = y'$. All values of x' and y' are given relative to the origin, i.e., $x' = 0$ and $y' = 0$ (the centre of the cylinder). For example, $y' = 0.25 = 0.05$ m away from $y' = 0$.
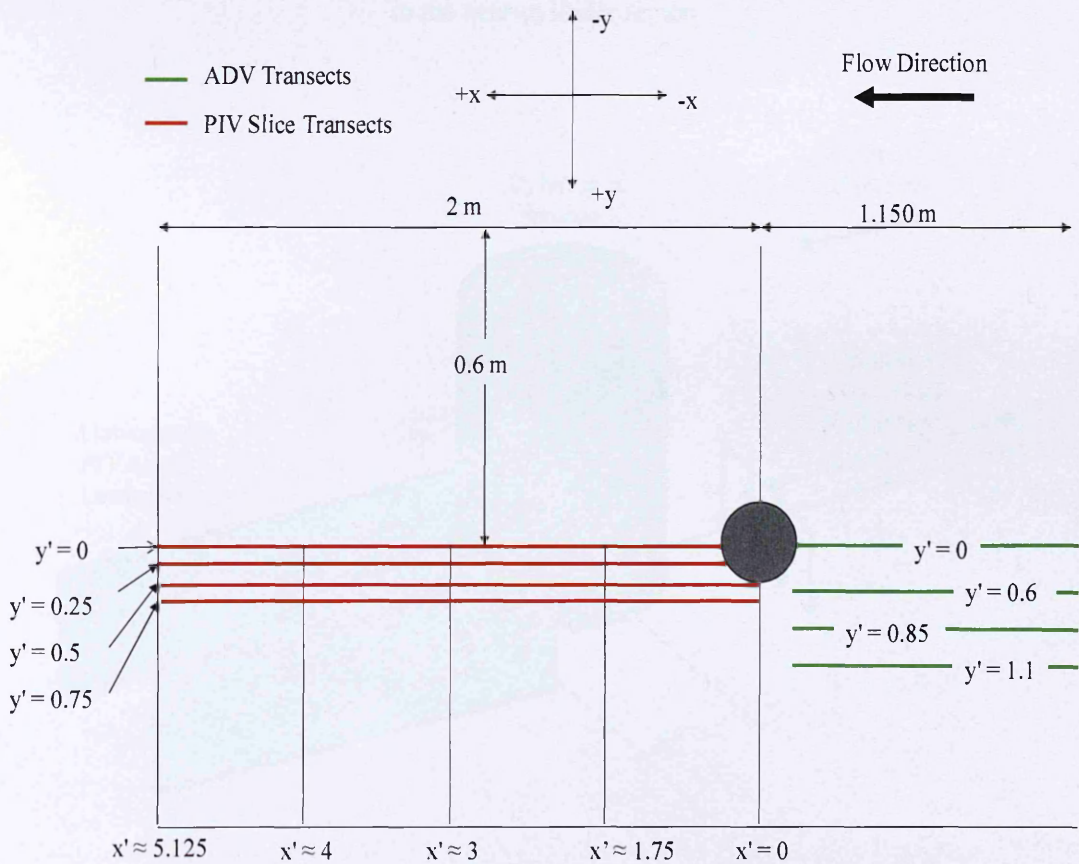
Figure 2-6. Schematic top-down view of the experimental set-up showing the ADV transects (green lines) and the PIV transects (red lines).

Cylinder of Diameter D

y' = 0

y' = 0.3

y' = 0.9

y' = 1.25

y' = 1.5
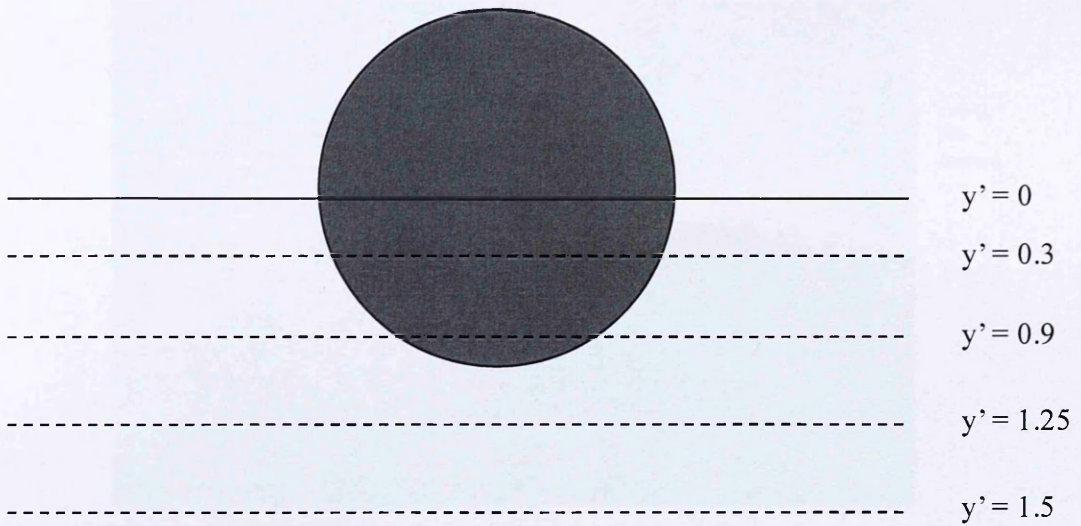
Figure 2-7. Schematic top-down view of the experimental set-up showing the ADV transects in the near-cylinder region.

Flow direction

Cylinder of Diameter D

Upstream ADV Data Collection

Downstream PIV Slice Locations
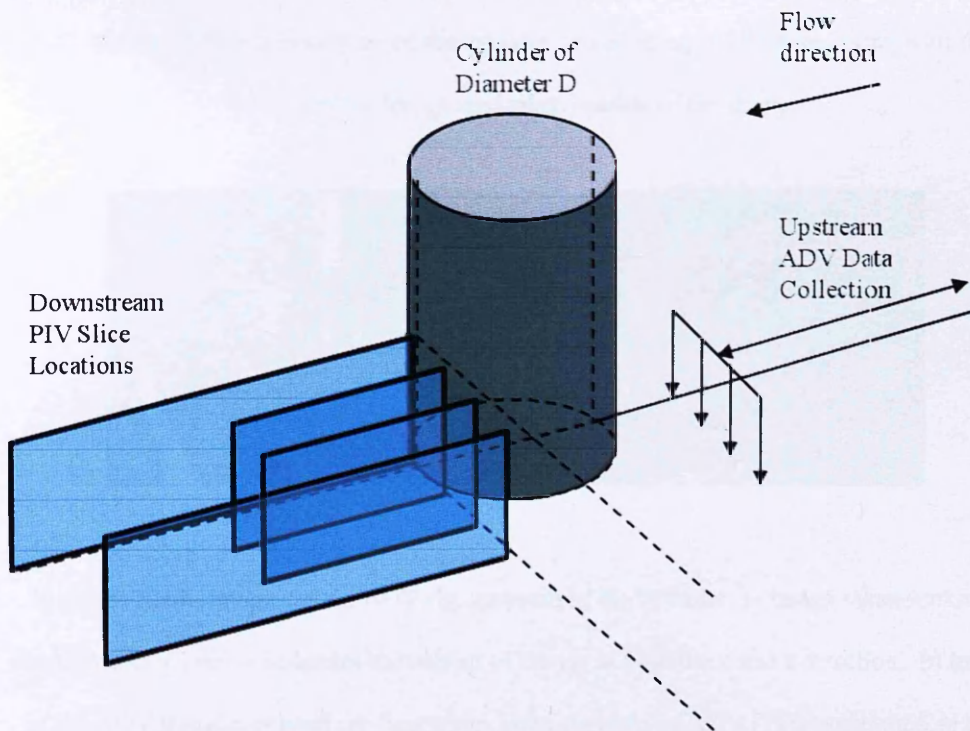
Figure 2-8. Schematic view of the experimental set-up showing the ADV collection area upstream and the PIV transects (blue planes).

Calibration plate (removed during tests)

PIV
camera

PIV Laser light sheet, view from
downstream

PIV Laser light sheet and camera, view from
outside flume
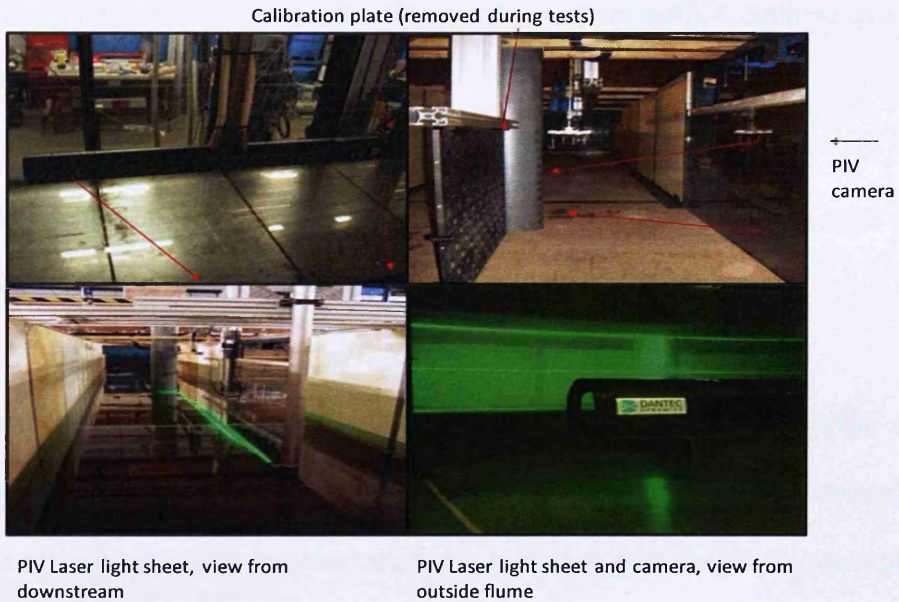
Figure 2-9 (clockwise from top left) Images of PIV cameras outside of the flume, calibration

plate and Perspex screen taken from downstream (red arrows indicate camera line-of sight),

image taken within the flume downstream of the cylinder looking outwards towards the side

with the laser firing downstream of the cylinder and an image of the laser firing with the

camera in the foreground taken outside of the flume.

a)

b)
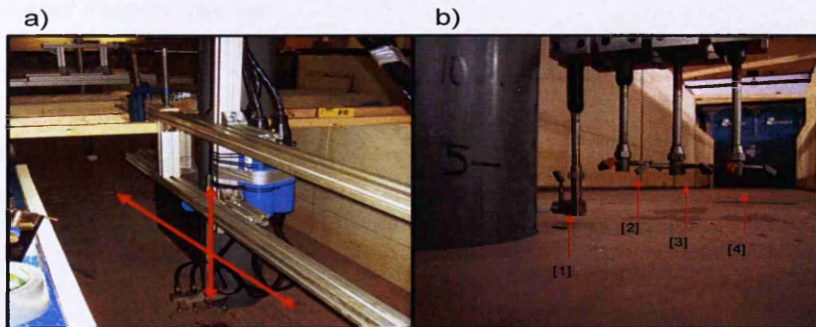
Figure 2-10a-b. Images of the ADV rig upstream of the cylinder. a) Image taken looking

downstream; red arrow indicates movement of the rig in both the x and z direction. b) Image

of the ADV transducer head configuration. The side-looking ADV [1] is positioned so the

sampling volume is directly on the centreline ($y' = 0$). The three down-looking ADV [2-4]

sample at $y' = + 0.12, + 0.17$ and $+ 0.22$ m.

The raw ADV data was despiked using the phase-space method outlined by Goring, (2002), as described in Appendix A2.

Further details on the set-up and calibration of the PIV are given in Appendix A3 and for the ADV in appendix A2, including an overview of their error.

As the cylinder is symmetrical, data was only collected on one side of the axis of symmetry (to the left when facing towards the cylinder from upstream). The assumption of symmetry has been applied in many previous studies (for example Graf and Yulistianto, 1999). Downstream vortex formation and shedding is well-defined and regular at the Reynolds numbers tested, meaning over a long enough time the vortices shed equally on both sides (Table 2-2 below, Figure 1-11 and Sumer et al., 1997).

2.1.2.3 Nortek Vectrino Set-up

A Nortek 50Hz Vectrino ADV (Figure 2-11), was used to record long period time-series velocity data along the downstream centreline at locations varying from $x' = 0.5$ - 10 at a range of z'. The Vectrino had a detached transducer head which decreased its profile in the flow, and afforded more freedom in sampling location (Figure 2-11). The raw data was despiked using the phase-space method outlined by Goring and Nikora, (2002), as described in Appendix A2.
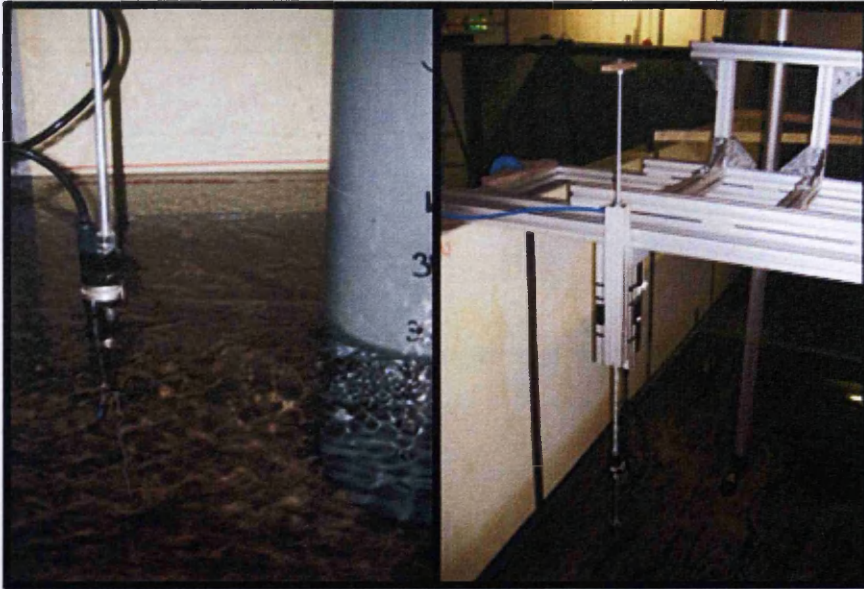
Figure 2-11. (left), the Nortek Vectrino sampling in the cylinder wake and (right), the Vectrino rig which could be manual positioned at any location downstream (the PIV laser, which is facing upstream can also be seen behind the Vectrino).

2.1.2.4 Pressure Sensors Set-up

In order to collect time-series water surface elevation data, 24 pressure sensors were installed underneath the marine plywood bed (Figure 2-12). The sensor end of the instrument was fitted through specially drilled holes so that it was flush to the bed. The data from two of these sensors is used in this thesis; one located 1.5 cm upstream of the cylinder on the centreline, and another located 1.5 cm downstream of the cylinder, also on the centreline. They are accurate to within +/- 1mm.
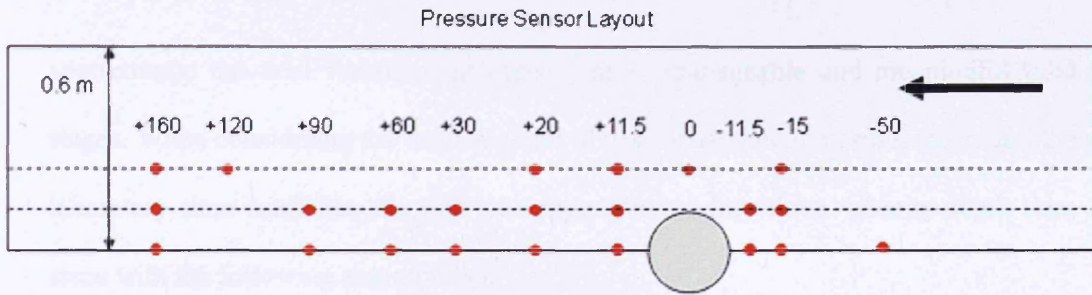
Figure 2-12. Pressure sensors arrangement around the cylinder.

2.2 Test Parameters, Scaling and Procedure

2.2.1 Experimental Design: Tidal Scaling

Tidal flow depths and velocity vary due to the morphology of the bed, depth of water, latitude and arrangement of nearby landmasses. It is not the intention of this thesis to address a particular prototype location, therefore, the ideal reproduction of tidal flow in the laboratory would be of a generic, if somewhat idealised tidal flow typical to the U.K coast, but based on conditions in the Liverpool Bay area of the Irish Sea. The tidal velocity and depth, though constantly changing in the prototype, are represented by a series of 'tidal stages' in order to take measurements of each different velocity-depth that occurs. In a typical prototype tide the time span at which velocity and depth do not significantly change during the tidal cycle lasts approximately 10 minutes (Soulsby, 1997). Ideally, the number of tidal stages tested would be scaled down from ten minute stages in the prototype, however, in the laboratory scale this would constitute an unrealistic time-frame in order to complete measurements for each step; the tidal stages would be far too short to take meaningful measurements within practical time limits. Hence several assumptions must be made in order to

approximate the tidal variation into fewer, more manageable and meaningful tidal stages. When considering the desired detail of data, the collection programme, and the laboratory time available, the tide was approximated into three velocity-depth time steps with the following assumptions:

1) The first assumption is that of a symmetrical sinusoidal tide, where the ebb and flow exhibit the same changes in velocity and depth with time. Such a tide is the idealised equilibrium tide that would occur if the Earth were covered to a uniform depth in water and the Moon was situated over the Equator (Brown et al., 2005). A truly symmetrical tide appears rarely in nature, if at all. Indeed, the variation in morphology of the seabed and coastline around the U.K. results in a complex variety of tidal ranges and current speeds; asymmetry is common and too varied to model effectively. Therefore, the assumption of a symmetrical tide is made in order to avoid constraining these tests to a particular prototype, and to concentrate on the assessment of the influence of the reversal of flow direction.

2) The second assumption is of a non-progressive or standing wave tide. In the deep ocean or along straight shore lines in relatively deep water, the tidal wave is a progressive one where velocities are highest near the crest and trough of the tidal wave before reducing to zero when the flow direction changes, (Brown et al., 2005). In shallower shelf seas particularly near irregular shorelines, tidal waves show lower velocities at the peak of the crest and trough (that is, the high and low tide 'slack waters', where velocity will become zero for a short time). Data collected in the Liverpool Bay area (held

by the British Oceanographic Data Centre, BODC), near where the prototype turbines are situated (see §2.1.1), indicates higher velocities during mid flood and ebb, with lower velocities at low and high tides (BODC and Appendix A11).

3) The third assumption is that the tide is bi-directional; i.e., the Coriolis force is treated as insignificant. While true in small bays and estuaries, in larger bays and the open sea the Coriolis force causes tidal currents to change direction constantly encouraging the water to move in rough elliptical paths (e.g., Fig 2-19 in Brown et al., 2005). Even so, such tidal ellipses often have a dominant direction which can be approximated to a bi-directional 'back-and-forth' motion.

With the above assumptions and along with data from BODC and NPower, (2008), (see appendix A11), the period of the tidal half cycle T can be split into three stages that vary from $T_{1/3}$ low-water medium-velocity to $T_{2/3}$ mid-water high-velocity to $T_{3/3}$ high-water low-velocity, before the direction of flow changes and the tide varies from high-water low-velocity to mid-water high-velocity before completing the cycle at low-water low-velocity (Figure 2-13). Using these data sets a set of mean values of velocity and depth for $T_{1/3}$, $T_{2/3}$, $T_{3/3}$ are given in Table 2-1.

These data are extracted from a BODC data set of velocity and depths (see Appendix A11). Other typical values gained from the data set are; tidal range of approximately 6.5 m, average water depth in which cylinder is sited of 9.1 m (Rhyll Flats wind farm), and maximum current velocity of 0.7 m s^{-1}.

Zero velocity

High tide

Depth

Mid tide

Maximum velocity

| Low tide time step | Mid tide time step | High tide time step | High tide time step | Mid tide time step | Low tide time step |

Low tide

Increasing time

Zero velocity

2 hours 2 hours 2 hours

6 hour interval equal to one tidal half-cycle.

As the tide is symmetrical, the second half cycle (6 hours) mirrors all time, depth and velocity changes from the previous half-cycle.

Velocity is taken as the mean velocity for each time-step

Flow Reversal

Flow Reversal

Figure 2-13. Schematic diagram showing how each time-step is identified in the sinusoidal tidal wave. Each time-step is 2 hours long. Mean velocity of each is derived from each time-step. Depth is taken from the maximum depth in the time-step.

The assumption of a symmetrical tidal range over a half period means that the water depth at time t is the same as at time $t + 12h$. During each time-step the flow depth will change as so; $T_{1/3}$ from low-water to 1/3 of high-water, $T_{2/3}$ from 1/3 high-water to 2/3 high-water and $T_{3/3}$ from 2/3 high-water to high-water. These are further simplified by defining the mean water depth for $T_{1/3}$ as the low-water, $T_{2/3}$ as median point in the tidal cycle, and $T_{3/3}$ as the high-water value (Table 2-1 and Figure 2-13).

	Average u [m s^{-1}]	Average h [m]
T$_{3/3}$ High-tide	18	8
T$_{2/3}$ Mid-tide	70	5
T$_{3/3}$ Low-tide	53	2

Table 2-1. Average velocity and depth values for a tidal flow (see also Figure 2-13). From

BODC data (Appendix A11).

2.2.2 Scaling of the Model Parameters

Choice of flow depth and velocity was made via the selection of parameters representative of typical tidal flow conditions in the Irish Sea Liverpool Bay area, and is described in detail in §2.2.1 and Table 2-1. However, these parameters are changed further in order to achieve appropriate scaling between model and prototype, as will be discussed in this section. The scale used is 1:20 to prototype conditions. Arrival at the parameter values used is described here.

The scaling of flow depth and geometry from the prototype to the model is governed by the geometric scaling criterion where length scales in the model are all set to a constant ratio of those in the prototype. In this case a scale of 1:20 is applied to the cylinder diameter and flow depth. For similitude to be satisfied between model and prototype, the dimensionless parameters in Equation 1-15 must be the same for the model as they are in the prototype. As the model and prototype are circular cylinders, and by assuming laterally uniform approach flow and uniform sediment grading the parameters Φ, σ_g, G, Sh and Al can be neglected giving:

$$\frac{d_{sc}}{D} = f\left(\frac{U}{U_c}, \frac{U^2}{gD}, \frac{h}{D}, \frac{D}{d}, \frac{\rho UD}{\mu}, \frac{\rho_s}{\rho}\right) \qquad (2\text{-}1)$$

The model cylinder is geometrically scaled to 1/20 of the prototype ensuring $[h/D]_m = [h/D]_p$, (where subscript m and p denote model and prototype respectively). D/d describes the ratio of cylinder diameter versus sediment size; this parameter is relevant to the mobile bed tests only. The remaining parameters in Equation 2-1 are U^2/gD, U/U_c, and $\rho UD/\mu$. $\rho UD/\mu$ is the cylinder Reynolds number (Re_D) which is a measure of the relative importance of viscous effects in the flow, and is often deemed unimportant to d_{sc} if the flow around the cylinder is fully turbulent (Ettema et al., 1998a). Re_D can be disregarded when $Re_D > 10^4$ (Hughes, 1993) which it is in both the model and prototype, as fully turbulent flow will then exist around the cylinder.

Therefore the accurate scaling of the model from the prototype requires similitude of the following parameters; U^2/gD, U/U_c, and h/D.

U^2/gD and h/D may be combined to give the Froude number $U/\sqrt{gh}$ which describes the relative importance of inertial and gravity forces on the flow and is an influential parameter in Equation 2-1 (e.g., Ettema et al., 1998a). This leaves two options for model prototype similitude; the similitude of particle mobility, and the similitude of Froude number (Ettema et al., 1998a). Both cannot be satisfied simultaneously because of the natural cohesive properties of sediment with $d < 0.06$ mm. Cohesive sediments behave differently to non-cohesive sediments as inter-particle electrostatic forces become an important factor in their mobility. It is not possible to use sediment in the flume which is finer than approximately 0.1 mm as such sediments have propensity to ripple. The result is an unavoidable under-scaling

of silica sediment in the flume where the grains are larger than geometric similitude

dictates, as a suitable non-silica substitute is both costly and difficult to deploy.

This will result in a lower particle mobility under the velocity scaled according to the

Froude criterion of similitude where $[U/\sqrt{gh}]_m = [U/\sqrt{gh}]_p$. Therefore, in order to

simulate particle mobility in under-scaled (too large) particles, i.e., to satisfy $[U/U_c]_m$

$= [U/U_c]_p$ the Froude criterion cannot be simultaneously satisfied. This unavoidably

leads to higher U in the model than the prototype (Table 2-2). This incomplete

similitude of parameters between the model and prototype is a common problem in

laboratory tests, (for example; Breusers et al., (1977), Ettema et al., (1998a) and

Ettema et al., 2006). Therefore, velocities in these experiments are raised from the

Froude scaled values in order to achieve flow similitude in U/U_c, and each time-step

in the model is named according its flow intensity value. This is deemed a more

important parameter on the evolution of scour Ettema et al., 1998a), and raises

interesting questions on the influence of the combination of clear-water and live-bed

conditions within a single tidal cycle on scour evolution. Therefore, low-tide is termed

Transition (as $U/U_c \sim 1$), the mid-tide is termed live-bed (as $U/U_c > 1$) and the high-

tide is termed clear-water (as $U/U_c \sim 1$).

Ettema et al., (1998a) comments that to satisfy similitude of particle mobility,

$[U/U_c]_m = [U/U_c]_p$. U, therefore, may be larger in the model than the Froude

criterion will suggest leading to a situation where $[U/\sqrt{gh}]_m > [U/\sqrt{gh}]_p$. As

discussed in §1.4.5, an increase in Froude number may result in an increase in

d_{sc}(Ettema et al., 1998a).

A further note on Re_D is required. Re_D does affect the nature of the boundary layer at the cylinder sides (Figure 1.11) thus influencing the vortex shedding regime, however, similitude of Re_D and Fr between the model and prototype cannot be simultaneously satisfied due to the inability to adjust the viscosity of water, and a lack of a suitable alternative fluid. The consequences of this dissimilitude will be discussed in §4.7.1.3.

Tidal Condition	U [m s^{-1}]	h [m]	h/D	D	U/U_c	Re_D	Flow Fr
Prototype Field Parameters							
Low-tide	1	2	0.5	4	1.02	2.9×10^6	0.23
Mid-tide	1.5	5	1.25	4	1.26	4.4×10^6	0.21
High-tide	0.7	8	2	4	0.57	2.1×10^6	0.08
Model							
transition	0.23	0.1	0.5	0.2	1.02	3.4×10^4	0.23
live-bed	0.33	0.25	1.25	0.2	1.26	4.9×10^4	0.21
clear-water	0.15	0.4	2	0.2	0.57	2.2×10^4	0.08

Table 2-2. Test conditions for rigid-bed tests. The prototype low, mid and high-tide parameter conditions relate to, in the scaled model to the 'transition' (low-tide), 'live-bed' (mid-tide) and 'clear-water' (high-tide) velocity-depth regimes.

Table 2-2 describes the model test parameters: there are three different test parameters that are each scaled from the prototype tidal condition. These are named according to their values of flow intensity U/U_c. The tests are the 'transition' where $U/U_c \approx 1$, (which is scaled from the prototype low tide condition), the 'live-bed' where $U/U_c > 1$ (scaled from the mid-tide prototype condition), and the 'clear-water' where $U/U_c < 1$, scaled from the high-tide prototype condition.

The time scale N_λ (i.e., λ_p/λ_m, where subscript p and m denote prototype and model respectively) of each tidal stage was scaled according the Froude criterion (Hughes,

(1993) where $N_\lambda = \sqrt{N_L/N_g}$. N_L is the ratio of the length scale between model and prototype (i.e, $[L]_p/[L]_m$), which in this case is 20 and N_g is the ratio of gravitational acceleration between model and prototype which is 1. The time-scale of the experiments, therefore, satisfies the Froude criterion: $N_\lambda = \sqrt{20} = 4.47$, which rearranges to give $\lambda_m = \lambda_p / 4.47$. Since λ_p for one half-cycle is 6 hours, λ_m for a half-cycle is 1 hour 20 minutes, and λ_m for each time-step is 27 minutes.

2.2.3 The Blockage Effect

The blockage effect occurs in flumes of limited width where the flow becomes slightly accelerated near the cylinder to preserve continuity of mass. Whitehouse, (1998) states that as long as $D \leq 1/6$ then the blockage effect is not significant to the results. In these experiments, the ratio was 1/6. Furthermore, comparisons between velocity measurements taken in the flume with and without the cylinder inserted showed no noticeable increase in velocity near the flume walls when the cylinder was in place.

2.2.4 Undisturbed Flow Tests

A series of undisturbed (i.e., no-cylinder) tests was performed for the conditions described in Table 2-2 to ensure that the flow in the flume was two-dimensional boundary layer flow, that the correct velocities were being generated by the pumps, and to provide control run values against which to compare results from the tests with monopoles present. The results from these no-cylinder test are presented in Appendix A5 and A6.

2.2.5 Test Procedure

The flume was set-up as described in detail in §2.1 Once the flume was filled to the required water depth, the pump was set to run at a predetermined frequency for the required flow velocity, which was confirmed with ADV readings at various points up and downstream of the cylinder. The flow was seeded with timoron particles of $d_{50} = 21$ μm; the seeding material required for the PIV. ADV measurements were taken after the PIV due to the coarser seeding particles required as the ADV seeding material was found to interfere with the PIV images if there was too much of it in suspension. Moreover, the flume was periodically emptied and cleaned. Once the measurement campaign was complete for a test, the parameters of which are detailed in §2.2.2, the flume was filled or drained to the next depth.

2.3 Mobile bed

To achieve objective four (as set out in §1.8.2) an extensive series of mobile bed experiments were conducted in the same flume as described in §2.1 over the period from February to March 2009. The flume was set up as for the rigid bed tests with the following changes: 1) a layer of sand ($d_{50} = 0.135$mm) 0.4 m thick was placed around the cylinder 1m both up and downstream of it. The remaining length of the flume was covered with 10 cm of sand with concrete breeze blocks raising the flume floor. At each end of the flume a layer of pebbles ($d_{50} = 0.02$ m) 0.5 m in width was placed on the surface of the sand. This was done to encourage a boundary layer to form and

prevent and scour occurring at each end of the flume. A schematic diagram is given in Figure 2-14.

In order to study the potential effects of the interaction of tidal flow on the scour development, in the mobile bed tests tidal flow was simulated by approximating an idealised prototype symmetrical (sinusoidal) non-progressive (standing wave) tide. One tidal cycle is divided into six 'time-steps' (Figure 2-13) with the incoming direction tide ('positive' herein) separated into transition (prototype low-tide, Table 2-3), live-bed (prototype mid-tide, Table 2-3), clear-water (prototype high-tide, Table 2-3) and outgoing reversed direction ('negative' herein) clear-water, live-bed and transition. With the reversal of flow direction, the upstream side of the cylinder changes. During positive flow the upstream side of the monopile is the 'A' side and the downstream side is the 'B' side, and during negative flow the upstream side is the 'B' side and the downstream side is the 'A' side (Figure 2-15). Table 2-3 shows the test parameters.

Time Step	Flow Direction	Upstream Side	Test Condition	Relevant Tidal Stage	Relevant Tidal Half-Cycle	U	h	U/U_c	h/D	Re_D	Fr
1	Positive	A	Transition	low-tide	1st	0.23	0.1	1.02	0.5	3.4×10^4	0.23
2	Positive	A	Live-bed	mid-tide	1st	0.31	0.2	1.24	1	4.6×10^4	0.22
3	Positive	A	Clear-water	high-tide	1st	0.15	0.4	0.54	2	2.2×10^4	0.076
4	Negative	B	Clear-water	high-tide	2nd	0.15	0.4	0.54	2	2.2×10^4	0.076
5	Negative	B	Live-bed	mid-tide	2nd	0.31	0.2	1.24	1	4.6×10^4	0.22
6	Negative	B	Transition	low-tide	2nd	0.23	0.1	1.02	0.5	3.4×10^4	0.23
7	Positive	A	Transition	low-tide	3rd	0.23	0.1	1.02	0.5	3.4×10^4	0.23
8	Positive	A	Live-bed	mid-tide	3rd	0.31	0.2	1.24	1	4.6×10^4	0.22
9	Positive	A	Clear-water	high-tide	3rd	0.15	0.4	0.54	2	2.2×10^4	0.076
10	Negative	B	Clear-water	high-tide	4th	0.15	0.4	0.54	2	2.2×10^4	0.076
11	Negative	B	Live-bed	mid-tide	4th	0.31	0.2	1.24	1	4.6×10^4	0.22
12	Negative	B	Transition	low-tide	4th	0.23	0.1	1.02	0.5	3.4×10^4	0.23

Table 2-3. Test conditions.

The test was run for the duration of two full tidal cycles allowing the scour hole to develop under two positive and negative tidal half-cycles in the order of positive (low, mid, high-tide) - negative (high, mid, low-tide) - positive (low, mid, high-tide) - negative (high, mid, low-tide). The scale of the experiments was 1/20 with prototype conditions and the time-scale of the experiments satisfies the Froude criterion: $\lambda = \sqrt{20} = 4.47$, leading to a time-step duration of 27 minutes and a half-cycle of one hour and 21 minutes (§2.2.1).
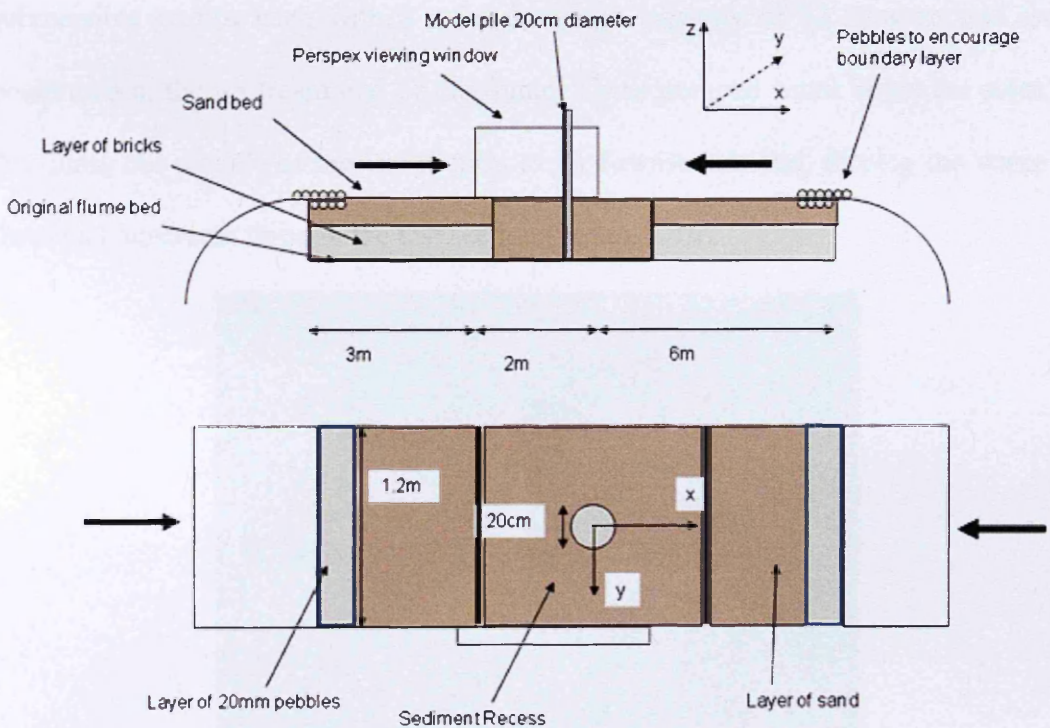
Figure 2-14. A schematic diagram of the mobile bed flume set-up.
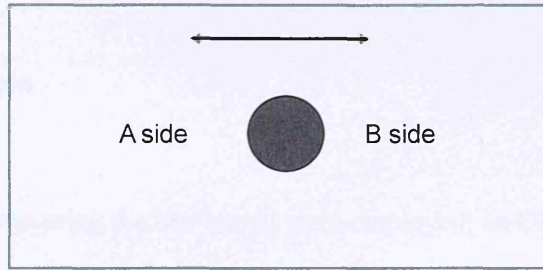
Figure 2-15. Schematic showing the naming of the A and B side.

2.3.1 Flow Reversing Pumps

The main pumps in flume are unidirectional. Therefore, to create flow reversal, 9 submersible pumps each with a rated discharge capacity of 12 litres/second were positioned at the upstream end of the flume. These pumped water down the sides of the flume but outside of the test section to its downstream end, forcing the water to flow back upstream through the test section (Figure 2-16).
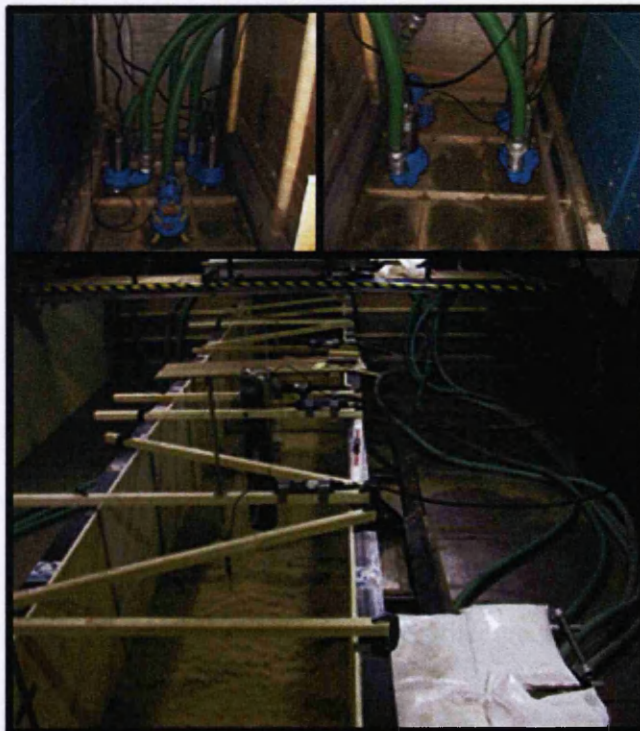
Figure 2-16. (Top row) submersible pumps positioned at the upstream end outlet, (bottom) pipes allowing water to be pumped into the discharge end outlet where flow is forced back down the flume in the centre.

2.3.2 Data Collection

Two methods of measuring the bed height were employed; an Ultrasonic Ranging System and a laser distance profiler. Their deployment is described here.

2.3.2.1 Ultrasonic Ranging System

The Seatek Ultrasonic Ranging System (URS) system uses acoustic transducers to measure the travel time of acoustic signals from the transducer to boundary and back to the transducer. By recording the travel time of these acoustic 'pings' the URS is able to calculate the distance from the transducer head to the boundary. In this deployment 12 transducers were positioned around the circumference of the pile at 0, 90, 180 and 270 degrees with radial intervals of 10 cm beginning at 6.5 cm from the cylinder's surface (Figure 2-17 and 2-18), which was the closest location to the monopole that the URS could be positioned given the experimental configuration used here.

The URS was set-up to take readings every ten seconds from the start of each time-step providing a detailed time-series data-set of scour hole development. Each reading is an average of 20 pings over one second with the highest and lowest three readings removed. The maximum resolution of the system is 0.1 mm and the error was +/- 0.2 mm. Specifications of the URS system and laser profiler are given Appendix (A4).
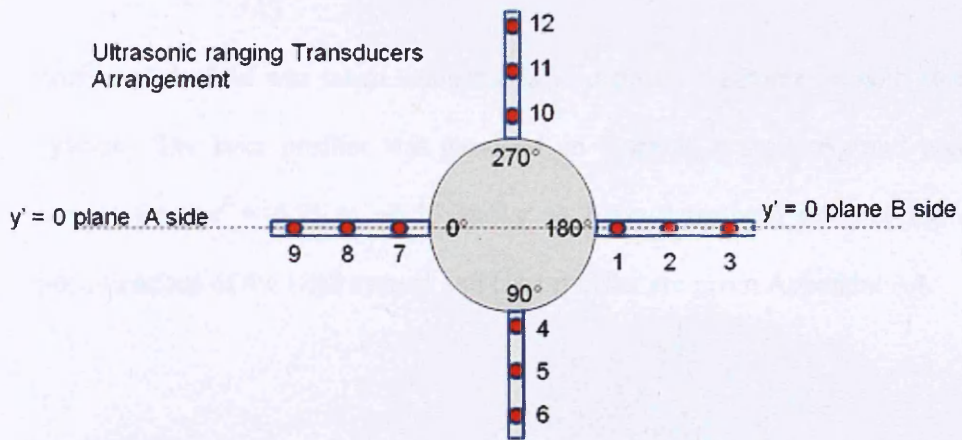
Figure 2-17. Schematic diagram of experimental set-up and URS positions, where the origin is

set at the cylinders centre.

Figure 2-18. Image of the URS deployment around the cylinder.

2.3.2.2 Laser Profiler

Full bed profiles on either side of the cylinder were made at the end of each mobile

bed test using a laser distance measurer (Leica Disto). At the end of the test a full

profile of the bed was taken using the laser distance measurer on both sides of the cylinder. The laser profiler was mounted on a specially made rig and was able to sample from $x' = 6.75$ to -6.75 and $y' = 2$ to -2 on both sides of the cylinder. Specifications of the URS system and laser profiler are given Appendix A4.

2.4 Collar and Helical Strake Cylinder Test Set-up

In order to achieve the aims and objectives described in §1.8, a series of rigid and mobile bed tests were conducted for a collared and helical strake cylinder in the flume described in §2.1 and §2.3 respectively. The experimental set-up for the rigid bed tests is described in §2-1 and the procedure and data collection was the same as in §2.1 and §2.2. The collared and helical strake cylinders were positioned in place of the smooth cylinder for these tests. The clear-water time-step was not investigated for the collared and helical strake cylinders as the rigid and mobile bed results (§3 and §4) showed very low velocity flow and turbulence fields and very little scour respectively relative to the transition and live-bed. The test conditions are given in Table 2-4.

Time Step	U	h	D	U/U_c	Re_D	Fr
Transition	0.23	0.10	0.2	0.88	3.4×10^4	0.23
Live-bed	0.33	0.25	0.2	1.26	4.9×10^4	0.21

Table 2-4. Test conditions for the straight and helical collared monopile.

The collared cylinder was also subjected to mobile bed tests as, from the results of the rigid bed tests (which are discussed in §5.2 - 5.6), it presented the most promising changes to the flow field that may reduce scour.

The collared cylinder (Figure 2-19, left) is 0.2 m in diameter and has five 0.0025 m wide 2 mm thick steel sheet horizontal collars around the circumference attached at 0.1 m intervals with the nearest to the bed being located at 0.1 m off the bed. The helical strake cylinder (Figure 2-19 right) consists of 0.0025 m wide steel sheet coiled around the circumference at an angle of 45° and at a spacing of 0.1 m. Figure 2-20 is an image of the collared (left) and helical straked (right) cylinder.
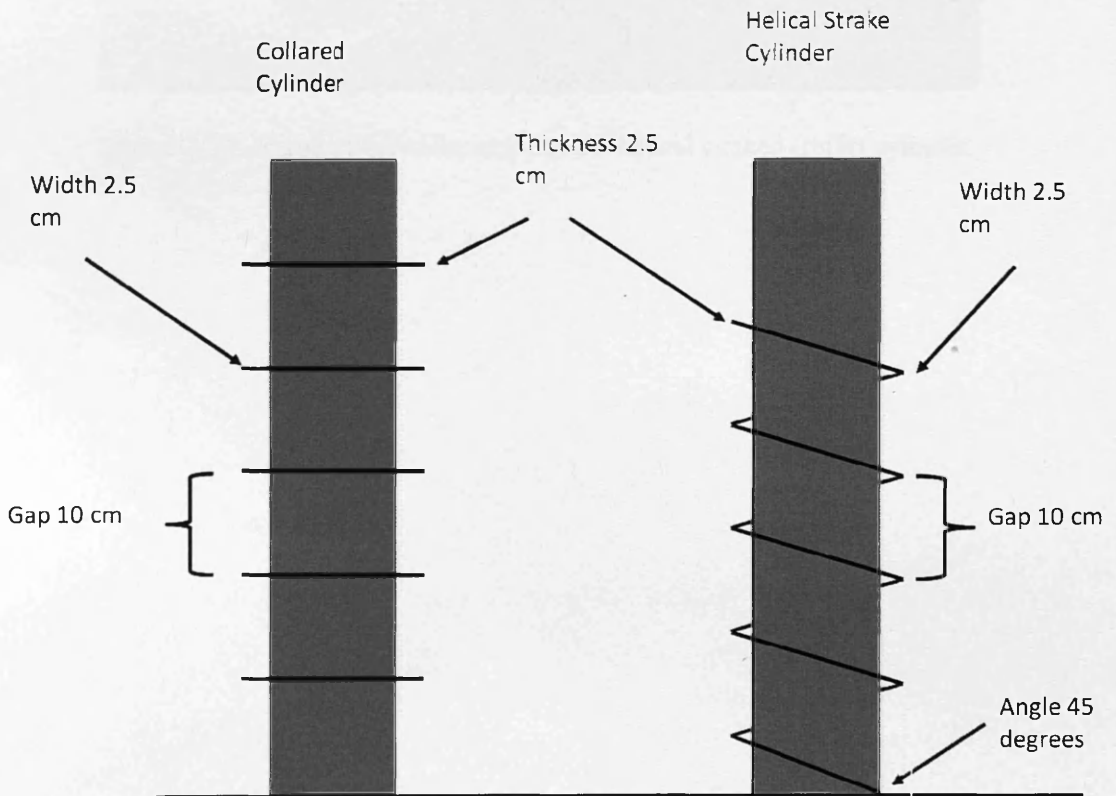
Figure 2-19. Schemiatic diagrams of the collared cylinder (left) and helical straked cylinder (right).
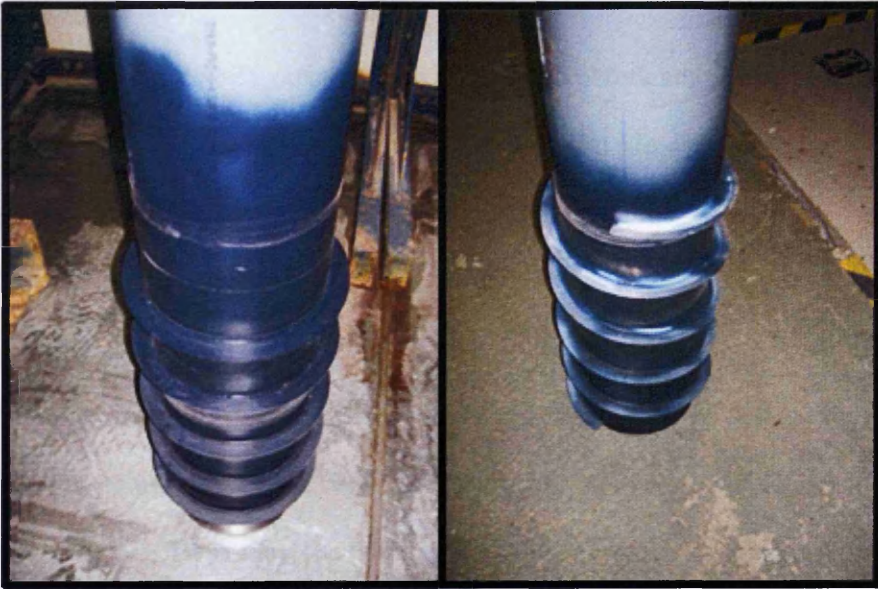
Figure 2-20. Image of the collared (left) and helical straked (right) cylinder.

Chapter 3: Rigid Bed Experiments on the Flow, Turbulence and Bed Shear Stress around the Cylinder in Tidal Flow

3.1 Introduction

This chapter presents results of a series of smooth rigid-bed tests designed to study the flow and turbulence fields and resulting amplification of bed shear stresses around the cylinder and how these may change under variable current velocities, depths that are scaled from tidal current flow. It addresses the objectives set out in §1.8, and the experimental design and procedure is given in §2. The results, given in §3.2, §3.3, §3.4 and §3.5, present the mean flow and turbulence measurements upstream of the cylinder, in the near-cylinder region, downstream of the cylinder and the amplification of bed shear stress around the cylinder respectively. A summary of the results is given in §3.6 before a detailed discussion is given in §3.7. Here the influence of Re_D, Fr_h, and h/D on the wake flow field, the influence of cylinder diameter on the upstream flow field, a discussion of Re_D dissimilitude between model and prototype, the horseshoe vortex in the tests, the influence of variable h between tests (pertaining to tidal range in the prototype), and the scour process under the three test conditions and its relation to the tidal scour process is discussed

3.2 Mean Flow and Turbulence Upstream of the Cylinder

3.2.1 Upstream Mean Flow Profiles

Three-dimensional time-averaged mean velocity data was derived from the ADV velocity time series recorded upstream of the cylinder. These velocities were normalised with the undisturbed depth-averaged velocity magnitude U_∞ which were recorded during control tests with no cylinder in the flume (Appendix A5), to give non-dimensional velocity components $u' = u/U_\infty$, $v' = v/U_\infty$ and $w' = w/U_\infty$. v and w were normalised by U_∞ and not the equivalent V_∞ and W_∞ as the undisturbed flow was essentially one-dimensional (i.e. $V_\infty/U_\infty \approx W_\infty/U_\infty = 0$). Profiles were recorded at various positions between $x' = -0.665$ and $x' = -5.75$ and along four planes parallel to each other at $y' = 0$, 0.6, 0.85 and 1.1, (as described in §2.1.2.2). In keeping with the nomenclature used in the literature, the $y' = 0$ plane will hereby be referred to as the centreline. Depth z is normalised with water depth h to give non-dimensional depth $z' = z/h$.

3.2.1.1 Changes in Streamwise Mean Flow (u'), Comparison between each Test

Figure 3-1 shows plots of u' for the clear-water, live-bed and clear-water tests (columns one to three respectively) with rows one to four (top to bottom) presenting plots along the centreline, $y' = 0.6$, 0.85 and 1.1 planes respectively. Along the centreline, there is a reduction in u' on approach to the cylinder, and in the live-bed and clear-water tests the profiles become more vertically uniform (a phenomenon also observed in Graf and Yulistiyanto, 1999 and Ahmed and Rajaratnam 1998), though in

the transition the profiles do not become as uniform as in the other tests. The relative amount of velocity reduction is similar in all tests (flow is slowed to $\approx 0.4U_\infty$).

The results from the $y' = 0.6$, 0.85 and 1.1 planes (hereby collectively termed off-centreline), indicate that there is also reduction of u' parallel to the centreline. The reduction is only observed along the $y' = 0.6$ and 0.85 planes at $x' > -1$ and -1.625 respectively, but it does indicate that the retardation effect is present along the off-centreline planes before it is subjugated by the constriction effect on approach to the cylinder. Flow constriction causes an increase in velocity along each of these planes with the maximum speed attained at $x' = -0.665$. In the $y' = 0.6$ plane the maximum speed is u' approximately between 1 - 1.1 U_∞ while in the $y' = 0.85$ and 1.1 planes, it reaches $u' \approx 1.1 - 1.2U_\infty$.
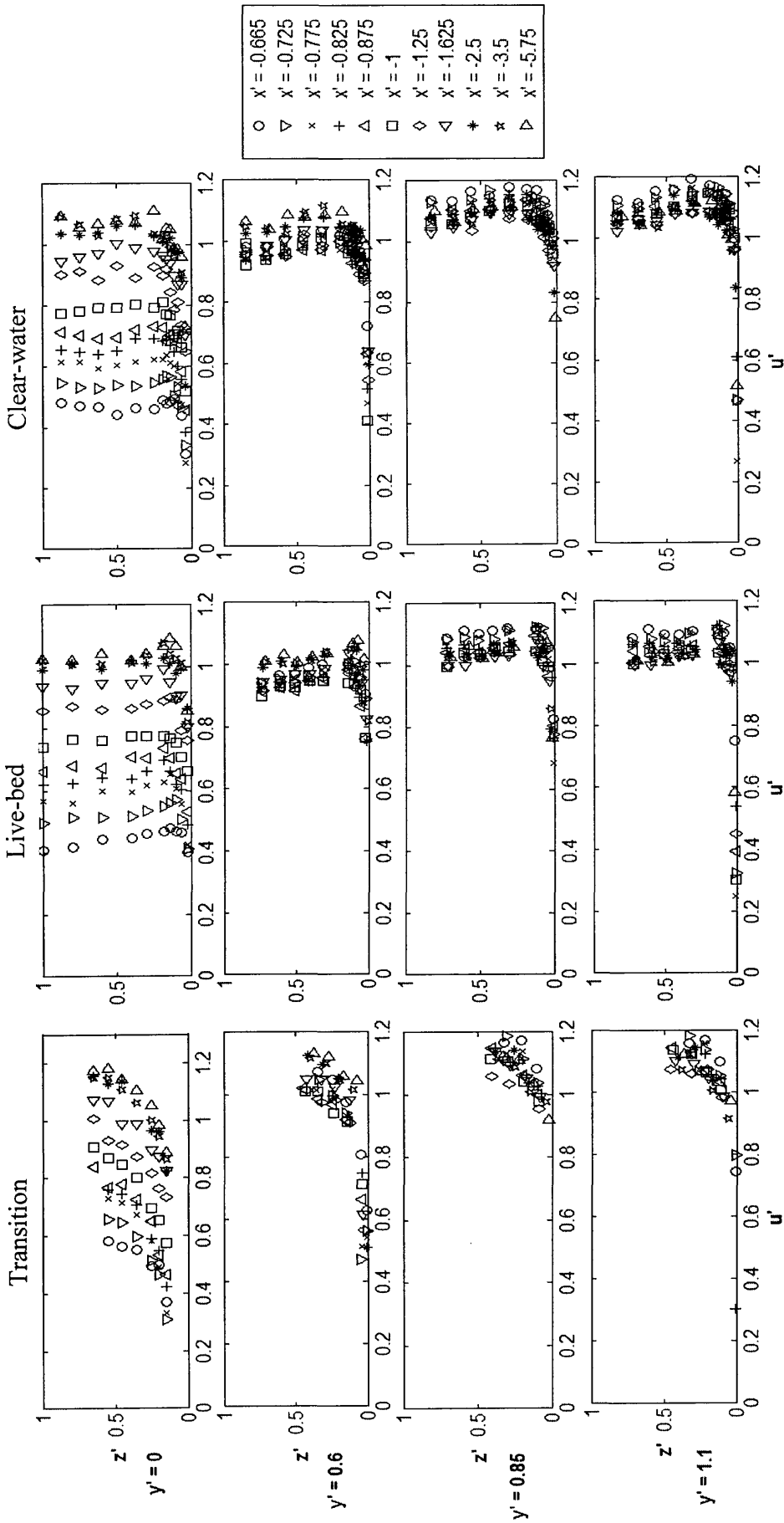
Figure 3-1. Mean u' flow velocity profiles for the transition (1st column), live-bed (2nd column) and clear-water (3rd column) along the $y' = 0$ (centreline), 0.6, 0.85 and 1.1 planes (top to bottom rows).

3.2.1.2 Lateral Mean Flow (v'), Comparison between each Test

Figure 3-2 presents plots of v' in the same way as for u' above. Along the centreline v' deviates from zero on approach to the cylinder as the flow is deflected around it. This can also be observed in the data presented by Graf and Yulistiyanto, (1999). The reason for recording $v' \neq 0$ along the centreline is most likely because the ADV sampling volume is wider than the centreline. It is assumed that there will be a plane where v' is zero that lies between flow deflected to the left and flow deflected to the right of the cylinder. In the clear-water test there is significant vertical shear in v', which is not seen in the transition or live-bed tests, where v' is relatively constant with depth. When compared to the transition and live-bed, this shear in v' does not seem to significantly affect the upstream distributions of w' and u', nor does it appear to have any effect on the turbulence distributions (which will be discussed later, Figure 3-6), or the downstream clear-water measurements (which are discussed in §3.4). The cause of this shear is unclear, though it does have characteristics of a secondary flow which may be generated by the flume. Velocity shear is observed in the no-cylinder control clear-water test (Appendix A5), which suggests a helical flow in the flume superimposed upon the two-dimensional downstream flow. The implication is that for the clear-water test, the free-stream flow is not strictly two-dimensional, however, apart from the shear in upstream v', this seems to have little observable effect on the results. There are some structures in the distribution of v' in the downstream PIV flow vector maps which are unique to the clear-water test, but these are minor features and the remaining flow field appears similar to the live-bed and transition tests (these structures will be discussed in §3.4). It appears that this helical flow is likely to be a

coincidental artefact of the flume dimensions and pump at the particular frequency at which it operates during the clear-water test.

In the live-bed and transition tests there is a general increase of v' towards the cylinder along the $y' = 0.6$ (approximately 0 - $0.4U_\infty$), 0.85 (approximately from -0.1 - $0.2U_\infty$) and 1.1 (approximately 0 - $0.25U_\infty$) planes as flow is deflected around its surface. The maximum value of v' along the $y' = 0.6$ and $y' = 0.85$ planes occurs at $x' = -0.665$, and in the $y' = 1.1$ plane slightly upstream at $x' = -0.725$, indicating that the constriction effect of the cylinder diminishes laterally in a similar way in each of the three tests. The magnitude of constriction is also comparable, raising v' to approximately $0.45 U_\infty$ in the transition and live-bed tests. The deflection of flow around the cylinder appears to be present as far upstream as $-5.75D$. In both tests negative (flow towards the centreline) v' is recorded in the profiles $x' = 5.75, 3.5$ and 2.5 along the $y' = 0.85$ plane, before becoming positive closer to the cylinder. This results in the maximum positive v' near the cylinder to be significantly less than it is on the $y' = 0.6$ plane. This feature does not appear in the no-cylinder transition and live-bed tests indicating that it may be caused by constriction of the flow causing some lateral shearing in the far upstream of the cylinder.
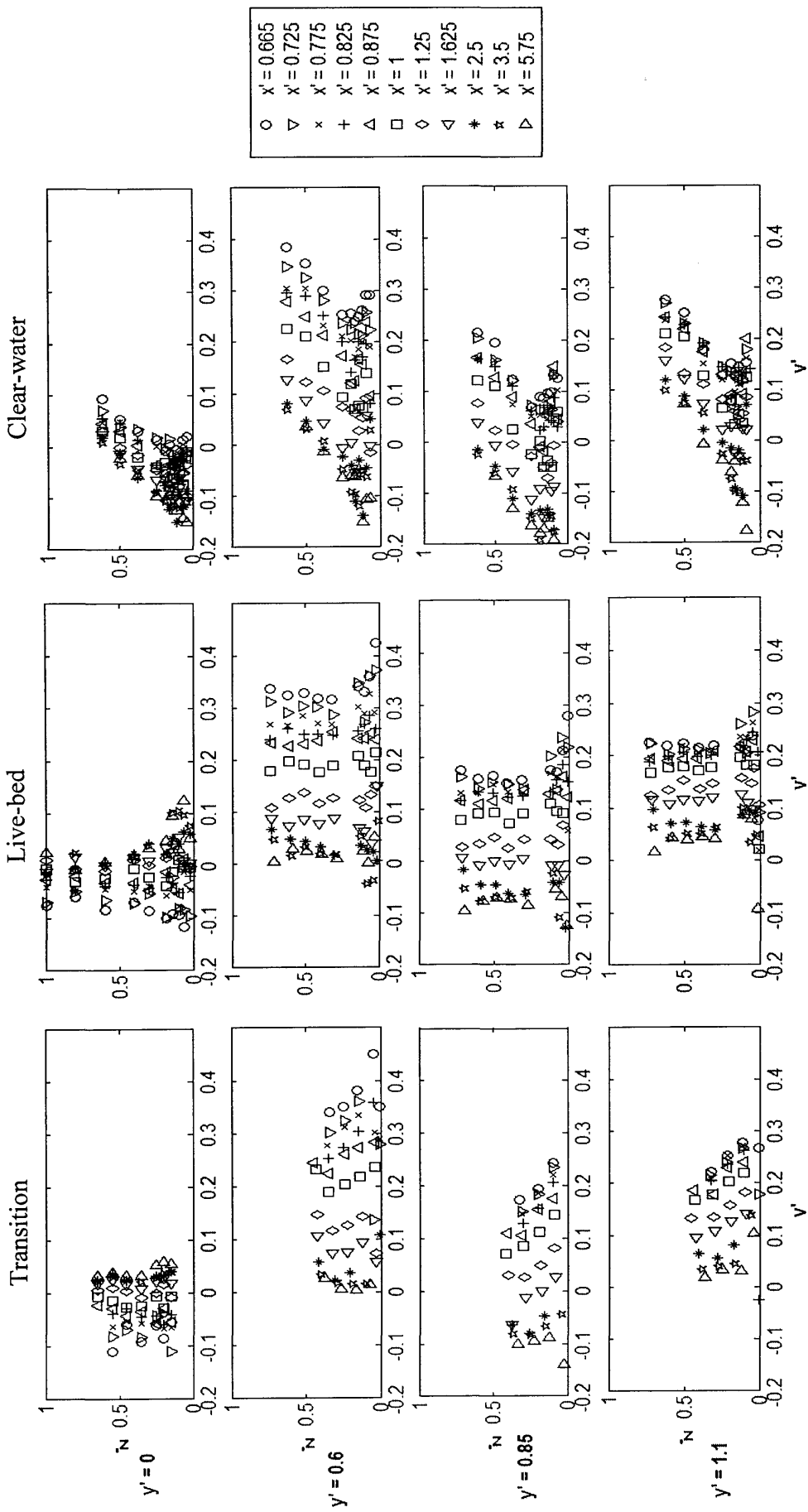
Figure 3-2. Mean v' flow velocity profiles for the transition (1st column), live-bed (2nd column) and clear-water (3rd column) along the $y' = 0$ (centreline), 0.6, 0.85 and 1.1 planes (top to bottom rows).

3.2.1.3 Vertical Mean Flow (w'), Comparison between each Tests

Figure 3-3 presents the w' measurements. Along the centreline w' remains relatively constant and close to zero in the region from $x' = -5.75$ to -0.825. Downstream of $x' = -0.825$, w' begins to increase and at $x' = -0.665$ a near-bed negative maximum appears, as is commonly observed in the literature indicating downflow (for example, Graf and Yulistiyanto, 1999 and Sarker, 1998). This maximum varies in depth between tests, being at approximately $z' = 0.25$, 0.1 and 0.18 for the transition, live-bed and clear-water tests respectively. Maximum w' occurs further from the bed with increasing distance upstream from the cylinder until the downflow becomes indistinguishable in all tests at $x' = -0.825$. The majority of its growth in strength to a maximum near the bed occurs within the boundary layer in the approaching flow (Table 3-1). The downflow appears to be at least 0.5 cm wide along the leading edge of the cylinder as this is equal to the width of sampling volume of the ADV. However, it is unlikely that the downflow will exist much further off the centreline than this because as the curvature of the cylinder falls away from the centreline, the flow stagnation and downward pressure gradient that cause the downflow to form will become increasingly less. Clearly on the off-centreline planes the downflow is non-existent as is any flow reduction near the cylinder; here constriction of flow is dominant as discussed above in §3.2.1.1. Indeed, the large increase in v' and negligible w' along the $y' = 0.11$ plane as discussed in §3.2.1.2 indicates that flow here is primarily deflected flow moving around the cylinder surface and that flow retardation is insignificant. This increase in w' near the bed along the centreline coincides with the increased values of v' along the adjacent $y' = 0.6$ plane near the cylinder. It appears that this is the result of the downflow being deflected around the

cylinder upon reaching the bed. Similar observations can be made in the data presented by Graf and Yulistiyanto, (1999).
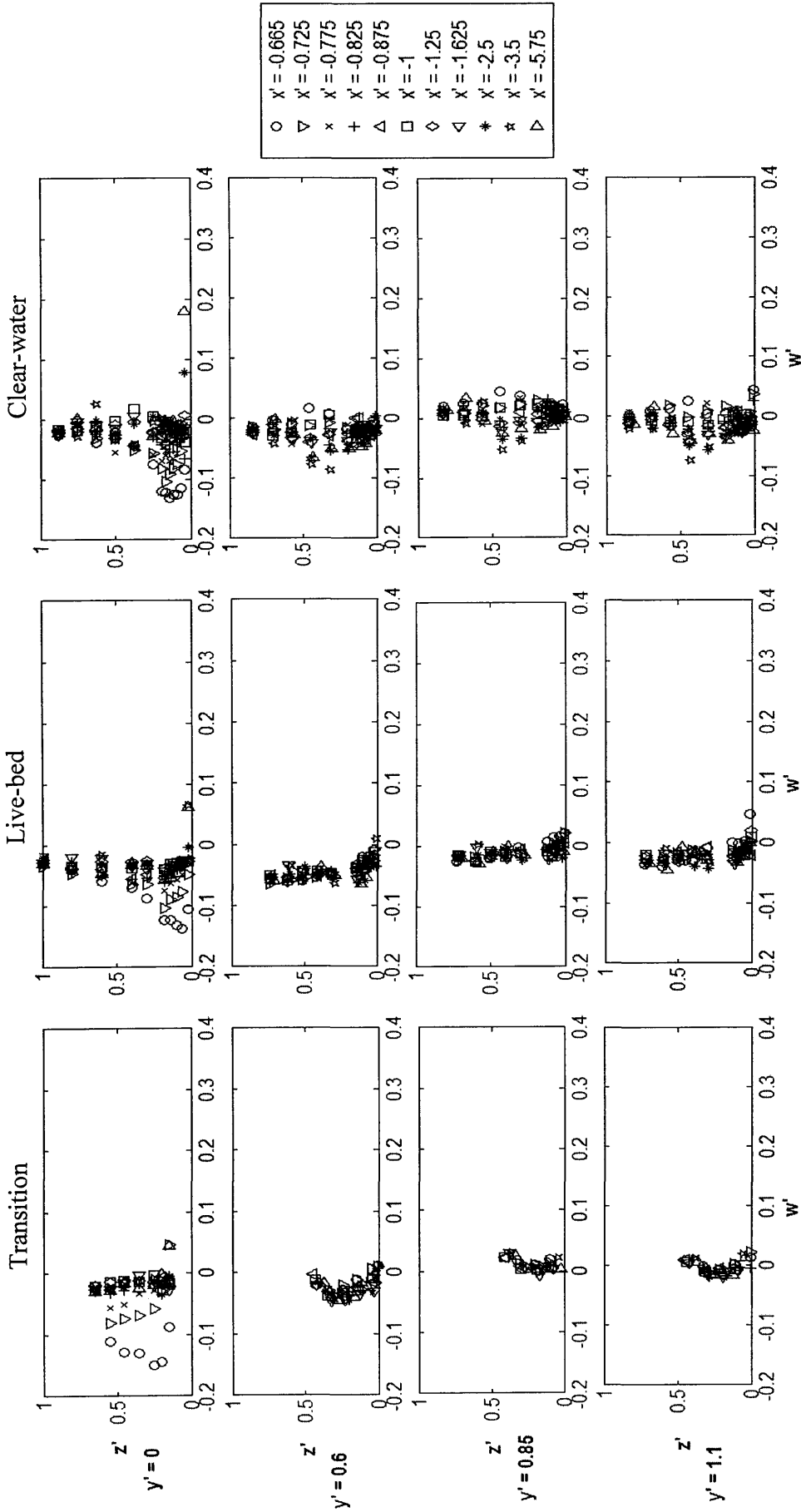
Figure 3-3. Mean w' flow velocity profiles for the transition (1st column), live-bed (2nd column) and clear-water (3rd column) along the $y' = 0$ (centreline), 0.6, 0.85 and 1.1 planes (top to bottom rows).

Time step	U [m]	h [m]	h/D	Approximate δ/h	Height at which the downflow appears z [m]
Clear-water	0.15	0.4	2	≈ 0.2	0.3
Live-bed	0.33	0.25	1	≈ 0.2	0.3
Transition	0.23	0.1	0.5	≥ 0.5	0.6

Table 3-1. The boundary layer depth δ to flow depth ratio (approximate calculation from logarithmic velocity plots, see Appendix A.10).

3.2.2 Turbulence Fields Upstream of the Cylinder

3.2.2.1 Turbulence Profiles, Live-bed Test

Six turbulence parameters were calculated from the velocity measurements upstream of the cylinder for the live-bed test (Figure 3-4). These comprised of three turbulence intensities (TI) $u^+ = \left(\overline{u''u''}\right)^{0.5}, v^+ = \left(\overline{v''v''}\right)^{0.5}$, and $w^+ = \left(\overline{w''w''}\right)^{0.5}$ and three Reynolds stress components $\tau_{uv} = -\rho\overline{u''v''}$, $\tau_{uw} = -\rho\overline{u''w''}$, and $\tau_{vw} = -\rho\overline{v''w''}$, (where $u'' = u - \bar{u}$, $v'' = v - \bar{v}$ and $w'' = w - \bar{w}$).

Along the centreline there were no significant changes with x' and the turbulence was approximately isotropic ($u^+ = v^+ = w^+$), except near the bed where there is boundary layer shear and u^+ is the strongest component along with slight increases in the other two TI components. Close to the cylinder, there are increases in TI near the bed that imply a small horseshoe vortex may be present, but this is not coupled with reversed flow (Figure 3-1), implying that the vortex is perhaps closer to cylinder than the nearest measurement point (as will be discussed further in §3.7.2). The distributions

along the centreline are similar to those observed in Graf and Yulistiyanto, (1999) and Ahmed and Rajaratnam, (1998). Off the centreline $u^+ = v^+ = w^+$, except near the bed were $u^+ > v^+ >> w^+$.

Reynolds stresses (which indicate the amount and orientation of momentum transfer between shear layers) τ_{uv}, τ_{vw}, and τ_{uw} are also plotted in Figure 3-4. Along the centreline τ_{uv} has a tendency to become negative near the bed and the cylinder while τ_{vw} remains fairly constant close to zero regardless of x'. A negative value of τ_{uw} indicates net upward transfer of momentum between shear layers, and vice versa. τ_{uw} becomes more positive closer to the cylinder and the near the bed. Off the centreline τ_{uw} generally behaves similarly as on the centreline, indicating normal boundary layer shearing near the bed, while τ_{uv} and τ_{vw} show no specific pattern of distribution with x' and y'.
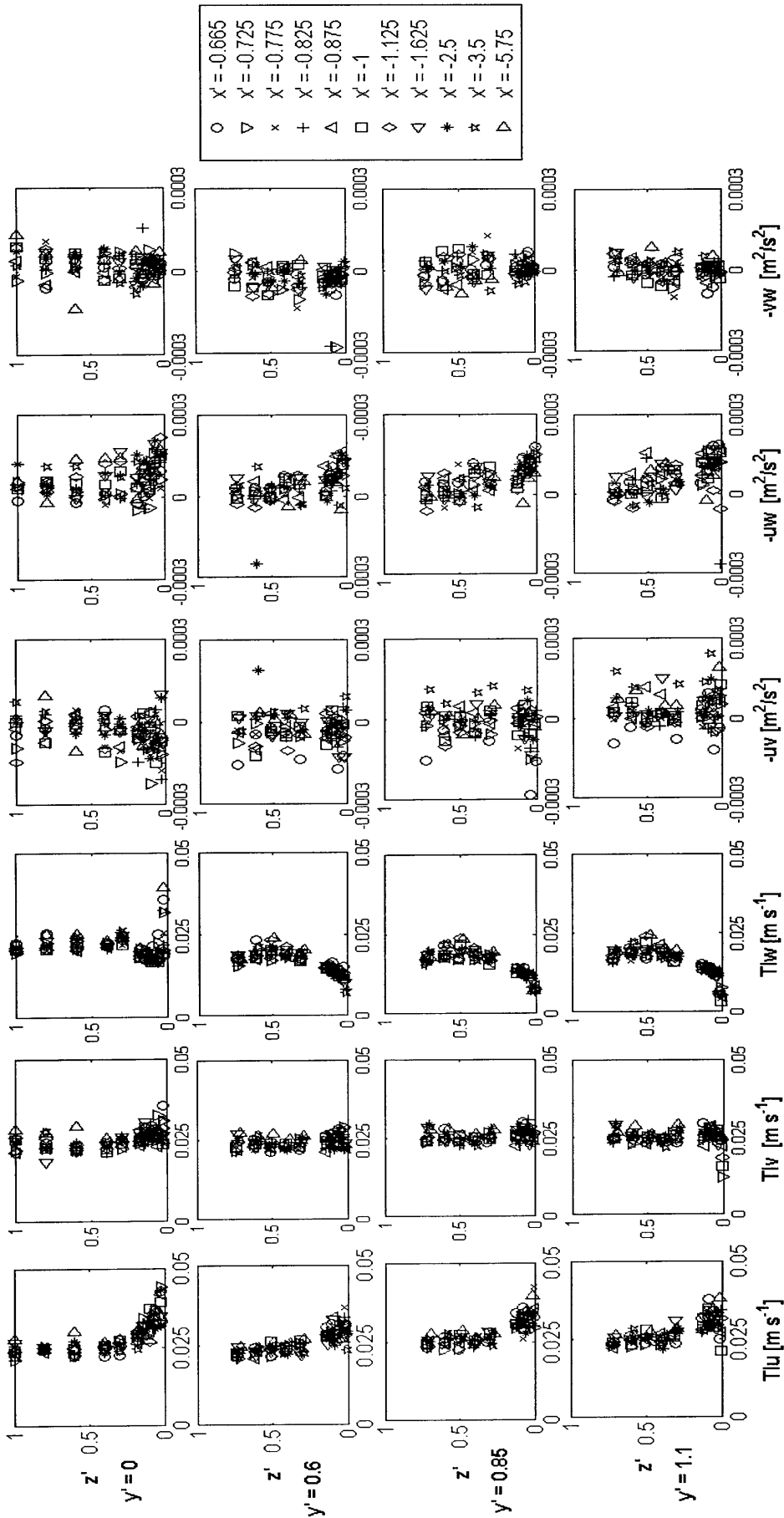
Figure 3-4. Distributions of TI, and Reynolds Stress along the $y' = 0$ (centreline), (first row), and the $y' = 0.6$, 0.85 and 1.1 m planes (second – fourth row respectively) for the live-bed test.

3.2.2.2 Turbulence Profiles, Transition and Clear-Water Tests

Figures 3-5 and 3-6 are plots of TI and Reynolds Stresses for the transition and clear-water tests respectively. Though $TI_{live\text{-}bed} > TI_{transition} > TI_{clear\text{-}water}$, the spatial distributions are similar to those in the live-bed tests, indicating a similar upstream turbulence field is present throughout each tidal stage.

Figure 3-5. Distributions of TI, and Reynolds along the $y' = 0$ (centreline), (first row), and the $y' = 0.6$, 0.85 and 1.1 m planes (second – fourth row respectively) for the transition test.
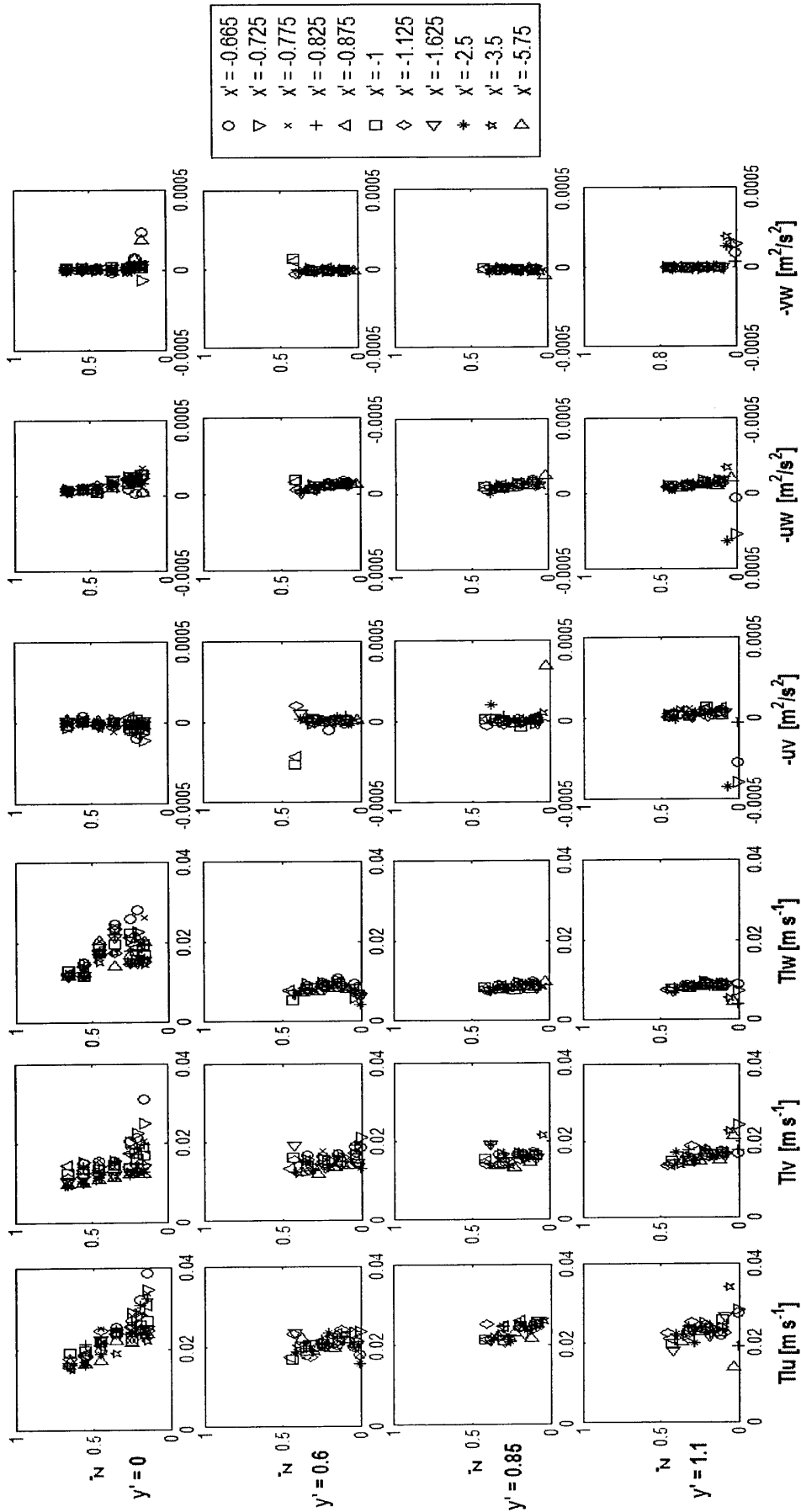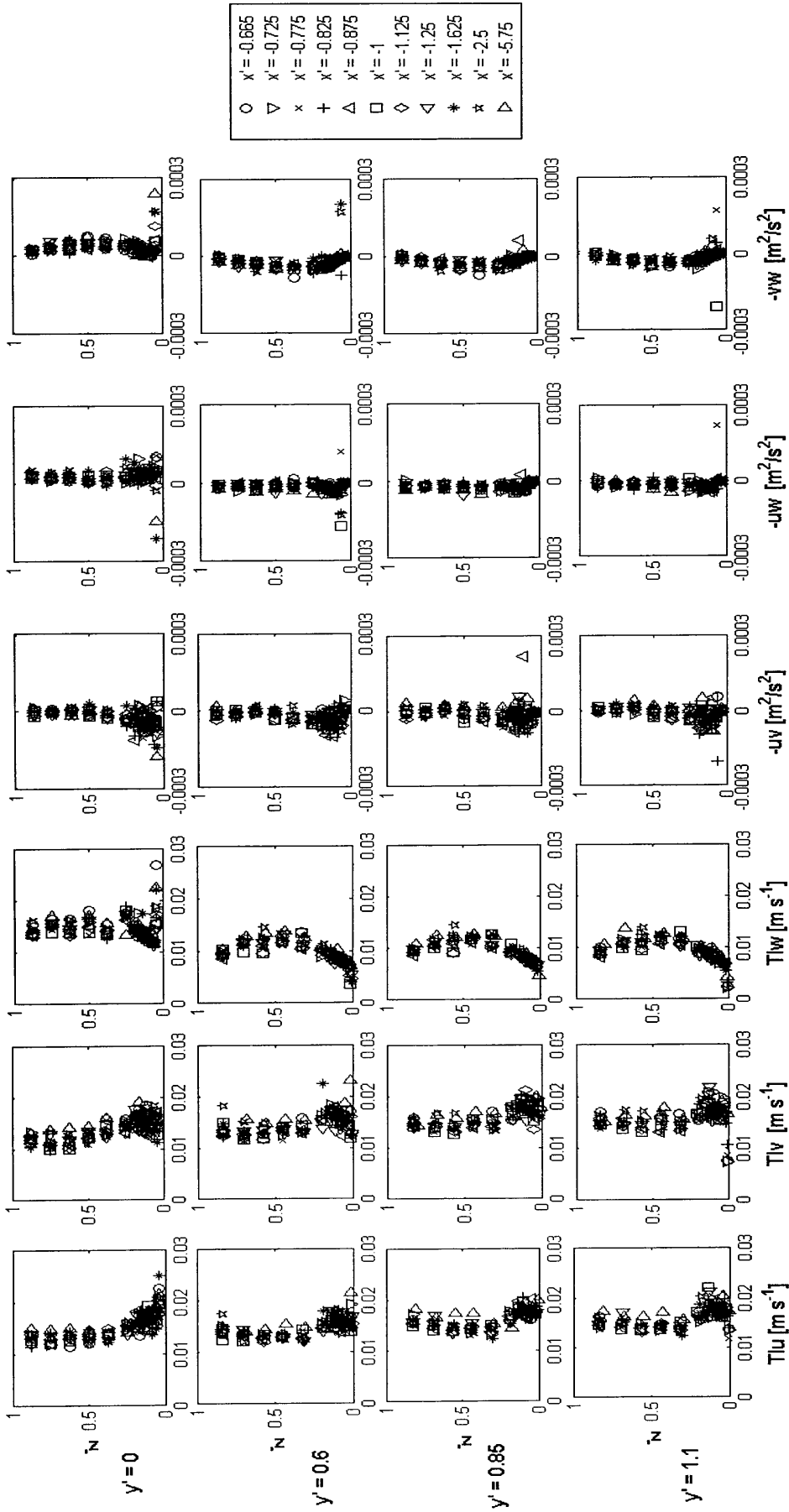
Figure 3-6. Distributions of TI, and Reynolds Stress along the $y' = 0$ (centreline), (first row), and the $y' = 0.6$, 0.85 and 1.1 m planes (second – fourth row respectively) for the clear-water test.

3.3 Mean Flow Velocities and Turbulence Profiles in the Near-Cylinder Region

3.3.1 Near-Cylinder Mean Flow Velocity Profiles

3.3.1.1 u', Comparison between Tests

Figure 3-7 shows plots of u' for the transition, live-bed and clear-water tests at the y' and x' positions described in (§2.1.2). Variation of u' in the $y' = 0.3$ is greater than in the other measurement planes. For the transition test the upstream profile at $x' = -0.6$ shows streamwise boundary layer sheared flow and $u' < U_\infty$, and has similar profile shape and velocity to the first downstream profile at $x' = 0.25$. This is also found in the live-bed and clear-water test. Between $x' = 0.5$ to 0.65 in the transition test the profiles show a trend of velocities decreasing upwards. Profiles $x' = 0.5$ and 0.6 exhibit essentially zero velocity except at the bed. The same distribution of velocity is observed in the clear-water test though with much more variability in the profiles including $u' > U_\infty$ near the bed at $x' = 0.65$, and flow reversal (negative u') near the surface at $x' = 0.5$ and 0.65. In the live-bed test between $x' = 0.5$ to 0.65 there is no reversal and $u' > U_\infty$. Common to all tests is the disappearance downstream of classical boundary layer flow, with distributions becoming rather variable indicating increased flow disturbance in the cylinders wake.
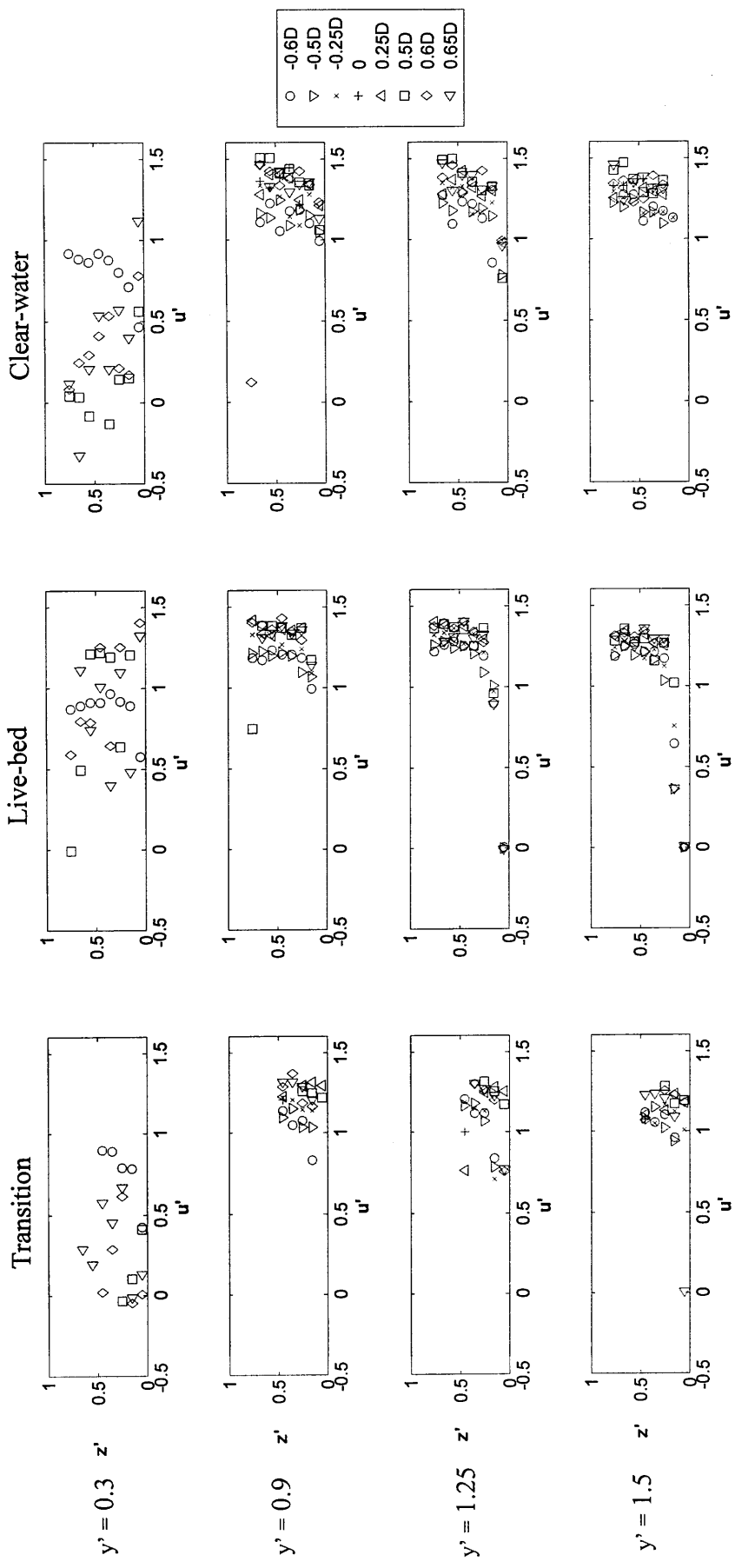
Figure 3-7. Near-cylinder mean u flow velocity profiles for the transition (first column), live-bed (second column) and clear-water (third column) along the $y' = 0.3$, (first row), and the $y' = 0.9$, 1.25 and 1.5 planes.

The point of lateral separation varies between the tests. In the measured region, no reversal is observed in the live-bed or transition test indicating the flow has not separated while separation does occur in the clear-water test as indicated by strong reversal of flow. This is to be expected as the lower velocity, and hence lower Re_D will encourage earlier separation in the clear-water (separation occurs at a point further upstream on the cylinder than at higher Re_D, §1.3.3). In the clear-water test the observation of higher bed velocities and very low or reversed surface velocities downstream of $x' = 0$ indicates that the point of separation changes with depth, being further upstream on the cylinder near the surface, and further downstream near the bed. A similar gradient is observed in the live-bed test, though without any reversal of flow. The results also indicate that the wake in the live-bed test is thinner behind the cylinder than in the clear-water, as would be expected due to the higher Re_D. This is implied by the observation that downstream of the cylinder velocity rarely decreases below 0.5 u' and increases above $u' = 1$, indicating that flow constriction is occurring. In the transition test velocity is reduced downstream of the cylinder to zero and remains relatively constant with depth. This suggests a zone of separation which is vertical, though as no reversed flow is observed it can be inferred that the wake here is also thinner than the clear-water wake. Figure 3-8 shows a (qualitative) schematic diagram of the relative change in position of separation between each test.
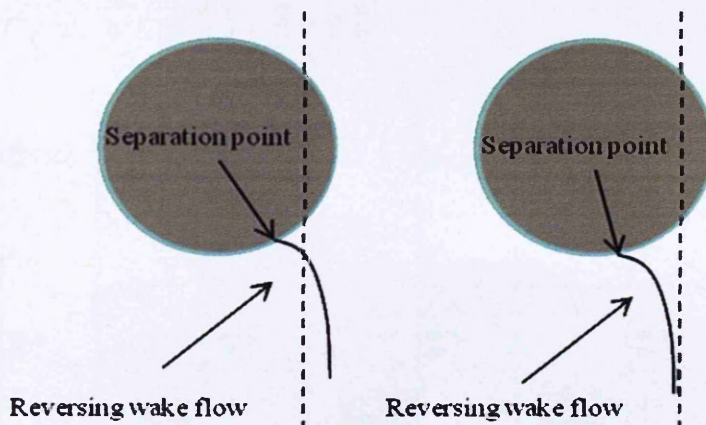
Figure 3-8. Schematic diagram showing the relative change in position of the lateral separation point between the clear-water (4-8a) and mid and transitions (4-8b).

In the $y' = 0.9$, 1.25 and 1.5 planes there is no reversal of flow and the following trend is observed at all positions: upstream profiles $x' = -0.6$ and -0.5 remain relatively constant, and from $x' = 0.25$ to 0.6 there is a marked increase to in speed. In these planes the constriction effect increases flow to a maximum of $\approx 1.5\ U_\infty$ in the clear-water test and to $\approx 1.4\ U_\infty$ in the low and live-bed tests.

3.3.1.2 v', Comparison between Tests

Figure 3-9 shows plots of v' for the transition, live-bed and clear-water tests at the y' positions described above. Variation of v' is greatest along the $y' = 0.3$ plane, upstream it is relatively constant at $\approx 0.5\ U_\infty$ for all tests. Downstream between $x' = 0.5$ to 0.65 v' reduces and in some places becomes negative, indicating a change in lateral direction (now flowing towards the centreline). In the live-bed test the v' component is exclusively negative implying flow towards the centreline. This is not observed in the transition and clear-water tests where both negative and positive are observed.
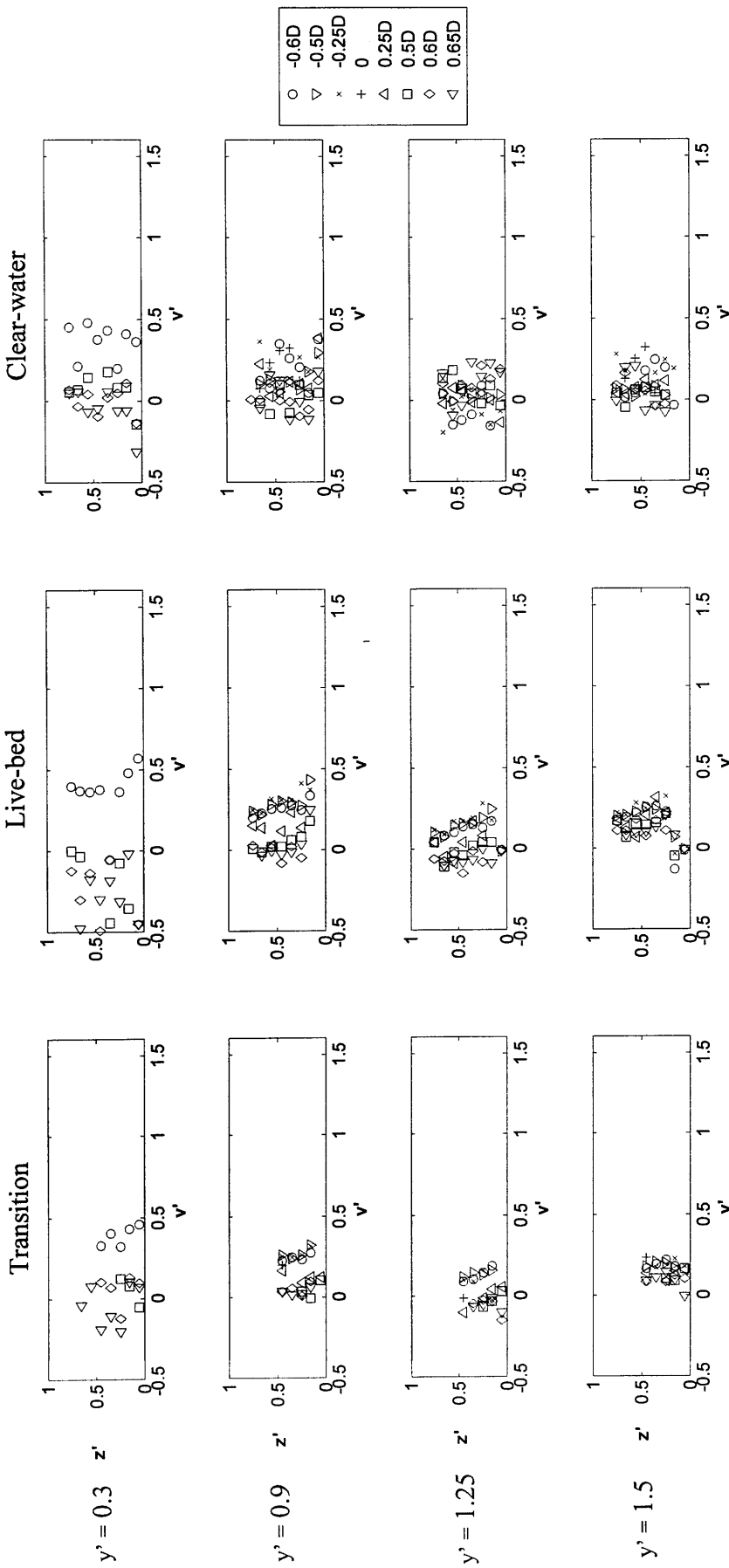
Figure 3-9. Near-cylinder mean v flow velocity profiles for the transition (first column), live-bed (second column) and clear-water (third column) along the $y' = 0.3$, (first row), and the $y' = 0.9$, 1.25 and 1.5 planes.

In the $y' = 0.9$, 1.25 and 1.5 planes v' is generally higher on the upstream side of the cylinder while it decreases sharply towards zero downstream, and in some areas becomes slightly negative. Upstream, v' enhancement reduces with distance from centreline.

3.3.1.3 w', Comparison between Tests

The distribution of w' shows the least variation between all velocity components (Figure 3-10). Along $y' = 0.3$ plane and downstream of the cylinder there is a slight increase in positive w' which indicates an upward flow. Along the $y' = 0.6$, 0.9 and 1.1 planes, w' remains negligible at all positions.
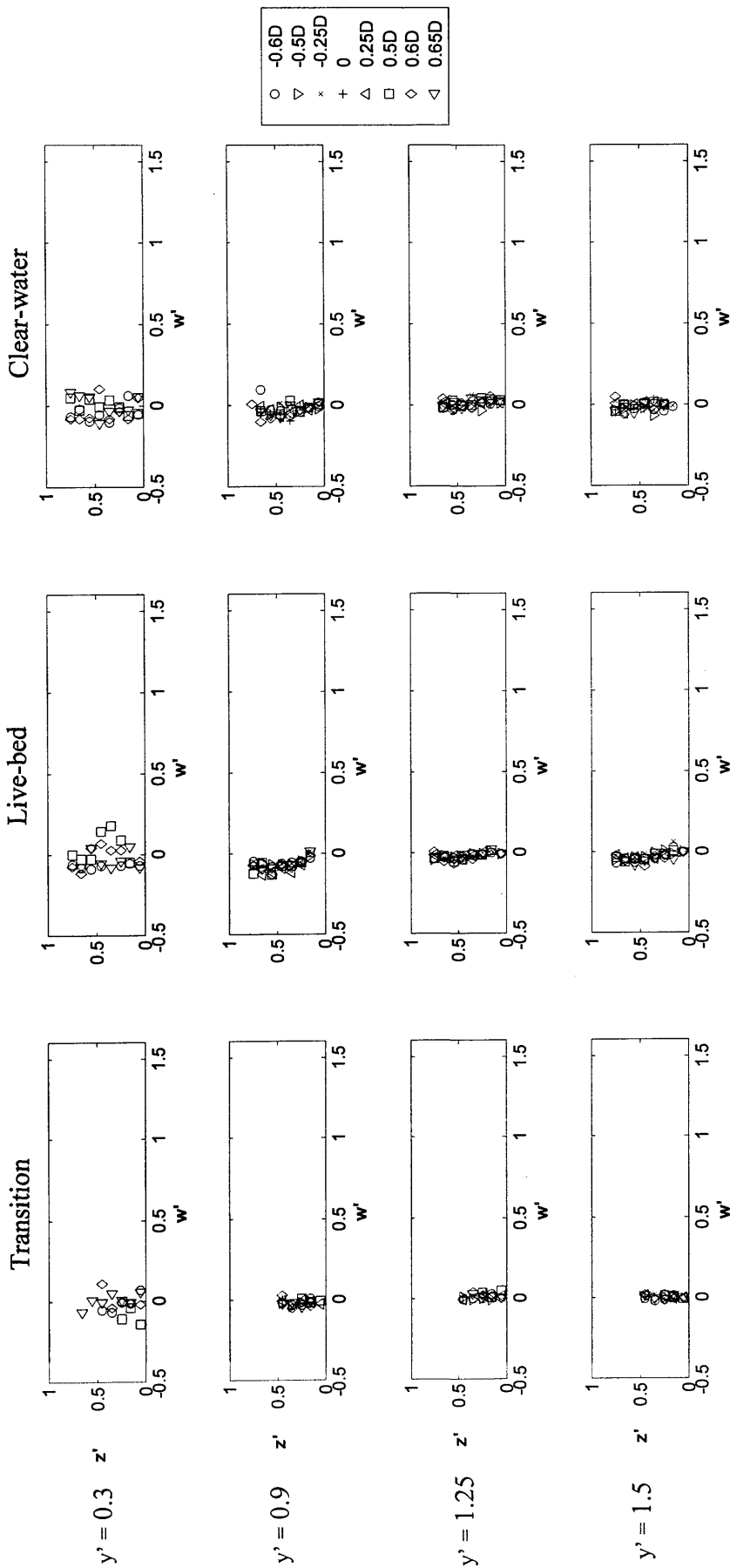
Figure 3-10. Near-cylinder mean *w* flow velocity profiles for the transition (first column), live-bed (second column) and clear-water (third column) along the $y' = 0.3$, (first row), and the $y' = 0.9$, 1.25 and 1.5 planes.

3.3.2 Near-Cylinder Turbulence Profiles

To help further understand the structure of the near-cylinder flow, the turbulence profiles are now analysed. The same parameters as analysed for the upstream profiles are presented below.

3.3.2.1 Live-bed Turbulence Profiles

Figure 3-11 presents the TI and Reynolds stress profiles for the live-bed test in the same order as above for the upstream profiles. In all tests TI is the largest and most varied along the $y' = 0.3$ plane. TI's u^+, v^+ and w^+ each show an increase towards the downstream side of the cylinder. On the $y' = 0.9$ plane constant values of ≈ 0.2 m s^{-1} for both u^+ and v^+ and ≈ 0.1 m s^{-1} for w^+ are observed and there is very little change either side of the cylinder apart from a very slight increase ($\approx < 0.01$) downstream. This trend is no longer present along the two remaining planes where the values remain essentially constant. The lack of an increase in TI at these planes indicate that the influence of flow separation on turbulence distribution is constrained to between the centreline and the $y' = 0.9$ plane.

Reynolds stress components along the $y' = 0.3$ plane are close to zero both upstream and downstream of the cylinder. Away from the $y' = 0.3$ plane the stress components are generally close to zero.
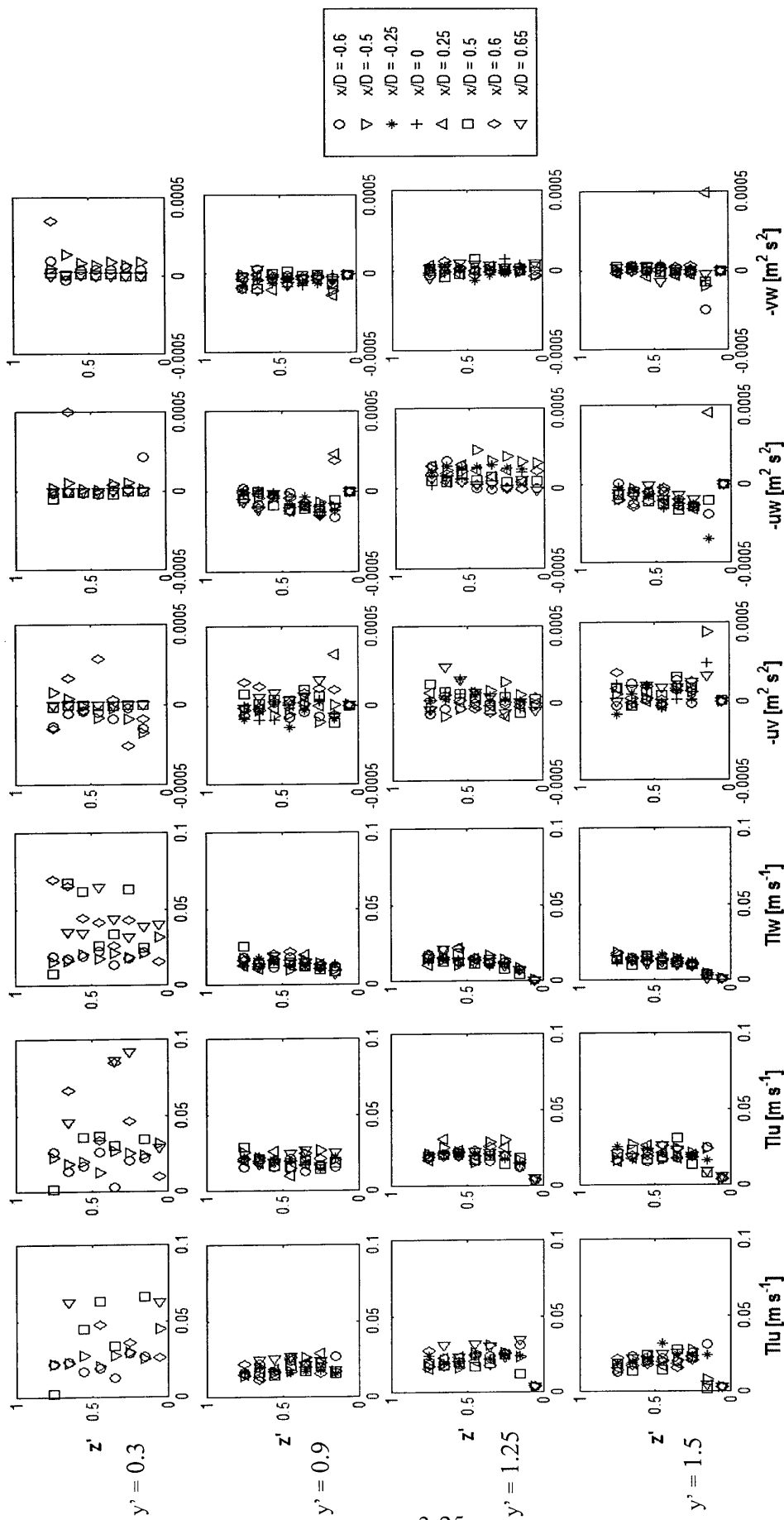
Figure 3-11. Distributions of TI, and Reynolds Stresses measured along the $y' = 0.3$, (first row), and $y' = 0.6$, 1.25 and 1.75 m planes (second – fourth row respectively) for the live-bed test.

3-25

3.3.2.2 Transition and Clear-water Turbulence Profiles, Comparison between the Tests

TI and Reynolds stress distributions for the transition and clear-water (Figures. 3-12 and 3-13 respectively) show a similar picture to the live-bed data: one of increasing TI downstream along the $y' = 0.3$ plane, and a rapid diminishment of TI and stress components laterally. Reynolds stresses are again most varied along the $y' = 0.3$ planes.
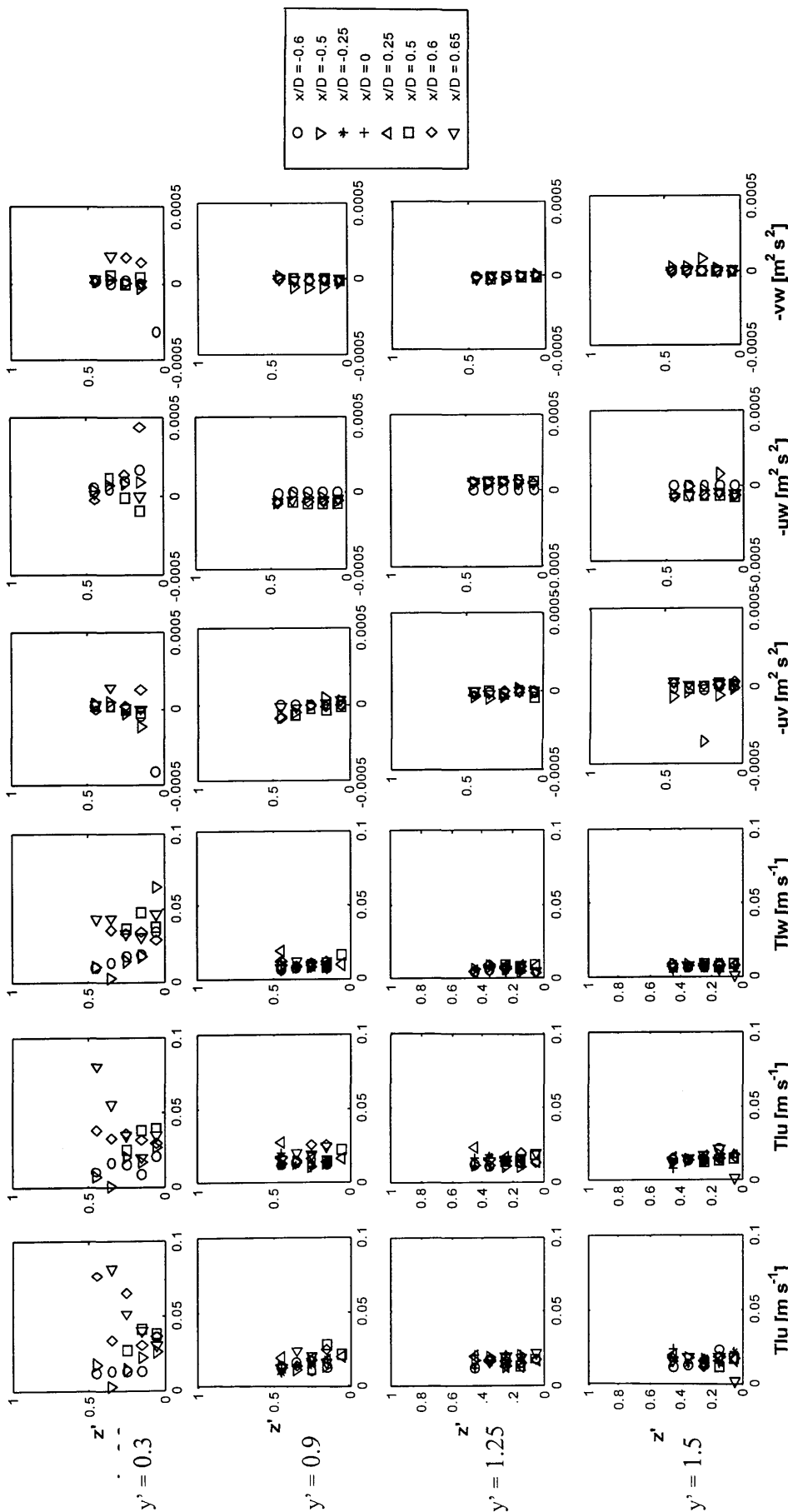
Figure 3-12. Distributions of TI, and Reynolds Stresses measured along the $y' = 0.3$, (first row), and $y' = 0.6$, 1.25 and 1.75 m planes (second – fourth row respectively) for the transition test.
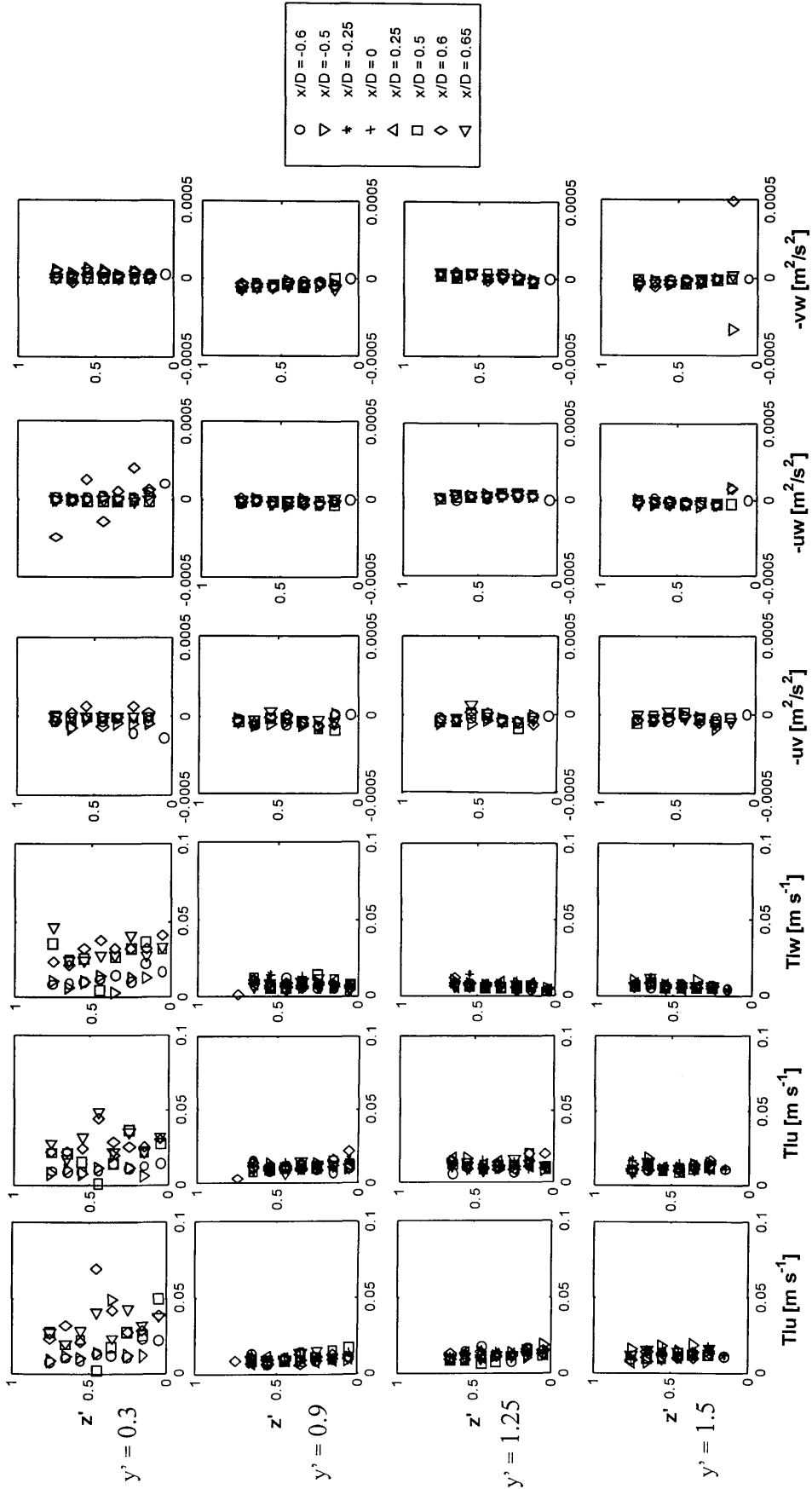
Figure 3-13. Distributions of TI, and Reynolds Stresses measured along the $y' = 0.3$, (first row), and $y' = 0.6$, 1.25 and 1.75 m planes (second – fourth row respectively) for the clear-water test.

3.4 Mean Flow and Turbulence Fields Downstream of the Cylinder

3.4.1 Flow Fields

3.4.1.1 Live-bed Test, Centreline Slices

Three-dimensional time-averaged mean velocity vector maps of the downstream centreline flow were recorded using PIV. Four consecutive vector maps (slices) are presented in Figure 3-14 1st row, which covers the downstream region from the cylinder edge to $x' \approx 5.15$. The vectors (whose magnitude and directions are given as $(u^2 + w^2)^{0.5}$ and arctan (w/u)), present u-w velocity while the contours present v velocity component. The data was collected using the PIV method as described in §2.1.2.1. To help visualisation, a three-dimensional schematic diagram of the flow is given in Figure 3-15. The diagram is drawn in order to highlight certain aspects of the flow field which are discussed in detail. Though the diagram is drawn from the analysis of the PIV results, its dimensions do not correspond to real dimensions and it is intended solely as qualitative visual aid. Numbered features in the diagram will be individually referred to in the text.
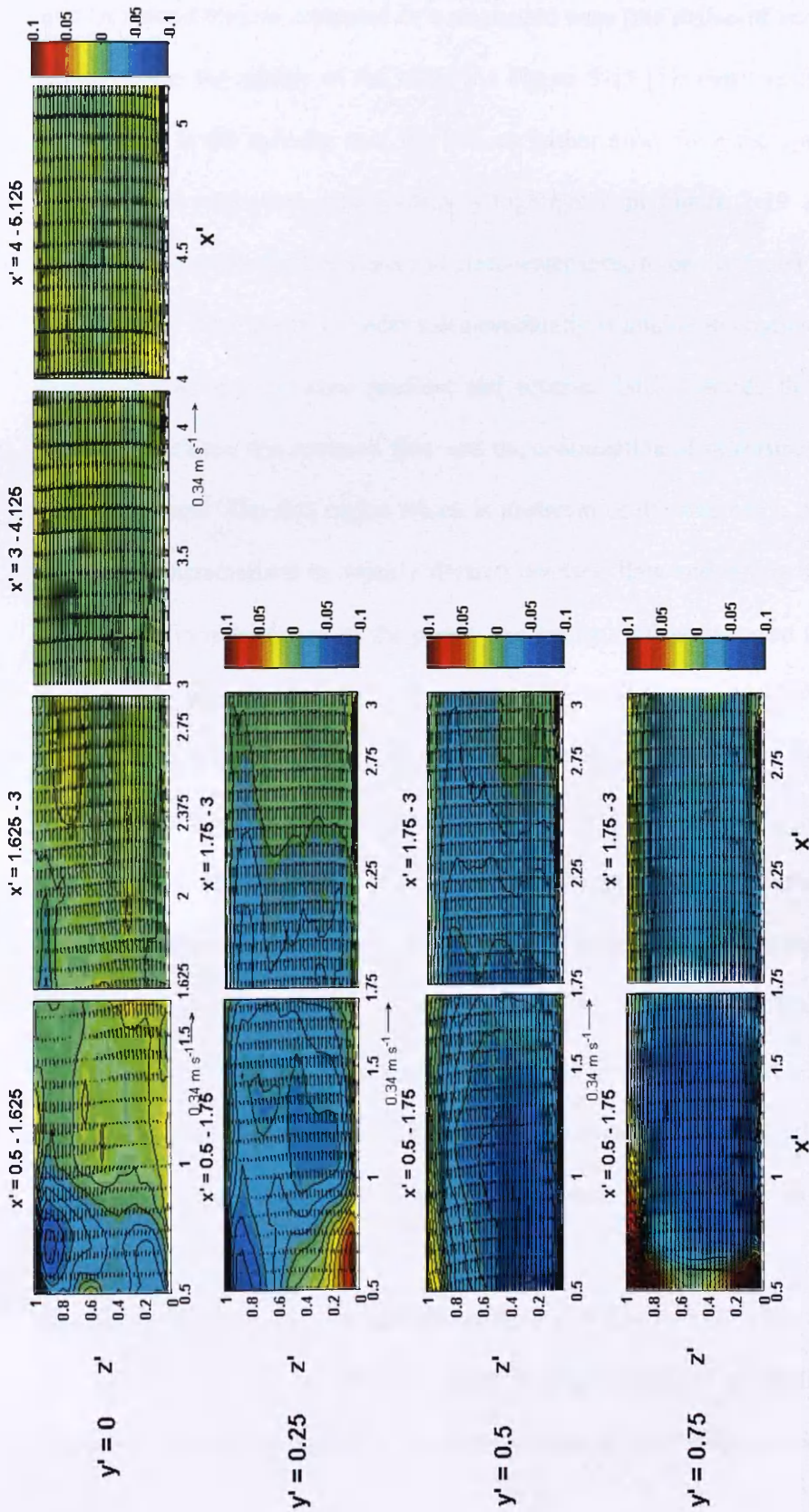
Figure 3-14. Vertical flow slices of the wake flow along the $y' = 0$ (centreline, top row), $y' = 0.25$ (2nd row), $y' = 0.5$ (3rd row), $y' = 0.75$ (bottom row) covering $x' = 0.5$ (the downstream edge of the cylinder) to $x' \approx 5$ depending on the y' plane (see also Figure 2-8). The vectors (whose magnitude and directions are given as $(u^2 + w^2)^{0.5}$ and arctan (w/u)), present uw velocity [m s^{-1}] while the coloured contours present v velocity [m s^{-1}] component.

Figure 3-14 (slice $x' = 0.5 - \sim1.625$) shows a complex flow field which can be divided into two broad regions separated by a stagnation zone (the region of very low velocity vector across the middle of the slice, see Figure 3-15 [1]) that stretches diagonally from closer to the cylinder near the bed, to further away from the cylinder near the surface. This stagnation zone (which is highlighted in Figure 3-19 along with the stagnation zones for the transition and clear-water tests, to be discussed later) forms as separation of flow on the cylinder sides eventually is unable to continue downstream due to the adverse pressure gradient and reverses back towards the cylinder; the boundary between this reversed flow and the continuation of downstream flow is this stagnation zone. The first region which is upstream of the stagnation zone (Figure 3-15 [2]), is characterised by weakly sheared reversed flow and strong negative lateral velocity v, (movement out of the page). The strength of the reversed flow decreases towards the cylinder edge. The second region which is downstream of the stagnation zone (Figure 3-15 [3]) is one dominated by downstream flow with a developing bed-boundary shear layer. The region around the stagnation zone contains relatively more vertical shear than the other regions due to the opposing flow directions. Lateral velocity v around the stagnation zone region and in the downstream region is weakly positive (movement into the page). The gradient ∂_x'/∂_y' of the boundary of the stagnation zone, which is calculated approximately from Figure 3-19, changes with z'. Between $z' = 0 - 0.3$ the gradient is close to 1, between $z' = 0.3 - 0.7$ it becomes much shallower as approximately 0.7 before increasing once more near the surface.

The downstream slices on the centreline (slices $x' = 1.625 - 3$, $x' = 3 - 4.125$ and $x' = 4 - \sim5.125$ Figure 3-14, 1st row) show a broad trend of gradually developing downstream boundary layer flow (no flow reversal is observed), with some evidence

3-31

of the advection of v downstream. The majority of flow disturbance appears to be confined to $x' < 2.5$.
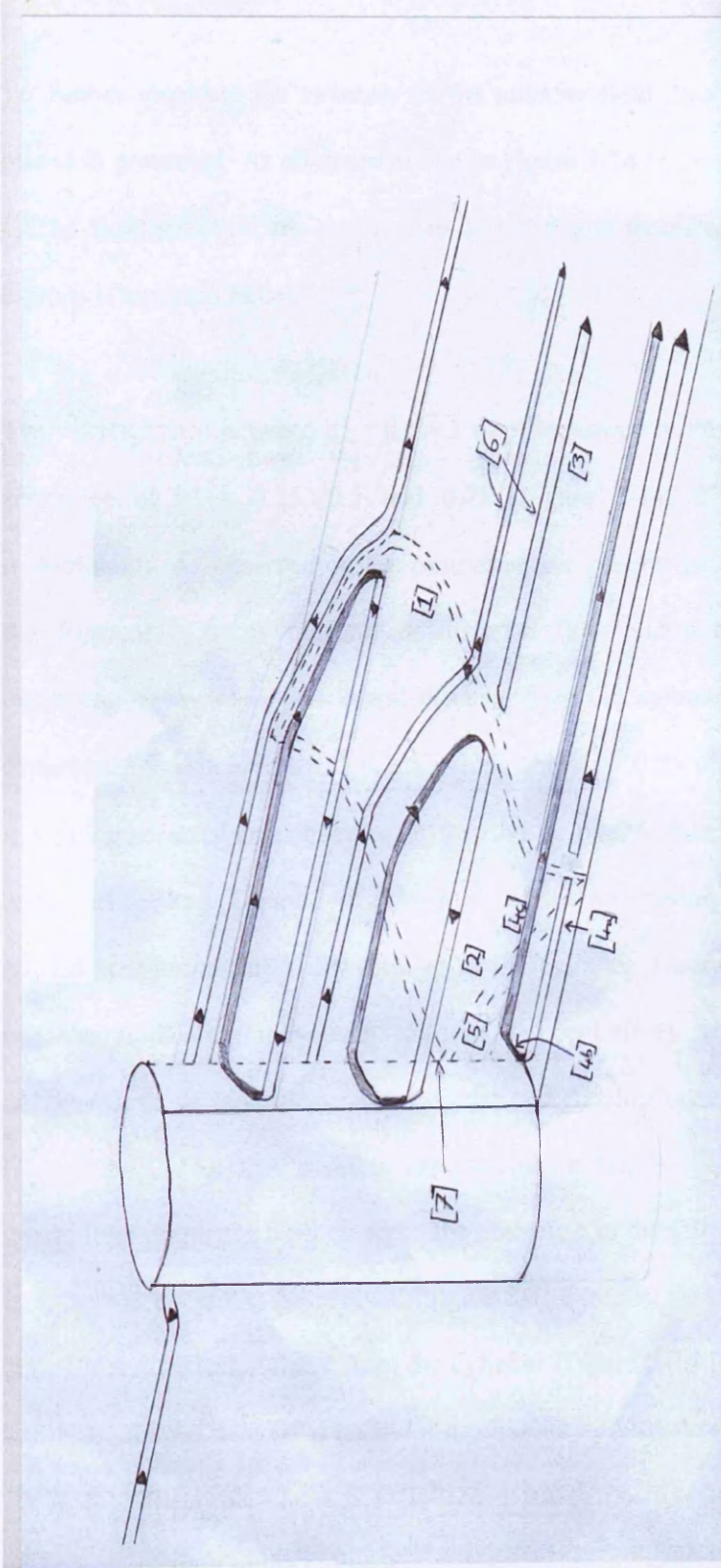
Figure 3-15. Schematic cartoon of the main live-bed and clear-water test downstream flow features where: [1] is the stagnation zone on the centreline, [2] is the reversed flow region, [3] is the downstream orientated flow downstream of the stagnation zone, [4a] is flow initially caught in the reversal before being deflected away from the cylinder [4b] and ejected downstream [4c], [5] is the stagnation zone location off the centreline, [6] is downstream flow that has not been caught in the reversal and [7] is the stagnation zone location off the centreline.

3.4.1.2 Live-bed Test, Slices along the $y' = 025$, 0.5 and 0.75

To further elucidate the structure of the velocity field data from the off-centreline planes is presented. As observed above in Figure 3-14 (1st row), the greatest changes on the flow structure are confined to $x' < 2.5$ and therefore, only data from these regions is analysed below.

The velocity field between $x' = 0.5 - 3$ were measured in three planes parallel to the centreline at $y' = 0.25$, 0.5 and 0.75 (Figure 3-14, 2nd 3rd and bottom row respectively). As observed on the centreline, the general pattern is one of a gradual development of more uniform downstream flow and undisturbed velocity with increasing downstream and lateral distance from the cylinder. The majority of flow disturbance is confined to $x' < 2.5$. Along the $y' = 0.25$ plane the stagnation zone separating reversed and downstream flow has moved further upstream and no longer intercepts the bed (Figure 3-15 [7]), implying the reversed flow occupies a half-bowl shaped area immediately downstream of the cylinder. Lateral v velocity is strongly negative (indicating movement towards the centreline), with the exception of a confined area of large positivity near the bed directly beneath the separation zone (Figure 3-15 [4a-c]). A possible explanation for this is that this positive near bed lateral flow originates from closer to the centreline in the following manner. Flow that initially was caught in the reversal (Figure 3-15 [4a]) is, upon returning to the rear of the cylinder, deflected away from the cylinder (Figure 3-15 [4b]) and underneath the half-bowl shaped reversal zone and is ejected out into the downstream flow (Figure 3-15 [4c]). This would cause it to inherit a strong positive v velocity indicating its movement away from the cylinder.

Stagnation and reversed flow are not observed along the $y' = 0.5$ and 0.75 planes meaning the reversal zone extends only to $y' < 0.5$. Both show increases in mean flow velocity due to flow constriction by the cylinder, along with relatively uniform boundary layer flow. A maximal increase in mean flow is observed along the $y' = 0.75$ plane at $x' \approx 0.75$. Here the depth averaged velocity $\bar{U}$ reaches a peak value of $1.18 U_\infty$ before reducing downstream. Depth averaged velocity is quoted here rather than point measurements because flow in this region is rather more uniform then at other regions around the cylinder. The profiles at $x' < 0.75$ show slightly lower depth averaged velocity increases. Measurements presented by Johnson and Ting, (2003) and Ahmed and Rajaratnam, (1998) give maximum velocity increases at the side of the cylinder of between 1.4 and $1.5 U_\infty$. Presumably therefore, there will be higher velocity increases than those measured on the $y' = 0.75$ plane. Negative v is predominant with the exception of an area of strong positive v near the cylinder along the $y' = 0.75$ plane, which is a result of continual outward deflection of flow from around the surface of the cylinder.

3.4.1.3 Transition and Clear-water Test Flow Fields

The corresponding data for transition and clear-water slices are presented below. Since the majority of the cylinder's influence on the flow is confined to the region $x' < 2.5$, only the corresponding slices are presented here. As for the live-bed, a schematic diagram based on the PIV results is drawn for the transition (Figure 3-16) and clear-water test (Figure 3-15 is used for both the live-bed and clear-water tests) flow fields to aid visualisation of the main features that are discussed.
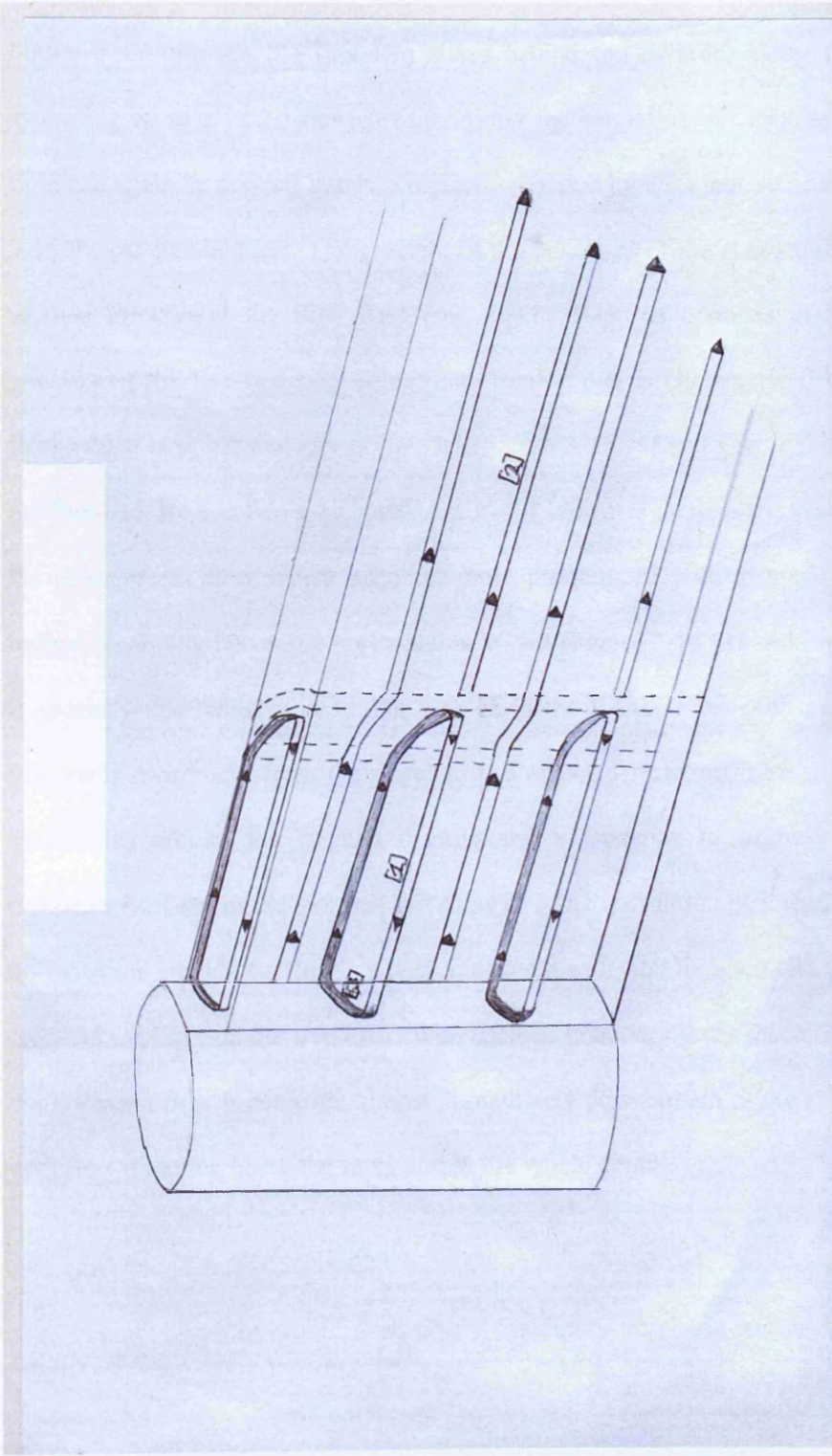
Figure 3-16. Schematic cartoon of the main downstream flow features in the transition test where; [1] is the reversed flow region, [2] is the downstream flow region and [3] is the deflection of flow away from the centreline (in a positive direction).

3.4.1.4 Transition Mean Velocity Fields

Figure 3-17 presents the first two slices behind the cylinder along the centreline extending up to $x' < 2.5$ downstream. Along the centreline the structure of the flow field can again be divided into two regions separated by a stagnation zone as in Figure 3-14 for the live-bed test. The gradient of the boundary of the stagnation zone is near vertical throughout the flow field (see Figure 3-19) as opposed to the shallower gradient of the live-bed stagnation zone. Region one is characterised by a reversed flow which is predominantly horizontal (Figure 3-16 [1] and Figure 3-17) similar to the live-bed. Region two which exists at $x' > 1$ indicates there is an upward motion to the downstream flow which becomes more pronounced with distance downstream, before eventually becoming horizontal at $x' \sim 3$ (Figure 3-16 [2] and Figure 3-17). v' is spatially distributed in a similar way as in the live-bed test with negative values (outwards movement from the page) in the reversed flow, positive values (inwards movement) around the stagnation zone and a tendency to become zero further downstream. Like in the live-bed test there is some translation of lateral flow ($v \neq 0$) downstream though the flow recovers quicker than in the live-bed test ($\sim x' = 2.5$, as opposed to $x' > 5$ in the live-bed). Well defined boundary layer shear flow similar to the upstream flow is achieved almost immediately downstream of the stagnation zone with flow direction being the same across the whole depth.
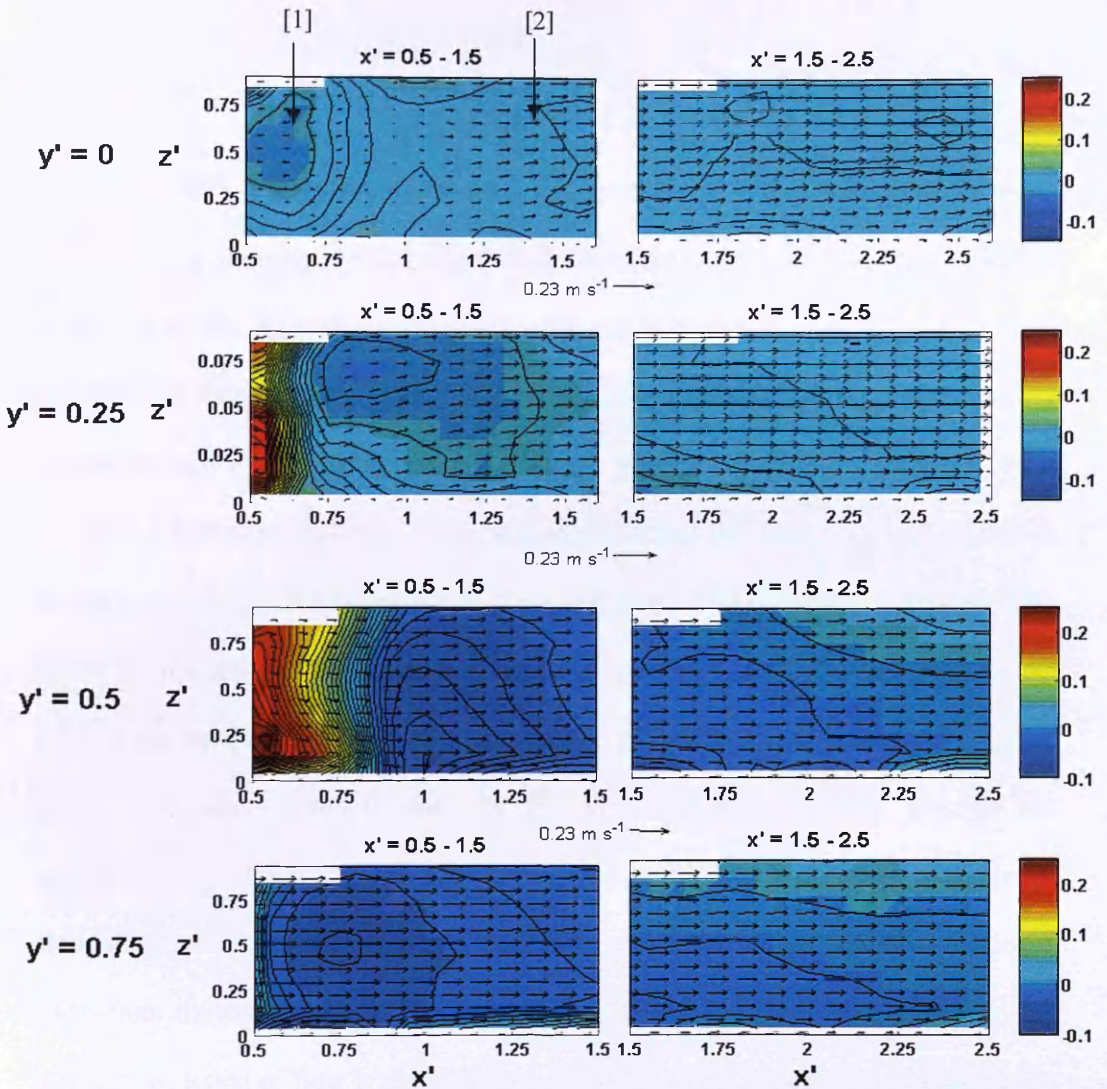
Figure 3-17. Vertical flow slices of the transition cylinder wake flow along the $y' = 0$ (top row), $y' = 0.25$ (2nd row), $y' = 0.5$ (3rd row), $y' = 0.75$ (bottom row) covering $x' = 0.5$ (the downstream edge of the cylinder) to $x' = 2.5$. The vectors (whose magnitude and directions are given as $(u^2 + w^2)^{0.5}$ and arctan (w/u)), present uw velocity [m s⁻¹] while the coloured contours present v velocity [m s⁻¹] component. Region [1] and [2] are highlighted in the $y' = 0$, $x' = 0.5$ - 1.5 flow slice.

3.4.1.5 Transition Test Mean Velocity Fields, Slices along the $y' = 0.25$, 0.5 and 0.75 Planes

As observed above, most of the significant spatial variations are confined to $x' < 2.5$ and hence only data from the corresponding slices is analysed below.

The 2nd, 3rd and bottom row of Figure 3-17 shows the $y' = 0.25$, 0.5 and 0.75 mean velocity maps covering $x' < 2.5$ respectively. Similar to the live-bed test the observed trend is one of a gradual diminishment of the cylinders influence on the flow both laterally and downstream. Along the $y' = 0.25$ plane the stagnation zone has moved further upstream and remains approximately vertical implying reversal of flow occupies a half-cylinder shaped area immediately downstream of the cylinder. v' is strongly positive in the reversed flow region (Figure 3-16 [3]) implying that the flow here is comprised of flow returning from the centreline back across the cylinder and towards the separation point on the side of the cylinder. Downstream of the stagnation zone lateral flow is weakly negative indicating movement of flow towards the centreline around the reversed flow region. No stagnation or reversal is observed along the $y' = 0.5$ and 0.75 planes. Though strong positive lateral flow (flow outward away from the centreline) is observed between $x' = 0.5$ - 0.875 along the $y' = 0.5$ plane, constriction of flow is not observed. In fact downstream velocity is reduced (to a minimum depth averaged velocity of $0.31U_\infty$) at $x' \approx 0.75$ before increasing where flow is bent back towards the centreline plane (region of negative v).

3.4.1.6 Clear-water Test Mean Velocity Fields

Due to the water depth exceeding the upper limit of the PIV slice in the clear-water tests, the flow field is captured in two separate time-averaged slices which are presented together to give the full flow field. From the evidence presented above (§3.4.1.4 and §3.4.1.5) for the transition and live-bed tests, and after initial analysis of

the clear-water test data it is clear that the main features of the flow are confined to x' < 2.5, and therefore only these slices will now be analysed.

3.4.1.7 Clear-water Test Mean Velocity Fields, Centreline Slices

Figure 3-18, top row presents the clear-water mean flow fields along the centreline from $x' = 0.5$ - 2.5 and they show a flow structure that is similar to that of the live-bed test. The stagnation zone is situated further downstream than the transition and live-bed tests and the steepness of its gradient is in between that of the live-bed and transition test. By $x' = 1.625$ flow has returned back to boundary layer sheared flow. Lateral velocity v distribution is similar to the transition and live-bed tests with negative (inward towards centreline) values in the reversed flow near the cylinder which become positive (outward) at $x' \approx 1$. This implies that like in the transition and live-bed tests, there is a large recirculation of flow in the near-wake behind the cylinder which originates from off the centreline before moving onto it and remaining there until eventually being forced back off the centreline closer to the cylinder (Figure 3-15 [4a-c]). Beyond this point lateral flow tends to diminish though remains $\neq 0$ in large areas of the flow.
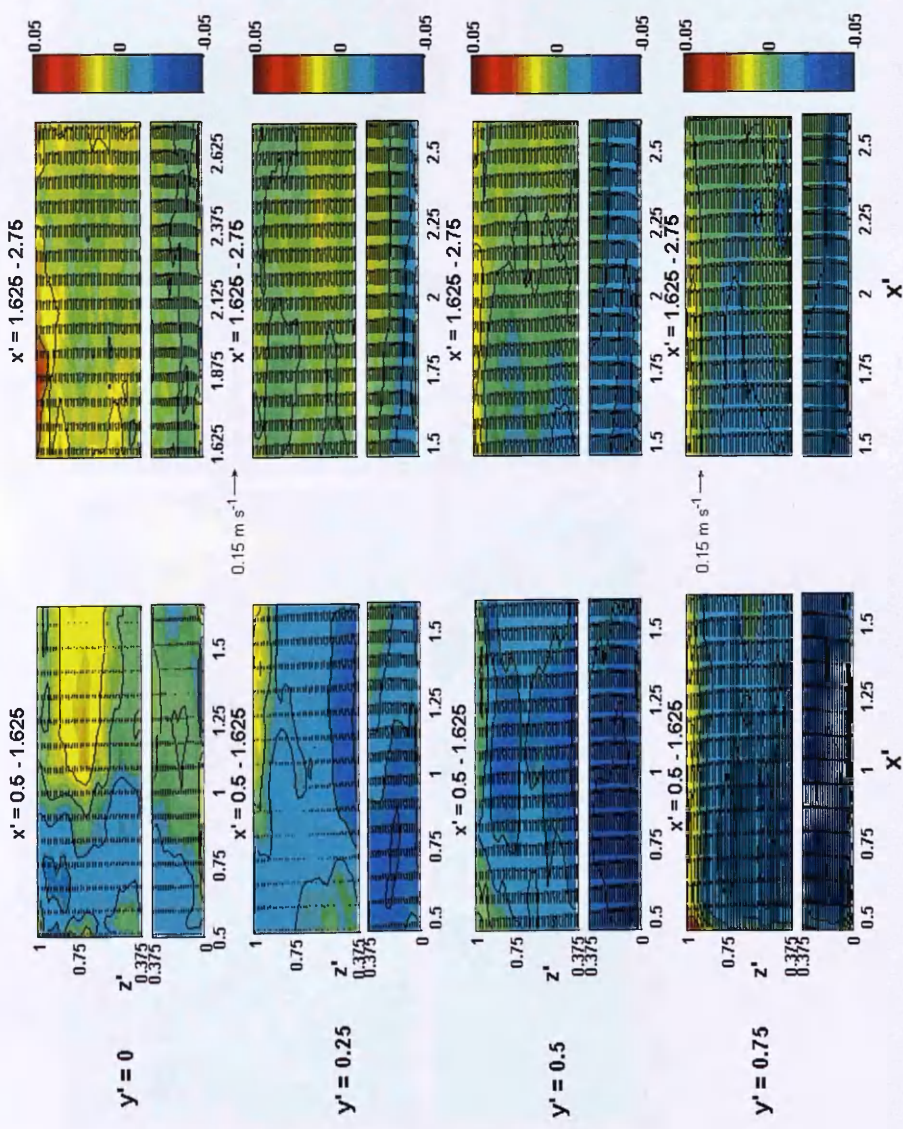
Figure 3-18. Vertical flow slices of the wake flow behind the cylinder for the clear-water test starting from $x' = 0.5$ to $x' \approx 2.75$ the $y' = 0$ (top row), $y' = 0.25$ (2nd row), $y' = 0.5$ (3rd row), $y' = 0.75$ (bottom row) covering $x' = 0.5$ (the downstream edge of the cylinder) to $x' = 2.5$. The vectors (whose magnitude and directions are given as $(u^2 + w^2)^{0.5}$ and $\arctan(w/u)$), present uw velocity [m s^{-1}] while the coloured contours present v velocity [m s^{-1}] component.
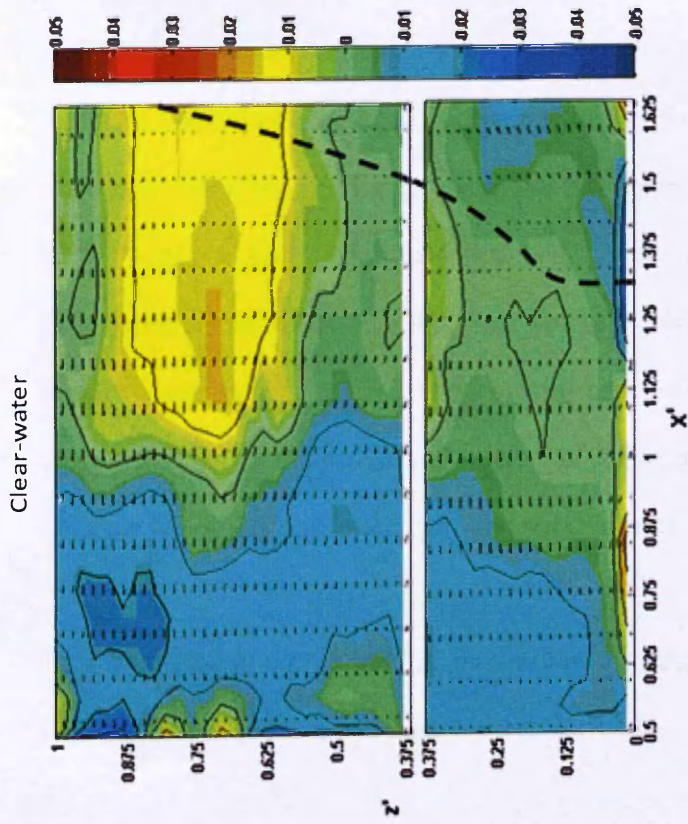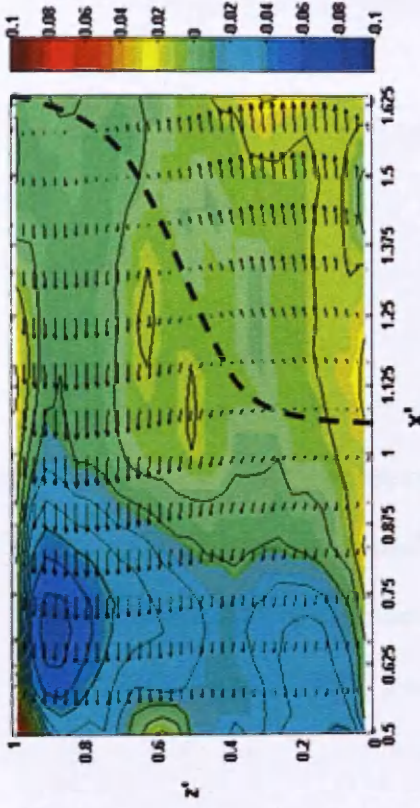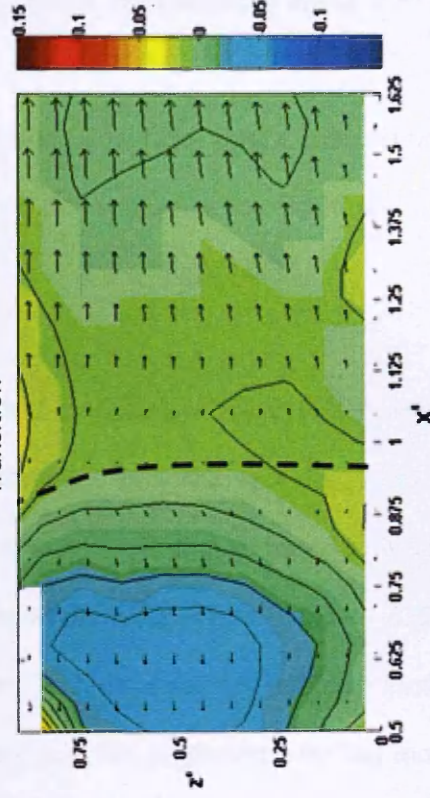
Figure 3-19. Stagnation zone borders for the high, mid and transition test (a, b and c respectively). The vectors (whose magnitude and directions are given as $(u^2 + w^2)^{0.5}$ and arctan (w/u)), present uw velocity [m s^{-1}] while the coloured contours present v velocity [m s^{-1}] component.

3.4.1.8 Clear-water Test Mean Velocity Fields, Off-Centreline Slices

The 2nd to 4th row in Figure 3-18 present the flow fields from off the centreline at $y' = 0.25$, 0.5 and 0.75 respectively from the corresponding positions of the slices described above.

The general pattern is one of a gradual reduction of the cylinders influence with increasing lateral and downstream distance from the cylinder. The majority of streamwise flow disturbance is confined to $x' < 1.75$ though lateral flow structures are again translated further downstream (Appendix A7.3). The $x' = 0.5 - 1.625$ slice along the $y' = 0.25$ plane which presents a flow field of similar structure to the corresponding flow field in the live-bed test, the stagnation zone has moved further upstream indicating the reversed flow region occupies a half bowl-shape though with steeper sides than the live-bed test. v is again strongly negative in all planes implying a similar wake flow structure is present as that in the live-bed test. There are some differences including the strongly negative v flow underneath the reversal (Figure 3-15 [5]) which is positive for the corresponding flow in the live-bed test (Figure 3-15 [4]), implying that the flow at this point does not originate from the centreline and is instead comprised of constricted flow moving past the cylinder sides (that is, it has not been caught in the separation and reversal of the near-wake). Such a flow feature is completely non-existent in the transition test due to its vertical stagnation zone.

Flow along the $y' = 0.25$ and 0.5 planes show a gradual return to uniformity, as seen in the transition and live-bed tests.

3.4.2 Turbulence Fields Downstream of the Cylinder

3.4.2.1 Live-bed Test, Centreline Slices

Six turbulence parameters were calculated from the centreline velocity slices downstream of the cylinder. These included three turbulence intensities (TI) $u^+ = (\overline{u''u''})^{0.5}$, $v^+ = (\overline{v''v''})^{0.5}$, and $w^+ = (\overline{w''w''})^{0.5}$ and three Reynolds stress components $\tau_{uv} = -\rho\overline{u''v''}$, $\tau_{vw} = -\rho\overline{u''w''}$, and $\tau_{uw} = -\rho\overline{v''w''}$. Plots of these parameters are presented along with the time-averaged mean flow vector map to enable observations of the relationships between turbulence and the mean flow field.

Figure 3-20 shows plots of turbulence intensities u^+, v^+ and w^+ and the corresponding vector maps for the slices covering from $x' = 0.5 - 5.125$ along the centreline of the live-bed test (1st column). u^+ and v^+ have similar spatial distributions, both showing their largest values downstream of the stagnation zone where mean flow is in the downstream direction. Values of v^+ are ≈ 0.1 m s^{-1} larger than u^+ at corresponding positions across the slice. Values of w^+ are generally lower than those of u^+ and v^+ and have a different spatial distribution which peaks in a broad area (to the right of the figure) spanning the stagnation zone. Observation of the three plots together suggests that the wake flow can be divided into three regions of different turbulence environments: 1) the region upstream of the stagnation zone where flow is reversed and TI is relatively at its weakest and reduces towards the cylinder with $v^+ > u^+ > w^+$; 2) a broad region around the stagnation zone where TI is intermediate but w^+ is relatively strong with $v^+ > u^+ \approx w^+$; and 3) the region downstream of stagnation zone where flow is downstream and TI is strongest with

$v^+> u^+ > w^+$ once more. These regions are numbered in Figure 3-20. The peak in w^+ around the stagnation zone appears to be caused by both the increased vertical motion in the flow, and increased vertical shear between the reversed and downstream flow either side of the stagnation zone. The weaker TI upstream of the stagnation zone relative to the downstream of it, is consistent with the observation that the upstream region exhibits more uniform, less-sheared mean flow than the downstream region. This is possibly due to the lower mean velocities and the relative shelter of the cylinder, whereas downstream of the stagnation zone there is convergence of increased bed shear flow and deflected flow on the centreline. The centreline distributions described above are similar to those from Graf and Yulistiyanto, (1999).

Reynolds stresses τ_{uw}, τ_{uv}, and τ_{vw} for centreline slice $x' = 0.5 - 1.625$ are plotted in Figure 3-21 for the live-bed test. In all three cases values are higher downstream than upstream of the stagnation zone. Unsurprisingly τ_{uv} is the strongest of the three, given the horizontal dominance of the turbulence shown in Figure 3-20. Negative τ_{uv} corresponds to the region upstream of the stagnation zone where v is strongly negative (outward flow - out of the page, away from the centreline), and likewise downstream of the stagnation zone where both τ_{uv} and v are positive. τ_{uw} is stronger than τ_{vw} implying that v'' and w'' are particularly poorly correlated while u'' and w'' are slightly more correlated and u'' and v'' are the most strongly correlated. An explanation of this is that the flow in this region includes weakly bed-sheared reversed and streamwise flow and a stronger lateral flow with very little bed-shearing or vertical directional component (Figure 3-15, [6]). The result is that v' (from the larteral flow) and w' (from the streamwise and reversed flow) are derived primarily from different flows of the flow field. Hence the stronger τ_{uv}, τ_{vw} and weak τ_{vw}.
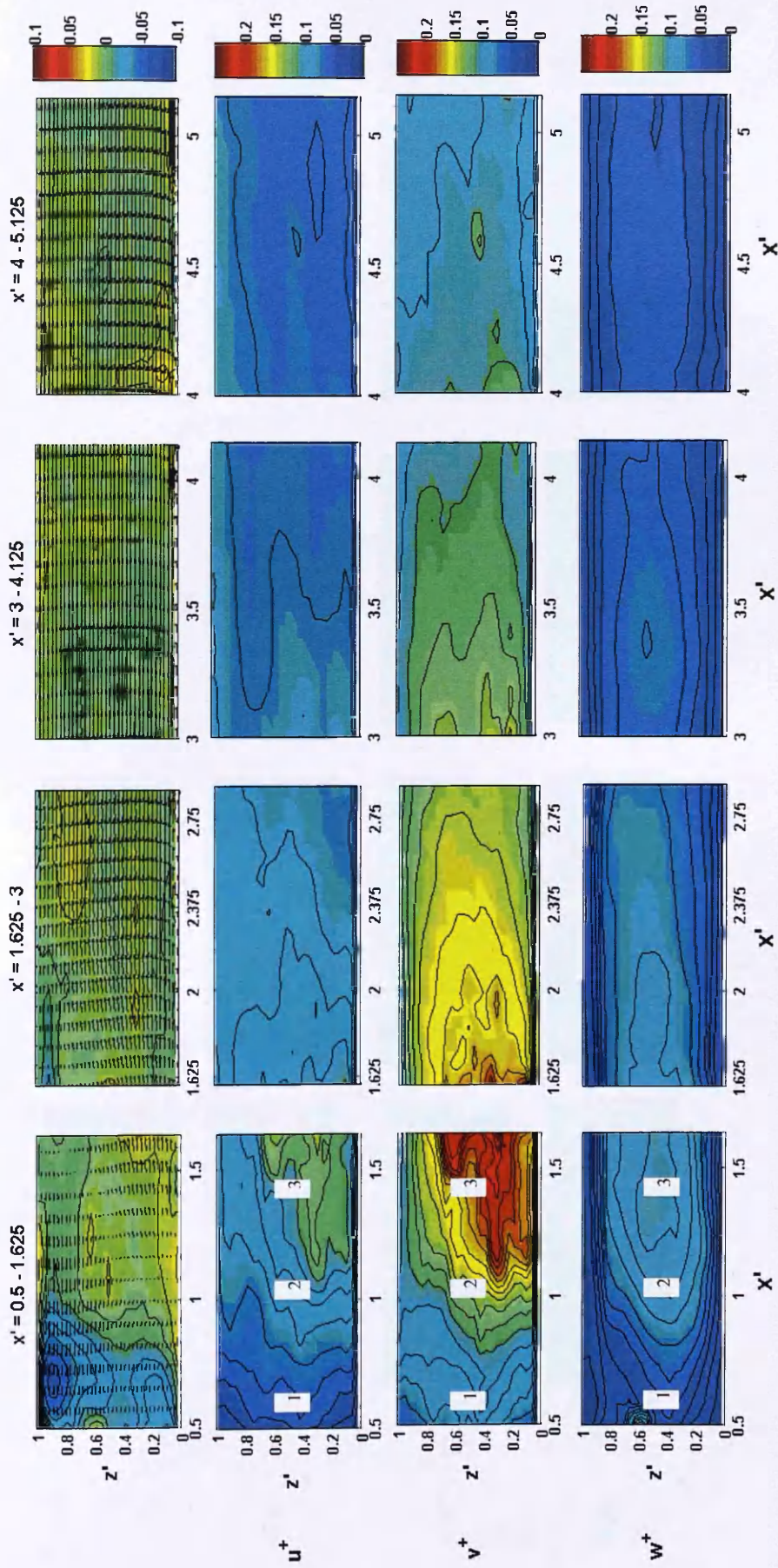
Figure 3-20. Turbulence intensities u^+, (2nd row) v^+ (3rd row), w^+ (bottom row) and mean flow (top row) for the live-bed test along the $y' = 0$ (centreline) plane (from Figure 3-14). The three regions of similar turbulence characteristics as described in the text above are labelled (1, 2 and 3) on the $x' = 0.5 - 1.625$ slice for each TI component.
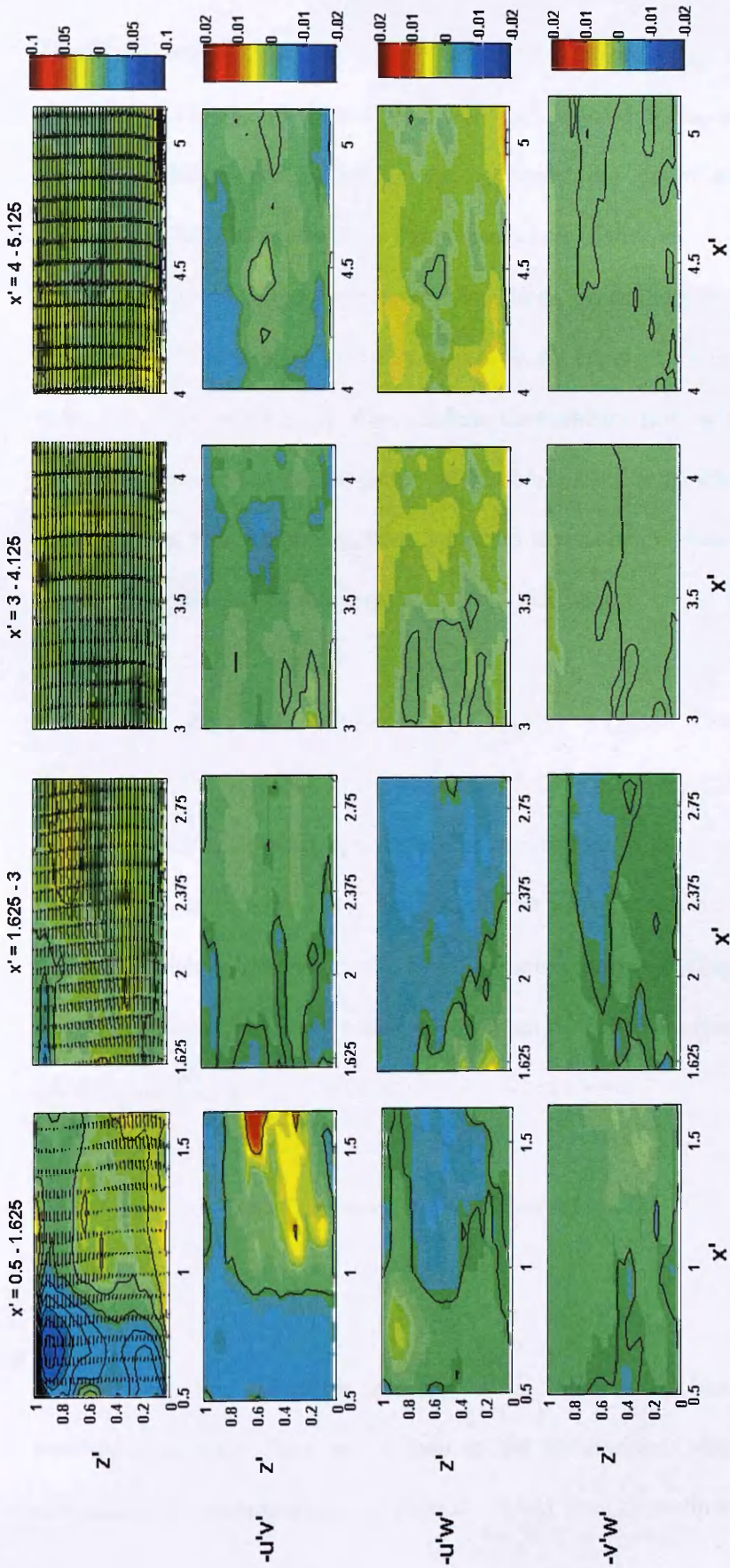
Figure 3-21. Reynolds Stress contours $-uv$, (2nd row) $-uw$ (3rd row), $-vw$ (bottom row) and mean flow (top row) for the live-bed test along the $y' = 0$ (centreline) plane (from Figure 3-14).

The 2nd, 3rd and 4th column of Figure 3-20 show turbulence intensity contours from x' = 1.625 - 5.125. In all these figures $v^+ > u^+ > w^+$ but this distinction gradually diminishes downstream, implying the continued but diminishing contribution of lateral wake flow and turbulence components here. Other than a tendency for higher values to be found across the middle of the slices, particularly in w^+ and v^+, there is little definable turbulence structure. There is no apparent evidence in the velocity maps (all show increasingly more uniform downstream flow with increasing x') for the local generation of such a pattern in TI distribution, suggesting that the enhanced turbulence in this region has been advected downstream from the region directly behind the cylinder depicted in the $x' = 0.5 - 1.625$ slice.

Similar to TI, Reynolds stress plots for the slices $x' = 1.625 - 5.125$ (Figure 3-21) also show a decrease of values with increasing x'. Downstream of $x' \approx 3$ the boundary layer has been established again, and this is reflected in the observation of positive values of τ_{uw} near the bed. τ_{uw} has become the strongest stress component, but there is continued lateral shearing as τ_{uv} is $\neq 0$ in regions corresponding to increased lateral flow v, suggesting some advection downstream of flow disturbance that is related to the deflected flow and streamwise flows discussed above.

3.4.2.2 Live-bed Test, Turbulence Distributions along the $y' = 0.25$, 0.5 and 0.75 Planes

The off-centreline TI fields are shown in Figure 3-22, and along with the corresponding mean flow vector map to aid comparison. Because most of the complex field structure occurs between $x' < 1.625$ from the cylinder (corresponding to

slice $x' = 0.5$ - 1.625), only data from this section of the downstream flow is analysed below. The remaining slices are provided in Appendix A8.2. Turbulence fields are measured at three planes parallel to the centreline at $y' = 0.25$, 0.5 and 0.75 and to $x' =$ 1.625.

As observed downstream along the centreline, the general pattern is one of a gradual transition to more uniform undisturbed flow with increasing distance from the cylinder. The TI fields along $y' = 0.25$ correspond to the mean flow closely in a similar manner as they do along the centreline. Both u^+ and v^+ are larger in the downstream flow region, with v^+ again as the largest. The apparent reason for this is the corresponding region of maximal mean lateral flow in the vector map as discussed in relation to the centreline TI fields above. Again w^+ is lower than both u^+ and v^+, but peaks in a region around the stagnation zone and upper region of the slice where vertical shear is strongest.

The patterns of distribution in the $y' = 0.5$ and 0.75 planes at $x' = 0.5$ - 1.625, are not similar to the $x' = 0$ - 1.625 slice along the centreline and $y' = 0.25$ plane due to the lack of stagnation and reversal. Turbulence fields tend towards uniformity with the exception of a region of enhanced u^+ and v^+ near $z' = 1$, which is evidently related to a region of large shear in the mean flow velocity at the corresponding positions.
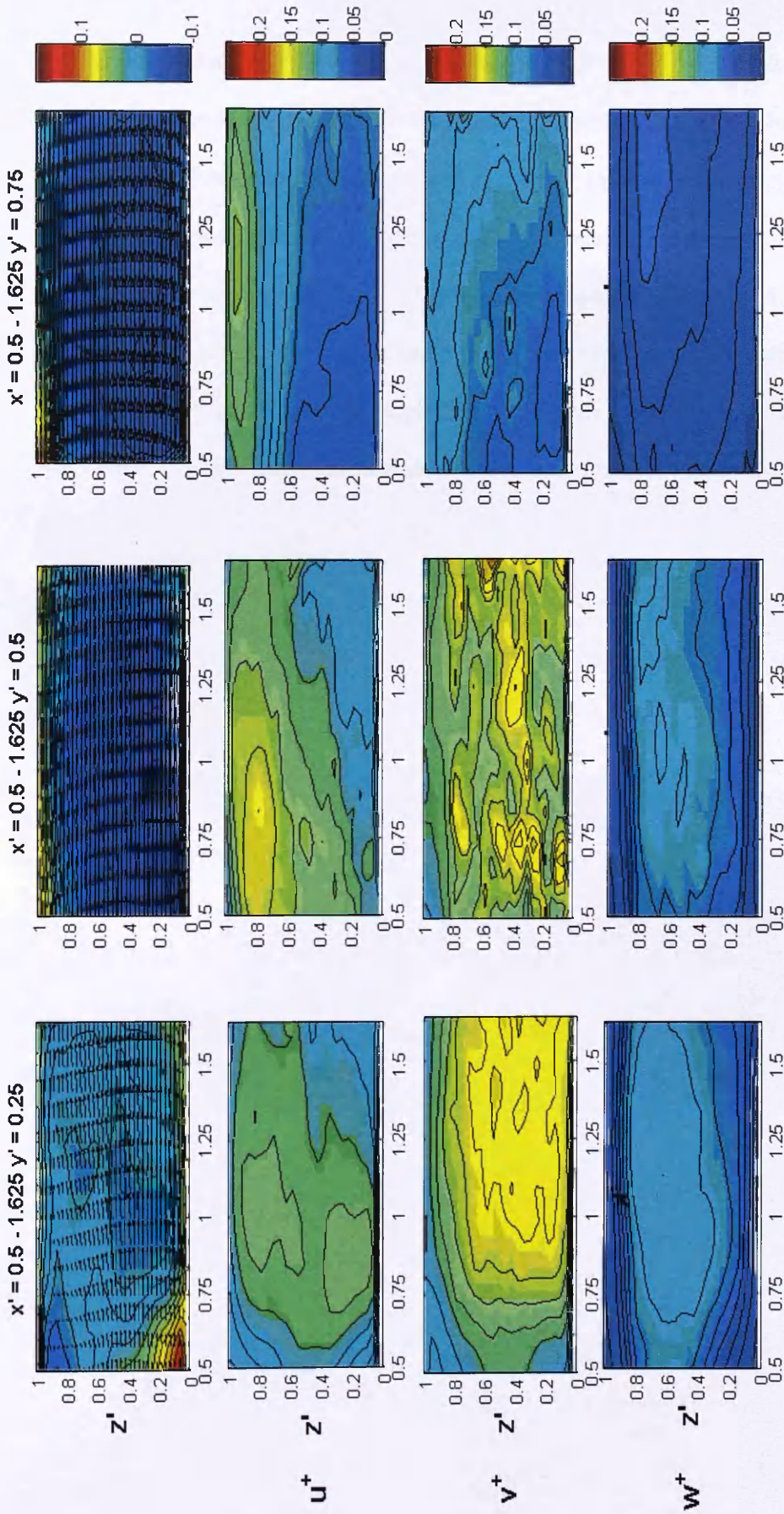
Figure 3-22 Turbulence intensities u^+, (2nd row) v^+ (3rd row), w^+ (bottom row) and mean flow (top row) for $x' = 0.5 - 1.625$ along planes $y' = 0.25$ (1st column), 0.5 (2nd column) and 0.75 (3rd column) for the live-bed test.

The corresponding Reynolds stress component plots for $y' = 0.25$, 0.5 and 0.75 (Figure 3-23). Peak τ_{uv} corresponds closely to the peak in mean lateral flow, which is upstream (at $x' \approx 1$) of the maximum in τ_{uw} ($x' > 1$), where boundary layer flow structure is beginning to reform. Again, τ_{vw} is very weak. The observations together provide further evidence to support the hypothesis stated above in §3.4.1.1 that the flow at these positions is a superposition of lateral mean flow and a weakly shearing downstream orientated boundary layer flow. The same pattern persists along the y' =0.5 and 0.75 planes but is found to weaken and tend towards uniformity, as in the TI fields.
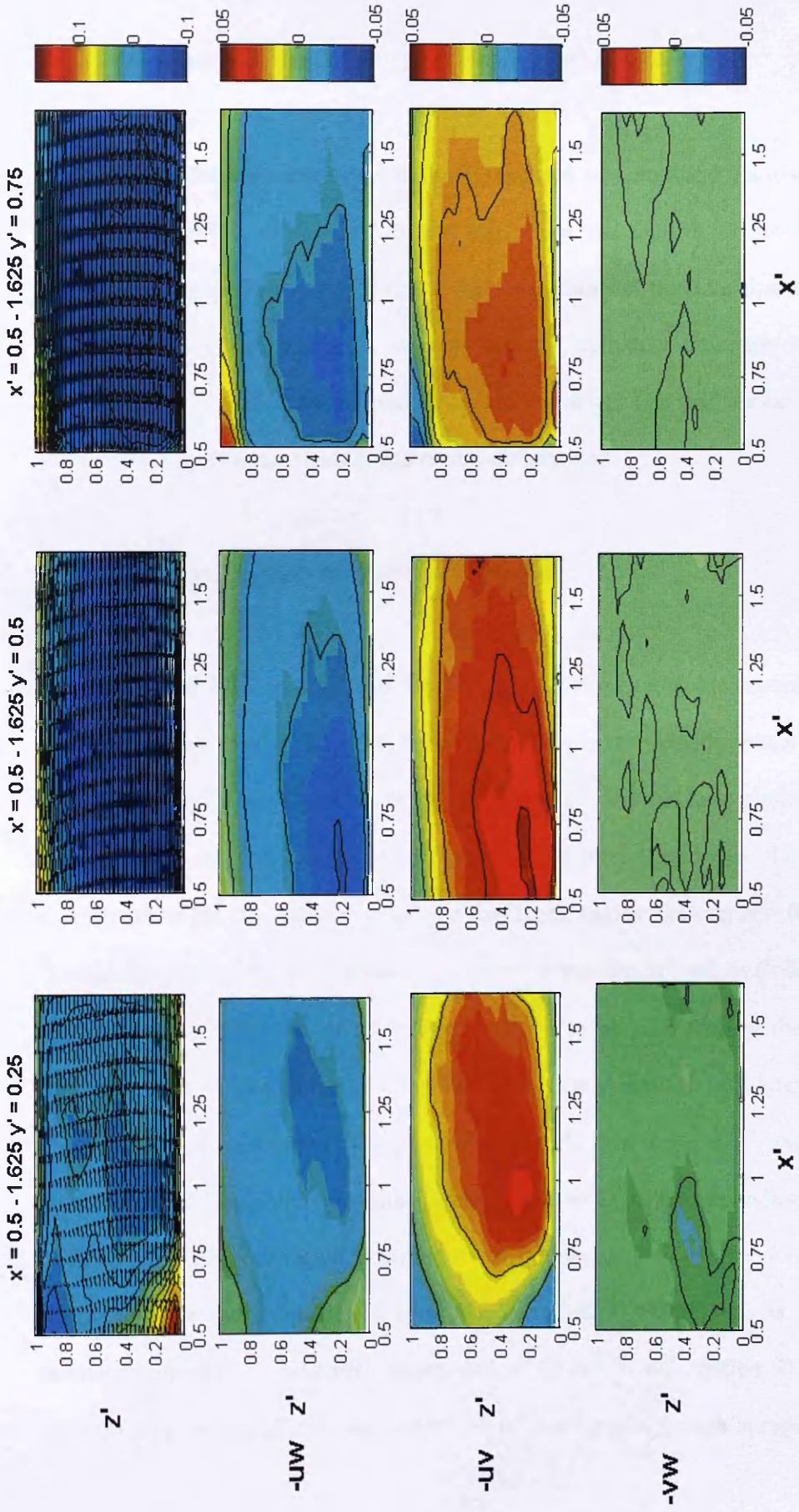
Figure 3-23 Reynolds Stress u^+, $(2^{nd}$ row) v^+ $(3^{rd}$ row), w^+ (bottom row) and mean flow (top row) for $x' = 0.5 - 1.625$ along planes $y' = 0.25$ $(1^{st}$ column), 0.5 $(2^{nd}$ column) and 0.75 $(3^{rd}$ column) for the live-bed test.

3.4.2.3 Transition and Clear-water Tests Turbulence Fields

The turbulence intensity and Reynolds stress fields are presented and discussed below in the same manner as for the live-bed test. From the analysis of the flow and turbulence fields in the live-bed test, and the comparisons of the transition and clear-water test flow fields above, it is clear that the cylinders influence is mainly constrained to $x' < 2.5$ downstream of its trailing edge. For this reason only the corresponding turbulence fields in this region are analysed.

3.4.2.4 Transition Test Turbulence Fields, Centreline $< 2.5 D$

Figure 3-24 and 3-25 show plots of TI and Reynolds stress along the centreline (first two columns) up to $x' = 2.5$ with the corresponding mean velocity vector map for comparison respectively. Like in the live-bed test, u^+ and v^+ have similar spatial distributions with the largest values occurring in the streamwise flow region downstream of the stagnation zone. v^+ has the largest values (peaking at ≈ 0.175 m s$^-$^{1}) which are again ≈ 0.1 m s^{-1} greater than the corresponding u^+ values (≈ 0.075 m s$^-$^{1}). The spatial distribution of u^+ and v^+ appears to be governed by the vertical stagnation zone as the contours of u^+ and v^+ are also near vertical, particularly in v^+. Values of w^+ are generally lower (peak < 0.04 m s^{-1}) than those of u^+ and v^+ and peak in a broad area in the downstream region, similar to the corresponding data for live-bed test. The three-region structure of the turbulence field can be defined here similarly as for the live-bed test, such that in region 1) where flow is reversed, turbulence intensity is relatively strong and $v^+ > u^+ > w^+$; region 2) there is downstream flow and TI is strong with $v^+ >> u^+ > w^+$ again, though in region 3) v^+

$> u^+ \approx w^+$ does not apply as well as for the live-bed test, as $w^+ < u^+$. Downstream ($x' = 1.625 - 3$) TI gradually tends towards uniformity with $v^+ > u^+ > w^+$. These regions are numbered in Figure 3-25.

Reynolds stresses τ_{uw}, τ_{uv} and τ_{vw} are plotted for slices $x' = 0.5 - 1.625$ and $x' = 1.625 - 3$ in Figure 3-25. Similar to the live-bed test, the distribution again appears to be governed by the stagnation zone, with its vertical structure defining the changes between positive and negative stress. Again τ_{uv} is strongest being negative in the reversed region and positive in the downstream region. τ_{uw} which is generally smaller than τ_{uv} shows positive values in the reversed flow region. τ_{vw} appears once more to be the weakest of the three stress components. It appears that here too the superposition of lateral (weakly vertically sheared) off centreline flow and downstream flow that respectively exhibit correspondingly large values and spatially similar distributions of v^+ and u^+ is responsible for the weak τ_{vw}. Downstream Reynolds stresses tend towards uniformity with τ_{uw} gradually becoming the most dominant.
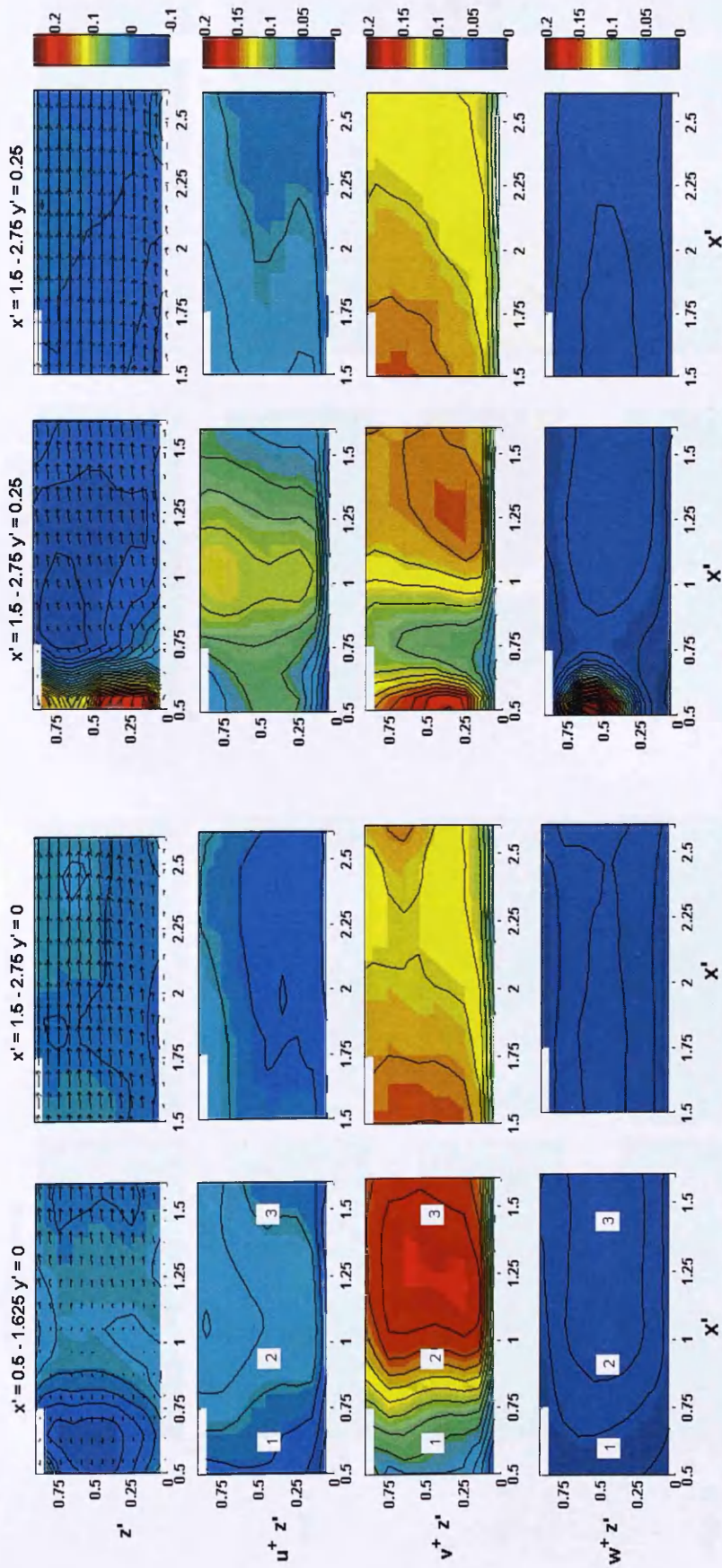
Figure 3-24. Turbulence intensity and mean flow for transition test $x' = 0.5 - 1.625$ (1st column) and $x' = 1.5 - 2.75$ (2nd column) along the $y' = 0$ (centreline) plane and $x' = 0.5 - 1.625$ and $x' = 1.5 - 2.75$ (3rd column) along the $y' = 0.25$ (4th column). The three regions of similar turbulence characteristics as described in the text above are labelled (1, 2 and 3) on the $x' = 0.5 - 1.625$ slice for each TI component.

3-55
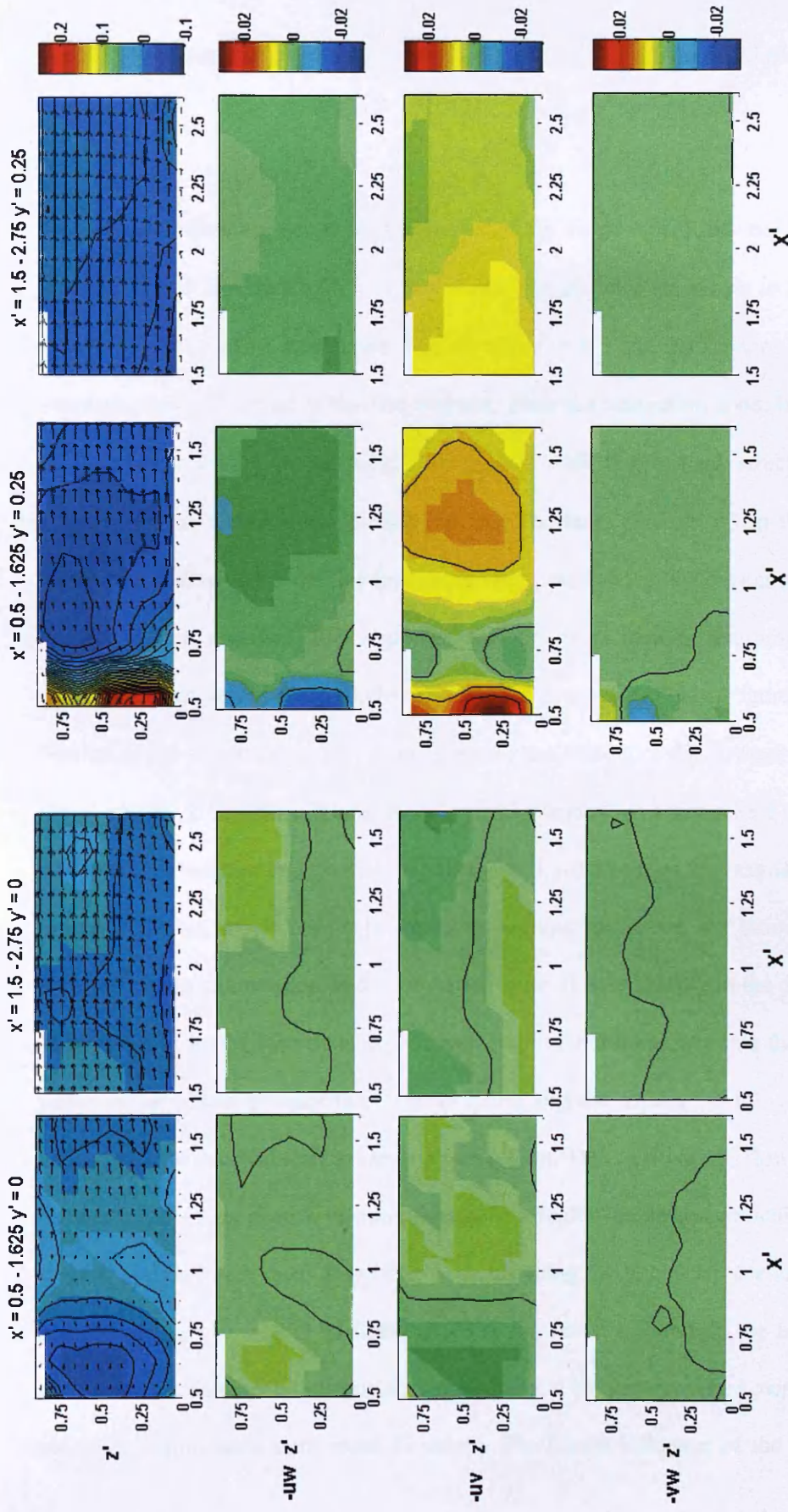
Figure 3-25. Reynolds Stress and mean flow for transition test $x' = 0.5 - 1.625$ (1st column) and $x' = 1.5 - 2.75$ (2nd column) along the $y' = 0$ (centreline) plane and $x' = 0.5 - 1.625$ and $x' = 1.5 - 2.75$ (3rd column) along the $y' = 0.25$ (4th column).

3.4.2.5 Transition Test Turbulence Fields along y' = 0.25, 0.5 and 0.75 planes at x' ~ < 2.5.

The same turbulence fields as above are plotted for the $y' = 0.25$, 0.5 and 0.75 planes covering $x' \sim < 1.6$ (the $x' = 0.5$ - 1.625 slice). The TI fields are shown in Figure 3-24 for the $y' = 0.25$ plane and Figure 3-26 for the $y' = 0.5$ and 0.75 planes. TI reduces downstream, as observed in the live-bed test. Near the stagnation zone, both v^+ and u^+ are larger in the downstream flow region with the vertical structure of the stagnation zone dictating the TI distributions. The large positive v^+ in the reversed region is not observed in the live-bed test; as suggested above, the reason v is strongly positive in the reversed flow region is that the flow here is returning from the centreline back across the cylinder towards the separation point (Figure 3-16 [3]). Similar to the live-bed test, w^+ is larger across the middle of the downstream end of the $x' = 0.5$ - 1.625 slice. Along the $y' = 0.25$ plane u^+ is the weakest of the three turbulence intensities, and shows a distinct rise downstream of the stagnation before rapidly reducing. v^+ is relatively strong throughout the slices, but strongest in the reversed region and weakest in the stagnation zone. It rises sharply in the downstream flow before reducing with distance downstream, but at a far slower rate than u^+. w^+ becomes very strongly positive (showing the highest values of all components, contrary to the live-bed test) in the reversed region. This positive w^+ flow appears to be the result of its spatial location which is a region of larger vertical shear and vertical motion in the mean flow. The TI fields along the $y' = 0.5$ plane are similarly distributed to the $y' = 0.25$ TI fields which is somewhat different to the live-bed test where at the corresponding position the absence of flow reversal was observed alongside significantly dampened TI values. The lateral influence of the cylinder is

subtly different in the transition test compared to the live-bed. The vertical structure of the stagnation zone remains intact and extends to the bed off the centreline; as a result no flow is able to escape underneath the reversal as in the live-bed test. By $y' = 0.75$ turbulence distribution is one of a general reduction and return to undisturbed flow, with some translation of v^+ downstream.
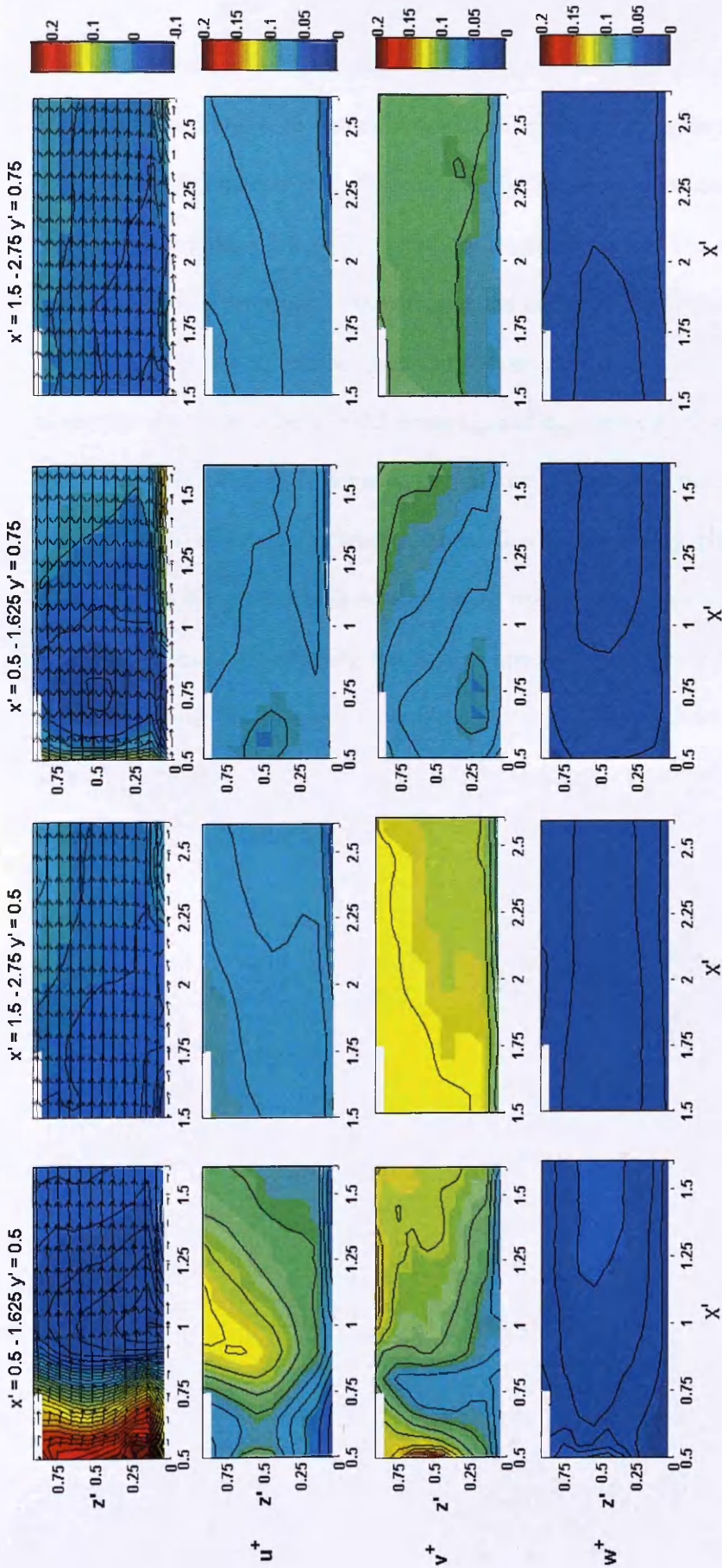
Figure 3-26. Turbulence intensity and mean flow for transition test at $x' = 0.5 - 1.625$ (1st column) and $x' = 1.5 - 2.75$ (2nd column) along the $y' = 0.5$ plane and $x' = 0.5 - 1.625$ and $x' = 1.5 - 2.75$ (3rd column) along the $y' = 0.75$ (4th column).

The Reynolds stress fields are shown in Figure 3-25 for the $y' = 0.25$, and Figure 3-27 for the $y' = 0.5$ and 0.75 planes. Reynolds Stress τ_{uv} are again strongly correlated with the distribution of v and v^+, being positive in the reversed and downstream flow regions while reducing to ≈ 0 around the stagnation zone. The negative τ_{uw} peak corresponds with the reversed flow region and becomes weakly positive downstream as the flow returns to uniform boundary layer shear flow, while τ_{vw} remains ≈ 0 across the slice. Along the $y' = 0.5$ plane τ_{uv} and τ_{uw} stresses are similarly distributed along the region of strongly negative lateral flow as they are in the corresponding live-bed test. The difference is brought about due to the strong positive lateral flow between $x' = 0.5 \sim 0.8$ which creates strong negative τ_{uw} stresses (due to the large near bed velocities transferring momentum upwards) and strong positive τ_{uv} which implies a strong shear opposite in direction to the downstream region. Reynolds stresses on the $y' = 0.75$ plane are distributed similarly to the corresponding live-bed stresses.
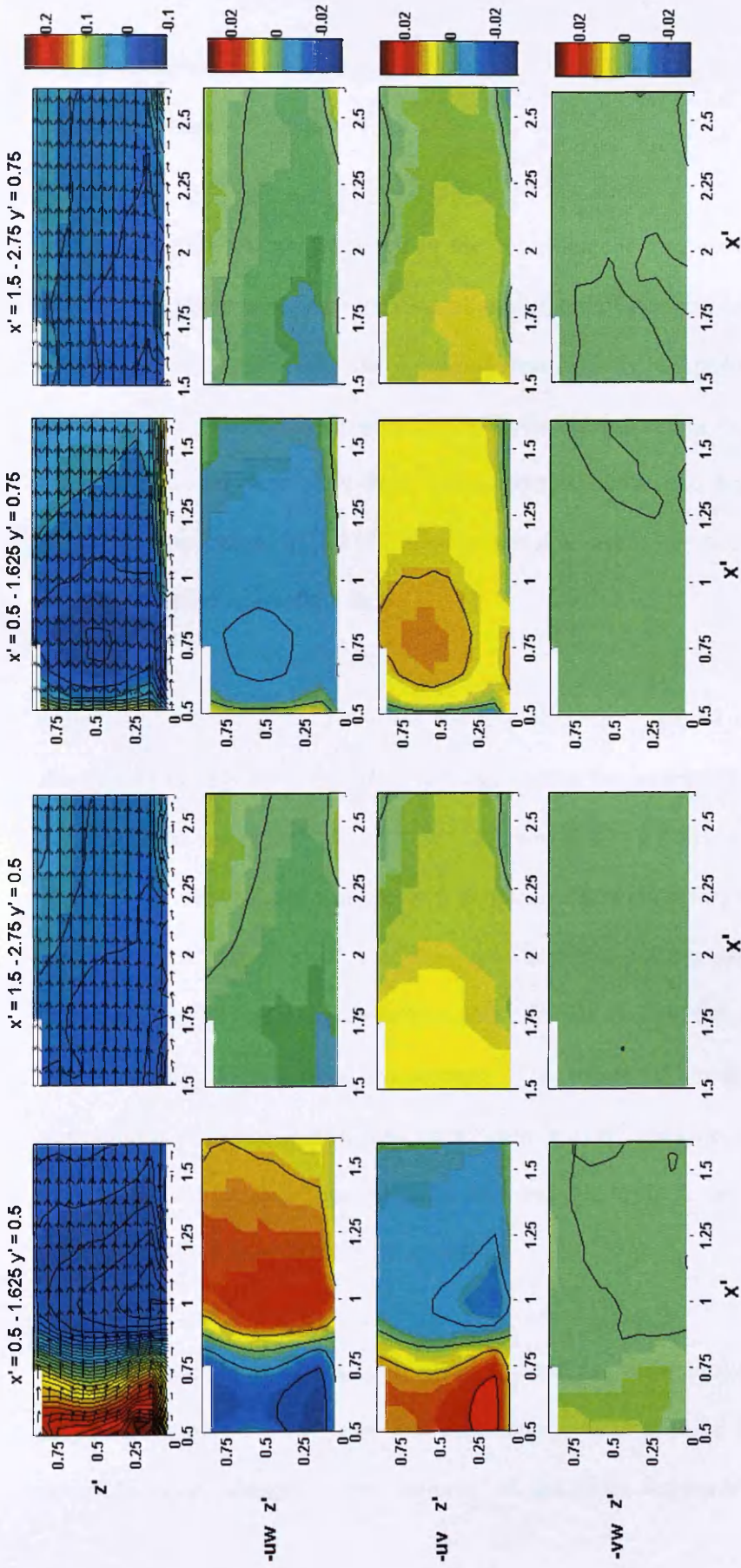
Figure 3-27. Reynolds Stress and mean flow for transition test at $x' = 0.5 - 1.625$ (1st column) and $x' = 1.5 - 2.75$ (2nd column) along the $y' = 0.5$ plane and $x' = 0.5 - 1.625$ and $x' = 1.5 - 2.75$ (3rd column) along the $y' = 0.75$ plane (4th column).

3.4.2.6 Clear-water Test Turbulence Fields along the $y' = 0.25$, 0.5 and 0.75 Planes,

Centreline Slices ~ < 1.6 D

The majority of cylinder influence in the clear-water is also confined to $x' < 2.5$. However, in order to reduce repetition of similar turbulence structures, only the first slice $x' < 1.625$ is analysed. The remaining data is given in Appendix A8.3. The TI and Reynolds stress fields are presented with the corresponding mean velocity field. As with the mean clear-water flow fields discussed above, the depth of the flow is greater than the height of the PIV slice so two time-averaged slices are presented in order to cover the whole flow field.

Figure 3-28 shows plots of TI for the centreline flow behind the cylinder. The structure of the TIs with $v^+ > u^+ > w^+$ that applies for the transition and live-bed is not applicable here as $v^+ >> u^+ \approx w^+$. v^+ which is ≈ 0.2 m s^{-1} tends to increase slightly with distance downstream and its spatial distribution follows the stagnation zone closely. u^+ and v^+ share a similar spatial distribution suggesting the tri-regional turbulence distribution structure defined above for the low and (particularly) live-bed test is present, though a lot less strongly. The region of strong w^+ around the stagnation zone in particular is difficult to identify as w^+ indicates only a very slight increase around the stagnation zone. As expected due to the lower free stream flow velocity, the TI is lower than the other tests.

Reynolds stress components (Figure 3-29) τ_{uw} and τ_{uv} show similar distributions to the transition and live-bed tests with negative τ_{uv} and positive τ_{uw} found in the reversed region, though in the majority of the field Reynolds stresses remain

negligible. τ_{vw} exhibits values that are comparable to the other stress components, which is not the case in the transition and live-bed tests where the values are significantly lower. This may be related to the upstream shear in v' as discussed in §3.2.1.2.
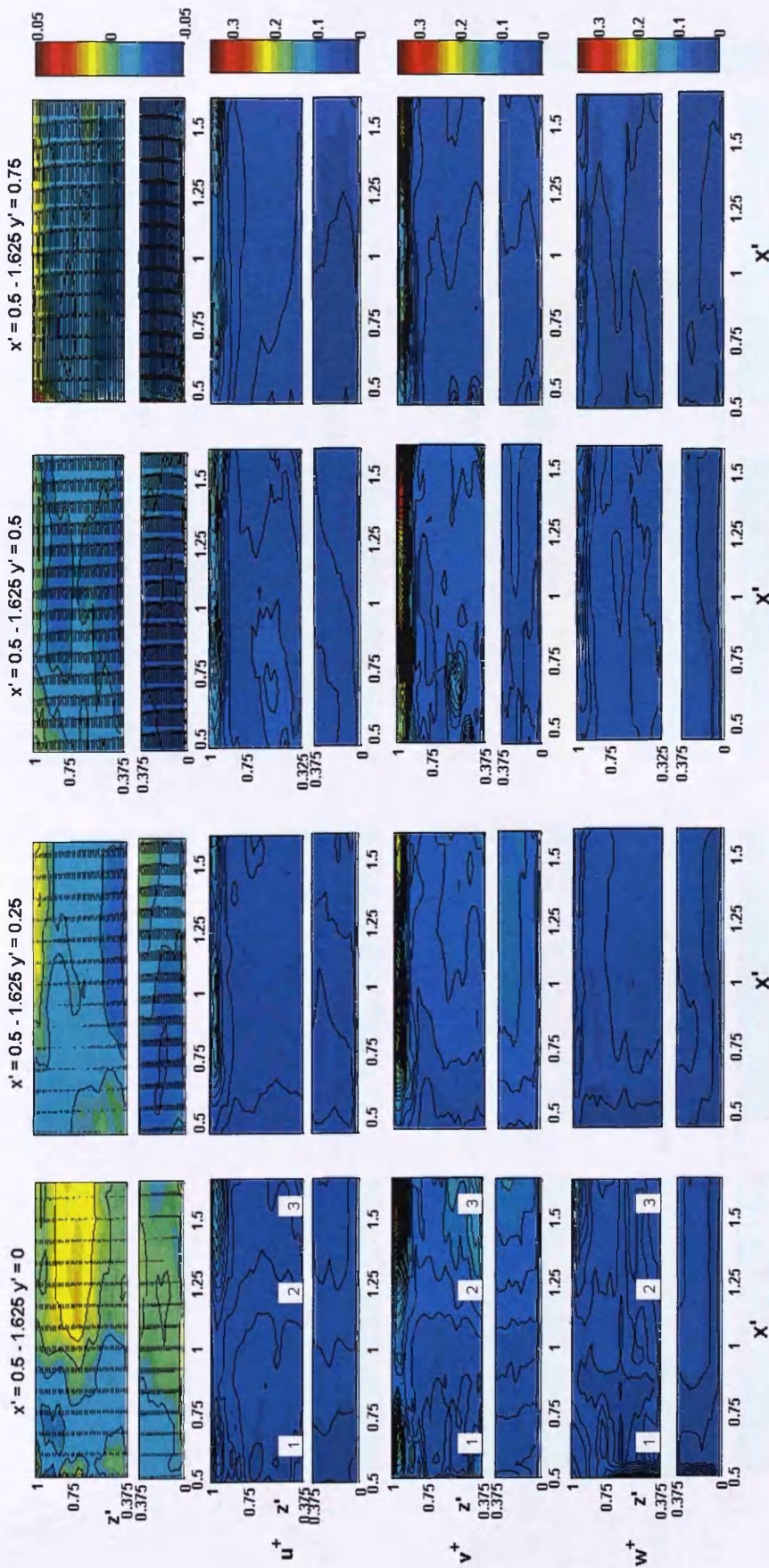
Figure 3-28. Turbulence intensity and mean flow for the clear water test at $y' = 0$ plane $x' = 0.5$ - 1.625 (1st column), $y' = 0.25$ plane $x' = 0.5$ - 1.625 (2nd column) along the $y' = 0.5$ plane $x' = 0.5$ - 1.625 (3rd column), $y' = 0.75$ plane $x' = 0.5$ - 1.625 (4th column). The three regions of similar turbulence characteristics as described in the text above are labelled (1, 2 and 3) on the $x' = 0.5$ - 1.625 slice for each TI component.
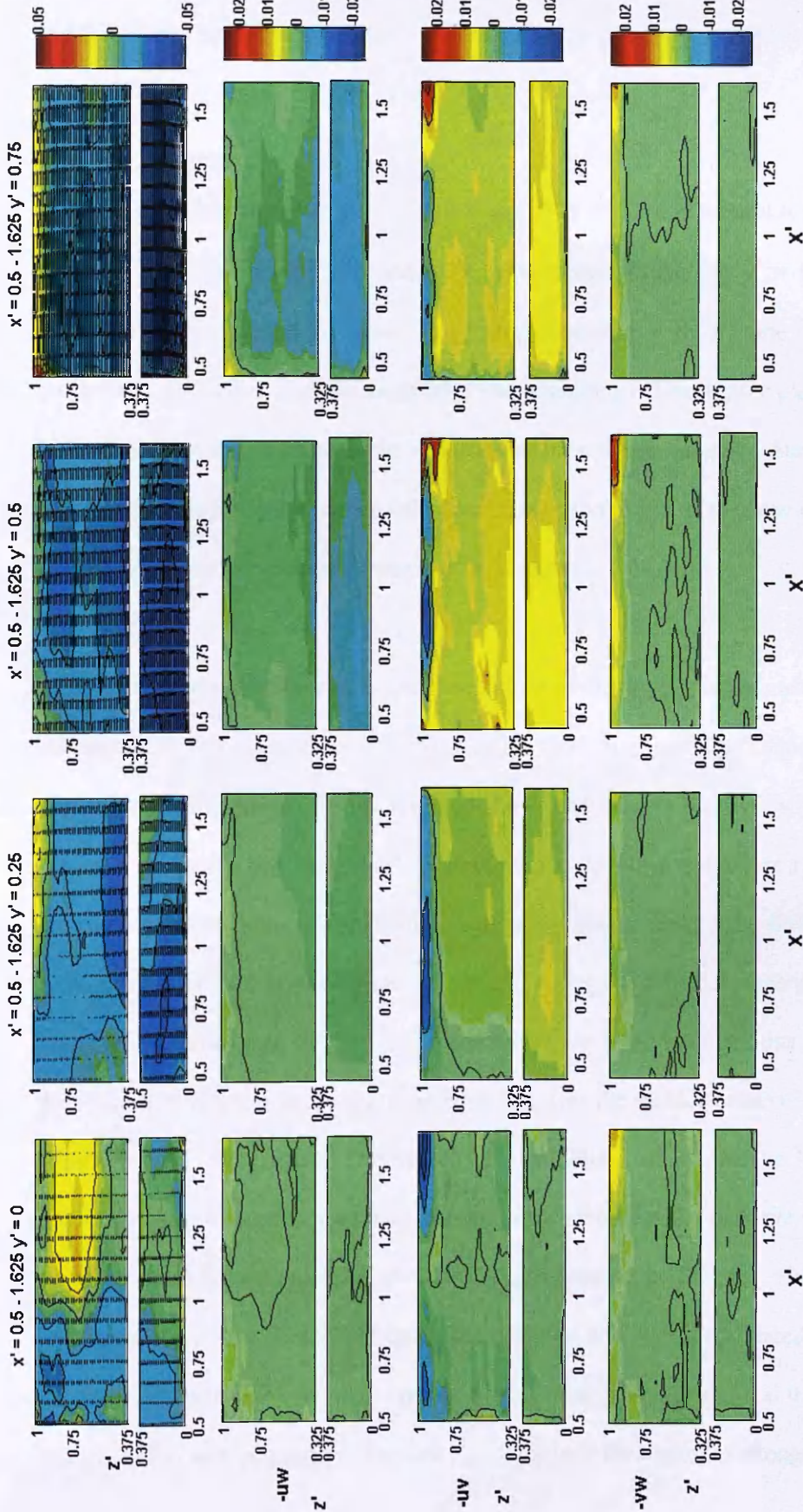
Figure 3-29. Reynolds Stress and mean flow for the clear water test at $y' = 0$ plane $x' = 0.5 - 1.625$ (1st column), $y' = 0.25$ plane $x' = 0.5 - 1.625$ (2nd column), $y' = 0.5$ plane $x' = 0.5 - 1.625$ (3rd column), $y' = 0.75$ plane $x' = 0.5 - 1.625$ (4th column).

3.4.2.7 Clear-water Test Turbulence Fields, Off-centreline ~ < 1.6 D and y' = 0.25, 0.5 and 0.75.

The off-centreline planes at $y' = 0.25$, 0.5 and 0.75 of TI and Reynolds stresses are also presented in Figures 3-28 and 3-29 respectively. Along the $y' = 0.25$ the TI distributions are similar to those along the centreline with v^+ the largest and particularly downstream of the stagnation. The remaining off-centreline planes show a picture of a gradual decrease in the influence of the cylinder laterally. Surface values of v^+ and u^+ in particular remain enhanced relative to the rest of the flow field, which may be related to the upstream shear in v' as discussed in §3.2.1.2.

The Reynolds stress τ_{uv} is consistently the largest of the three stress components at all off-centreline planes. On the $y' = 0.25$ plane there is a distinct division between slightly negative stress in the reversed flow and larger positive stress in the downstream flow; a relatively similar distribution to the other tests. Here τ_{uw} and τ_{vw} are comparable in value, both remaining very small across most of the flow field with a tendency to become positive near the surface. Along the $y' = 0.5$ plane τ_{uv} exhibits larger stress values than the previous plane which are essentially positive throughout the slice. The exception is strong negative stress near the surface correlating with the sheared flow in this region. This region also exhibits a small positive lateral flow implying movement away from the centreline which explains the opposite stress. This may be related to the upstream shear in v' as discussed in §3.2.1.2. This opposite surface flow is observed at all off-centreline positions and is well correlated in τ_{uv} and τ_{vw} which in particular is poorly correlated in all other tests. Along $y' = 0.5$ and 0.75 there is an increase in negative near-bed τ_{uw}. This is in the region of stronger near bed

velocities than away from the bed which suggests that there is some transfer of momentum upwards through the water column.

3.5 Bed Shear Stress Distributions

Bed shear stress τ_b quantifies the shearing force applied to the bed by the flow over it and is often dominant in determining how much sediment transport takes place. Various methods for calculating τ_b exist including the logarithmic method (Kim et al., 2000), the Reynolds stress method (Soulsby, 1986), and the TKE method (Soulsby, 1986 and Kim et al., 2000). After preliminary investigation, the logarithmic stress and Reynolds stress methods were found to be inappropriate here due to non-uniformity in the flow, particularly downstream of the cylinder. Therefore bed shear stress is calculated using the TKE method (Equation 3-1).

$$\tau_b = C_1\left[0.5\rho\left(\overline{u''^2} + \overline{v''^2} + \overline{w''^2}\right)\right] \qquad 3\text{-}1$$

Where C_1 is a constant of proportionality for which the value of 0.19 given by Soulsby, (1986) and Kim et al., (2000) is used here.

Bed shear stress amplification α, ($\alpha = \tau_b/\tau_\infty$, where τ_∞ is the undisturbed value of bed shear stress calculated from control test profiles in Appendix A9) was calculated from the turbulence data described above using Equation 3-1.

3.5.1 Upstream Bed Shear Stress Estimates

The estimates of α from the upstream measurement locations are plotted in Figure 3-30 for the transition, clear-water and live-bed tests. The upstream distribution of α with x' is similar between all tests. α upstream of $x' = -1.625$ the cylinder is generally ≤ 1, as the reduction of velocity in the flow approaching the cylinder reduces the bed shear stress applied. On the centreline α increases dramatically from $x' = -1.25$ to -0.665 due to the increased turbulence and velocity, and closer to the cylinder, from the downflow. Along the $y' = 0.6$, 0.85 and 1.1 planes there is no apparent increase in α which is expected as the turbulence distributions shown in Figures 3-4, 3-5 and 3-6 also exhibit lower values than are found on the centreline, even though velocity increases towards the cylinder due to flow constriction.

3.5.2 Near-Cylinder Bed Shear Stress Estimates

Figure 3-31 presents plots of α along from $x' = -0.6$ to 0.6 and $y' = 0.3$, 0.9, 1.25 and 1.5 in the near-pile region. There are again similarities between all tests with α becoming as large as 11-12 along the 0.3 plane. α reaches maximum on the upstream side of the $y' = 0.3$ plane, the location and value of which is in general agreement with data presented by Hjorth (1975), Melville (1977), Baker (1979) , Niedoroda and Dalton, (1982) and Ahmed and Rajaratnam, (1998). Along the $y' = 0.9$, 1.25 and 1.5 planes α is barely > 1, even though velocity increases along these planes were shown to be < 1.5 (Figure 3-7). Turbulence values are, however, greatly reduced along these planes leading to the lower α factor.
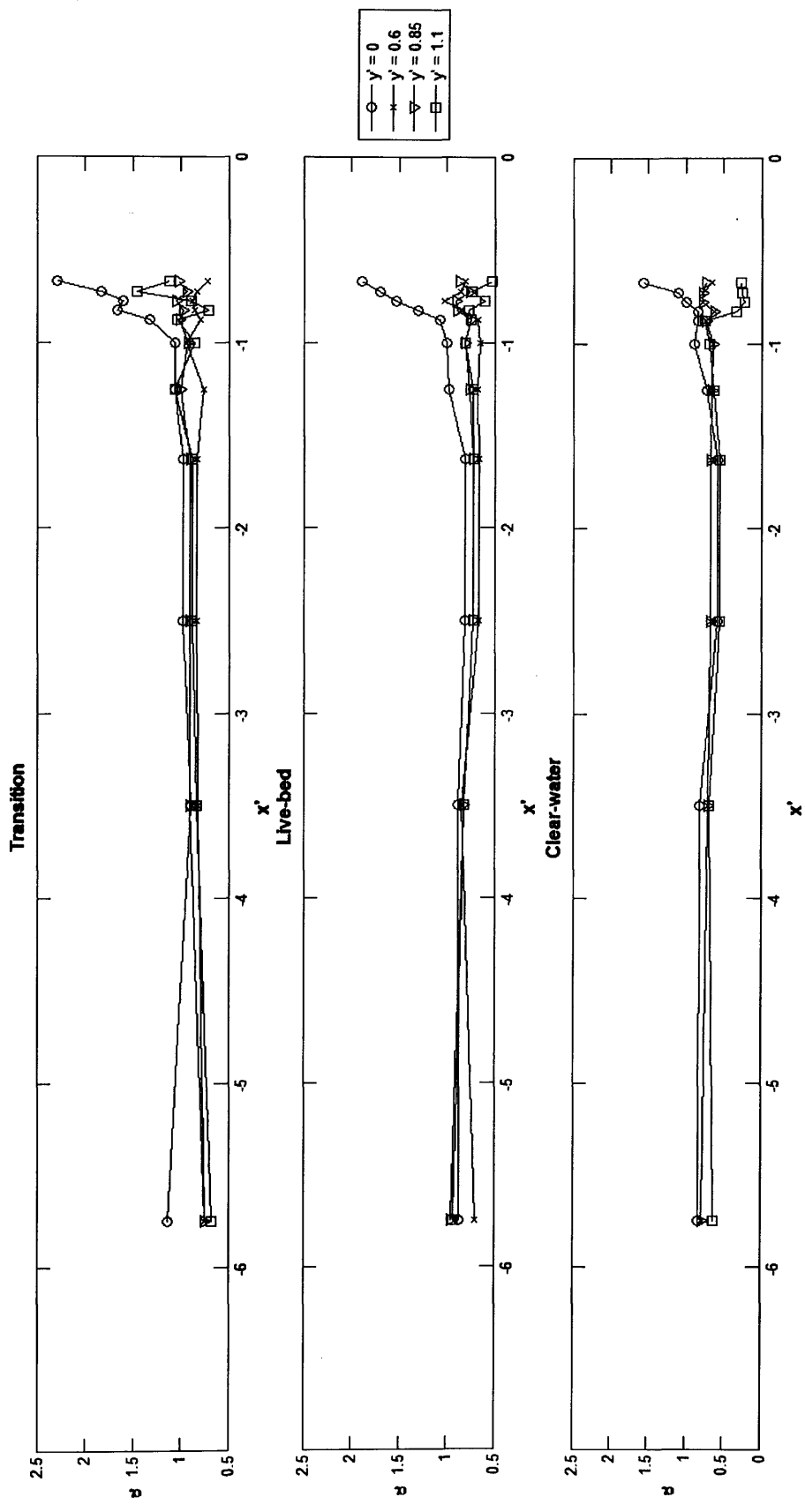
Figure 3-30. Upstream estimates of α for each test.
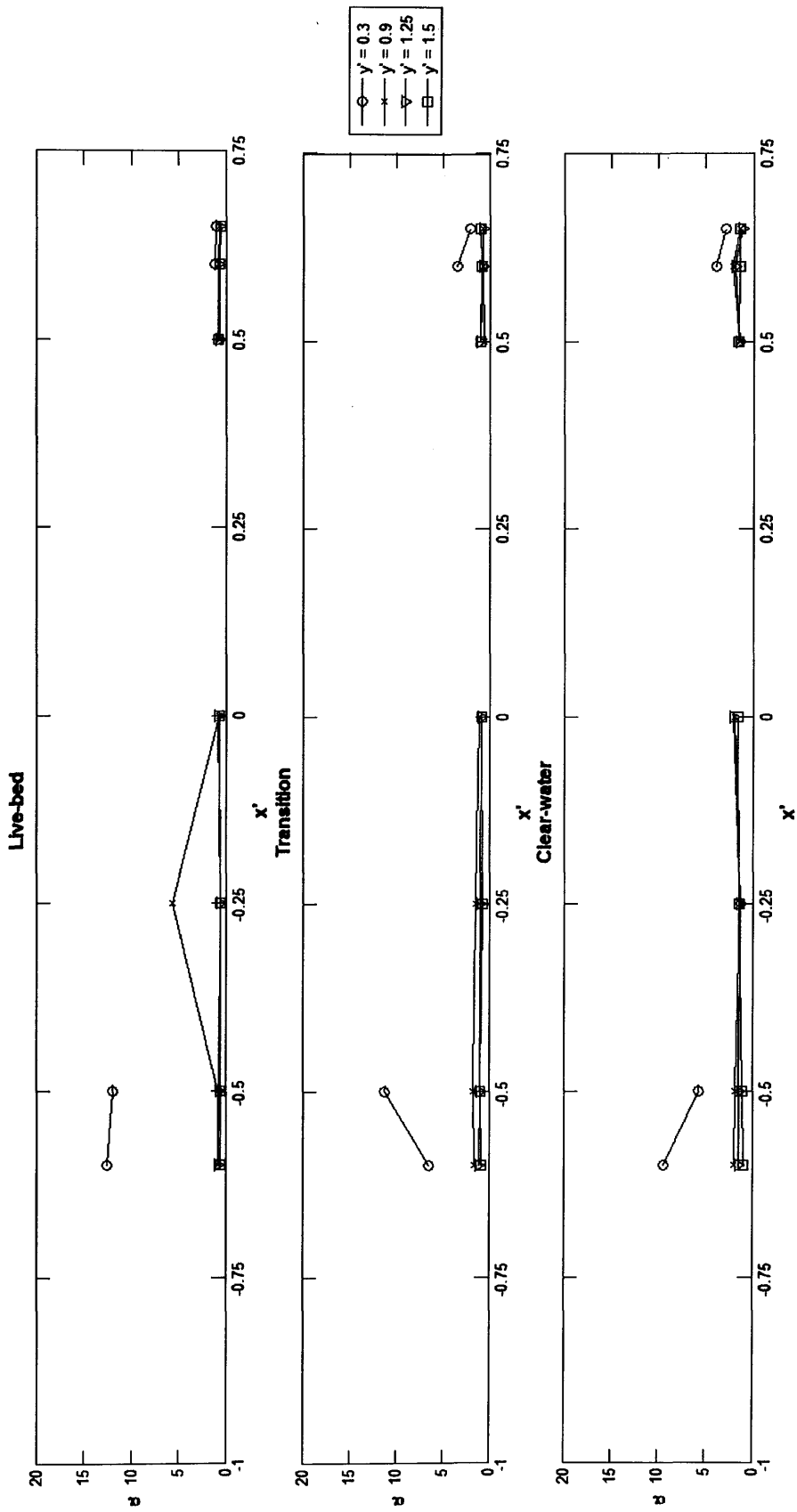
Figure 3-31. Near-pile estimates of α for each test.

3.5.3 Downstream Bed Shear Stress estimates

Figure 3-32 top row present plots of α from $x' = 0.5$ - 2.875 downstream of the cylinder for the live-bed test using the data from the PIV slices presented above in §3.3. Along the centreline there is a gradual increase in α with distance downstream, peaking at ≈ 2 at $x' = 1.25$, which is where downstream flow is reforming near the bed after which α gradually decreases. α reduces to below < 1 at $\approx x' = 2$ and remains so thereon due to the lower values of U and lack of significant turbulent motions. Off-centreline at $y' = 0.25$ α (being larger than along the centreline) increases with the centreline values until becoming more or less constant at $x' = 0.875$, though rarely > 1.3. It is finally exceeded by the centreline α at $x' = 1.25$ and decreases to < 1 at $x' \approx 2$. Along the $y' = 0.5$ plane α never exceeds 1 whereas along $y' = 0.75$ it attains the maximal value across all positions near the cylinder due to the significant constriction of flow in this region (Figure 3-14) before decreasing. The distribution of α is clearly dictated by location of the stagnation zone.

This is also observed in the clear-water test but in the transition test the $y' = 0.25$, and 0.5 planes all behave similarly to the centreline with only the $y' = 0.75$ plane showing the increased bed shear stress amplification near the cylinder. Along the centreline α distribution is similar to the live-bed test in both the transition and clear-water tests, the values peak just downstream the stagnation zone. The changes in the spatial distribution of the wakes and in particular the locations of stagnation between each test evidently alter the distribution of maximum α upstream of stagnation being along the $y' = 0.25$ as opposed to $y' = 0.75$ for the transition test and $y' = 0.5$ for the clear-water test. Downstream α begins to reduce towards one, and though it doesn't reach 1

within the limit of measurement, the trend suggests this will occur further downstream.
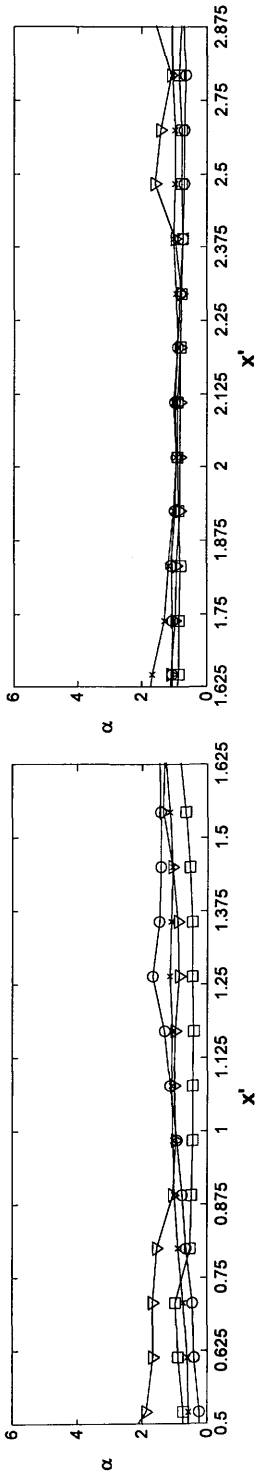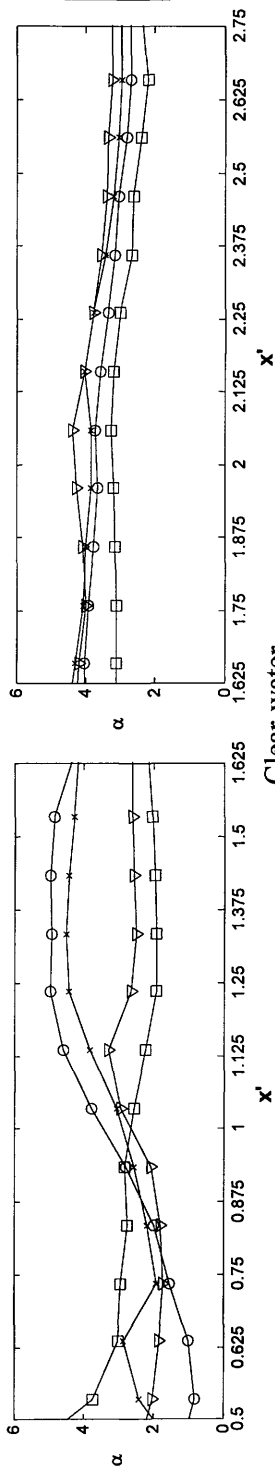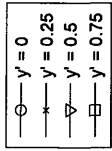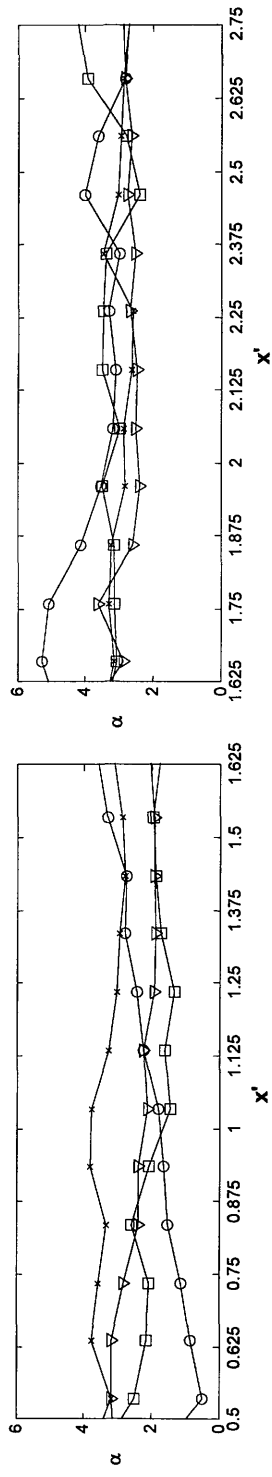
Figure 3-32. Downstream estimates of α for each test.

3-73

The observation that bed shear stress amplification factor α is similarly spatially distributed in the upstream and near-cylinder regions in all tests implies that scour will begin at similar positions regardless of the incumbent flow parameters at cylinder insertion. Table 3-2 presents the measured bed shear stress maximums around the cylinder during each tidal stage. Maximum measured bed shear stress is, as expected, greatest in the live-bed test. Although the α values are similar in each tidal stage the amount and rate of scour that will take place in each test is quite different based on the calculated bed shear stress values with the most scour occurring during the live-bed as flow intensity U/U_c is already > 1 and α raises to its largest overall values (Table 3-2).

	soulsby (1997) critical shear stress	undisturbed value from data	upstream	approx max α	near-pile	approx max α	downstream	approx max α
high-tide	$0.158\,\text{N m}^{-2}$	$0.09\,\text{N m}^{-2}$	$0.135\,\text{N m}^{-2}$	1.5	$0.99\,\text{N m}^{-2}$	11	$0.45\,\text{N m}^{-2}$	5
mid-tide	$0.158\,\text{N m}^{-2}$	$0.22\,\text{N m}^{-2}$	$0.44\,\text{N m}^{-2}$	2	$2.64\,\text{N m}^{-2}$	12	$1.1\,\text{N m}^{-2}$	2
low-tide	$0.158\,\text{N m}^{-2}$	$0.1\,\text{N m}^{-2}$	$0.2\,\text{N m}^{-2}$	2.4	$1\,\text{N m}^{-2}$	10	$0.5\,\text{N m}^{-2}$	5

Table 3-2. Approximate maximum values of α in the upstream, near-pile and downstream regions.

3.6 Summary of Results

The flow and turbulence fields in the upstream, near-cylinder and downstream regions have been described in detail in the above sections. During all three tests, the approaching upstream flow is characterised by a slowing of u' velocity and an

increase of v' and w' on the centreline. To a lesser extent, u' reduction is present along all off-centreline planes reaching a minimum further upstream before increasing closer to the cylinder. An initial radial increase of v' off-centreline and away from the cylinder is followed by a decrease. Most of the major changes in the upstream mean flow field are confined close to the centreline where in all tests flow is slowed, forced downward towards the bed and deflected around the cylinder. Streamwise u' exceeds 1 in the $y' = 0.85$ and 1.1 planes near the cylinder. The distribution of turbulence intensity upstream of the cylinder during the live-bed test is relatively constant with x' with the largest values (u^+) consistently found along the centreline, but the difference between centreline and off-centreline values is not large. Reynolds stress components τ_{uv} and τ_{vw} are small and show no particular pattern suggesting that there is no significant shearing in these stress orientations.

In the near-cylinder region there is an upstream increase in v' and u' due to the constriction and deflection of flow around it. Downstream of the cylinder the distributions become more varied; v' becomes negative (indicating flow back towards the centreline) while u' reduces and near the surface in the clear-water, reverses back towards the cylinder. Reversal of u' is not recorded in the measured region in the transition and live-bed tests, indicating that the point of separation and lateral extent of the near-wake region on the downstream side of the cylinder is not the same across the three tidal stages. The downstream side of the cylinder shows increased turbulence levels in comparison to the upstream side in all tests. Close to the separated flow (or in the case of the clear-water within the separated flow region, as denoted by the reversed flow observed there) which is present at $y' < 0.3$ and $x' < 0.5$ turbulence levels are significantly higher than both the upstream values and the lateral near-

cylinder values. In each test, all three TI and stress components have similar values which show a tendency to increase on the downstream side of the cylinder, implying three-dimensionality in this region.

In the downstream region of the live-bed test the near-wake is characterised by a bowl-shaped region of flow reversal extending downstream to $x' \approx 1.625$ and laterally to $y' \approx 0.25$ - 0.5. Within this region mean velocity and turbulence is relatively weak. The region is bounded by a flow stagnation zone which extends diagonally from $x' \approx 1.0625$ near the bed, to $x' \approx 1.625$ near the surface. Vertical shear is maximal within this region and so too is the vertical turbulence intensity component. Off the centreline the stagnation zone does not extend to the bed. Downstream of the stagnation zone region, the flow is a superposition of reforming downstream orientated boundary layer flow and a lateral flow which is flowing around the near-wake and back towards the centreline. This lateral mean flow is weakly sheared as τ_{vw} is uniformly low, but the region as a whole is relatively strongly turbulent, with the v^+, and τ_{uv} dominating. Moving downstream and laterally away from the cylinder the described pattern gradually weakens and blurs with increasing lateral and downstream distance from the cylinder. There is some advection of vertical turbulence motions downstream, and the presence of lateral mean flow is still apparent to at least $x' = 5$ (in the live-bed) downstream and at least up to $y' = 1$ laterally. Throughout the three tests, certain aspects of the flow field are common such as flow reversal, stagnation, and reformation of downstream boundary layer shear flow. Other aspects are variable such as the shape of the stagnation zone and the consequent re-circulation and the downstream and lateral extent of the cylinders influence.

3.7 Discussion

Clearly the upstream flow field is not significantly spatially altered between the tests with only the strength of the observed phenomena changing. Certain aspects of the downstream flow field are common in each testp such as flow reversal, stagnation, and reformation of downstream boundary layer shear flow. Other aspects are variable such as the location of lateral flow separation, the gradient and downstream location of the stagnation zone, the consequent re-circulation of flow, and the downstream and lateral extent of the cylinders influence on the flow. This variation will now be discussed further.

3.7.0.1 Boundary Layer Thickness Calculations

In the following discussion, the thickness the boundary layer δ is referred to frequently. This is calculated using the assumption of a logarithmic boundary layer as the boundary layer behaves logarithmically, (Appendix A10)

Time step	U	h	Re_D	Fr	Approximate δ	Approximate δ/h
High-tide	0.15	0.4	2.2×10^4	0.075	≈ 0.035	≈ 0.09
Mid-tide	0.33	0.25	4.9×10^4	0.21	≈ 0.045	≈ 0.2
Low-tide	0.23	0.1	3.4×10^4	0.23	≈ 0.055	≈ 0.6

Table 3-3. Boundary layer heights estimated from logarithmic plots of velocity in test with and without the cylinder in the flume.

3.7.1 The Variation of the Flow between the Tests

3.7.1.1 The Influence of Parameters Re_D, Fr_h, and h/D on the Wake Flow

Using Figure 1-11, it can be hypothesised that the downstream flow and turbulence fields will have similar spatial distributions while exhibiting lower or higher flow and turbulence values according to the free stream velocity. This hypothesis is based on the realisation that the cylinder-Reynolds number Re_D is relatively similar in each test (Table 3-3); all three Re_D values remain in the subcritical separation regime ($300 < Re_D < 3 \times 10^5$, Figure 1-11e). However, there is clearly defined variation in the downstream flow between the tidal stages. These variations include; the spatial location and gradient of the stagnation zone, the point of lateral separation, and differences in the structure of the wake flow, as described above in §3.4. These variations occur over a relatively small range of Re_D, but a wider range of U, h and hence Fr_h (as $Fr_h = U/\sqrt{gh}$), indicating that the velocity and turbulence field in the wake is influenced more by Re_D than U, h and Fr_h. This is consistent with the cylinder-wake flow results of Johnson and Ting, (2003), and is of some interest as most scour equations relate equilibrium scour depth to relative water depth h/D and Fr_h, and consider Re_D to be insignificant (e.g., Ettema et al., 1998a and Johnson and Ting, 2003). In this case it seems further research is required to define the effect of Re_D and understand its role in the scouring process and wake flow. However, the results do suggested that the variation of h, or more importantly the boundary layer depth δ (Table 3-3) plays a role in defining the structure of the wake. There appears to be a relationship between the thickness of the boundary layer and the gradient of the stagnation zone in the wake. Notably in the transition test where the boundary layer is

relatively thicker (δ/h is ≈ 0.5) than in the live-bed and clear-water tests (where δ/h is ≈ 0.2), there is a different structure to the stagnation zone (vertical until near the surface). In the live-bed and clear-water tests, the gradient of the stagnation zone is vertical only to the approximate thickness of the boundary layer off the bed before becoming shallower (see Table 3-3 and Figure 3-19). It is suggested that it is this lower water depth that causes the vertical stagnation zone rather than the velocity, as at lower and higher velocities (clear-water and live-bed) the stagnation zone has a gradient $\neq 1$.

The downstream length of the reversal zone, often described as the near-wake in the literature (Zdravkovich, 1997), changes between each test. The length of the reversal zone G is greatest in the clear-water test where it is situated downstream at $\sim 1.3D$ at the bed and $> 1.625D$ at the surface. In the live-bed and transition the length G at the bed and surface is $\sim 1.06D$ and $\sim 1.625D$ and $\sim 0.96D$ and $\sim 0.9D$ repsectively. Figure 3-33 shows plots of G against δ/h and Re_D. Re_D does not seem to affect G; a qualitatively similar finding was presented by Testik et al., (2005) in their study of horizontal cylinder wakes. δ/h does seem to affect G with a lower δ/h resulting in a larger G. The data however is very limited and more extensive data would be required to confirm this relationship.
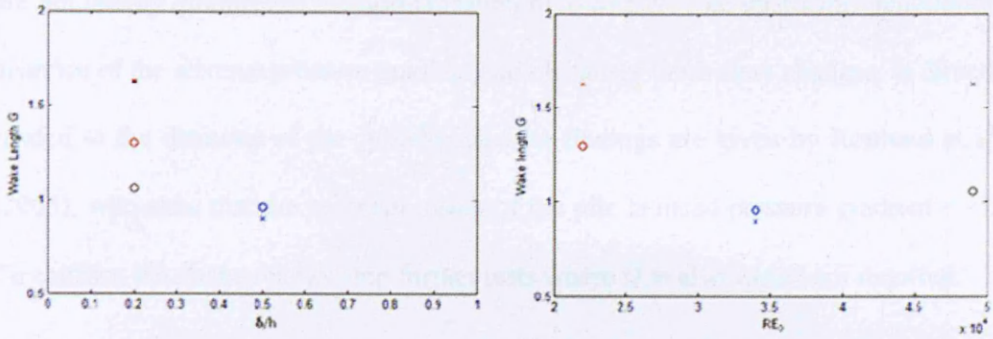
Figure 3-33. Wake length G plotted against δ/h and Re_D, where the red, black and blue circles and crosses present the high, mid and transition wake length at the bed, and surface respectively.

3.7.1.2 The Influence of D on the Upstream Flow and Turbulence Fields

All three tests share very similar upstream spatial characteristics in the flow relative to D (i.e., the distances at which the flow is changed in the presence of the cylinder). The variation in U and h between the tests seems mostly to affect the magnitude of the flow and turbulence upstream of the cylinder. As described in §3.2, the upstream flow shares the same characteristic features in all three tests, namely the stagnation, downflow and deflection of flow. The only constant parameter between all the tests is the cylinder diameter D, implying that the flow structure is chiefly governed by D and is due to the finite distance upstream that the cylinder is felt by the flow. This conclusion is arrived at with the following evidence in mind. 1) the downflow is present only $< x' = 0.875$ in all tests, 2) off-centreline flow reduction is present only at $x' > 1$, after which the flow velocity begins to increase, 3) increases in v' and subsequent decreases laterally and downstream are found at the same locations in each tidal stage (except in the clear-water test due to the secondary flow §3.2.1.2). It is the consistency of changes in the flow over each tidal stage that suggest that these trends

3-80

are not simply artefacts of the normalisation of x with D. The upstream 'penetration' distance of the adverse pressure gradient, which causes these flow changes, is directly related to the diameter of the cylinder. Similar findings are given by Roulund et al., (2005), who state that the upstream reach of the pile induced pressure gradient $< 1D$. To confirm the above relationship further tests where D is also varied are required.

3.7.1.3 Discussion of Re_D Dissimilitude between Model and Prototype

There will be some scale effects in the model associated with the dissimilitude of Re between the model and the prototype (see §2.2.2). While the dissimilitude of Re_h will have negligible effect between the model and prototype as both are fully turbulent (see Tables 3-4, 3-5 and Hughes 1993), there is a scale effect due to the dissimilitude of Re_D, (Table 3-4 and 3-5, §2.2.2). It is important to discuss the possible implications of this dissimilitude on the results of these experiments.

In these rigid bed experiments the dissimilitude of Re_D affects the lateral separation regime at the cylinder sides; being subcritical in the model and in the upper transition in the prototype (Figure 1-11 and Table 3-5). From Figure 1-14, which shows the Strouhal number ($St = f_v/D$, where f_v = the frequency of vortex shedding) as a function of Re_D, the rate of vortex shedding at prototype Re_D (~ 0.2 for the transition and live-bed test, and ~ 0.1 for the clear-water test) is similar to rate at the model (~ 0.2 throughout). Therefore, the separation regimes of both the model and prototype exhibit similar St values. Shedding vortices play only a minor role in sediment pick-up in the downstream region; their main contribution to scour is through the downstream transport of sediment (e.g., Melville, 1977 and Breusers et al, 1977).

Therefore, though separation regime dissimilitude does exist between the model and prototype, the main consequence of this is the reduced strength of the prototype vortices. The dissimilitude of St number is not as significant, being approximately similar between the model and the prototype, and as scour is more dependent on the horseshoe vortex, downflow and flow constriction, this will have limited affect on the scour depth. Indeed, if the bed were mobile, the artificially raised values of U/U_c will generate greater scour in the model (as discussed in §2.2.2), nullifying the loss of vortex strength.

However, as the results presented from these experiments indicate that Re_D is highly influential on the wake flow, and as such the above analysis clearly illustrates that the role and importance of Re_D on scour, and the modelling of scour, remains not fully well understood.

Time step	U [m s^{-1}]	h [m]	U/U_c	h/D	Re_D	Re_h	Fr	Stagnation zone
Clear-water	0.15	0.4	0.55	2	2.2×10^4	4.4×10^4	0.075	diagonal
Live-bed	0.33	0.25	1.28	1	4.9×10^4	6.1×10^4	0.21	diagonal
Transition	0.23	0.1	1	0.5	3.4×10^4	1.7×10^4	0.23	straight

Table 3-4. Parameters of the three tests.

Tide	U [m s^{-1}]	h [m]	U/U_c	h/D	Re_D	Fr
Transition	1.00	2.00	0.88	2.00	2.9×10^6	0.23
Live-bed	1.37	5.00	1.26	1.00	4×10^6	0.21
Clear-water	0.70	8.00	0.57	0.50	2.1×10^6	0.08

Table 3-5. Prototype parameters of the three tests.

3.7.2 The Horseshoe Vortex through the Changing Test Conditions

The horseshoe vortex is not directly recorded upstream of the cylinder, though its presence is implied by increased turbulence intensity near the cylinders upstream face (§3.2.2.1). The horseshoe vortex is caused by rotation in the incoming boundary layer which separates upstream of the cylinder under the influence of the adverse pressure gradient caused by its presence (see §1.3.2). The horseshoe vortex in front of the cylinder is governed by the δ/D ratio and the Re_D (Baker, 1979). Sumer and Fredsoe, (2002a) point out that the point of separation X_S/D (which is analogous to the upstream extent of the horseshoe vortex, and therefore a measure of its length) where X_S is the position upstream where separation occurs, moves closer to the cylinders upstream face with decreasing δ, and for very small δ/D, separation may not occur at all. Numerical results published by Roulund et al., (2005) indicate the lower limit for the existence of the horseshoe vortex occurs at $\delta/D < 0.01$ and an upper limit of maximum size occurs at $0.95D$ for $\delta/D > 0.5$. The calculated values of δ/D (Table 3-3) show that δ/D in all three tests exceeds the lower limit indicating a horseshoe vortex should be present, and should, in all three cases be large enough to be recorded at $x' = 0.665$ which is the nearest measurement point to the cylinder (Figure 22 in Roulund et al., 2005,). The model presented in Roulund et al., (2005) is for flow over a smooth bed based on a higher Reynolds number (2×10^5) than these experiments (for which $Re_D \sim 10^4$), but for turbulent boundary layers where $Re_D > 30,000$, data compiled in Figure 3.4 in Sumer and Fredsoe, (2002b, p. 154), indicates the relationship remains the same (Sumer and Fredsoe, 2002b). Thus the horseshoe vortex is likely to be in existence on the analysis of the literature above, and the recording of increased turbulence intensities near the cylinder. If in existence, its small size

indicates that the relationship between Re_D and δ/D and X_s/D is still not fully understood.

3.7.3 The Influence of Tidal Range

The tidal range modelled in this experiment is 8 m which is a typical range found in the Irish Sea in the Liverpool Bay area (Appendix A11). Such a range is large compared to many other coastal areas in the U.K. A further difference is the type of tide that is simulated (see §2.2.1). Tides take the form of progressive waves where the current is strongest at the crest and trough of the wave. Progressive tides are found in the open ocean, and along straight deep coastlines bounded by cliffs. The tide modelled here is a standing wave tidal form; such a tide exhibits the highest velocities during the mid ebb and floods. Such standing wave tides are found in areas where there are irregular coastlines, bays and shallow shelf seas, such as the Liverpool bay area in the Irish Sea, (Brown et al., 2005).

A lower tidal range in a standing wave tide would result in increases of δ/h. This, as observed above, may affect the structure of the near-wake but is less likely to affect the upstream flow as this appears to be controlled by U and D (as discussed above). In a progressive wave tide, as U is the primary influence on flow and turbulence magnitudes, the clear changes would be that the clear-water and transition tests would exhibit the greatest scouring potential (as they would exhibit larger U and possibly live-bed conditions), as opposed to the live-bed (which will no longer exhibit live-bed conditions).

3.7.4 Tidal Scour Process

The results show that the overall spatial structure of the flow and turbulence fields in each test share typical features of unidirectional flow around a cylinder as described in §1.3. Whitehouse, (2004) states that the instantaneous flow in a tidal current is essentially the same as that of a unidirectional - a reasonable conclusion. These results are consistent with his analysis; the upstream flow features a strong downflow, flow reduction and deflection, and the downstream flow exhibits flow separation, stagnation and reversal, all clearly identifiable phenomena in unidirectional flow (eg., Melville 1977, Breusers et al, 1977, Breusers and Raudkivi, 1991 and Melville and Coleman, 2000). However, the results do show that just as must be the case in different rivers and different flows, the changes of U, h and Re_D over the (tidally based) changes in flow intensity of the three tests cause changes in the detailed structure of the flow field beyond those of increases or decreases in velocity and turbulence. And unlike in long term river flow, in tidal flow these changes are cyclical, large and relatively constant. The spatial changes in the flow and turbulence fields, and the amplification of bed shear stress that have been quantified above imply three things must be considered in the study of tidal flow around the cylinder; 1) the temporal changes in the magnitude of flow and turbulence as U increases or decreases; and 2) the influence of the changing value of Re_D (due to changes in U) which has a clear affect on the structure of the wake; and 3), the influence of the changing boundary layer height on the flow and turbulence field[1]. All of the above mentioned considerations are neglected if the tidal current is approximated to a steady

---

[1] Values of δ/h in prototype shallow sea tidal boundary layers are often = 1. Therefore variation of δ/h may not be as important. However, the changing gradient of the boundary layer throughout the tide may have an effect.

reversing unidirectional current as by Jensen et al., (2006), and Margheritini et al., (2006). Simplifying the tidal cycle into a steady reversing unidirectional current also results in a failure to take into account the variation of U/U_c between clear-water and live-bed regimes whose effect on the time-development and equilibrium scour depth is well documented (§1.4.2).

With these results in mind, it can be hypothesised that the overall rate of scour in a tidal current will not follow a smooth asymptotic curve as in unidirectional currents due to the variations in U/U_c, h/D and Re_D. The fact that bed shear stress is greatest during the live-bed test will mean the most scour will be generated during the live-bed conditions in a tidal current, and due to its high flow intensity, it will occur much faster than in transitional conditions which itself would be faster than in clear-water conditions. Clearly to accurately determine tidal scour depth and time-development consideration and further understanding of the effects of time-varying flow velocity and water depth is required, particularly when it is considered that the three stage tide that the three tests in these experiments is based on is a reasonable simplification of a sinusoidal symmetrical tide - not a common phenomenon in nature.

This experimental programme was conducted to quantify the changes that occur during the various stages of variable flow representing tidal flow, as well as serving as a supplementary examination of the cylinder flow field by providing a high level of spatial detail around the cylinder including in previously less well researched areas of the flow field. However, this is only the first step in fully understanding the changes to the rate and depth of scour under tidal currents. Building on the information gleaned from these experiments, the next chapter details a set of mobile bed experiments

where the three-stage (tidally based) flow is employed and the current direction is reversed simulating alternating tidal flow conditions. Moreover, it is hoped that the results presented will provide a useful data set for the calibration of numerical models to tackle the complex 3D simulation of the cylinder flow and turbulence fields and scour.

3.8 Summary

This chapter has presented observations from the flow velocity and turbulence data recorded during the rigid bed tests around the smooth cylinder under tidally based changes in flow intensity and depth. Data was presented for the live-bed, transition and clear-water tests. Using extensive ADV measurements upstream and around the cylinder, and with PIV measurements downstream of the cylinder, the spatial characteristics of the flow field in each test have been described and compared in detail. Each test showed similar spatial characteristics upstream with the main differences in the magnitude of flow and turbulence. The differences between the test became more apparent downstream of the cylinder where the location of lateral separation and stagnation in the wake is different for each test. The following general features are common to the clear-water, live-bed and clear-water wakes: 1) a two-region flow on the centreline; 2) a lateral and downstream diminishment of cylinder influence; 3) a three-dimensional reversal of flow in the near-wake of the cylinder; and 4) a relatively quick recovery of boundary layer shear flow downstream, with some translation of lateral flow suggesting a superposition of the two flows in this region; 5) a three region downstream turbulence distribution that is broadly similar in

each test along the centreline. There are, however, some interesting and subtle differences between, in particular the transition test and the live-bed and clear-water tests: 1) the near-vertical stagnation zone observed suggests a different wake structure which is better described as a half-cylinder than that of the live-bed and clear-water tests; 2) lateral flow is positive in the reversed flow along the $y' = 0.5$ plane; 3) flow constriction is only present along the $y' = 0.75$ plane; 4) the flow recovers by $\sim 3D$ as opposed to $5D$ in the live-bed test; 5) variations in the relative strength of the flow velocities and turbulence intensity components in each test.

The aim of these experiments was a) to understand the changes on the flow field during the tidal cycle and b) increase the general understanding of the velocity and turbulence fields around the cylinder and make original additions to the available data already present in the literature. The observed variations during the tests are significant enough to suggest that the accurate prediction of scour under tidal currents will require the inclusion of time-varying flow velocity and depth. The results shed light on the complexity of the flow and turbulence fields and their variability between the tests indicating that the tidal scour process may be more complex than the unidirectional scour that is relatively well understood in the literature. The following chapter (§4) aims to understand the process and rate of scour under tidal currents and the results presented here will be used to help that assessment.

4. Time Development of Scour around the Cylinder in Variable and Reversing Currents

4.1 Introduction

One of the conclusions discussed in §3.6 indicated that the instantaneous structure of the tidally induced flow field around the monopile is broadly analogous to the unidirectional current flow field (in agreement with Whitehouse, 1998). The changes in the flow and turbulence fields between the clear-water, transition and live-bed tests quantified in §3 were not simply in magnitude of the flow and turbulence fields around the monopile, but also in their spatial structure. These differences, along with the inherently different time-development of scour that these tests will generate (as detailed in §1.4.2), will result in distinctively different scour hole time-developments and equilibrium depths for each test. A combination of the three flow regimes will occur in tidal flow which, therefore, will be inevitably more complex than those in steady unidirectional currents where flow intensity generally remains either live-bed or, more often in rivers, clear-water. The results presented in §3 suggest that there may be four main differences between unidirectional and tidal scour: 1) firstly it is unclear as to whether equilibrium scour depth will be characterised by the live-bed threshold peak, or the clear-water equilibrium (Figure 1-16b, §1.4.2), 2) the equilibrium depth may be smaller in any case due to the infilling of the scour hole when flow is reversed (that is, the deposition of previously eroded sediment back into the scour hole when the flow is reversed); 3) the time-development to equilibrium scour depth may not follow a smooth asymptotic curve as for unidirectional currents due to changes in scour rate from different flow intensities, and the reversal of flow

direction; 4) scour hole shape will not be elongated downstream; due to current reversal it will be more symmetrical in shape, (as observed by Jensen et al., 2006 and Margheritini et al., 2006).

This chapter presents results from the mobile bed tests. The tests employed variable current speed, water depths and reversing direction (herby called variable reversing currents) in order to simulate a tidal flow over 2 tidal cycles as described in §2.2. §4.2 presents the time-series development of the scour depth around the cylinder under both unidirectional steady constant depth and variable reversing currents. This section also presents the laser bed profiles of the scour hole at the end of both tests. §4.3 provides detailed discussion of the results including the time-development of scour in the tests, the scour hole shape, and the equilibrium scour depth. Using the results and the above four points of discussion mentioned above, the scour is also related to scour under tidal currents. Before the results are presented for the mobile bed tests, the following hypotheses are provided using the knowledge gained from the analysis in the previous chapter of the rigid bed tests.

4.2 Results

4.2.1 Smooth Cylinder Variable Reversing Current Test, Ultrasonic Ranging System (URS)

Figures 4-1, 4-3, 4-5 and 4-6 show the time-series change in scour depth for time-steps one to 12. The probe locations are described in Figure 2-17. In each figure the initial scour depth present at the start of the time-step is presented by the black crosses

on the solid line and the end scour depth by the red crosses on the solid line. Time-series depth readings taken at 5, 10, 15, 20 and 25 minutes presented. Due to large amounts of suspended sediment in the downstream side of the cylinder during all time-steps, only the start and end scour depth readings are presented as these are taken in still water conditions. The suspended sediment was found to reduce the accuracy of the URS likely by scattering the signal resulting in increased error in the depth reading. The Cartesian coordinate system used in the rigid bed tests (§3) is also applied here with x denoting longitudinal position (positive on the B side, see Figure 2-15 and §2.3) and y denoting lateral position (positive to the right on the 90° plane when looking towards the A side from the cylinder centre, Figure 2-15). From hereon, the x and y positions are normalised with cylinder diameter D, where $x/D = x'$ and $y/D = y'$.

In time-step one (Figure 4-1) which starts over a flat bed, scour begins and increases to the largest depth at the sides of the cylinder with some asymmetry between the 90° (2.4 cm) and 270° (3.3 cm) planes. Along the centreline on the A side scour begins only after approximately 20 minutes of flow at $x' = 0.325$ as the hole gradually expands upstream from the cylinder edge. By the end of time-step one (TS1) less scour has occurred here (0.8 cm) than at the cylinder sides with the hole only extending upstream to $x' < 0.825$. On the downstream side there is deposition of 1.9 cm of sediment at $x' = 0.325$. This deposition reduces downstream but remains above the original bed level beyond $x' = 1.325$. The rate of scour increases dramatically during TS2 remaining the greatest on the 90° and 270° planes (with the greatest depth along the 90° plane of 6.8 cm). The dependence of the rate of scour on x' is different along both planes but particularly so on the 270° plane where the bed level is observed

to increase above the original flat bed at $x' = 1.325$. During this time-step rippling was observed both upstream, downstream and around the monopile and these ripples remained throughout the rest of the test (i.e., up to the end of one complete 'tidal' cycle, Figure 4-2). Along the centreline scour depth is greatest on the downstream 'B' side where it extends to $x' \approx 0.825$ and achieves a final maximum depth of 5.2 cm. There is only a slight reduction in depth at $x' \approx 0.825$ and no change at $x' = 1.325$. On the upstream 'A' side the scour depth increases steadily to a maximum of 3.9 cm and remains confined to $x' < 0.825$. During TS3 the changes in scour depth are very small.
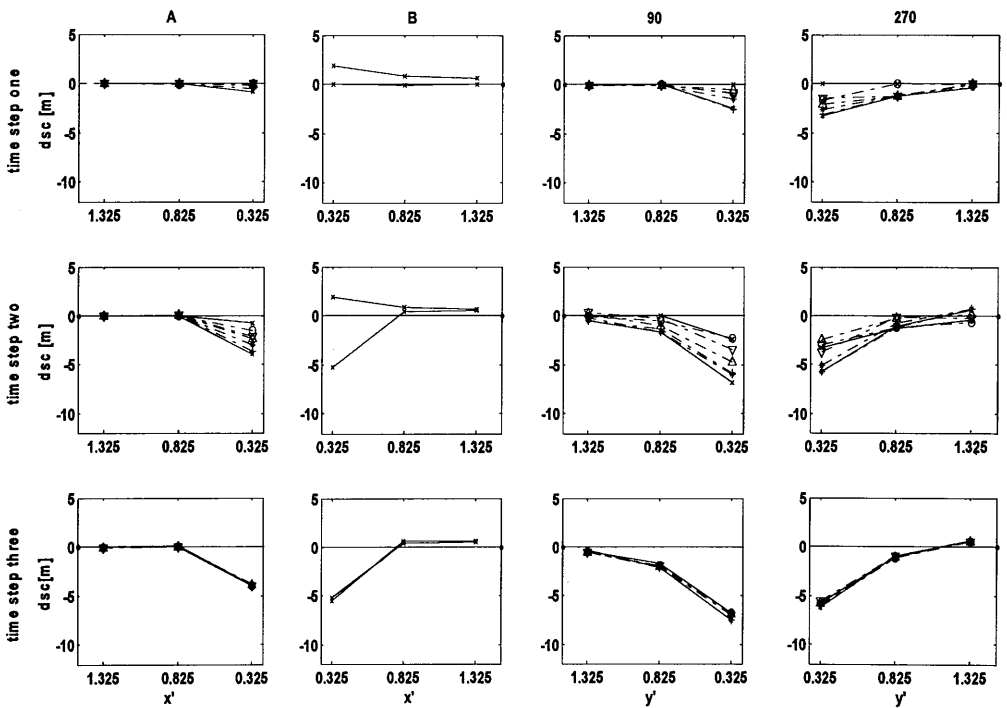
Figure 4-1. URS time series scour development between time steps 1 - 3. Time-series depth readings at 5, 10, 15, 20 and 25 minutes are represented by the circles, down-triangles, up-triangles, stars, and plus signs respectively on solid blue lines.
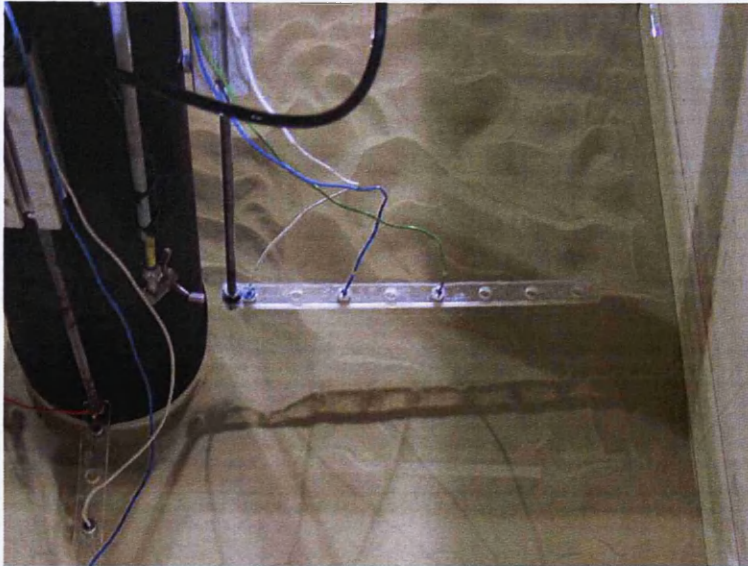
Figure 4-2. Rippling of the bed after time-step two.

Figure 4-3 shows TS4-6 in which the current direction is reversed (negative); here the A and B side of the centreline are downstream and upstream of the monopile respectively. During TS4 there is essentially no change in scour depth along centreline. As both TS3 and 4 are clear-water time-steps where the flow is slower ($U/U_c = 0.54$) than in the live-bed and transition time-steps, this suggests that the lack of scour in these cases is due to this weak flow state. The largest changes in scour depth in the half-cycle occur during TS5. On the (now downstream) A side there is a significant increase in scour depth (8 cm at the end of TS5), the scour hole now extends beyond $x' = 1.325$, and the gradient of the scour hole slope is constant between the data points (shallower than in TS3). On the (upstream) B side there is a delay in the continuation of scour particularly at $x' = 0.325$ where after five minutes the scour depth has decreased by ≈ 0.5 cm (Figure 4-4), before increasing to a maximum of 7.5 by the end of the time-step. This decrease in scour results from infilling of sediment back into the scour hole due to the new flow direction; such infilling did not occur significantly during TS4, evidently due to the weak flow

intensity. At $x' = 1.325$ on the B centreline there is steady deposition throughout the time-step resulting in an increase in bed level to 1.8 cm above the original flat bed. It appears that the reversed bed morphology encountered by the new flow direction causes a depositional zone upstream of the monopile which is not present in unidirectional current flow. The gradient of the slope between $x' = 1.325$ and 0.825 increases steadily, while the gradient between $x' = 0.825$ and 0.325 remains relatively constant. Melville and Coleman, (2000) suggest that the steepness of the scour hole will continue to increase until the angle of repose is achieved, indicating that the slope between $x' = 0.825$ and 0.325 is at or near the natural angle of repose for the sediment.

While the now upstream slope is steepened, the steeper sloped downstream side is eroded, becomes shallower, and its length downstream increases. This continues into TS6. This change in scour hole morphology indicates that the hole adjusts to a unidirectional asymmetrical shape in each half-cycle, which is in agreement with the observations of Margheritini et al., (2006). Along the 90 and 270° planes scour depth continues to increase with a constant gradient along each plane both of which are steeper than the gradient on the (upstream) B side of the centreline. The rate of scour is similar along both planes with an approximately 30 % of the total scour increase for the time step occurring between the 5th and 10th minute of the time-step. After this initial high rate of scour the rate reduces. A similar observation can be made for the (upstream) B side of the centreline but not the (downstream) A side. The variable rate of scour during this time-step may be a consequence of several things; the natural asymptotic time development of scour but also the affect of the presence of a scour hole at the start of the time-step, and the initial infilling of that scour hole before the continuation of scour. At the end of the half-cycle (the end of TS6) scour depth is

similar between each opposing measurement plane with the greatest depth recorded along the lateral planes (being 9.6 and 9.1 cm on the 90 and 270 planes as opposed to 8.2 and 7.7 cm on the A and B sides of the centreline respectively).
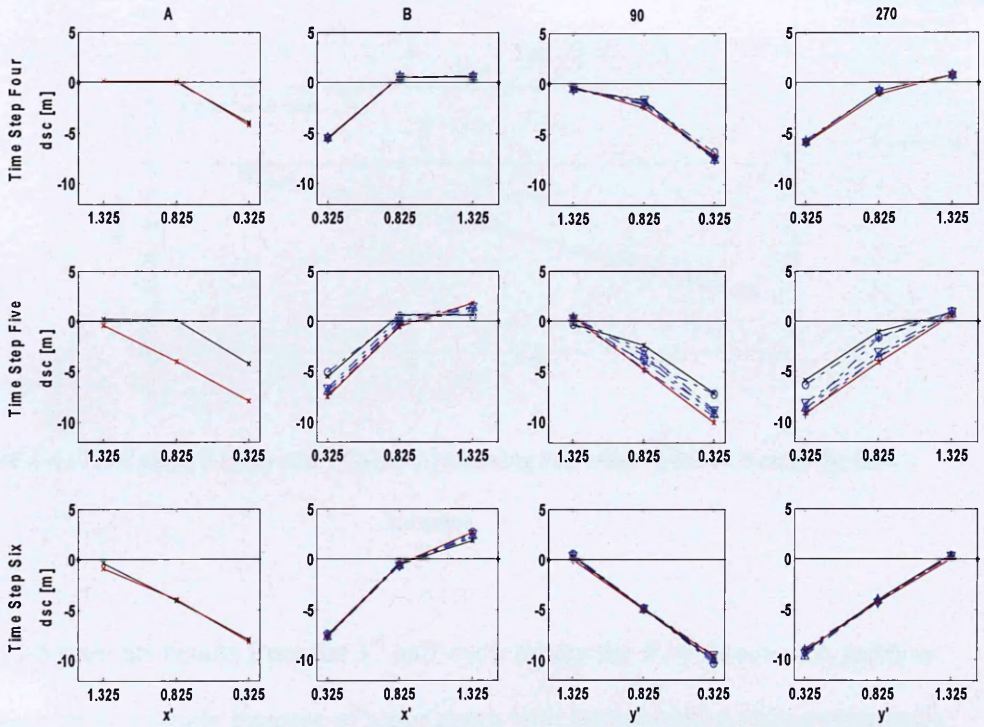
Figure 4-3. URS time series scour development between time steps four to six. Symbols as in Figure 4-1.
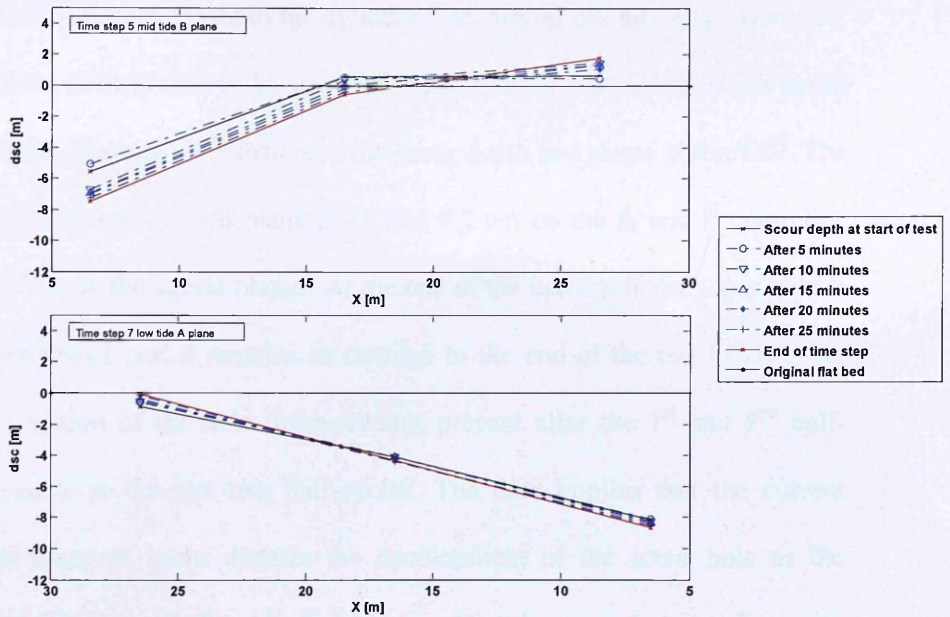
Figure 4-4. Time steps 5 (top) and 7 (bottom) showing the delay in scour during the first 5 minutes.

Figure 4-5 presents results from the 3rd half-cycle where the flow direction is positive. All planes show a steady increase of scour depth with the centreline planes eventually recording a similar depth to the lateral planes. The deposition of sediment observed above in the negative flow TS4-6 on the (then upstream) B centreline plane (Figure 4-3) is now steadily removed as the scour hole deepens and widens. This removal is greatest in TS7 and 8 (transition and live-bed conditions); by the end of the clear-water in TS9 the sediment level at $x' = 1.325$ on the (downstream) B side of the centreline has moved below the original bed level meaning that either deposition in this area is no longer greater than the rate of scour, or that deposition has ceased all together. The B side slope of the centreline also becomes progressively smoother and shallower throughout times steps seven to nine. Along the (upstream) A side of the centreline the slope of the scour hole remains approximately constant during TS7, but in TS8 there is a steepening of the slope between $x' = 0.325$ and 0.825 indicating a

slightly greater rate of scour closer to the cylinder than further out laterally. Along the lateral planes there is little change in slope and only a small increase in scour depth mainly during TS8. There is little change to the scour depth and shape in the TS9. The maximum depth achieved at each plane is 10 and 9.2 cm on the A and B centreline planes, and 10.7 cm on the lateral planes. At the end of the half cycle the scour hole is effectively symmetrical, and it remains so through to the end of the test (TS12); the asymmetry (elongation of the hole downstream), present after the 1st and 2nd half-cycle is not present in the last two half-cycles. The data implies that the current direction at the onset of scour dictates the development of the scour hole as the reversed flow of the second half-cycle first has to adjust the scour hole to align with the new flow direction before continuing to increase the depth of the scour hole (though this is based on one data set, and as such requires further investigation). However, after one full cycle the scour hole has developed enough depth and steep enough slope gradients for it to retain relative symmetry regardless of flow direction. This is contrary to the observations of Margheritini et al., (2006) which show that the scour hole continues to adjust its morphology in response to a reverse in current direction during the 3rd and 4th half cycles. The current experiments include the transition and clear-water tests which both generate far less scour than the live-bed test meaning that the scouring potential of the flow in the half cycle is less than it is for Margheritini et al., (2006) and so any tangible change in scour hole morphology in response to the new flow direction will take longer. However, some of the experiments conducted by Margheritini et al., (2006), (i.e., tests 2.10 - 2.18) have similar parameters (with $U = 0.3$, $h = 0.1 - 0.29$, $d_{50} = 0.0015$ and $D = 0.2$ and half cycle length of 30 mins) to the current tests (the live-bed), which suggests that the incorporation of tidally based variations in flow velocity/depth and direction the

present experiments plays a more active role in keeping the hole symmetrical, possibly by facilitating infilling.
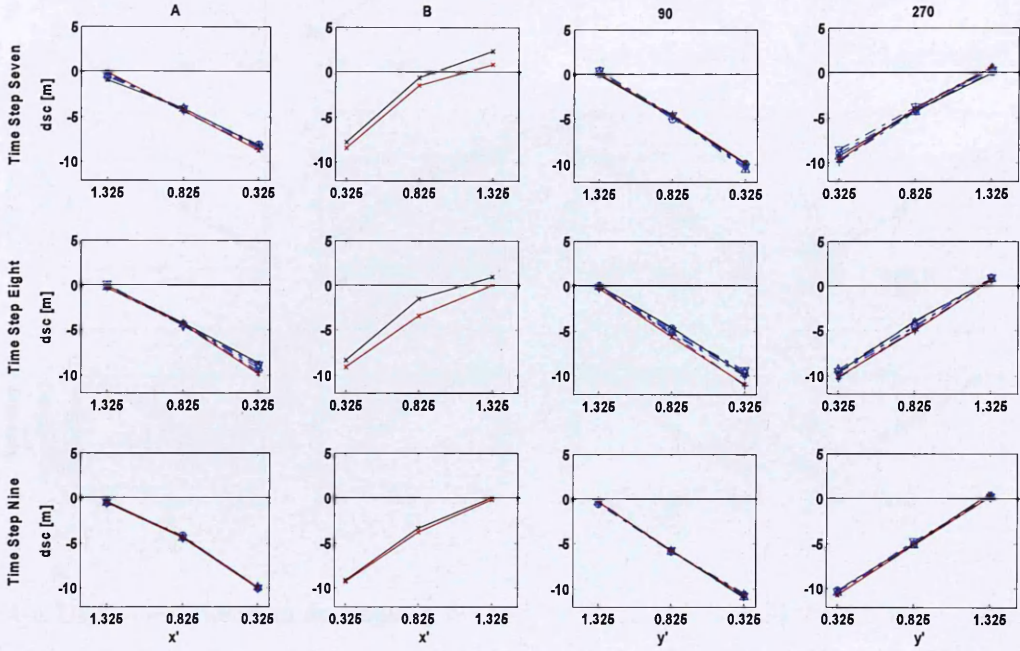
Figure 4-5. URS time series scour development between time steps seven to nine. Symbols as in Figure 4-1.

In Figure 4-6 the maximum scour depth does not significantly change during TS10-12, only increasing on the (upstream) B side by approximately 1 cm resulting in a maximum scour depth of 10.4 cm there. On the A centreline plane the maximum depth is 9.9 cm (essentially unchanged as the URS error is +/- 0.2 mm), 10.1 cm on the 90° plane and 11.1 cm on the 270° degree plane.
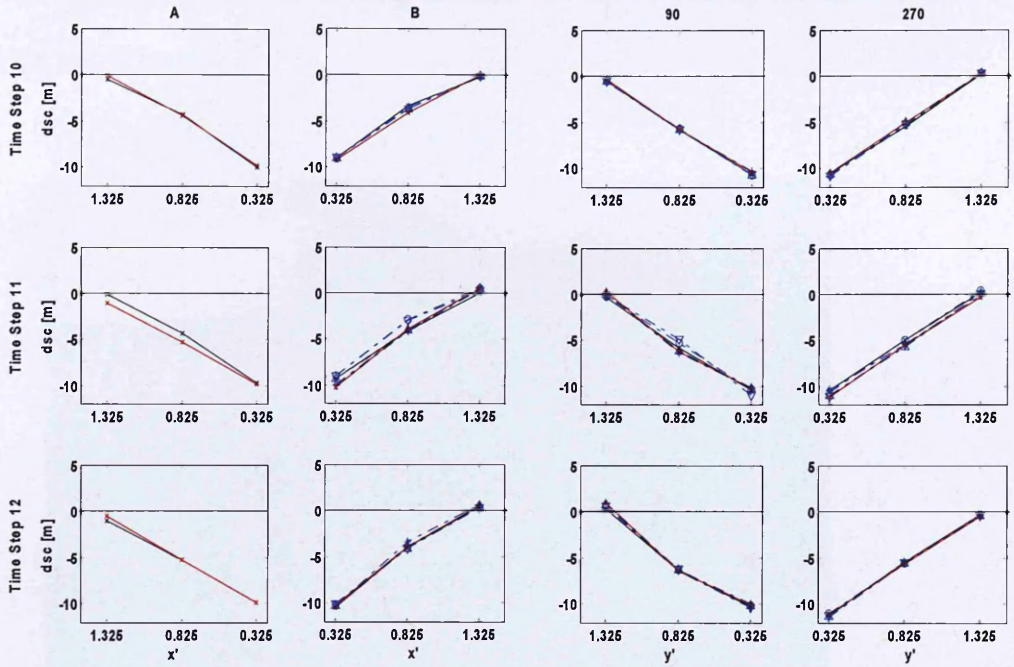
Figure 4-6. URS time series scour development between TS10-12. Symbols as in Figure 4-1.

4.2.2 End of Variable Reversing Current Test Laser Bed Profiling

At the end of the test the flume was drained to allow the bed around the cylinder to be profiled using the laser distance measurer, (Figure 4-7). Figure 4-8 shows the unidirectional scour hole bed profile after 2.7 hours of steady current from right to left. The scour hole is asymmetrical with a depositional mound on the downstream side. This scour hole shape is commonly observed in the literature, for example Hoffmans and Verheij, (1997) and Melville and Coleman, (2000). Figure 4-9 shows the laser bed profile for the variable reversing current taken at the end of the test. Deposition is present on both sides of the scour hole and over a larger area than the smaller and more defined depositional mound of the unidirectional current scour hole in Figure 4-8. The gap in data on either side of the scour hole in both figures is due to

the cross boom of the scaffold holding the laser profiler preventing the laser from seeing the bed, (Figure 4-7).
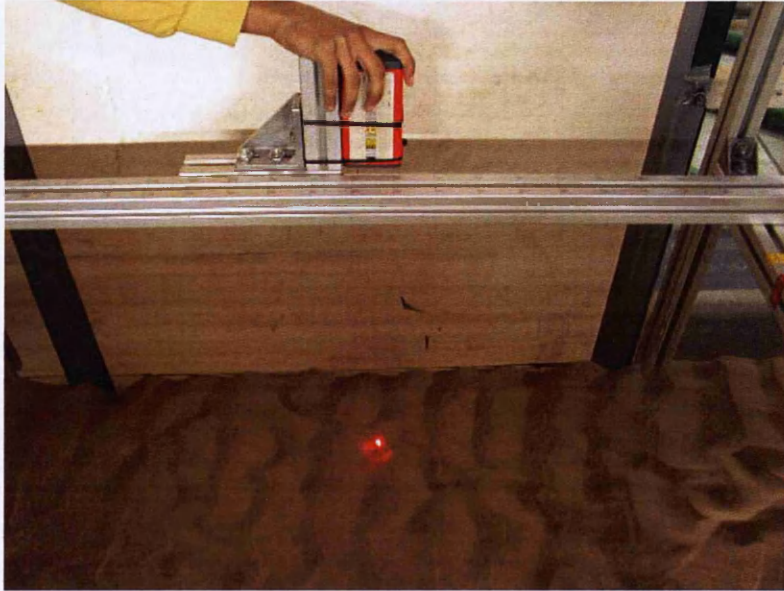
Figure 4-7. Image of the laser bed profiler showing cross boom (far right) which prevents measurement below its location.
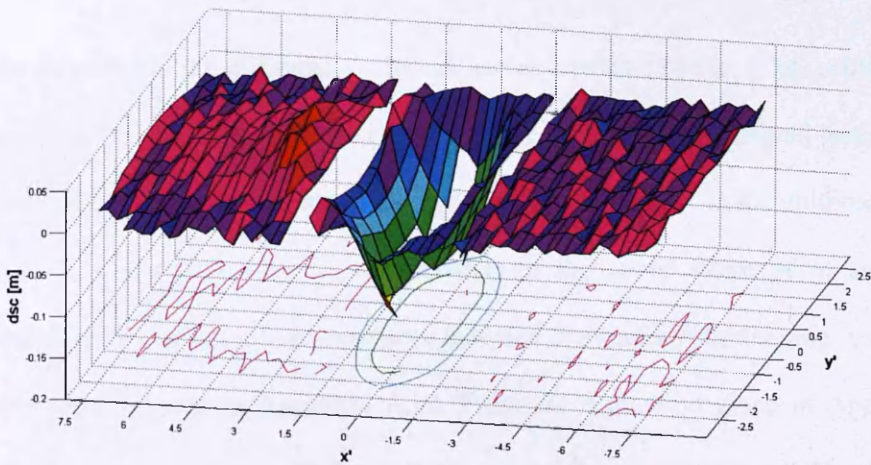
Figure 4-8. End of unidirectional test bed profile where $u = 0.31$ is from right to left, $h = 0.25$ and $u/U_c = 1.28$.
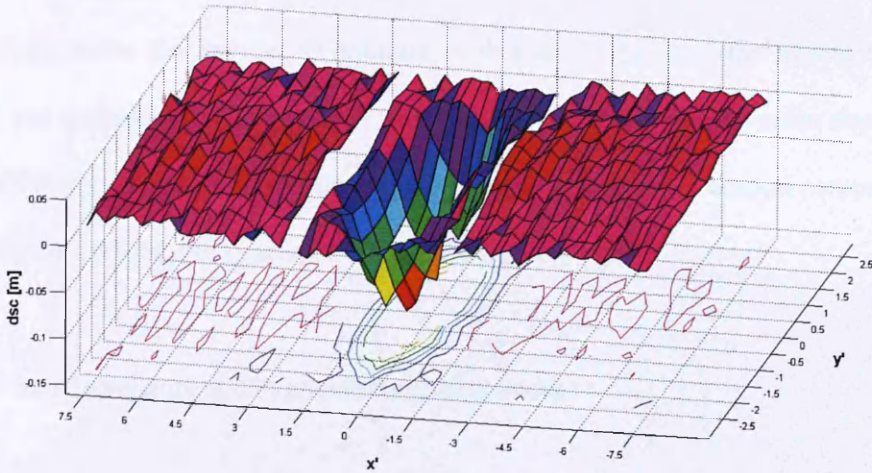
Figure 4-9. End of variable reversing test bed profile where $u = 0.31$ is from right to left, $h = 0.2$ and $u/U_c = 1.24$.

4.3 Discussion

4.3.1 Smooth Cylinder Unidirectional Current Test URS

In order to ascertain the differences between variable reversing (i.e. tidal) scour time development and unidirectional scour, a unidirectional test was performed lasting the equivalent of one cycle (2.7 hours) at the live-bed test conditions. In the unidirectional test $U = 0.31$ and $h = 0.25$. An explanation of the raised value of h, and the consequential limits of any comparison between the unidirectional and variable reversing tests is given in Appendix A.12. From the discussion given in Appendix A.12, the increase in scour depth due to the increased flow depth of $h = 0.25$ m in the unidirectional test is < 10% greater than it would be if $h = 0.2$ m. Any comparison between the unidirectional and variable reversing test is, therefore, limited to

differences in scour depth that are greater than 10%. The unidirectional test was performed under the live-bed conditions as this would produce the fastest rate of scour, and according to Escarameia, (1998), may produce the greatest scour depth if it were tidal. The time series URS data for the unidirectional test is used in comparative analysis with the tidal time series URS data below.

4.3.2 Time-Development of Variable Reversing Scour

To provide a comparison of variable reversing scour development with unidirectional scour development, the transition and clear-water time development curves are calculated using the method described in Melville and Chiew, (1999). The method provides an estimation of the time for scour to reach equilibrium in days ($t_{e(days)}$) by using Equation 4-1, and is only suitable for clear-water scour conditions. $t_{e(days)}$ is defined as the time at when scour depth increases by < 5% in 24 hours.

$$t_{e(days)} = 30.89 \frac{D}{U}(\frac{U}{U_c} - 0.4)(\frac{h}{D})^{0.25} \quad \text{for} \quad h/D \leq 6 \qquad (4\text{-}1)$$

Then the scour depth d_s at a particular time t is given by Equation 4-2

$$d_s = \exp\{-0.03 \left|\frac{U_c}{U} ln\left(\frac{t}{t_e}\right)\right|^{1.6}\} d_{sc} \qquad (4\text{-}2)$$

For the live-bed test, the method described by Sumer et al., (1992a) is used to predict time development as it is suitable for live-bed conditions. From data collected over an extensive series of tests, Sumer et al., (1992a) define the time-scale of scour using Equation 4-3.

$$d_{sc} = d_{sc}(1 - \exp(-t/t_e)) \qquad (4\text{-}3)$$

where t is determined from the experiments as:

$$t_e = \frac{D^2}{(g(s-1)d^3)^{1/2}} \frac{1}{2000} \frac{h}{D} \left(\frac{u_*^2}{g(s-1)d}\right)^{-2.2} \qquad (4\text{-}4)$$

In these experiments it is not clear that equilibrium depth d_{sc} is reached at the end of the test so it is predicted using equations given in the literature. The choice of equation requires some thought as the literature is host to a large number of d_{sc} prediction equations (e.g., §1.5). Some of the more commonly used ones are reviewed by Johnson, (1995) who compared selected equations against field data. Using the conclusions arrived at in that study, the most suitable equation for determining equilibrium scour depth in the transition, live-bed and clear-water conditions of these tests appears to be that of the Breusers et al, (1977); Equation (4-5).

$$d_{sc} = Df[2\tanh(h/D)] \qquad (4\text{-}5)$$

where,

$$f = 0, \text{ for } U/U_c \geq 0.5 \qquad (4\text{-}5\text{a})$$

$$f = 2\,U/U_c - 1, \text{ for } 0.5 < U/U_c \leq 1 \qquad (4\text{-}5\text{b})$$

$$f = 1, \text{ for } U/U_c > 1 \qquad (4\text{-}5\text{c})$$

Table 4-1 presents the predicted equilibrium scour depth for each time-step.

time step	dsc [m]	equation
Transition	0.18	4-5c
Live-bed	0.23	4-5c
Clear-water	0.03	4-5b

Table 4-1. Predicted scour depths for the transition, live-bed and clear-water

The time development of scour depth under each time-step is plotted in Figure 4-10. Melville and Chiew, (1999) and Summer et al., (1992a) do not specify the location at which the scour prediction applies (assumed to be the maximum depth recorded at any position around the monopile); here it is compared with the URS measurement nearest to the monopile on each radial plane (probes 1, 4, 7 and 12, Figure 2-17). The time development of the unidirectional scour depth at probe one is also plotted on Figure 4-10.
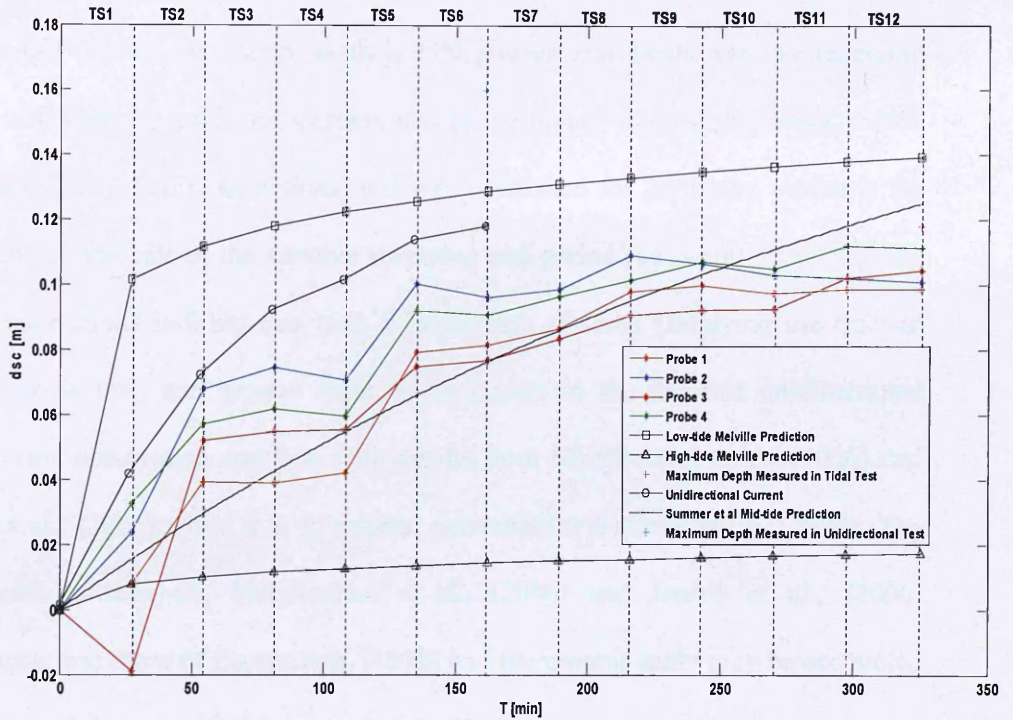
Figure 4-10. Time development of scour at URS probes 1, 4, 7 and 10 (Figure 2-17) with the Melville and Chiew, (1999) curve for the low and clear-water prediction and the Sumer et al., (1992a). The rate of scour is fastest for the live-bed, followed by the transition and the clear-water. Note the less-smooth development of scour recorded by the URS probes in comparison to all prediction curves.

The first observations from Figure 4-10 is that the scour depth recorded by each probe is not representative of the maximum scour depth at that particular time, as this occurs closer to the monopile than the location of the probes. The maximum scour depth recorded at the end of the variable reversing test was 0.118 m by the laser profiler at $x' = -0.75$ and $y' = -0.5$ (magenta cross, Figure 4-10). This is well below the predicted equilibrium depth of the 0.18 and 0.23 m for the transition and live-bed conditions respectively (Table 4-2), but well in excess of the clear-water prediction (0.03 m). The

actual recorded maximum scour depth for the unidirectional test (16 cm) at $x' = -0.75$ and $y' = -0.5$ (cyan cross, Figure 4-10) is 25% greater than for the variable reversing current test, with the predicted increase due to the higher water depth being < 10% (Appendix A.12). The unidirectional test was conducted for 2.7 hours, which is the equivalent of one half of the variable reversing test period (i.e., a full 'tidal' cycle). These observations indicate that both a faster rate of scour (implying the time to equilibrium is less) and greater scour depth occurs in the live-bed unidirectional current. This observation conflicts with results from Margheritini et al., (2006) and Jensen et al., (2006) while it is in general agreement with Escarameia, (1998). The differences between the Margheritini et al., (2006) and Jensen et al., (2006) experiments and those of Escarameia, (1998) and the present study may be accounted for with consideration of the nature of the 'tidal' simulation. These experiments attempt to employ a sinusoidal tide and Escarameia, (1998) also accounts for the sinusoidal changes in depth and velocity, though not concurrently. Margheritini et al., (2006) and Jensen et al., (2006) employ a square tide at the live-bed maximum flow with no changes in depth and velocity and as live-bed scour has a significantly shorter t_e than clear-water their scour hole develops much faster than the data presented above (for example, equilibrium is stated to be achieved in the first half-cycle in some of the tests in Margheritini et al., 2006).

The clear-water time development prediction greatly underestimates the overall rate of variable reversing current induced scour. The transition curve appears to overestimate the scour rate at the start before slowing to a more comparable rate until towards the end of the second cycle ($t \geq 162$) where the variable reversing scour rate reduces further, (though the depth remains significantly lower - likely a combination of the

probe location, and the slower rate of scour). It is clear that most of the scour takes place during the first cycle (TS1 - 6, Figure 4-10 and Table 4-1). The live-bed curve appears to follow the tidal time development during the first cycle quite well, though the individual live-bed stages show a greater scour rate than the theoretical prediction (TS1 - 6, Figure 4-10; Table 4-1). During the second cycle, the variable reversing scour rate reduces dramatically and the live-bed curve no longer describes it well. The slower rate for variable reversing scour during the second cycle than the transition and live-bed curves also indicates that the equilibrium depth may be less, assuming the relationship is asymptotic. Figure 4-11 shows an exponential curve fitted to the variable reversing scour data in Figure 4-10. The maximum depth achieved according to the curve is ~ 0.101 m. Scour depth according to the curve at the end of the 2nd half cycle has increased by 26% from the depth at the end of the 1st half-cycle (from 0.064 m to 0.087 m). The percentage increase between the 2nd and 3rd half-cycle reduces to 9% (from 0.087 m to 0.096 m). The percentage increase in scour depth in the 4th half-cycle is reduce to 5% (from 0.096 m to 0.101 m). Equilibrium as defined by Melville and Chiew, (1999) is achieved when there is a < 5% increase in scour depth over 24 hours. Though this is not achieved by the end of the test, the reduction in scour rate indicated by the curve implies, assuming it continues to reduce exponentially, that equilibrium scour depth is lower than the transition and live-bed predictions. variable reversing scour equilibrium will be discussed further in §4.3.4.
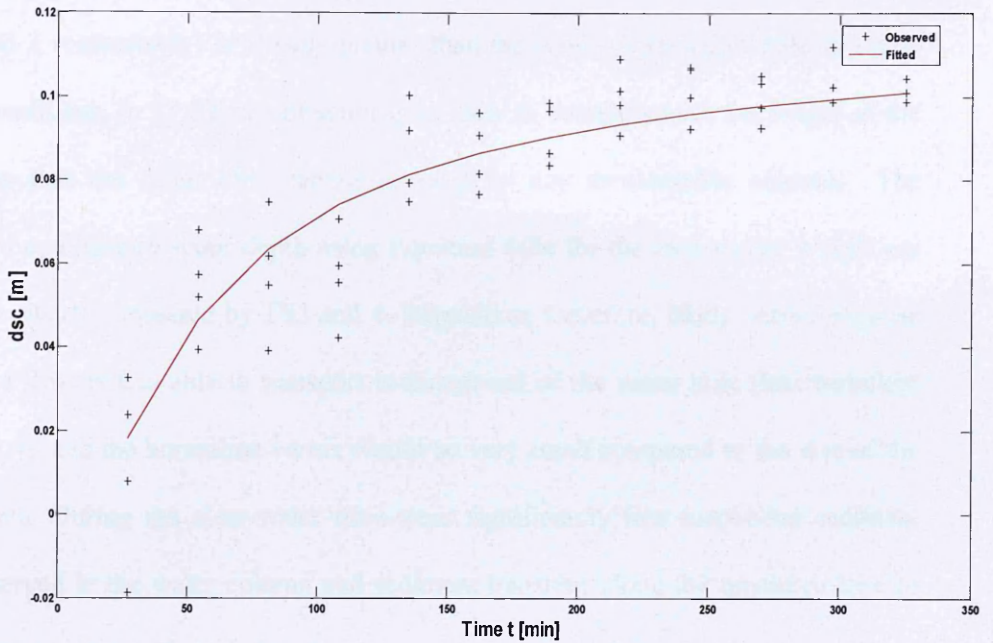
Figure 4-11. Exponential curve fitted to the data from probes 1, 4, 7 and 9 (top).

From Figure 4-10, the variable reversing scour time-development is not as smooth as the predicted curves or the unidirectional curve. There are significant changes in the rate of each variable reversing stage with time. This is to be expected due to the changes in flow properties in each time step and flow direction as hypothesised in §4-1 and observed in §3. In the first half-cycle the scour hole develops the most under the live-bed time-step conditions. During the following clear-water time-step, the scour depth continues to increase a small amount as the flow direction is still orientated with the previous time-step. However, when the tide reverses, the clear-water TS4 does not cause any further scour to occur. Clearly the flow intensity of 0.54 is not high enough to affect the scour hole in both TS3 and TS4. In itself, the clear-water flow intensity should be large enough to generate scour (as $u/U_c > 0.5$, Hoffmans and Verheij, 1997), leaving two possible reasons that no scour occurs during the clear-water TS3

4-20

and 4; 1) the scour hole generated by the previous transition and live-bed time-steps (TS1 and 2 respectively) is already greater than the scour depth achievable in clear-water conditions, or 2) the rate of scour is so slow in comparison to the length of the time-step that the scour hole cannot develop by any measureable amount. The predicted equilibrium scour depth using Equation 4-5c for the clear-water is 0.03 cm which is clearly surpassed by TS3 and 4. Deposition, therefore, likely occurs because the wake flow is less able to transport sediment out of the scour hole (less turbulent wake §3.4), and the horseshoe vortex would be very small compared to the size of the scour hole. During the clear-water time-steps significantly less suspended sediment was observed in the water column and sediment transport along the upstream face of the cylinder was significantly lower.

While there is essentially no change to the depth and orientation of the scour hole during TS4, once TS5 begins, the scour hole's orientation is first adjusted to the new flow direction (the upstream side becomes deeper and the downstream side due to the low intensity of the wake is subject to deposition closer to the downstream side of the monopile) before the depth is increased, (Figure 4-4). Deposition does not occur during the transition reversal in TS7 likely because the flow field is turbulent and energetic enough to keep sediment in suspension for longer allowing it to be transported out of the hole. The adjustment of the scour hole to the new flow direction occurs relatively quickly within the time-step, (Figure 4-4). There is no change in scour depth after 5 minutes at $x' = 0.375$ and 0.875, though there is an increase of $\sim$ 0.5 cm at $x' = 1.325$. Further tests would be required to shed light on whether the smaller delay in scour depth increase during TS7 is due to flow intensity or due to the fact that the scour hole is more developed at this point.

Figure 4-12 shows the time development of variable reversing scour at each of the probes closest to the cylinder along the centreline and lateral plane. It is often stated that the scour depth will reduce during a reverse flow period (for example, Hoffmans and Verheij, 1997, Escarameia, 1998, Jensen et al., 2006 and Margheritini et al., 2006), however, the observations in Figure 4-12 show that the scour depth along the centreline both up and downstream (yellow and red line respectively) increases in all time steps with the exception of TS1 for probe 7, and TS10 for probe 1. The scour depth along the lateral planes at 90° and 270° of the monopile (blue and green lines respectively) does decrease when the flow reverses in both clear-water reversals (TS4 and 9) and during transition reversal (TS10). Reduction on the 90° plane continues throughout TS9-12. Infilling does appear to have an effect on the time development of scour by delaying the onset of scour close to the cylinder. However, it is only a minor one. The changes in the flow depth and flow intensity appear to be the main influencing factors on the time development of variable reversing scour with each different time step exhibiting different rates of scour.
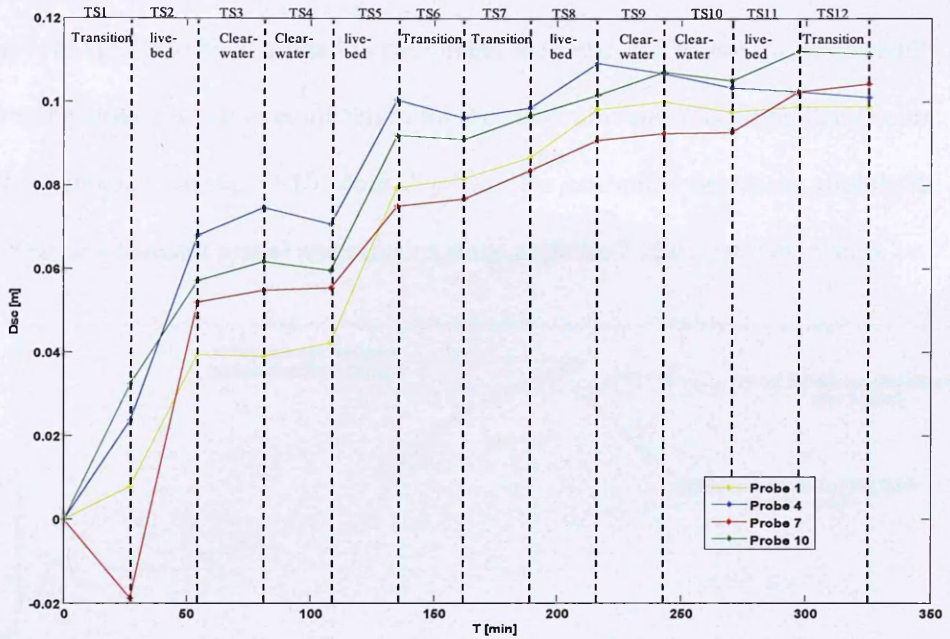
Figure 4-12. Variable reversing scour time-development for the closest probes to the

cylinder at each radial position.

From Figure 4-13, which shows the variable reversing test time series scour development plotted with the unidirectional test scour development, the cause of the slower rate and shallower depth of scour in the variable current is clearly associated with the slower rates of scour in the transition and virtually non-existent scour in the clear-water time-steps. In the first cycle, the most scouring occurs during the live-bed TS2 and 5 ($\approx$ 86% of the total scour that occurs in the cycle). The remaining contribution to scour is from the transition TS1 ($\approx$ 10 %). The transition TS6 and clear-water TS3 and 4 cause very little additional scour. On the lateral planes during TS4 and 6 there is a small amount of infilling, though scour continues to increase along the centreline plane. Clearly it is the variation of U/U_c rather than infilling due to flow reversal that is the main reason for the slower rate of scour in the first cycle.

4-23

Infilling does appear to have a small impact in the second cycle, where the scour depth appears to be close enough to equilibrium for the small amount of infilling that occurs to make an impact. During TS10 scour depth on the centreline decreases slightly at probe 1 (the downstream plane) and remains static at probe 7 (the upstream plane).

×	**1st, 3rd, 5th, 7th, 9th and 11th time steps of the variable reversing current**
×	**2nd, 4th, 6th, 8th, 10th and 12th time steps of the variable reversing current**
•	**Unidirectional scour depth time series**
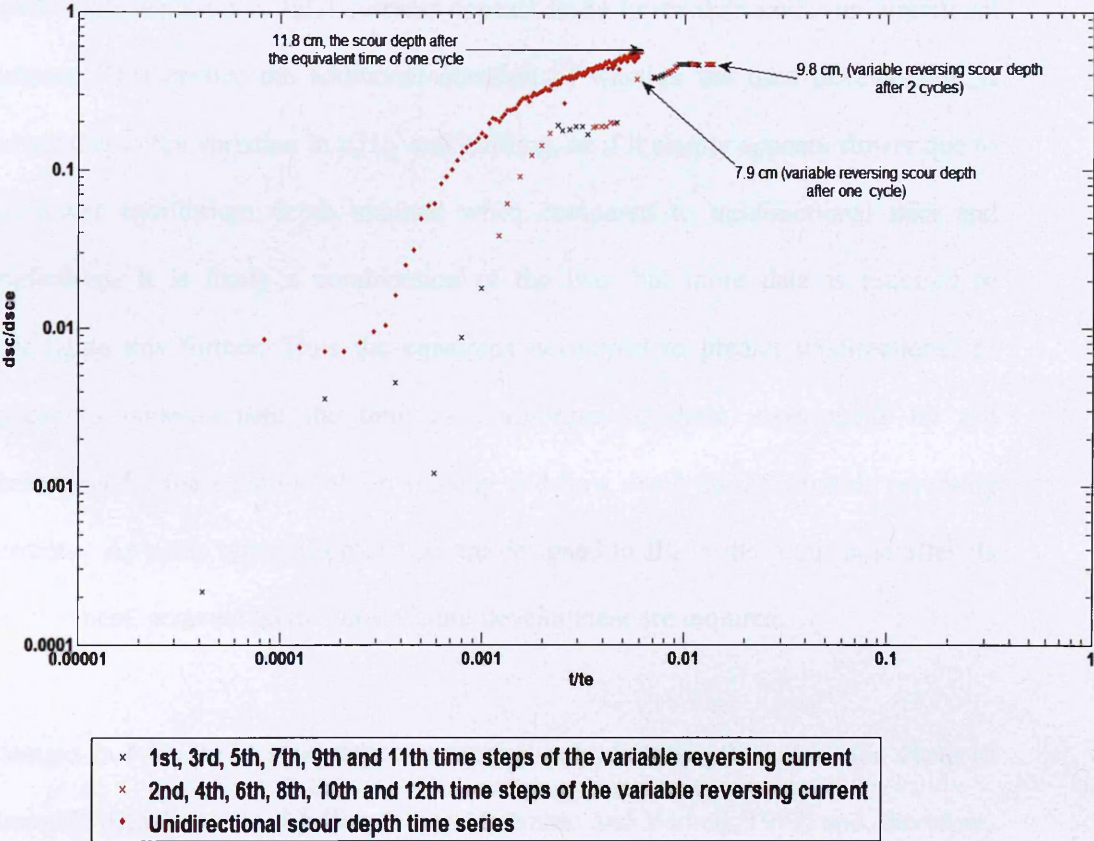
Figure 4-13. Time series plots of scour development against time. Recorded scour depth d_{sc} is normalised with the predicted equilibrium scour depth dsc_e (as calculated using Equation 4-1) and time t is normalised with time to equilibrium t_e (as calculated using Equation 4-3).

Figures 4-10 and 4-13 show the overall rate of scour is slower under the variable reversing currents than it is under unidirectional currents. The reason for this appears to be the result of the combination of the different scour rates during each time-step,

4-24

rather than infilling of scour under the reversed currents (a reason often given, e.g.; Hoffmans and Verheij, 1997 and Escarameia, 1998). The main parameter influencing this is u/U_c, with scour occurring the most in the live-bed time-steps where $u/U_c = 1.24$, with the clear-water $u/U_c = 0.54$ causing very little scour. However, there is some uncertainty in this conclusion because, as will be discussed in §4.3.4, the equilibrium depth under tidal currents appears to be lower than under unidirectional currents. This creates the additional question of whether the time development is slower due to the variation in u/U_c and infilling, or if it simply appears slower due to the lower equilibrium depth attained when compared to unidirectional data and predictions. It is likely a combination of the two, but more data is required to investigate this further. Thus the equations developed to predict unidirectional t_e appear to underestimate the time to equilibrium in these experiments by not accounting for the variation of the velocity and flow depth during variable reversing currents. As some types of protection are designed to fill in the scour hole after its development, accurate predictions of time-development are required.

Changes in h/D are less important as scour is only directly affected by the depth to monopile diameter ratio if $h/D < 1$ (e.g. Hoffmans and Verheij, 1997) and, therefore, only becomes a factor in the transition time-step where it may reduce slightly the amount of scour that occurs as the surface roller (see §1.3.7) interacts with the downflow causing it to weaken. In general, however, u/U_c is the more important parameter; scour rate during the transition time-step (when $U/U_c \approx 1$) remains significantly higher than during the clear-water as (when $u/U_c < 1$).

4.3.3 The Variable Reversing Current Scour Hole Shape

Figure 4-14 shows the centreline end of test depth cross sections for the unidirectional current (red, flow from right to left) and variable reversing current (blue). The unidirectional scour hole extends to between approximately 2 - 2.5D downstream and approximately 2D upstream. There is also a region of rippling which remains below the original bed level which increases the upstream extent of the scour hole to < 5D. Upstream of this point the ripples become wider and larger and rise above the original bed level. The variable reversing scour hole is more symmetrical than the unidirectional one and is thinner in width extending from 2 - 2.5D on either side of the monopile. Depositional mounds are present on both sides of the hole and appear to extend beyond the measurement field. Both are wider but slightly smaller in height than the unidirectional downstream mound. The scour hole shape observed in these results is in general agreement with Margheritini et al., (2006) and Jensen et al., (2006).
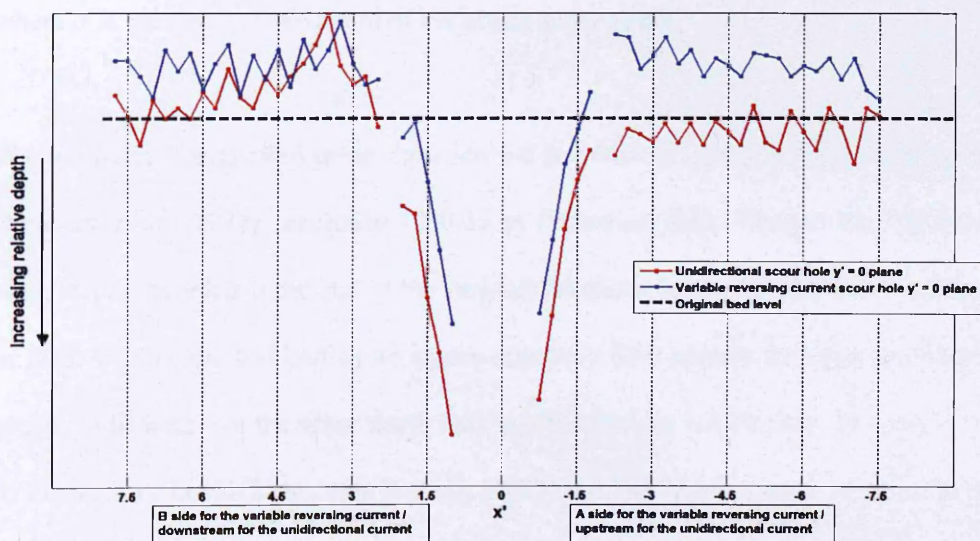
Figure 4-14. Centreline depth comparisons between the unidirectional (red) and variable reversing test (blue).

4.3.4 Equilibrium Scour Depth under Variable Reversing Currents

It is not in the scope of this research to investigate equilibrium scour depth. From the scour test data presented above (Figure 4-11 and 4-13) it is not clear whether equilibrium is reached by the end of the test. However, as mentioned in §4.3.2 there is evidence that indicates equilibrium scour depth under the variable reversing current test is lower than it will be under the unidirectional test and predictions. The variable reversing scour results presented in Jensen, (2006) indicate that under a square tide the scour depth reaches the same equilibrium depth as unidirectional scour, and along with Equation 1-33, can be represented by the following equation proposed by Sumer and Fredsoe, (2002a).

$$d_{sc}/D = 1.3 \qquad \text{where } \sigma_{d_{sc}/D} = 0.7 \qquad (4\text{-}6)$$

where σ is the standard deviation of the actual scour depth.

The scour depth suggested using Equation 4-6 is ≈ 0.26 m which is very similar to the Breusers et al, (1977) prediction of 0.25 m (Equation 4-5). Though the maximum scour depth recorded at the end of the variable reversing test (11.8 cm) falls well short of these depths, the last half-cycle shows relatively little change in scour depth at all probes indicating that the scour depth may be approaching equilibrium. In comparison to Figure 2.12 in Hoffmans and Verheij, (1997) the time development of scour in the second cycle could be described as in the stabilisation stage (that is the rate of scour is decreasing with time and the depth is nearing equilibrium). Furthermore, the

extrapolation of an exponential curve fitted to the data in Figure 4-11 shows that the equilibrium scour depth is < 0.12m Collectively these observations indicate that the equilibrium depth may be lower under the sinusoidal tide, than a square tide or unidirectional current. Consequently Equation 4-6 does not describe the variable reversing scour equilibrium depth well. From the data, the reason for a lower equilibrium appears to be the significant slowing of the rate of scour in the second half cycle, and consequent increase of the relative affect of infilling of the scour hole when the current reverses; infilling becomes more important because there is less scour. The conclusion is in agreement with Escarameia, (1998), (who employed sinusoidal-type tides) but in disagreement with Jensen et al., (2006) and Margheritini et al., (2006), (both of which employ square tides). The fact that equilibrium scour depth is less in variable reversing currents than unidirectional currents is of some interest as it would reduce the amount, and therefore cost of any scour protection that may be required. Prediction of scour at offshore structures using unidirectional current equations, as is the current norm, may be overestimating the equilibrium depth and therefore the mitigation required. Furthermore, the conservative design limits for such offshore structures. However, this conclusion is based on limited data that has not reached equilibrium and requires further investigation to confirm.

4.5 Summary

This chapter has presented results of an experiment designed to address the development of scour under variable reversing currents. The scaled tide was divided into half-cycles which each consisted of 3 time-steps; a transition, live-bed and clear-

water. Each half-cycle followed on from the previous but current flow was in the opposite direction. The test ran for a total of four half-cycles.

In the first half-cycle the development of scour occurs in the same manner as for unidirectional scour with the scour hole adopting an elongated shape with deposition occurring downstream. The rate of scour was found to change according to flow intensity with the most scour developing during the live-bed condition and the least during the clear-water (this remained the case in all half-cycles). The 2nd half-cycle shows scour to continue to deepen; however, there was deposition on the downstream side of the scour hole while the depositional mound on the upstream side remained. The second half-cycle shows an increase and widening of the downstream side but not to the same depth or width as the downstream side during the first half-cycle. In the first half cycle the scour hole shape remains asymmetrical, orientated by the initial current direction, but after the second half-cycle, the scour hole shape is more symmetrical.

After two half-cycles the development of scour changes significantly. Changes in scour depth are small indicating that the depth is close to equilibrium. Changes scour depth and shape in the third half-cycle is significantly smaller than in the previous two half-cycles. The affect of the reversed flow field (the fourth half-cycle) on the shape and slope of the scour hole is reduced with the hole becoming symmetrical in shape and no longer orientating to the flow direction.

The time development of scour under the variable reversing currents used here (where variations of flow speed and depth are represented by three stages of flow per half-

cycle) was compared with theoretical predictions and experimental data of unidirectional scour. The tidally based variable reversing current scour was found to be slower than it is under unidirectional currents or square tidal currents. This appears to be due to the variation in the rate of scour between each stage in the variable reversing current and to some extent, infilling. Through comparing the experimental resultsthis with theoretical predictions and experimental data, the equilibrium scour depth that occurs in the variable reversing current appeared to be lower than that of a unidirectional current. Possible reasons for lower equilibrium scour depth include infilling though to a lesser extent that often suggested in the literature. The lower scour depth, however, appeared mainly to be due to the inherently different scour rates that occur under the different variable reversing flow conditions, something which is not attributed to lower equilibrium depths in the literature. The live-bed time-step has a significantly faster rate than the transition and clear-water rates. The extrapolation of these findings to prototype conditions and tidal currents will potentially reduce the amount of scour protection required and therefore the costs of scour protection. This will require more research to confirm.

At the end of the variable reversing test the surrounding bed is raised above the original bed level on both sides of the cylinder indicating that the reversal of flow results in deposition both sides of the cylinder, and that this deposition is not removed significantly when the flow reverses. This indicates that the U/U_c at this point remains < 1. The flow over the mound, which is upstream of the scour hole is not significantly changed by the presence of the mound – at least not enough to generate sediment transport in the locality of the mound. As scour continues to increase in the scour hole,

the upstream flow appears not to affect the flow in the scour hole, though this requires velocity measurements within the scour hole to confirm.

Chapter 5: Flow Field Alteration and Reduction of Scour through the use of Collared and Helical Strake Cylinders

5.1 Introduction

This chapter presents results from a series of rigid and mobile bed tests involving the collared and helical straked cylinders. From the observations of the experimental data in §3 and §4 the variability of the variable reversing (i.e., tidal) flow field around the cylinder and the differences in the rate and morphology of scour from unidirectional flow have been determined. The results, given in §5.2, §5.3, and §5.4, present the mean flow and turbulence measurements upstream of the cylinder, in the near-cylinder region, downstream of the cylinder and the amplification of bed shear stress around the cylinder respectively. In §5.5 comparisons of the flow velocity fluctuations behind the smooth, collared and helical straked cylinders using the quadrant analysis technique are made. In §5.6 results from the pressure sensors are presented showing the changes in water surface elevation up and downstream of the smooth, collared and helical straked cylinders. In §5.7 the mobile bed results are presented for the collared cylinder under the transition to live-bed to clear-water test sequence with reversing current direction. In §5.8 the reduction of the downflow, downstream flow and turbulence field changes and suppression of vortex shedding is discussed. Here the reduction of scour around the collared cylinder during the mobile bed test is also discussed and recommendations for the reduction of scour around an off shore cylinder are made. §5.9 provides concluding remarks.

Firstly the results discussed in §4 are used to provide a context for the experiments. These results along with the literature review given in §1.7.3 raise two areas requiring further research in the use of scour protection:

1. The cost-effectiveness of the current deployment of static scour protection. The results discussed in §4 indicate that the use of unidirectional current derived prediction methods to predict scour in tidal currents may in fact over-estimate the depth of scour. This may lead to over-compensation in selection of the required amount of scour protection needed. While it is acknowledged that protection levels should be conservative, it is important to try to define the level of conservatism required in order to reduce costs. The first step towards this is a better understanding of how active scour protection works. As discussed in §1.7.3, effective scour mitigation (in-filling holes as they form) or standard scour protection (rip-rap insertion at the time of construction) relies on accurate estimates of maximum scour depth d_{sc} and its time of development t_e. The results presented in §4 indicate that both d_{sc} and t_e may not be accurately predicted using unidirectional current methods. Therefore, static scour protection at offshore wind turbines may currently be being used in a less cost-effective way than is possible.

2. The necessity for scour protection in the first place. The results produced from the experiments in §4 indicate that the scour depth achieved after a full tidal cycle appears to be lower than the scour depth under a corresponding unidirectional current. A reduction in the cost of scour mitigation could be made by allowing the scour to take place while considering that the extra

stability afforded to an appropriately deeper-piled cylinder may increase the scour depth which the structure can sustain. The scour depth may be further reduced by altering the flow field around the cylinder in such a manner as to reduce its scouring potential which, in conjunction with deeper piling, may reduce the need for static scour protection.

This chapter assesses the effectiveness of both a collared cylinder and a helical strake cylinder on the reduction of scour at the cylinder and, therefore, the potential for reducing scour at the offshore wind turbine cylinder.

5.2 Upstream Mean Flow and Turbulence Profiles

The flow and turbulence fields around the straight collared and the helical collared cylinders are presented below in the same manner as for the smooth cylinder in §3.

5.2.1 Upstream Mean Flow Velocity Profiles

Three-dimensional mean velocities were recorded using an ADV as described in §3.2.1 upstream of the collared and helical strake cylinders.

5.2.1.1 Live-bed and Transition Test Streamwise Velocity u′, Helical Strake and Collared Cylinders

As in §3.2.1, normalised velocity profiles of u' (first column), v' (second column), and w' (third column) for the collared and helical strake cylinder, live-bed and transition test are given in Figure 5-2 (where $u' = u/U_\infty$, $v' = v/U_\infty$ and $w' = w/U_\infty$).

Along the centreline for the collared cylinder in the live-bed test flow reduction is present similar to the corresponding smooth cylinder test (Figure 4-1) though velocity does not reduce significantly below 0.5 U_∞ (which is slightly less than the reduction to 0.4 U_∞ in the smooth cylinder tests). Off-centreline the decrease of u' upstream is again followed by an increase on approach to the cylinder in much the same manner as for the corresponding positions in the smooth cylinder. The distribution of u' in the transition test is also very similar to the corresponding data upstream of the smooth cylinder. The lowest collar is essentially at the water surface (0.1 m off the bed) so its influence is minimal.
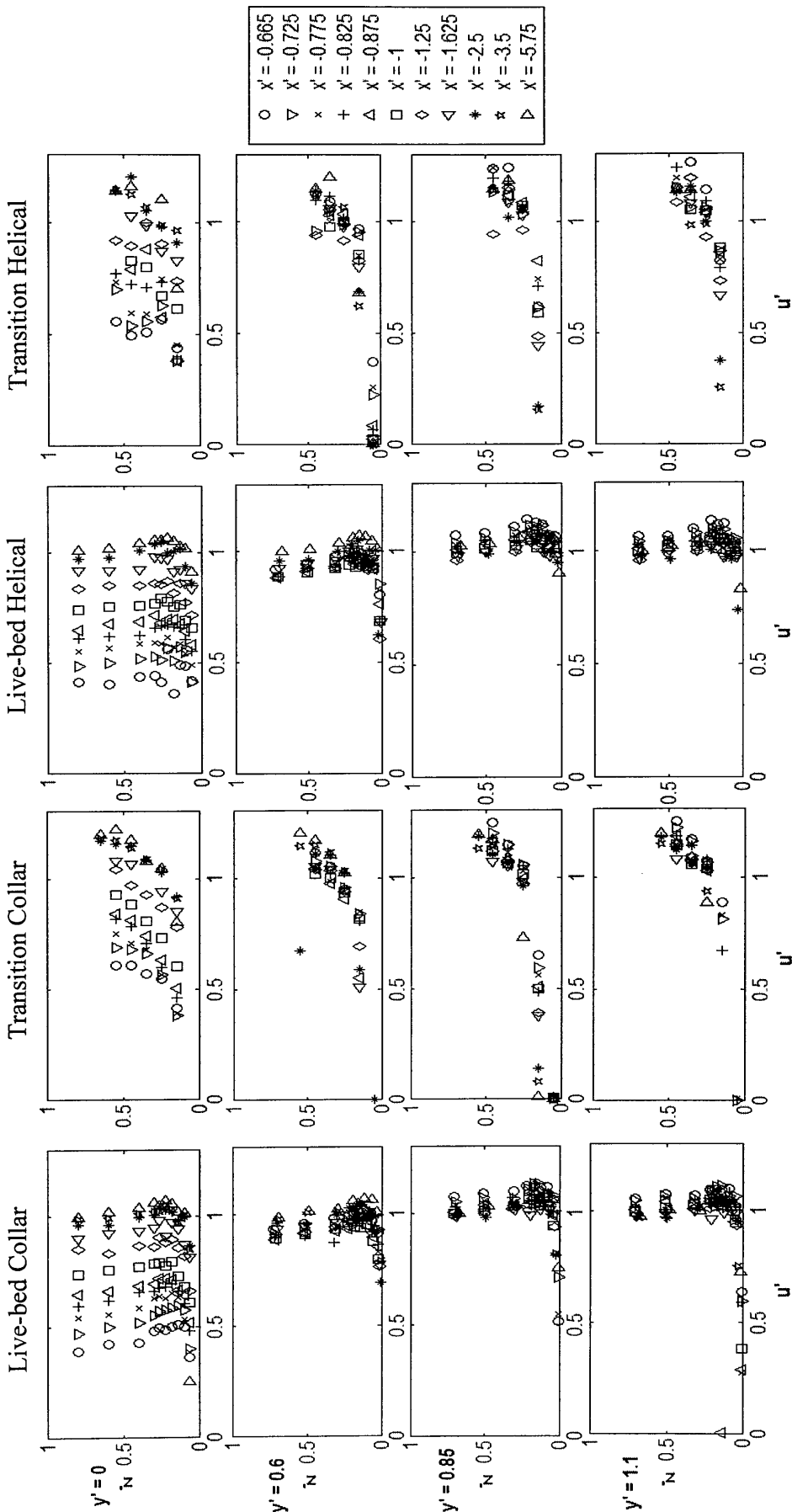
Figure 5-2. Live-bed and transition u' profiles upstream of the collared and helical cylinder.

Legend:

Symbol	Value
○	$x' = -0.665$
▷	$x' = -0.725$
×	$x' = -0.775$
+	$x' = -0.825$
◁	$x' = -0.875$
□	$x' = -1$
◇	$x' = -1.25$
▽	$x' = -1.625$
＊	$x' = -2.5$
☆	$x' = -3.5$
△	$x' = -5.75$

Panel column headings: Live-bed Collar, Transition Collar, Live-bed Helical, Transition Helical

Row labels: $y' = 0$, $y' = 0.6$, $y' = 0.85$, $y' = 1.1$

In the live-bed and transition tests for the helical straked cylinder the distributions of u' velocity on the centreline are similar to those of the collared cylinder. Between $x' = 0.825$ and 0.665 there is, however, a decrease in u' just above the bed followed by an increase just above the bed in both the transition and live-bed.

5.2.1.2 Live-bed and Transition Test Lateral Velocity v', Helical Strake and Collared Cylinders

Figure 5-3 shows distributions of v' upstream of the collared and helical strake cylinder in the live-bed and transition test. The distributions are very similar to those at corresponding positions upstream of the smooth cylinder both on and off the centreline (Figure 4-2). Again, the helical strake cylinder shows some variation from the smooth and collared cylinder. Between $x' = 0.825$ and 0.665 the distribution of v' becomes less coherent and varies with z'. Overall however, the maximum velocity achieved at the bed is similar between the helical strake, collared and smooth cylinders.

5.2.1.3 Live-bed and Transition Test Lateral Velocity w', Helical Strake and Collared Cylinders

Figure 5-4 shows distributions of w' upstream of the collared and helical strake cylinder in the live-bed and transition test. Along the centreline of the collared cylinder in the live-bed the downflow at $x' = 0.665$ exhibits a double peak in velocity. The highest value appears at $z' \approx 0.4$ which is just above the lowest collar. Below this the downflow reforms and gains strength with increasing depth but to a lower velocity

5-6

peak than that reached above the collar before reducing just above the bed. The peak value reached above the bed is lower than it is for the smooth cylinder ($\approx$ 0.13 as opposed to $\approx$ 0.15). This does not occur in the transition test for the collared cylinder as the lowest collar is positioned at the water surface.
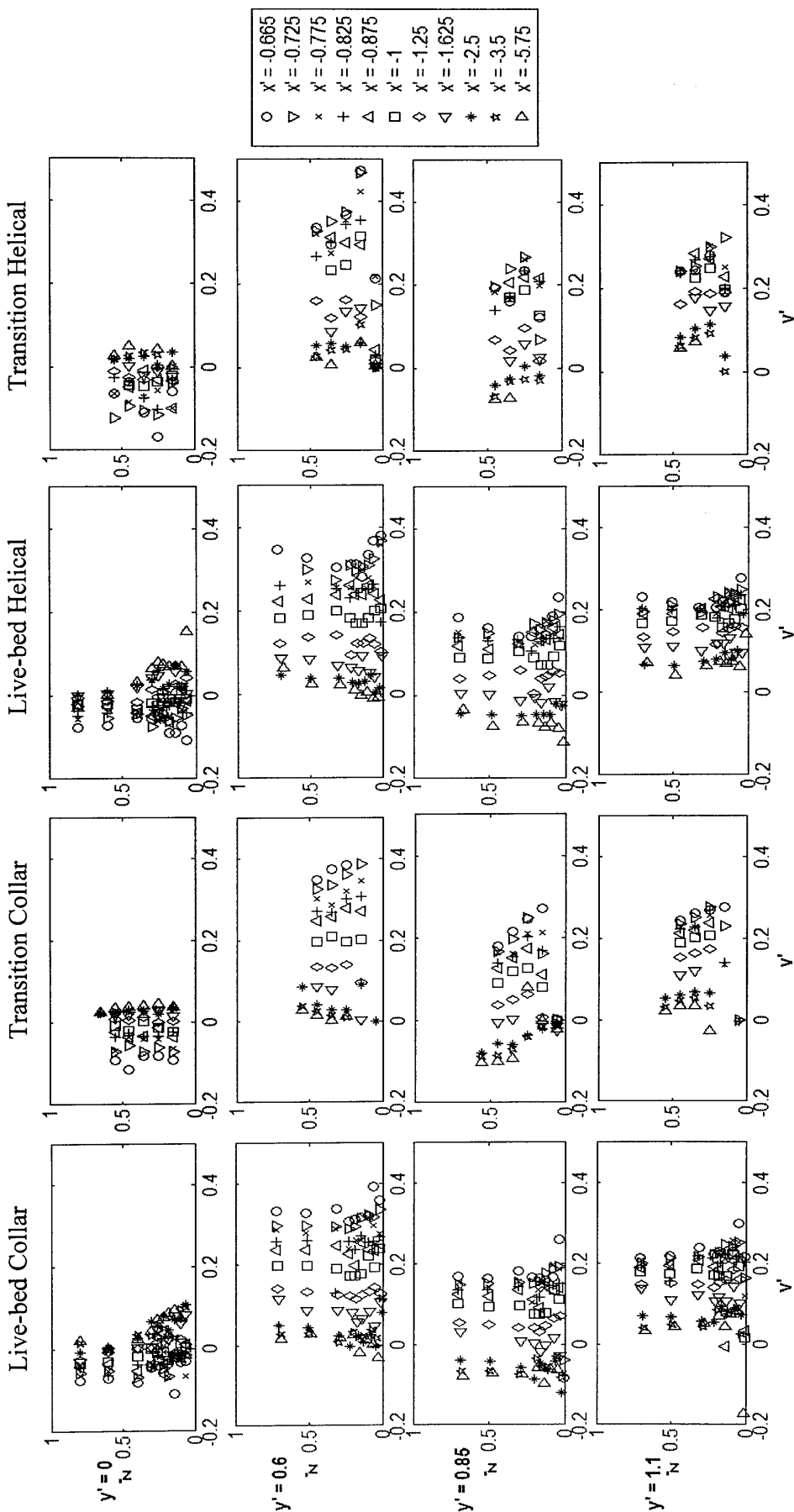
Figure 5-3. Live-bed and transition v' profiles upstream of the collared and helical cylinder.
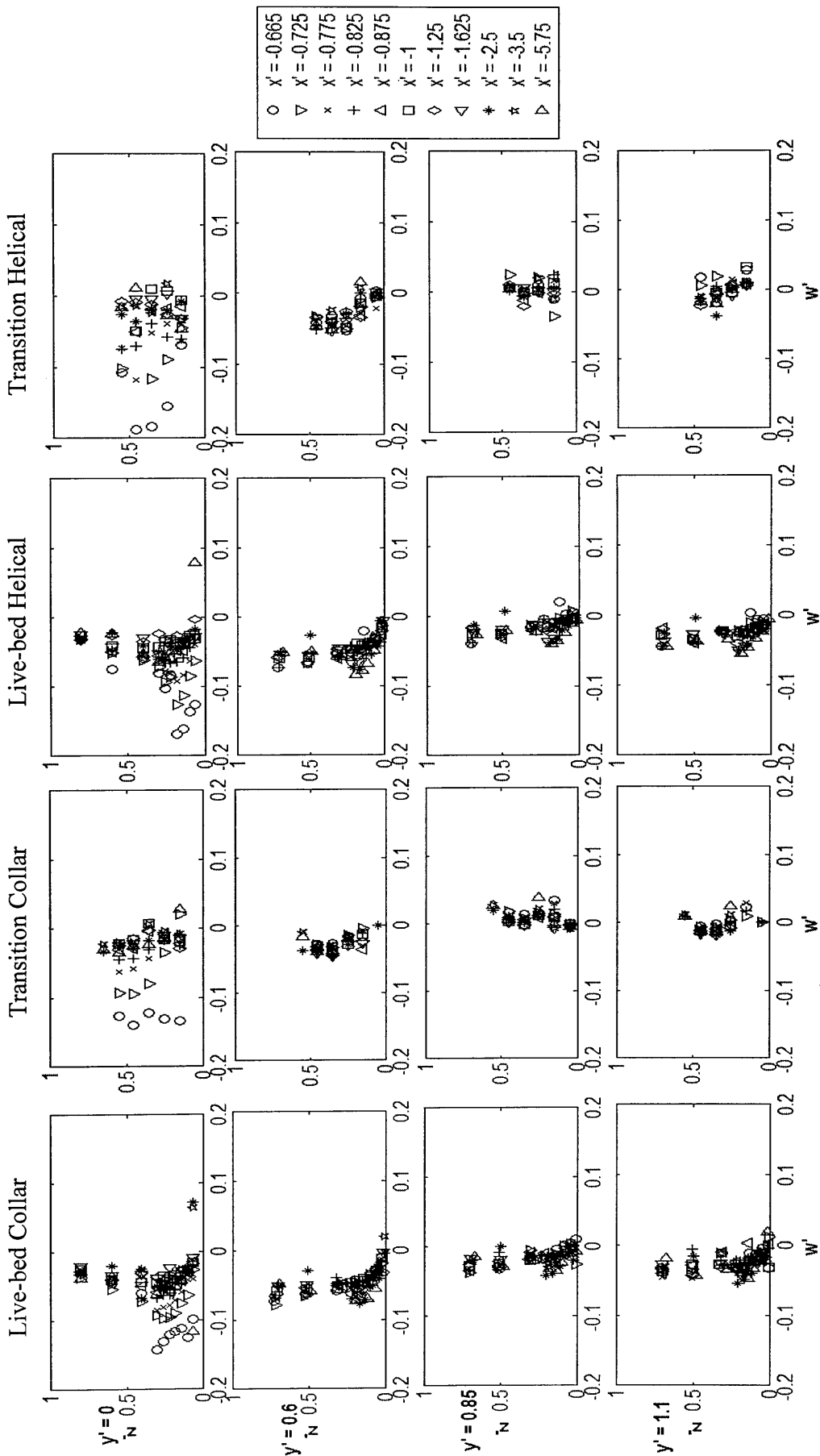
Figure 5-4. Live-bed and transition w' profiles upstream of the collared and helical cylinder.

Legend:
- ○ $x'=-0.665$
- ▷ $x'=-0.725$
- × $x'=-0.775$
- + $x'=-0.825$
- △ $x'=-0.875$
- □ $x'=-1$
- ◇ $x'=-1.25$
- ▽ $x'=-1.625$
- * $x'=-2.5$
- ☆ $x'=-3.5$
- △ $x'=-5.75$

Column headings: Live-bed Collar, Transition Collar, Live-bed Helical, Transition Helical

Row labels: $y'=0$, $y'=0.6$, $y'=0.85$, $y'=1.1$

The live-bed distribution of w' for the helical strake cylinder is similar to the smooth cylinder with an increase in strength to a near-bed peak. This near-bed peak is slightly stronger than it is in the smooth and collar cylinders being $\approx 0.2U_\infty$ as opposed to $\approx 0.15U_\infty$. Off-centreline and in both the collared and helical strake cylinder live-bed and transition tests, the downflow no longer exists. There is a general downward component to the flow which reduces to zero at the bed as observed in the smooth cylinder (Figure 3-3). It appears that the helix does not have a significant effect on the downflow. This is likely because the angle of the helix is too steep; a shallower helix would presumably behave more like the collar, a suggestion also made by Dey et al., (2006).

5.2.2 Upstream Turbulence Profiles; Collared and Helical Strake Cylinders.

The same six turbulence parameters analysed from the velocity profiles in §3.2.2 were calculated from the upstream velocity measurements described above for the live-bed test (Figures 5-5 and 5-6 for the collared and helical strake cylinder respectively) and transition test (Figures 5-7 and 5-8 for the collared and helical strake cylinder respectively) at each y' position.

Figures 5-5 and 5-6 both show that distributions of TI and Reynolds Stresses upstream of the collared and helical strake cylinder are for the most part very similar to those upstream of the smooth cylinder during the live-bed tests. A similar observation is made for Figures 5-7 and 5-8 in the transition test.
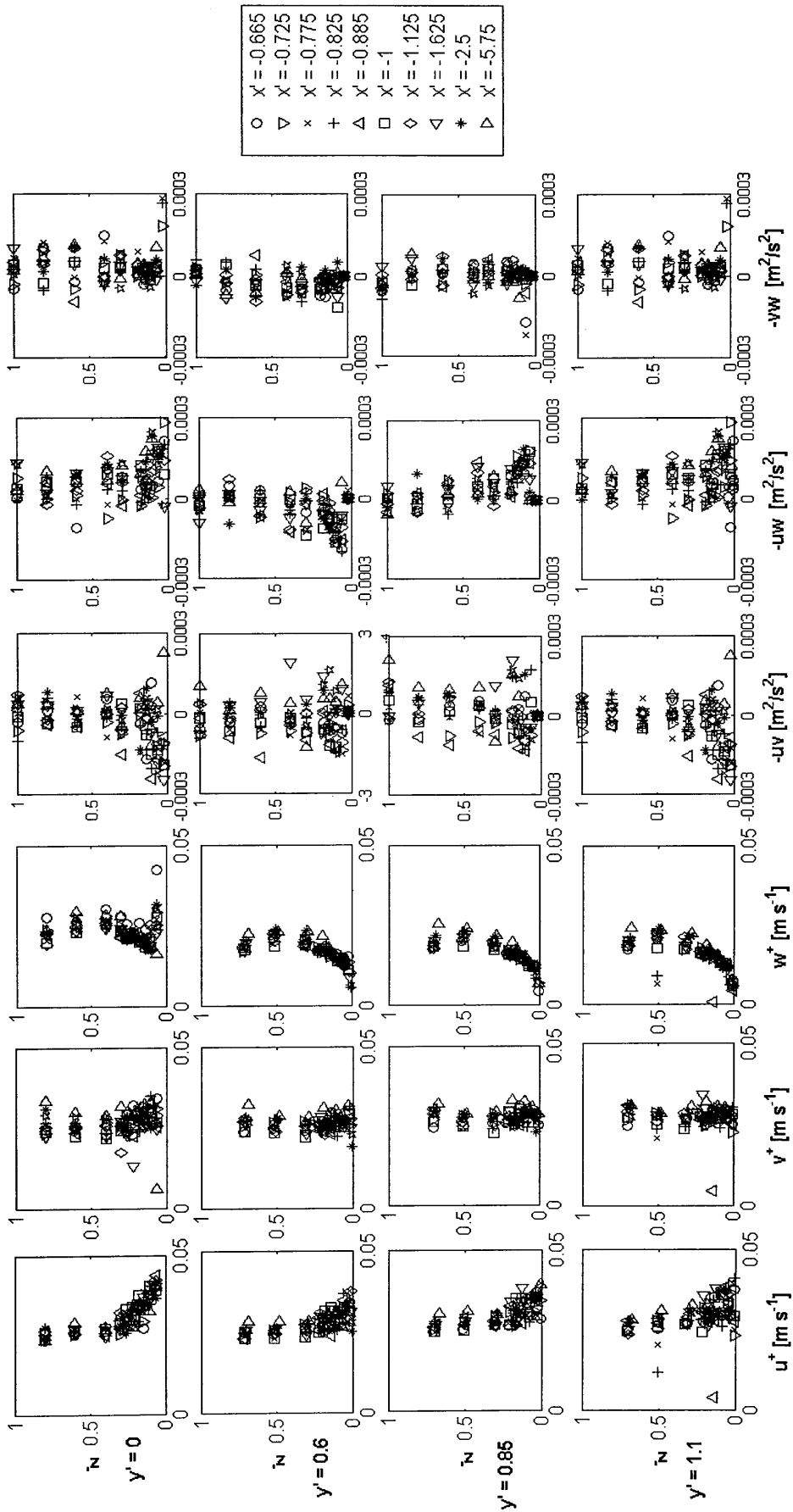
Figures 5-5. Distributions of TI, and Reynolds Stress along the $y' = 0$ (centreline), (first row), and the $y' = 0.6$, 0.85 and 1.1 m planes (second – fourth row respectively) for the collared cylinder live-bed test.
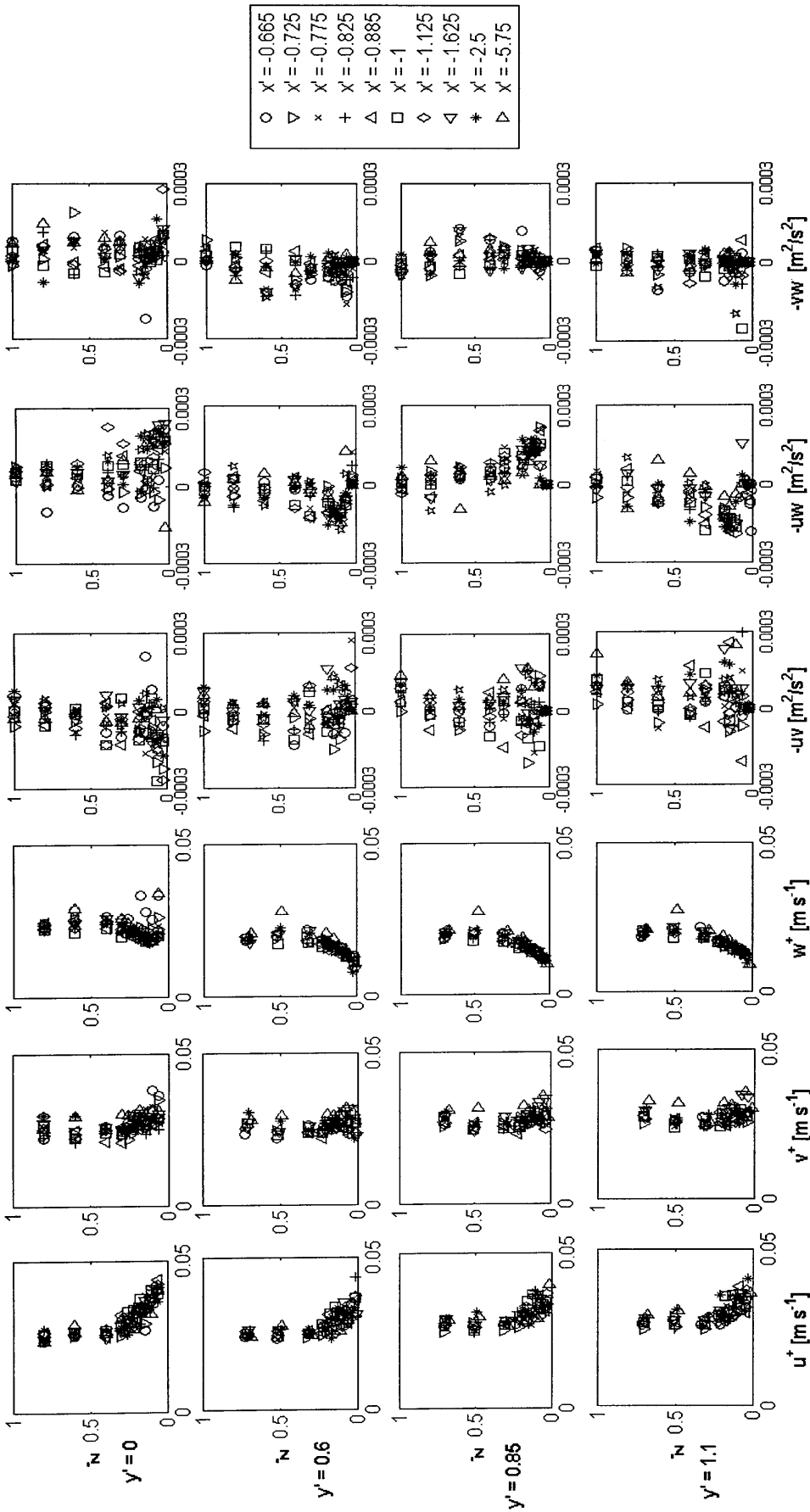
Figures 5-6. Distributions of TI, and Reynolds Stress along the $y' = 0$ (centreline), (first row), and the $y' = 0.6$, 0.85 and 1.1 m planes (second – fourth row respectively) for the helical cylinder live-bed test.
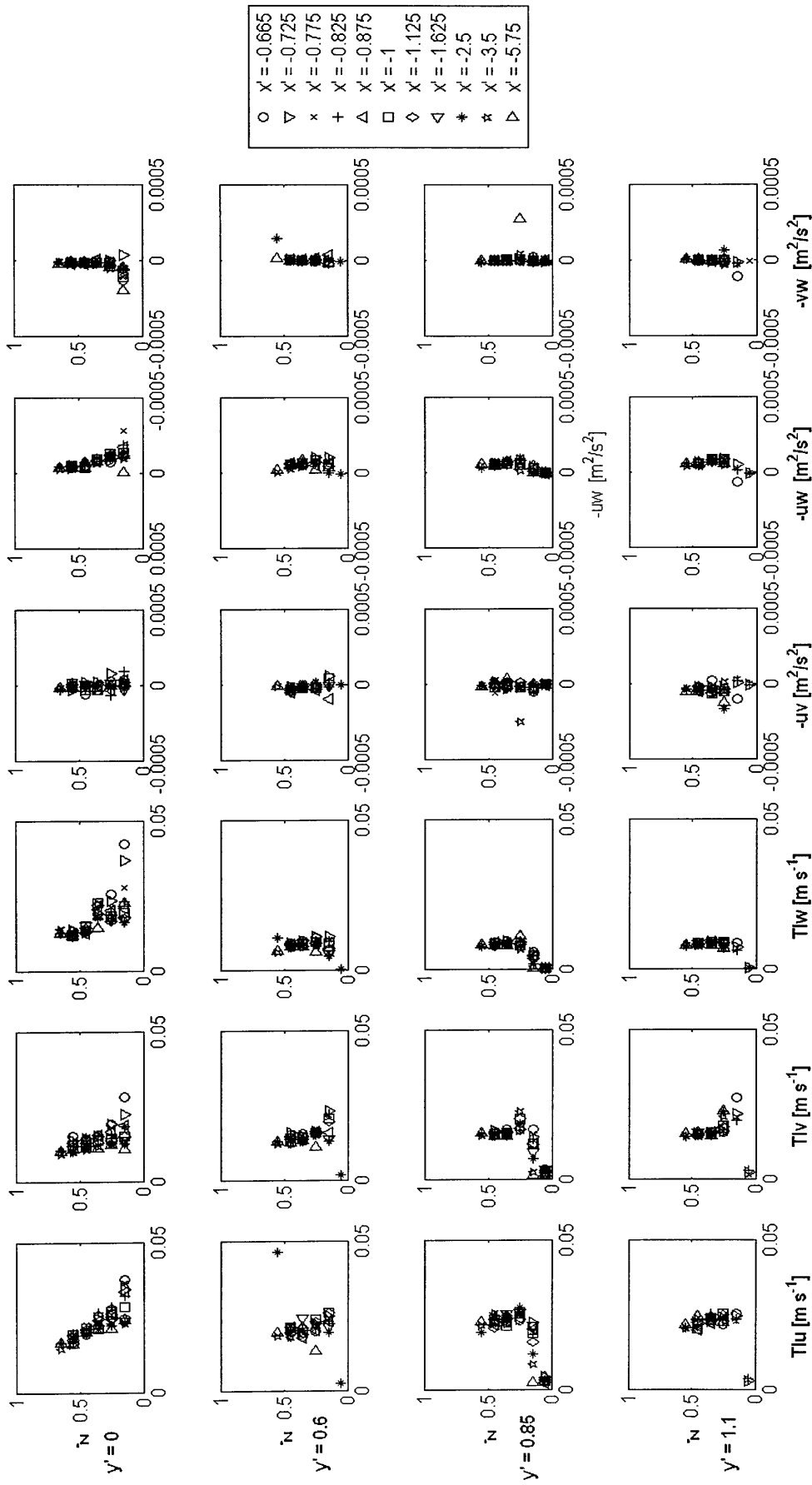
Figures 5-7. Distributions of TI, and Reynolds Stress along the $y' = 0$ (centreline), (first row), and the $y' = 0.6$, 0.85 and 1.1 m planes (second – fourth row respectively) for the collared cylinder transition test.
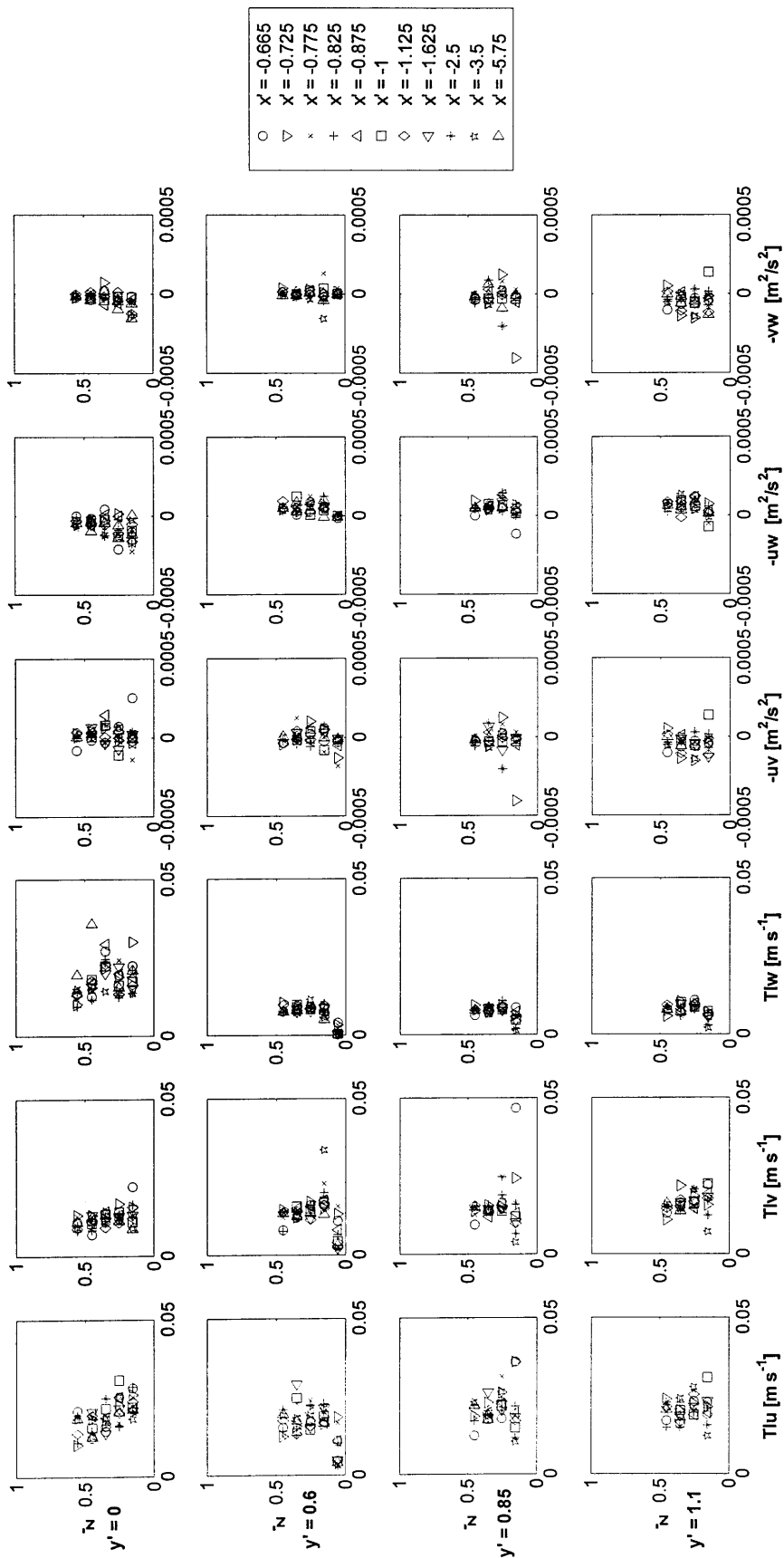
Figures 5-8. Distributions of TI, and Reynolds along the $y' = 0$, (first row), and the $y' = 0.6$, 0.85 and 1.1 m planes (second – fourth row respectively) for the helical strake cylinder transition test.

5.3 Near-pile Flow Velocity and Turbulence Profiles

5.3.1 Flow Velocity Profiles

Near-pile flow velocity was measured around the collared and helical strake cylinder using the ADV in the same way as for the smooth cylinder (§3.3). The results are presented below.

5.3.1.1 Near-pile u′ Distributions; Collared and Helical Strake Cylinder

Figure 5-9 shows profiles of u' around the collared and helical strake cylinders for the live-bed and transition tests at the y' and x' positions described in §3.3. In the live-bed around the collared cylinder along the $y' = 0.3$ plane the distribution of u' can be divided into two regions: upstream of the cylinder there is continued increase of velocity towards the cylinder with a retention of the boundary layer sheared profile structure, while downstream there is a loss of this structure to a highly varied distribution with depth with lower, and some negative, velocity. Clearly there is much similarity between the collared and helical strake cylinder and the distributions around the smooth cylinder (Figure 3-7) in both the live-bed and transition tests. The exception is the observation of some negative u' downstream of the collared cylinder indicating reversed flow. At the corresponding positions downstream of the smooth cylinder there is no reversal and a large increase of u' downstream indicating that separation has not yet occurred. The implication of this is that the wake is slightly wider behind the collared cylinder than it is around the smooth cylinder. Off-

centreline, the distribution of u' is much the same as for the smooth cylinder for both the collared and helical strake cylinder.
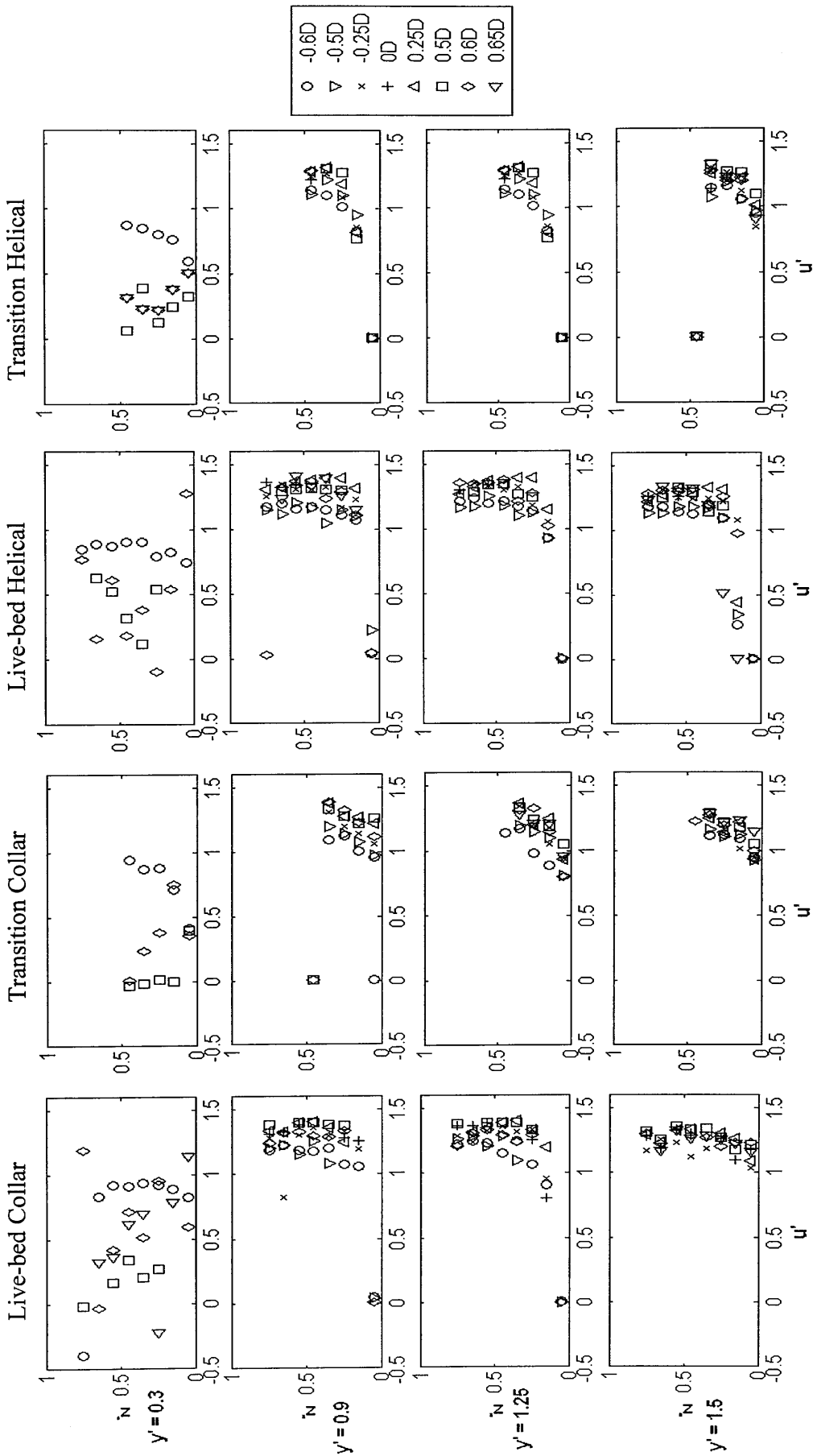
Figure 5-9. Live-bed and transition u' profiles in the near-cylinder region of the Collared and helical strake cylinder.

5.3.1.2 Near-pile v′ Distributions; Collared and Helical Strake Cylinder

Lateral velocity $v′$ along $y′ = 0.3$ planes of both cylinders in the transition and clear-water tests is distributed similarly to the smooth cylinder (Figure 5-10). However, there are some subtle differences, for example the distinctly negative downstream $v′$ observed in the live-bed smooth cylinder data (Figure 3-9) is not present downstream of the collared and helical cylinders. The distribution of $v′$ is more varied between positive and negative, implying (as in the $u′$ distributions above in Figure 5-9) flow separation occurs further upstream along the cylinders resulting in a wider near-wake than behind the smooth cylinder. The transition distributions along the $y′ = 0.3$ plane are similar to those around the smooth cylinder (Figure 3-9). Off-centreline distributions of $v′$ are similar to the smooth cylinder.
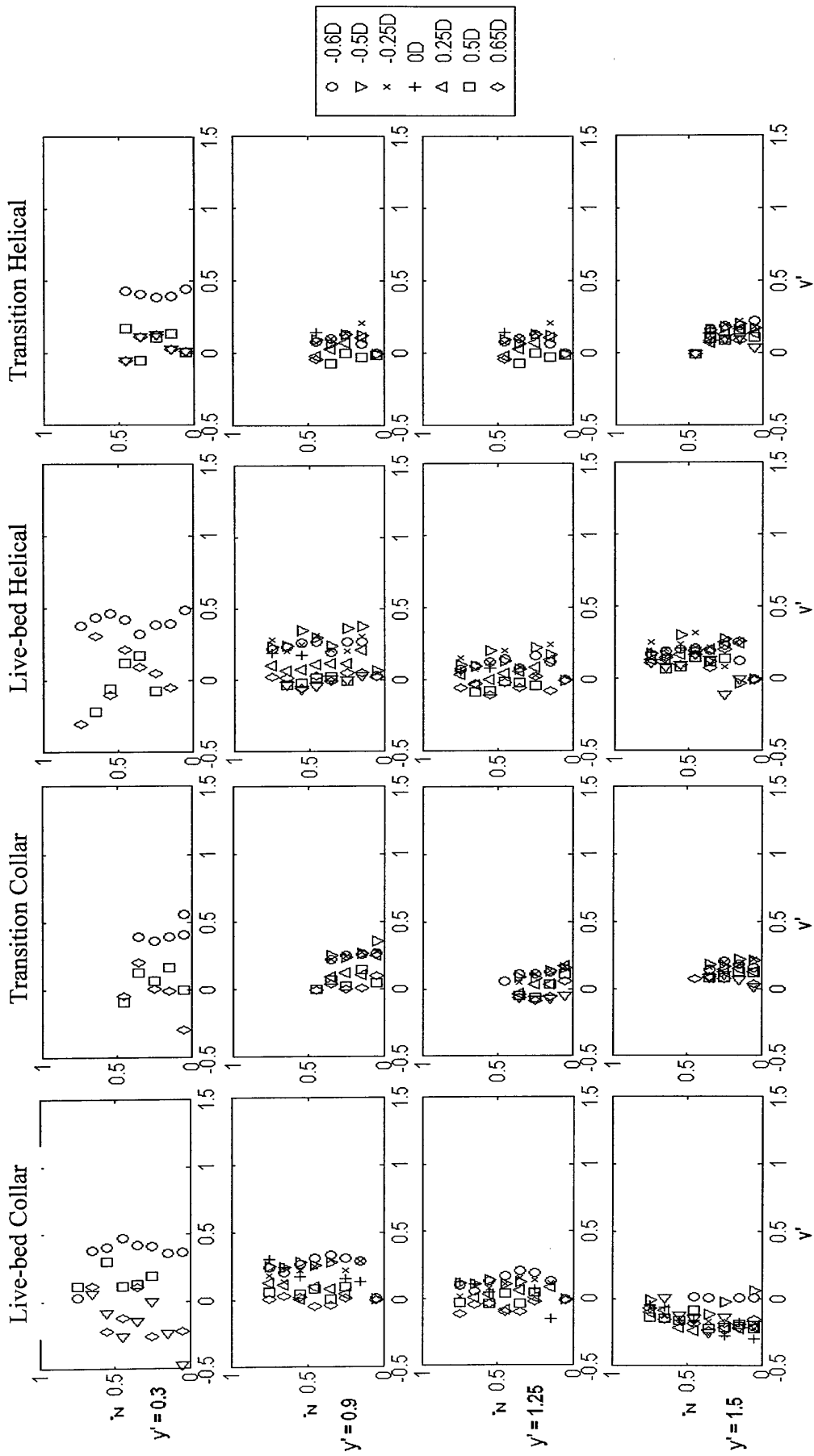
Figure 5-10. Live-bed and transition test v' profiles in the near-cylinder region of the collared and helical strake cylinder.

5.3.1.3 Near-Cylinder w' Distributions; Collared and Helical Strake Cylinder

The distribution of w' in Figure 5-11 shows little difference to that around the smooth cylinder at all positions. Along $y' = 0.3$ there is a very small negative w' upstream and positive w' downstream, similar to the smooth cylinder (Figure 3-10).

5.3.2 Near-Cylinder Turbulence Profiles

5.3.2.1 Live-bed Turbulence Profiles, Collared Cylinder

Figure 5-12 presents the TI and Reynolds stress profiles for the collared cylinder in the live-bed test in the same manner as above for the upstream profiles. TI is the largest and most varied along the $y' = 0.3$ plane as it is for the smooth cylinder (Figure 3-11). Values of u^+ are larger than they are for the smooth cylinder (up to 0.2 m s^{-1} as opposed to up to 0.1 m s^{-1} for the smooth cylinder). The higher values of u^+ are likely to be due to the apparent earlier separation of flow at the cylinder side, as indicated in the mean flow results in §5.4. v^+ shows similar distributions of lower upstream, and higher and more varied downstream values, similar to the smooth cylinder. w^+ exhibits similar behaviour either side of the cylinder but with lower intensities (generally < 0.05). At the remaining y' positions TIs are distributed similarly to those around the smooth cylinder. Reynolds stresses are also distributed similarly to those around the smooth cylinder. τ_{uv} shows the greatest variability at all y' positions. Off-centreline u^+, v^+ and w^+ are distributed similarly to the smooth cylinder; all are low and constant with x'.
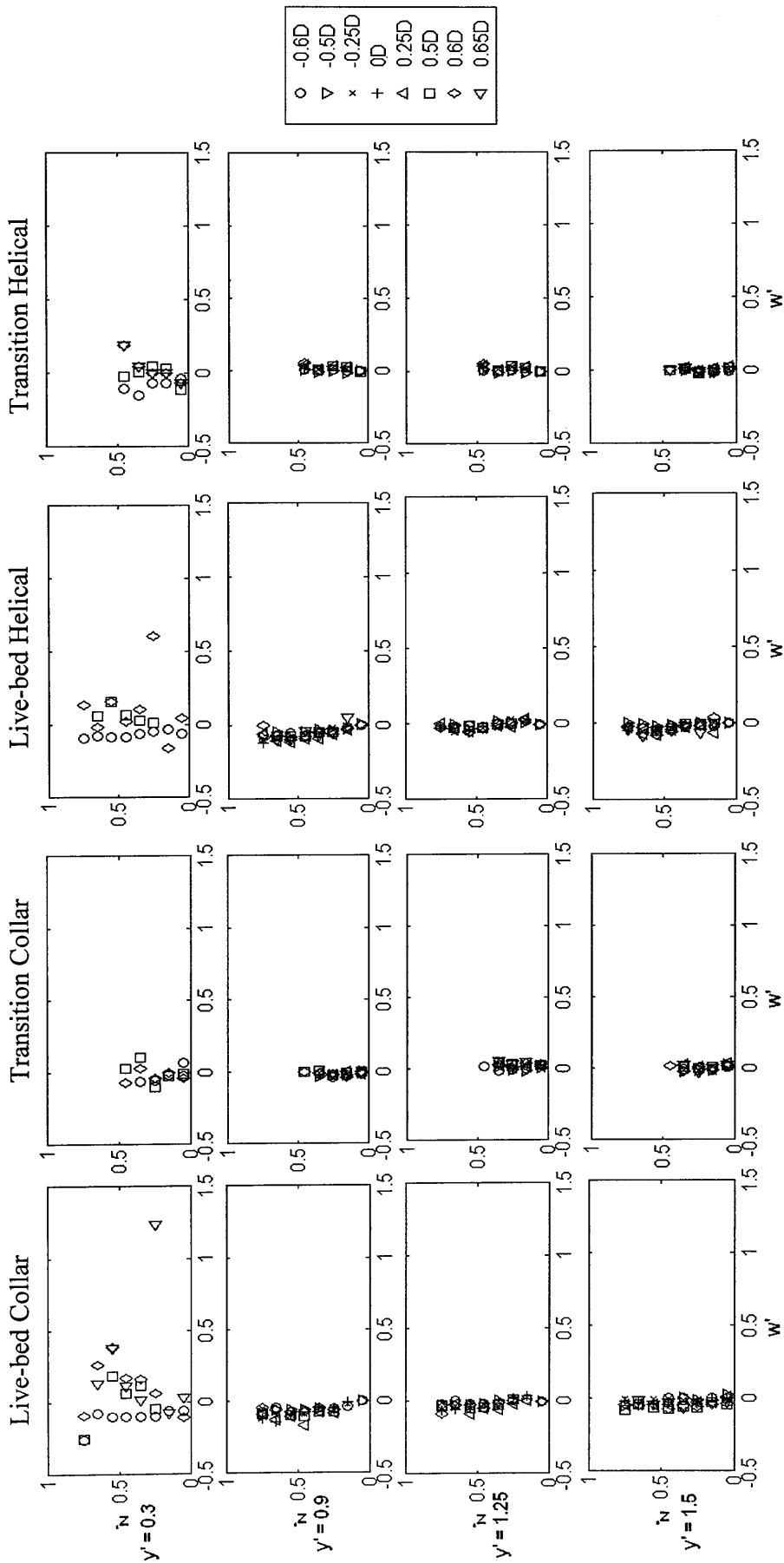
Figure 5-11. Live-bed and transition test w' profiles in the near-cylinder region of the collared and helical strake cylinder.
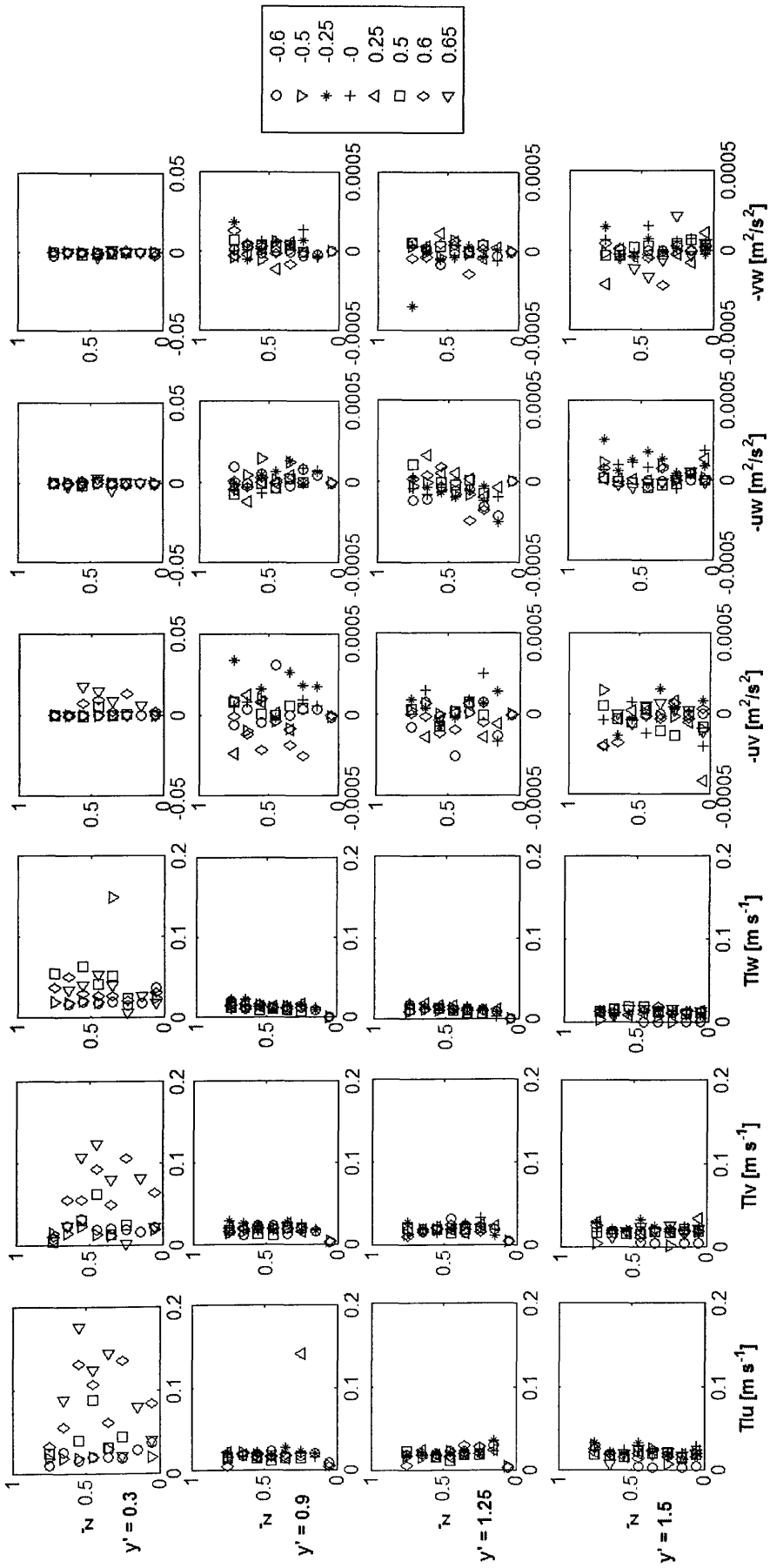
Figure 5-12. Distributions of TI, and Reynolds Stresses measured along the $y' = 0.3$, (first row), and $y' = 0.9$, 1.25 and 1.5 m planes (second – fourth row respectively) for the collared cylinder in the live-bed test.

Reynolds stresses along the $y' = 0.3$ plane are similar to the smooth cylinder until $x' = 0.6$ and 0.65 downstream, where τ_{uv} is significantly higher than it is in the corresponding positions around the smooth cylinder (note the different scale used in Figure 5-12, top row). Off-centreline stresses are similar to the smooth cylinder.

5.3.2.2 Live-bed Turbulence Profiles, Helical Strake Cylinder

TI and Reynolds stress distributions around the helical strake cylinder are presented in Figure 5-13. They are very similar to those described above for the collared cylinder and by implication, similar to the smooth cylinder.

5.3.2.3 Transition Turbulence Profiles, Collared and Helical Strake Cylinder

The distributions of TI and Reynolds stress around the collared and helical strake cylinder are shown in Figures 5-14 and 5-15 respectively. TIs in both figures are lower upstream and higher downstream of the respective cylinders and correspond well with the respective data for the smooth cylinder (Figure 3-12). On the $y' = 0.3$ plane TI is low upstream of the cylinders before increasing downstream at $x' > 0.25$. Reynolds stresses are most varied along the $y' = 0.3$ plane and become essentially zero with increasing distance from the cylinder.
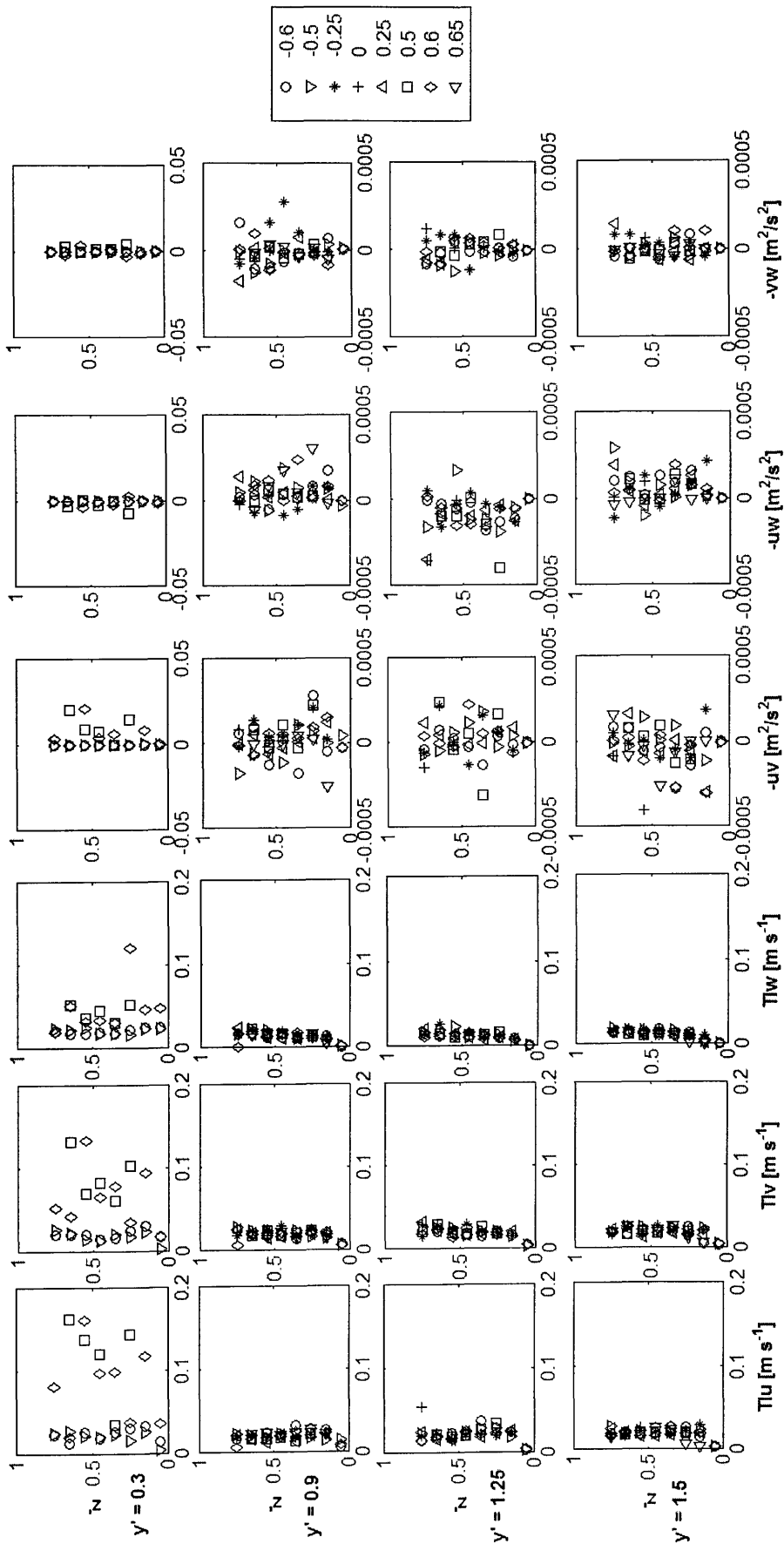
Figure 5-13. Distributions of TI, and Reynolds Stresses measured along the $y' = 0.3$, (first row), and $y' = 0.9$, 1.25 and 1.5 m planes (second – fourth row respectively) for the helical strake cylinder in the live-bed test.
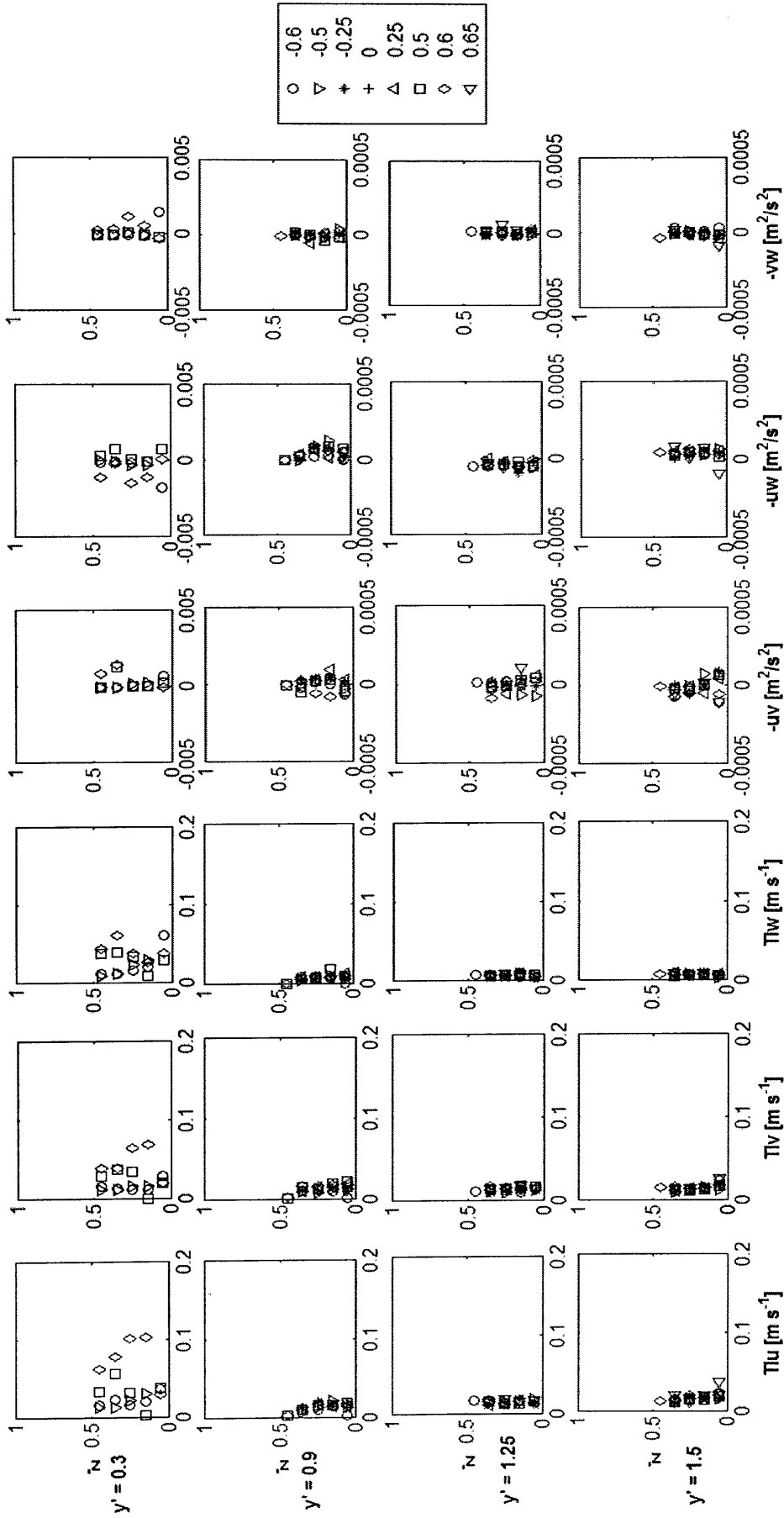
Figure 5-14. Distributions of TI, and Reynolds Stresses measured along the $y' = 0.3$, (first row), and $y' = 0.9$, 1.25 and 1.5 m planes (second – fourth row respectively) for the collared cylinder in the transition test.
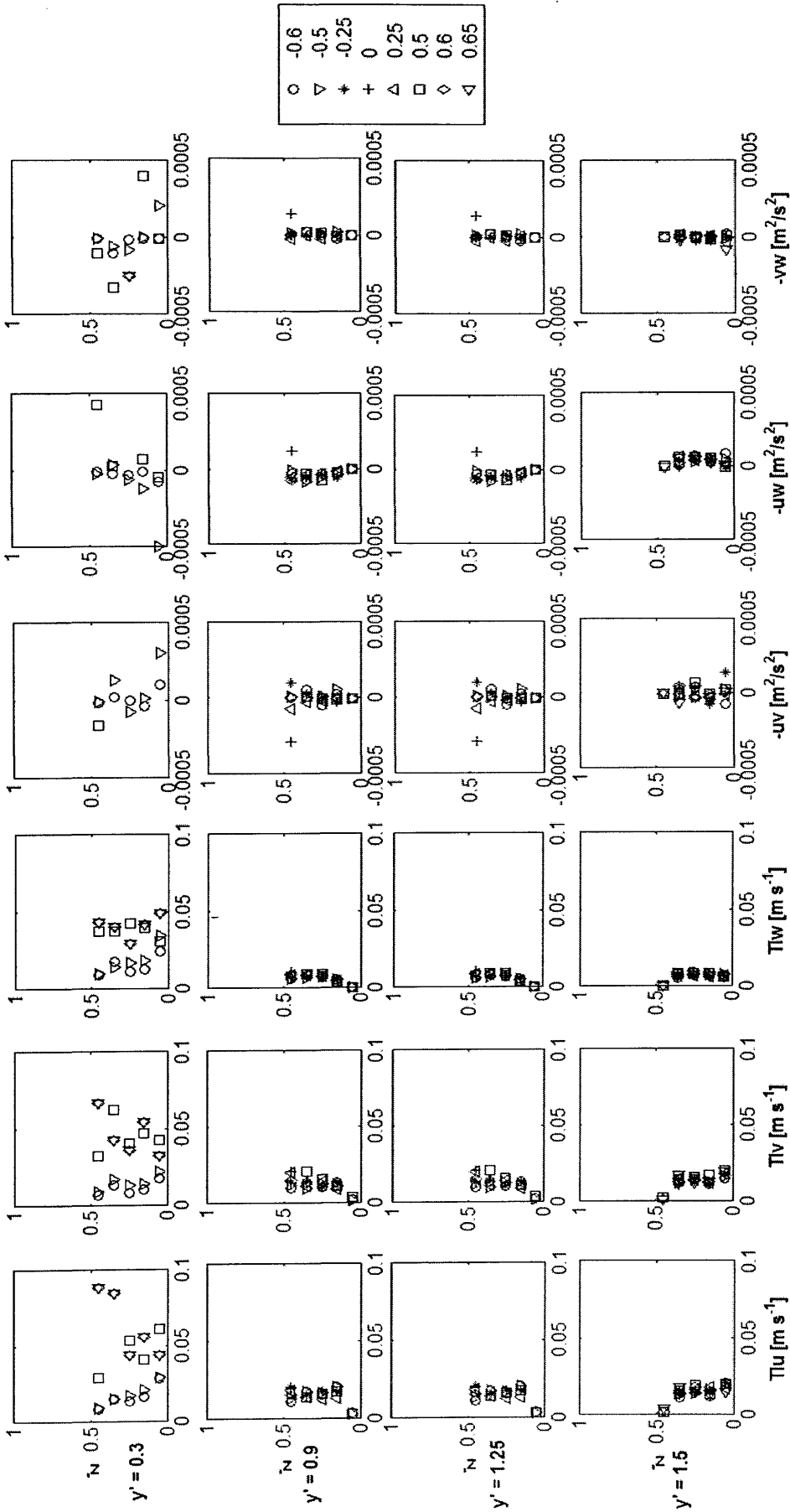
Figure 5-15. Distributions of TI, and Reynolds Stresses measured along the $y' = 0.3$, (first row), and $y' = 0.9$, 1.25 and 1.5 m planes (second – fourth row respectively) for the helical strake cylinder in the transition test.

5.4 Mean Flow and Turbulence Fields Downstream of the Cylinders

5.4.1 Mean Flow Velocity Slices, Collared Cylinder

5.4.1.1 Centreline Slices, Collared Cylinder

Three-dimensional mean velocity vector maps of the downstream centreline flow were recorded using PIV in the same locations as for the downstream smooth cylinder flow (§3.4). Four consecutive slices are presented in Figure 5-16 covering the downstream region from the edge of the collared cylinder edge to $x' \approx 5.125$. The collars are located at $z' = 0.4$ and 0.8.

The flow in the slice covering $x' = 0.5 - 1.625$ immediately downstream of the cylinder reveals a very different flow field to the one behind the smooth cylinder (Figure 3-14). The flow is not characterised by a stagnation zone and reversal but by a large vortex with a horizontal axis accompanied by two strong and opposite lateral flows. The vortex rotates anti-clockwise with reversed flow located above the rotation and downstream orientated flow below it. Near the bed there is a particularly strong downstream flow which cuts across the strong lateral (v) flow component. The strong negative v flow is located between the two collars starting at $z' = 0.4$ and dissipating below the second collar which is located at $z' = 0.8$. Flow velocity is greater than the undisturbed value in the region just above the lower collar, though it reduces dramatically below the lower collar and towards the bed. The strong negative area of v' is bounded below by a positive lateral flow of similar strength and above by a less strong positive lateral flow.
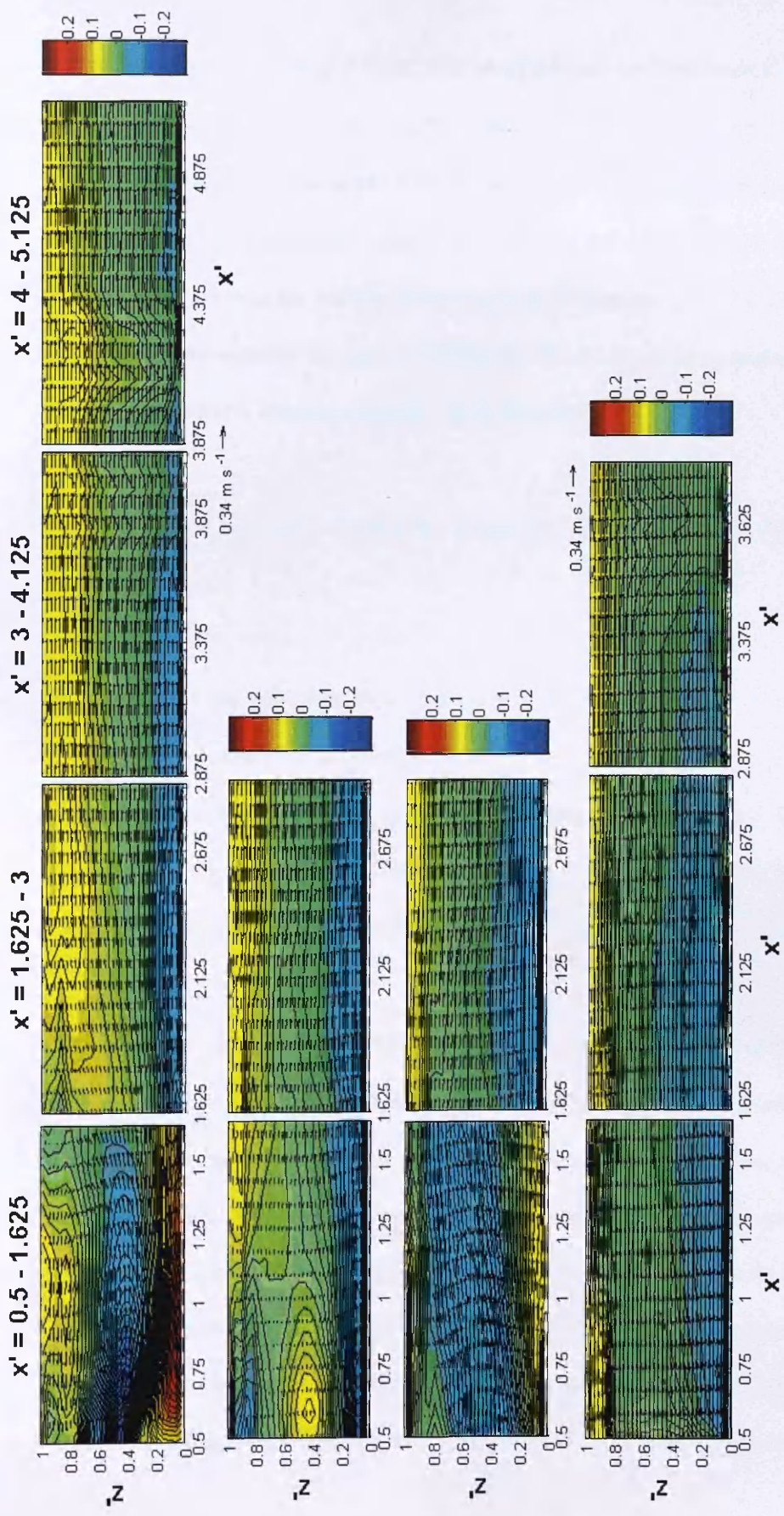
Figure 5-16. Vertical slices of the flow from the live-bed collared cylinder wake flow along the $y' = 0$ (top row), $y' = 0.25$ (2nd row), $y' = 0.5$ (3rd row), $y' = 0.75$ (bottom row) covering $x' = 0.5$ (the downstream edge of the cylinder) to $x' \approx 5$ depending on the y' plane. The vectors (whose magnitude and directions are given as $(u^2 + w^2)^{0.5}$ and arctan (w/u)), present uw velocity [m s^{-1}] while the coloured contours present v velocity [m s^{-1}] component.

Downstream, boundary layer sheared flow re-establishes itself between $x' = 1.625 - 3$ and the flow is relatively similar to the smooth cylinder. Between $x' = 1.625 - 3$ streamwise flow velocity is larger near bed and is accompanied by broadly negative v'. Near the surface streamwise velocity is slower and upward orientated with positive v' dominating towards the surface. These patterns progressively fade with increasing distance from the cylinder but are still observed $> 5D$ downstream indicating that flow recovers more slowly downstream of the smooth cylinder.

5.4.1.2 Live-bed Test Off - Centreline Slices (y' = 025, 0.5 and 0.75), Collared Cylinder

Observations of the centreline flow indicate that the main influence of the collared cylinder on the wake flow is confined to $x' < 2.875$, therefore, only data from this region is analysed below (also presented in Figure 5-16). Velocity fields were measured in three planes parallel to the centreline at $y' = 0.25$, 0.5 and 0.75, and cover a downstream region from the cylinder edge to $x' \approx 3$.

In the $y' = 0.25$ plane, the horizontal-axis vortex that dominated the centreline slice appears to have moved further upstream and its axis of rotation lies beyond the slice edge. Above and downstream of the vortex, flow velocity is very low and has, for the most part, a negative lateral component. Below this there is an area of relatively stronger positive lateral flow, with weakly sheared horizontal downstream flow. Near the bed there is a layer of stronger negative lateral flow. The downstream flow is similar to that observed along the centreline; slower live-bed and surface flow velocities and faster flow near the bed. Lateral velocity is generally positive at the

surface and negative near the bed. Along the $y' = 0.5$ plane the rotation is still present and has moved further upstream and higher up in the flow field which apart from the near bed and surface, has exclusively negative lateral flows. Mean flow velocity is enhanced across the middle of the slice and has a distinct upward motion. Towards the surface the velocity reduces greatly. In the $y' = 0.75$ plane, the picture is one of a steady return to downstream boundary layer shear flow. The negative bed and positive surface lateral velocities remain but become less strong with increasing distance downstream. Flow velocity between $x' = 1.625 - 3$ is greater than the undisturbed value due to flow constriction around the cylinder. The flow is approximately two-dimensional dominated by downstream orientated boundary sheared streamwise flow with very weak lateral flows that are negative near the bed and positive at the surface.

5.4.2 Mean Flow Velocity Slices, Helical Strake Cylinder

5.4.2.1 Centreline Slices, Helical Strake Cylinder

Four consecutive three-dimensional mean flow velocity slices of the centreline are presented in Figure 5-17 covering the downstream region from the cylinder edge to x' ≈ 5.125. Along the centreline the flow field immediately behind the cylinder is similar to the collared cylinder. Again a horizontal axis vortex replaces the stagnation driven reversal and a strong positive lateral flow is bounded by negative flows above and below it. Like in the collared cylinder wake, the rotation is anticlockwise but it is slightly smaller, and is located between the strands of the helical strake which are located at $z' = 0.8$ and 0.4. Lateral velocity distribution is similar to the collared cylinder though opposite in direction at the corresponding locations. It is likely that

the orientation of the helical strake to the flow direction plays a significant role in determining the direction of lateral flows.

Downstream the flow recovers to normal boundary layer sheared flow by $x' \approx 3$ though, as for the collared cylinder, there is advection of lateral flows downstream to $x' > 5.125$.
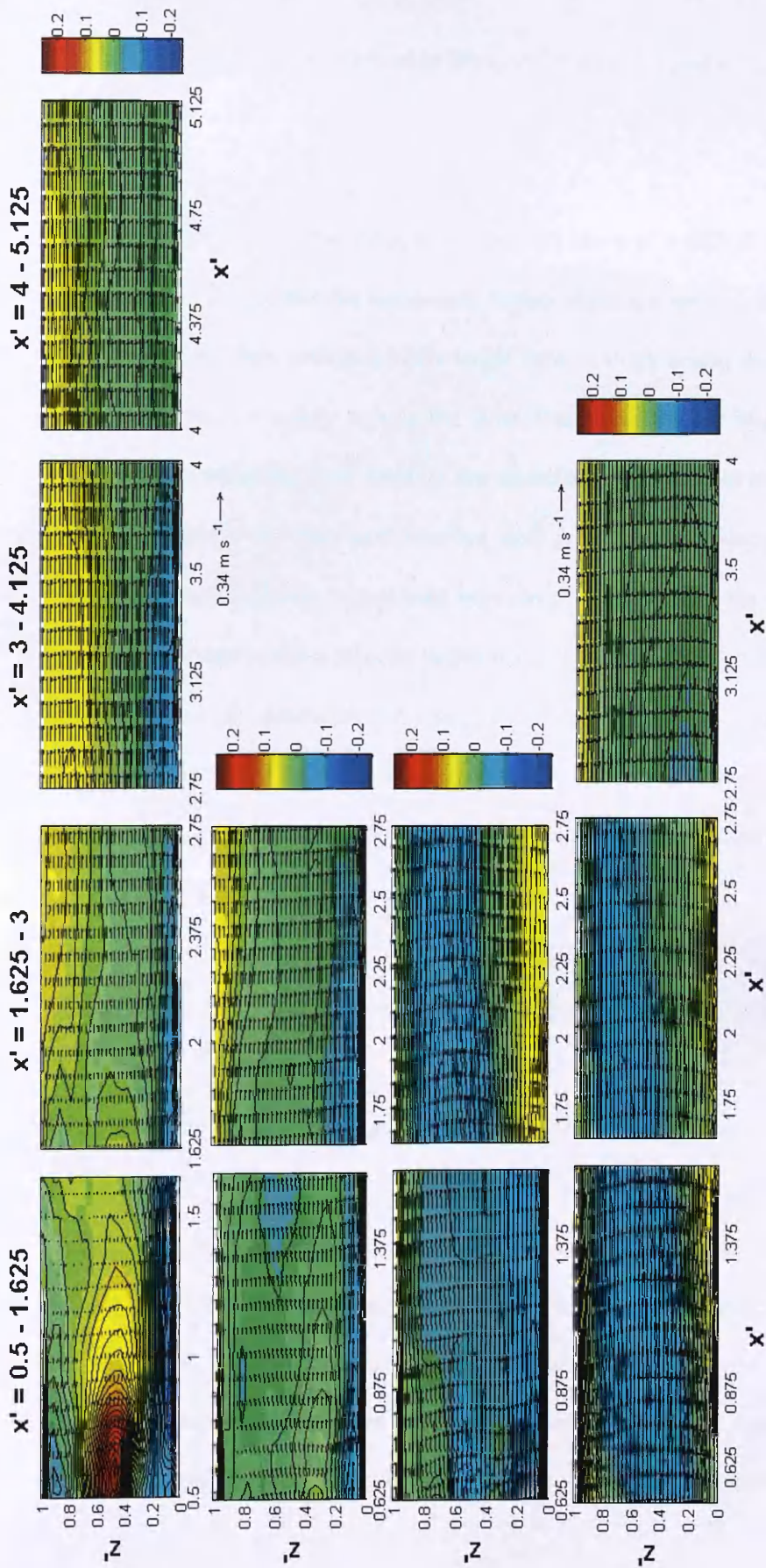
Figure 5-17. Vertical slices of the flow in the live-bed helical strake cylinder wake flow along the $y' = 0$ (top row), $y' = 0.25$ (2nd row), $y' = 0.5$ (3rd row), $y' = 0.75$ (bottom row) covering $x' = 0.5$ (the downstream edge of the cylinder) to $x' \approx 5$ depending on the y' plane. The vectors (whose magnitude and directions are given as $(u^2 + w^2)^{0.5}$ and $\arctan(w/u)$), present uw velocity [m s^{-1}] while the coloured contours present v velocity [m s^{-1}] component.

5.4.2.2 Live-bed Test Off - Centreline Slices (y' = 025, 0.5 and 0.75), Helical Strake Cylinder

Figure 5-17 also presents the mean flow velocities along $y' = 0.25$, 0.5 and 0.75 plane the rotation is still present but has moved further upstream and closer to the surface. Downstream, the flow (which exhibits larger flow velocity nearer the bed) gradually returns to normal boundary layer shear flow. Lateral velocity v is mostly negative near the bed, (indicating flow towards the centreline) and positive elsewhere. Along the $y' = 0.5$ plane the enhanced near-bed flow is greater than along the $y' = 0.25$ plane. Negative v velocity is dominant between $x' = 0.5$ - 1.625 but is accompanied by a large near-bed positive velocity between $x' = 1.625$ - 3. Along the $y' = 0.75$ plane flow is exclusively downstream orientated. Between $x' = 0.5$ - 1.625 the flow is enhanced near the bed where stronger negative lateral flow is observed. Downstream the flow gradually returns to boundary layer sheared flow and lateral flow becomes very small across most of the slice.

5.4.3 Downstream Transition Test Mean Flow Velocity Slices, Collared Cylinder

5.4.3.1 Transition Test Centreline Slices, Collared Cylinder

Figure 5-18 (top row) presents the centreline slices downstream of the collared cylinder during the transition test. The flow field is very similar to the corresponding smooth cylinder data (Figure 3-17). There is a linear stagnation zone located at $x' \approx$ 1.2 (slightly further downstream than for the smooth cylinder). Lateral flows are negative in the reversed and downstream regions and are positive around the

stagnation zone. Clearly, as the lowest collar is situated at the surface its influence on the flow field is minimal. Downstream the flow returns to boundary layer sheared flow and lateral velocity becomes essentially equal to zero at $x' = 3$.
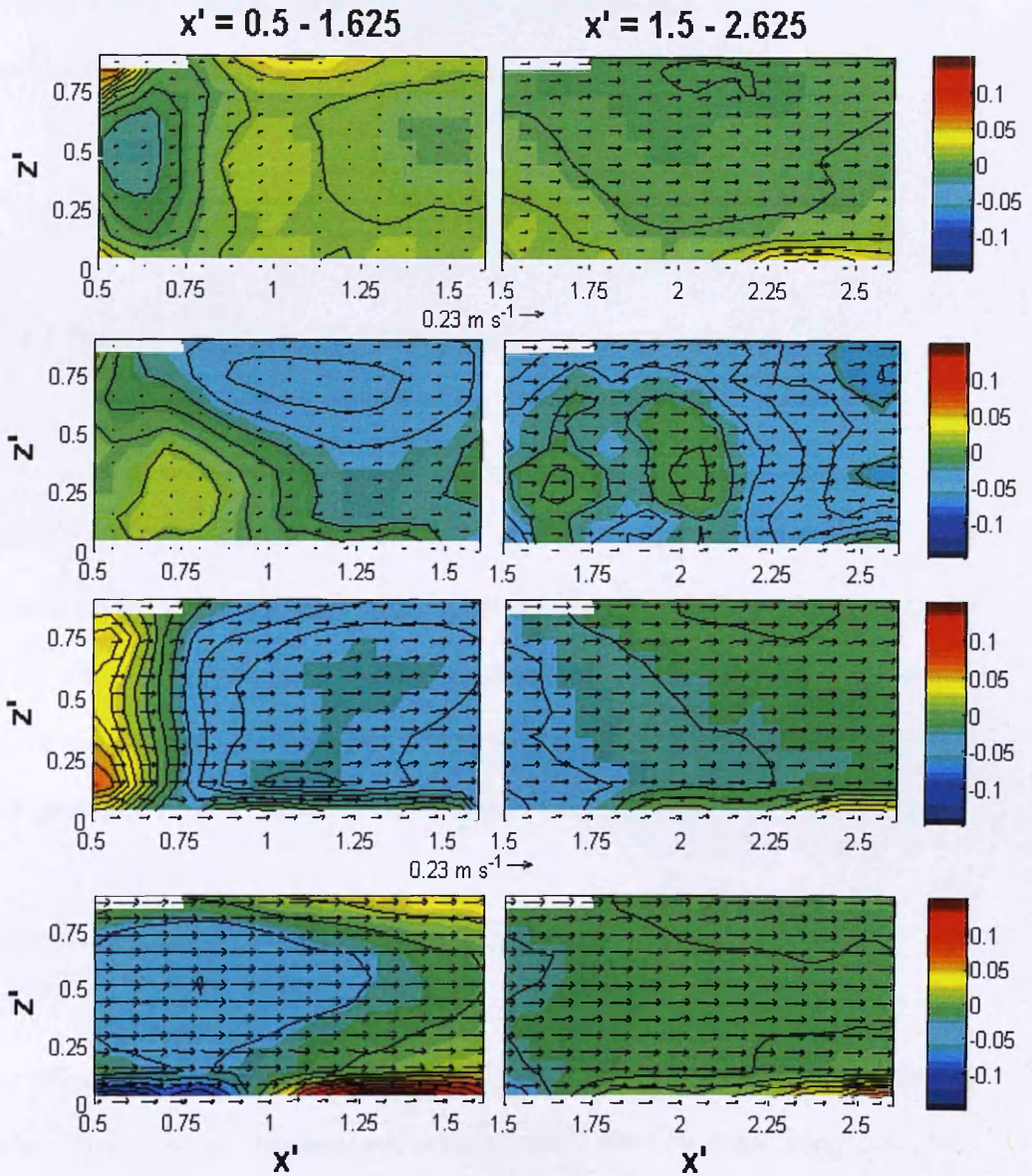
Figure 5-18. Vertical flow slices of the transition test collared cylinder wake flow along the $y' = 0$ (top row), $y' = 0.25$ (2nd row), $y' = 0.5$ (3rd row), $y' = 0.75$ (bottom row) covering $x' = 0.5$ (the downstream edge of the cylinder) to $x' \approx 2.5$. The vectors (whose magnitude and directions are given as $(u^2 + w^2)^{0.5}$ and arctan (w/u)), present uw velocity [m s^{-1}] while the coloured contours present v velocity [m s^{-1}] component.

5-34

5.4.3.2 Transition Test Off - Centreline Slices (y' = 025, 0.5 and 0.75), Collared Cylinder

Figure 5-18 shows the off-centreline $y' = 0.25$, 0.5 and 0.75 slices downstream of the collared cylinder during the transition test. The flow fields along each plane are similar to the corresponding smooth cylinder fields.

5.4.4 Downstream Transition Flow Velocity Slices, Helical Strake Cylinder

5.4.4.1 Transition Test Centreline Slices, Helical Strake Cylinder

Figure 5-19 presents the centreline slices for the downstream transition helical strake cylinder test. The upstream slice for the $y'=0$ plane which covers $x' = 0.5 - 1.625$ appears highly anomalous, and does not fit with the other data – after checking for errors in the data processing – and finding none – this remains unexplained, but may be due to malfunctions during data collection. From $x' = 1.5$ downstream the mean flow gradually increases back to the undisturbed value, and lateral v' velocity is low.

5.4.4.2 Transition Off-Centreline Slices, Helical Strake Cylinder

The off-centreline $y' = 0.25$, 0.5 and 0.75 slices for the downstream transition helical strake cylinder test are also presented in Figure 5-19. The flow fields along each plane are very similar to the corresponding collared cylinder mean flow fields.
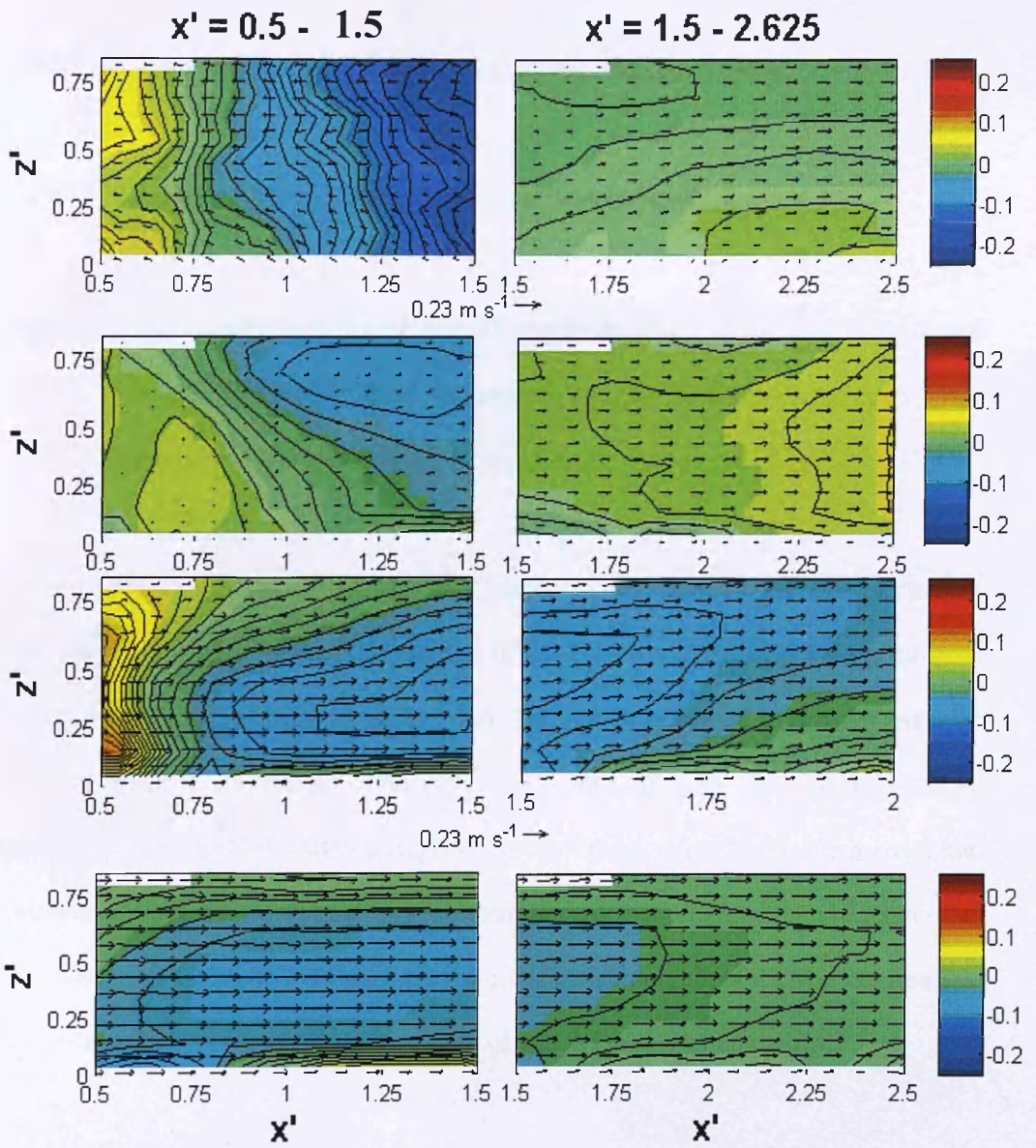
Figure 5-19. Vertical flow slices of the transition helical strake wake flow along the $y' = 0$ (top row), $y' = 0.25$ (2nd row), $y' = 0.5$ (3rd row), $y' = 0.75$ (bottom row) covering $x' = 0.5$ (the downstream edge of the cylinder) to $x' \approx 2.5$. The vectors (whose magnitude and directions are given as $(u^2 + w^2)^{0.5}$ and arctan (w/u)), present uw velocity [m s^{-1}] while the coloured contours present v velocity [m s^{-1}] component.

5.4.5 Downstream Mean Flow Field of the Collared and Helical Strake Cylinder

5.4.5.1 Time Series 2D PIV, Collared Cylinder Downstream Centreline Flow

In order to help understand the complex downstream flow field behind the collared cylinder and how this differs from the smooth cylinder, a selection of time-series vector maps are presented below.

Figure 5-20 shows time-series 2D vector maps representing nine seconds of flow at one second intervals. These data are part of the 2 minute time-averaged vector map for the same position shown in Figure 5-16. The data is presented in two-dimensional form as the three-dimensional form is very complex and much harder to interpret at this time-scale. The time-series does provide vector maps every $1/15^{th}$ of a second, but this was found to be too short a time to determine any meaningful structure within the flow field. Annotated on the figure are red circles which highlight the vortices and red arrows that indicate downstream flow both of which are referred to below.

The figure describes clearly the main features of the flow field shown in Figure 5-16 for example; the large rotation above the lower collar at $z' = 0.4$ clearly visible at 3, 5, 6 and 7 seconds, and the strong streamwise downstream flow situated above the lower collar at $z' = 0.4$. Other features are present in these time series that are averaged out over two minutes for example; the interaction of three vortices, one below the lower collar, the main rotation above it and a third near the surface in line with the upper collar at $z' = 0.8$. The two collars, which are situated at $z' = 0.4$ and 0.8, clearly act as separation points with flow reversal present below the lower collar clearly defined

from the strong downstream flow. Below the lower collar, there is flow reversal and often a vortex is formed of the opposite sign to the main rotation above the collar and is shed downstream. The main vortex is present in the majority of the flow slices and also appears to be periodically shed downstream. In some slices (for example slice seven and nine) there is a third vortex that has an opposite sign of rotation (clockwise) to the main vortex.
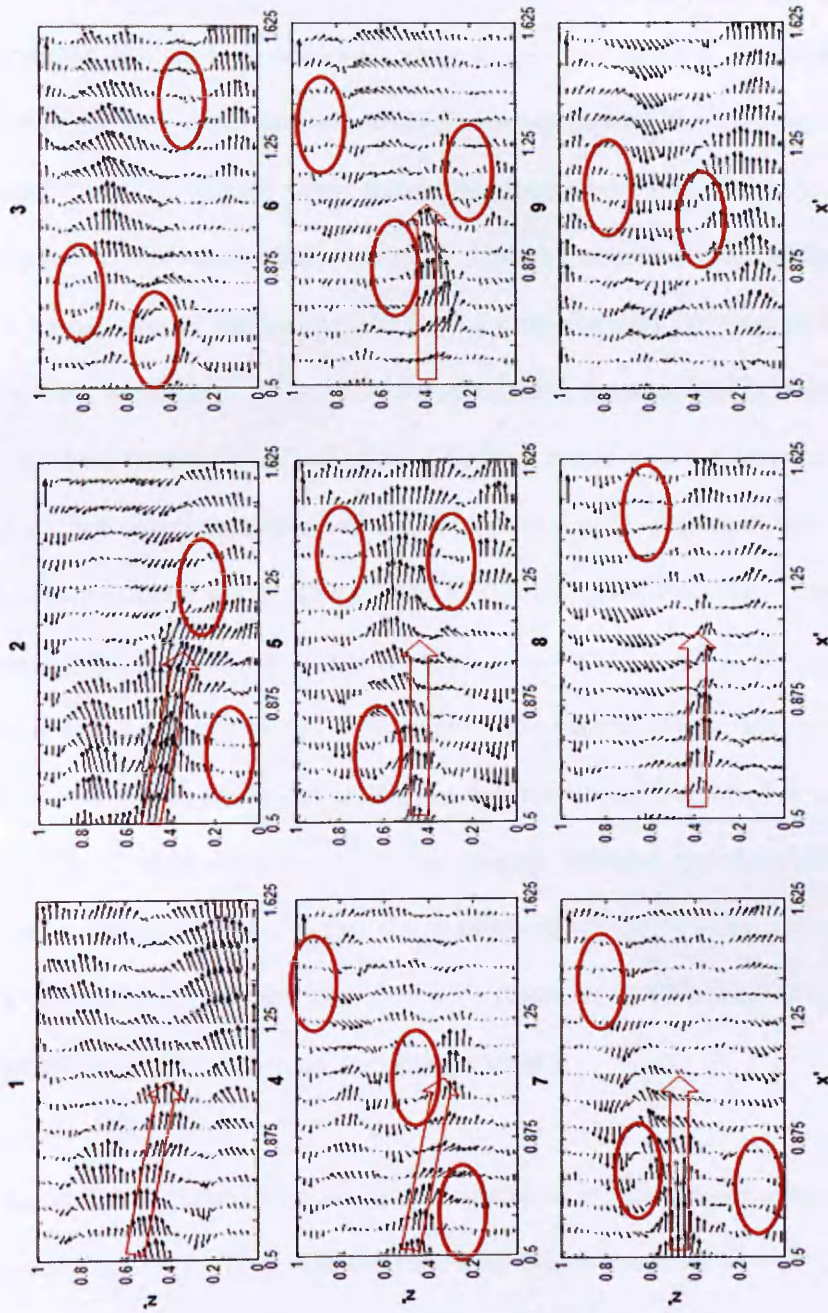
Figure 5-20. Time-series 2D vector maps taken at one second intervals of the centreline flow behind the collared cylinder.

5.4.5.2 Downstream Mean Flow Field of the Collared and Helical Strake Cylinder

The overall picture provided by the observations is of a flow field which is highly complex and three-dimensional. Flow in the u-w plane is dominated by a large horizontal axis vortex that reduces in size and strength with increasing distance off the centreline. The rotation wraps around the downstream side of the cylinder becoming weaker with distance off the centreline. On the downstream side of the rotation there is a small area of stagnation. As both the time-averaged and time-series vector maps have shown (Figures 5-16 and 5-20 respectively), there appears to be little evidence of the lateral formation and shedding of vortices common to the smooth cylinder (§3.4). Any such vortex formation and shedding is lost in the flow field which is dominated by the horizontal vortex. This is particularly clear in the time-series data (Figure 5-20) which shows the formation and shedding of horizontal vortices on the centreline. The flow near the bed is oriented downstream and enhanced. The v component distribution is more complex and harder to describe than the streamwise flow but indicates that the rotation is three-dimensional. Some analogy between the downstream horizontal vortex and the horseshoe vortex can be made, as both seem to share similar properties; a horizontal axis of rotation, three-dimensionality with strong lateral flow, and a location close to the cylinder, wrapping around it.

The following description of the downstream flow field can be given in light of the results described above. On the centreline the downstream flow at the base of the vortex originates from off the centreline from the adjacent lateral measurement plane and is directed towards the centreline and the un-measured side of the cylinder. The reversed near-surface flow is laterally positive indicating movement away from the

centreline (i.e., into the page). Along the next lateral plane (i.e., the $y' = 0.25$ plane) the distribution of v is opposite to that on the centreline with negative flow at the bed and surface either side of a positive flow below the vortex. The configurations in the remaining two lateral measurement planes revert back to the centreline distribution with positive near bed and surface flow, and negative flows at mid-depth. The helical straked cylinder downstream flow field is very similar to the collared cylinder. Centreline v distribution is opposite to the collared cylinder with negative near-bed and surface flows and positive flow near the rotation and across the midddle of the slice. Along the off-centreline planes v is negative across the majority of the slices indicating movement towards the centreline. The implication is that the centreline flow vortex is three dimensional with significant lateral flow causing the flow to rotate three dimensionally around its axis. In the helical cylinder wake the vortex is smaller and is not present at the first off-centreline plane, as in the collared cylinder wake.

5.4.6 Downstream PIV Turbulence Slices for the Collared and Helical Straked Cylinder

5.4.6.1 Live-bed Collared Cylinder, Centreline Slices

Plots of the turbulence parameters are presented along with the time-averaged mean flow vector map to enable observations of the relationships between turbulence and the mean flow field. Figure 5-21 presents plots of u^+, v^+ and w^+ and the corresponding vector map for $x' = 0.5 - 1.625$. The largest value of TI is in v^+ as observed downstream of the smooth cylinder. The location of maximal v^+ spans the region of greatest lateral shear between positive and negative v in the mean flow

which is located between $x' = 0.5 - 1$. u^+, which is slightly weaker than v^+, is enhanced in the regions of largest streamwise shear: near the bed, below and within the rotation. w^+ is the least strong TI and is broadly stronger in the live-bed flow and weaker near the bed and surface.

Reynolds stress distributions are presented in Figure 5-22. τ_{uw} and τ_{uv} have coherent distributions of larger values in and around the vortex where shear in u and w is greatest. τ_{vw} is the weakest and least coherent component. The strong values of τ_{uv} are not surprising given the horizontal dominance of TI observed above. However, unlike the smooth cylinder (Figure 3-21) τ_{uw} is as equally strong as τ_{uv} due to the large vertical shear in u.

The observations of TI and Reynolds stress distributions above present an image of a wake flow that is dominated by strong lateral movements, but also strong shear and streamwise turbulence, unlike for the smooth cylinder. The very close relationship between τ_{uw} and τ_{uv} distributions further implies a strong lateral component in the downstream vortex.
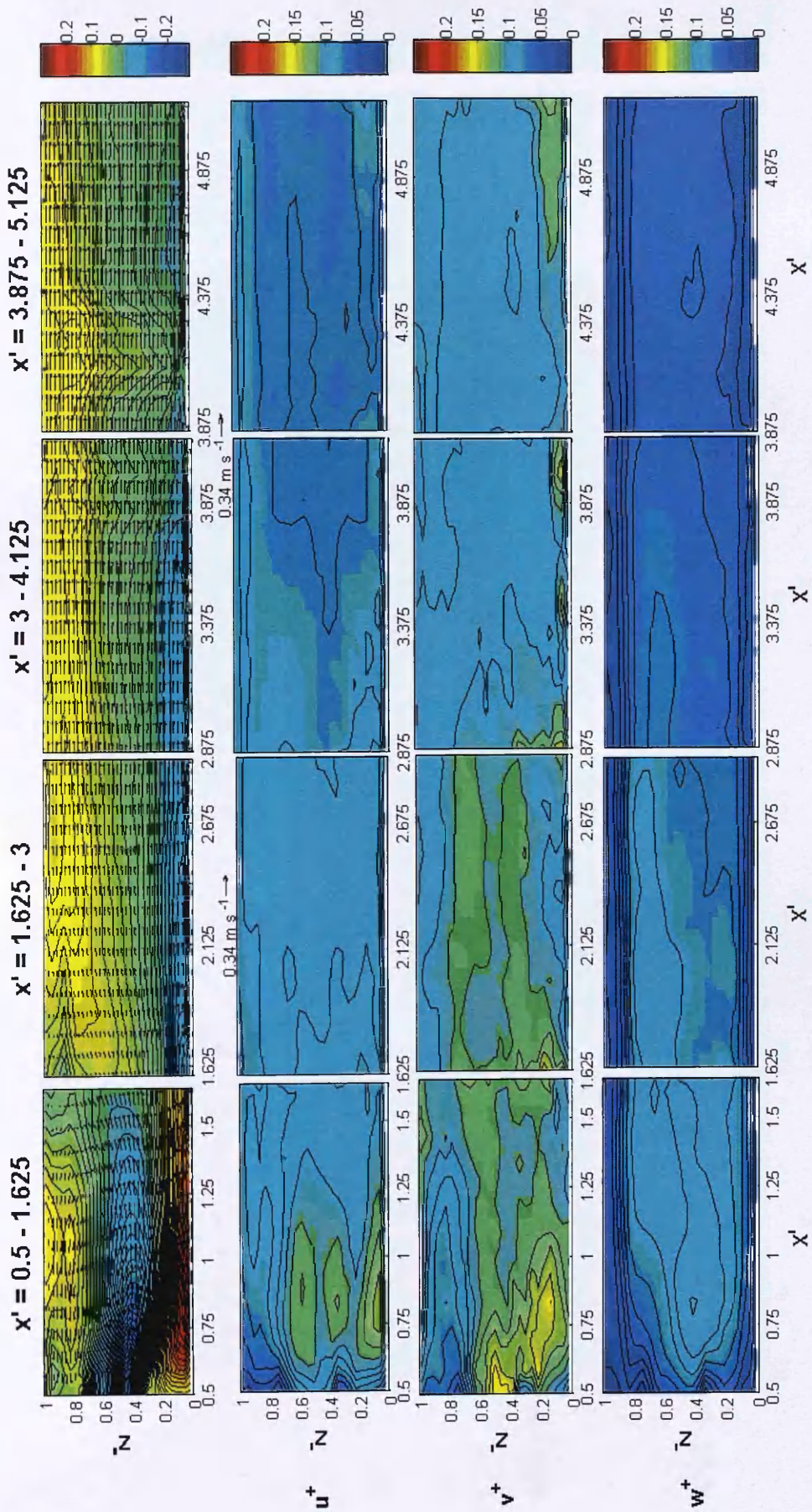
Figure 5-21. Turbulence intensities u^+, (2nd row) v^+ (3rd row), w^+ (bottom row) and mean flow (top row) for the live-bed test collared cylinder along the $y' = 0$ (centreline) plane.
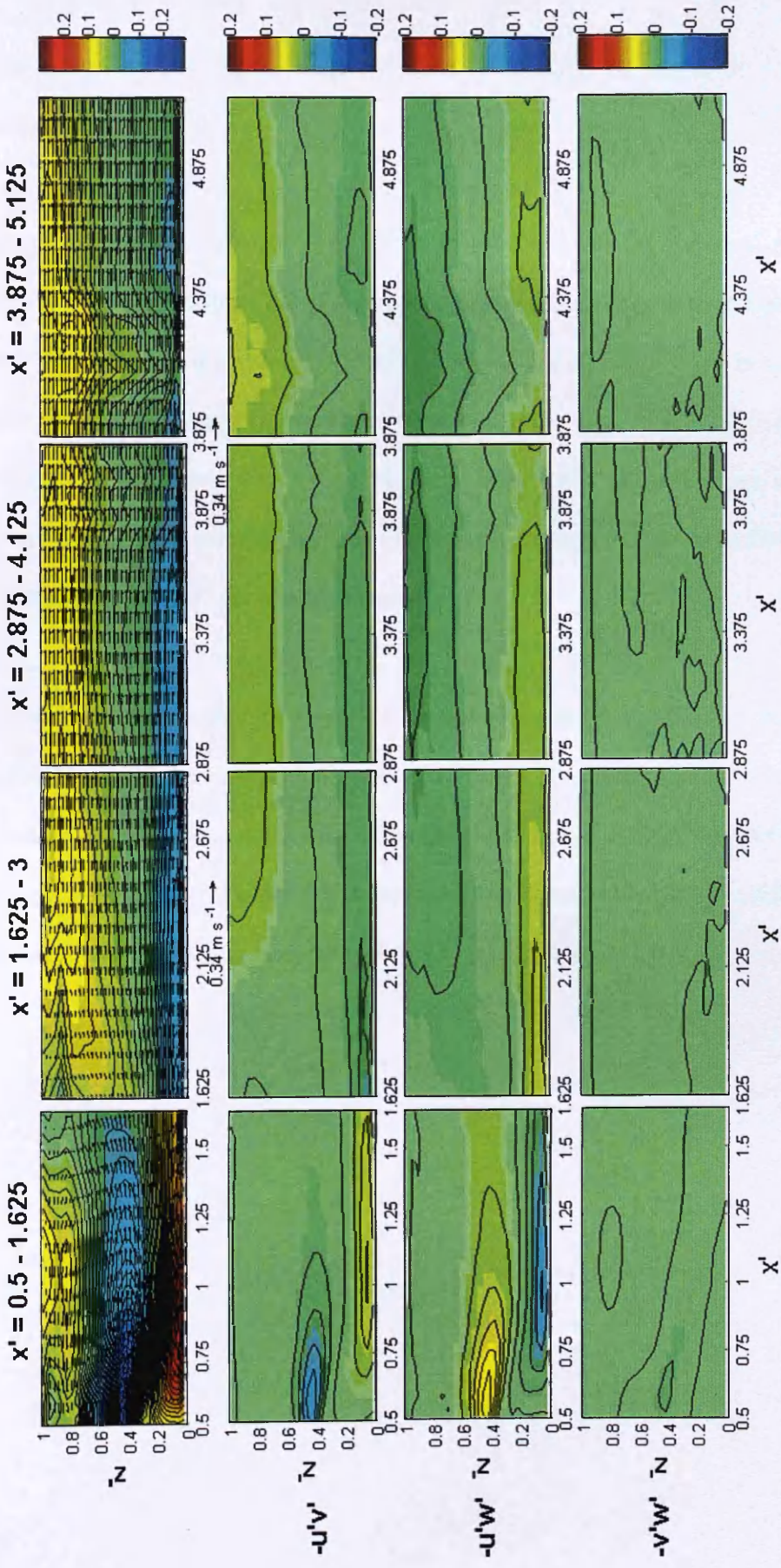
Figure 5-22. Reynolds Stress contours $-uv$, (2nd row) $-uw$ (3rd row), $-vw$ (bottom row) and mean flow (top row) for the live-bed test collared cylinder along the $y' = 0$ (centreline) plane.

5.4.6.2 Live-bed Test, Off - Centreline Slices (y' = 0.25, 0.5 and 0.75), Collared Cylinder

Figures 5-23 presents plots of TI along the $y' = 0.25$, 0.5 and 0.75 planes. At $y' = 0.25$, v^+ is again the strongest TI (near the bed where there is greatest lateral shear) followed closely by u^+ with w^+ significantly lower but also distributed in a similar lobe shape which extends outwards from underneath the vortex. In the $y' = 0.5$ and 0.75 planes where there is no reversal or vortex, values of u^+ are the largest with v^+ second largest and remaining high due to the relatively large lateral flow still present in this region, while w^+ remains the lowest.

Figure 5-24 presents plots of Reynolds stresses along the $y' = 0.25$, 0.5 and 0.75 planes. In the $y' = 0.25$ plane plots show raised values of τ_{uw} and τ_{uv} in the region of enhanced positive lateral mean flow below the rotation. τ_{uw} and τ_{uv} are particularly strong along the $y' = 0.5$ plane due to the strong lateral and streamwise shear in these regions. These then become less strong in the $y' = 0.75$ plane.
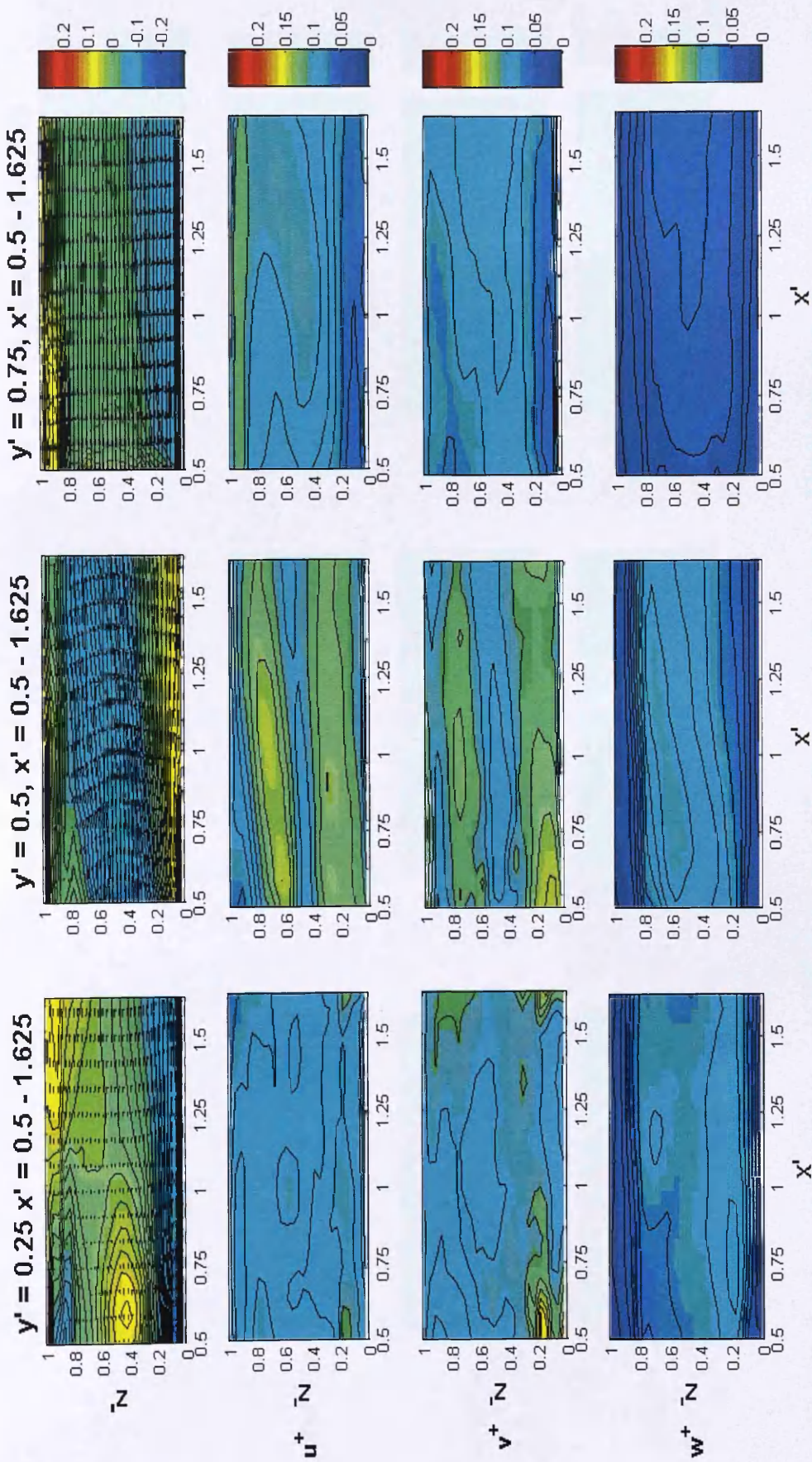
Figure 5-23. Turbulence intensities u^+, (2nd row) v^+ (3rd row), w^+ (bottom row) and mean flow (top row) for the live-bed test collar cylinder along the $y' = 0.25$, 0.5 and 0.75 planes.
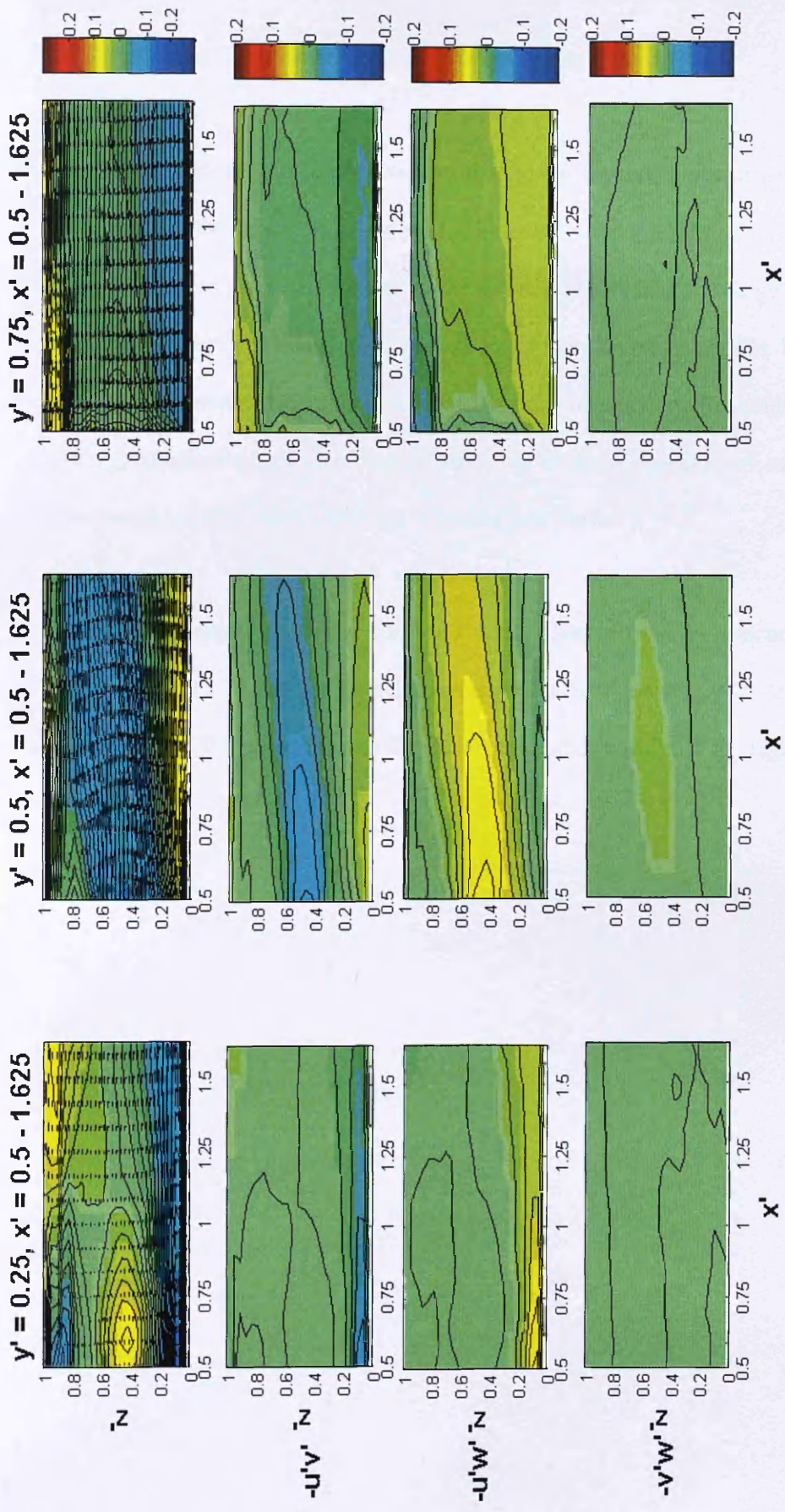
Figure 5-24. Reynolds Stress contours $-uv$, (2nd row) $-uw$ (3rd row), $-vw$ (bottom row) and mean flow (top row) for the live-bed test collar cylinder along the $y' = 0.25$, 0.5 and 0.75 planes.

5.4.6.3 Live-bed Test, Centreline Slices, Helical Strake Cylinder

Figure 5-25 presents the TI distributions and the corresponding vector maps for $x' = 0.5 - 5.125$ for the helical strake cylinder. The distribution of TI shows $v^+ > u^+ > w^+$. Large v^+ and u^+ is located close to the cylinder where there is large lateral and streamwise shear. w^+, though significantly lower than the other two TIs, is increased just below the vortex where there is significant downward flow. Reynolds stress τ_{uv} and τ_{uw} distributions are also closely correlated to the two regions of strong lateral flow (positive below the rotation, and negative near the bed).

Figure 5-26 presents centreline Reynolds stress plots and the corresponding vector maps for $x' = 0.5 - 5.125$ for the helical strake cylinder. τ_{uv} and τ_{uw} are largest while τ_{vw} is close to zero across most of the slice but becomes positive in the region of large positive lateral velocity.
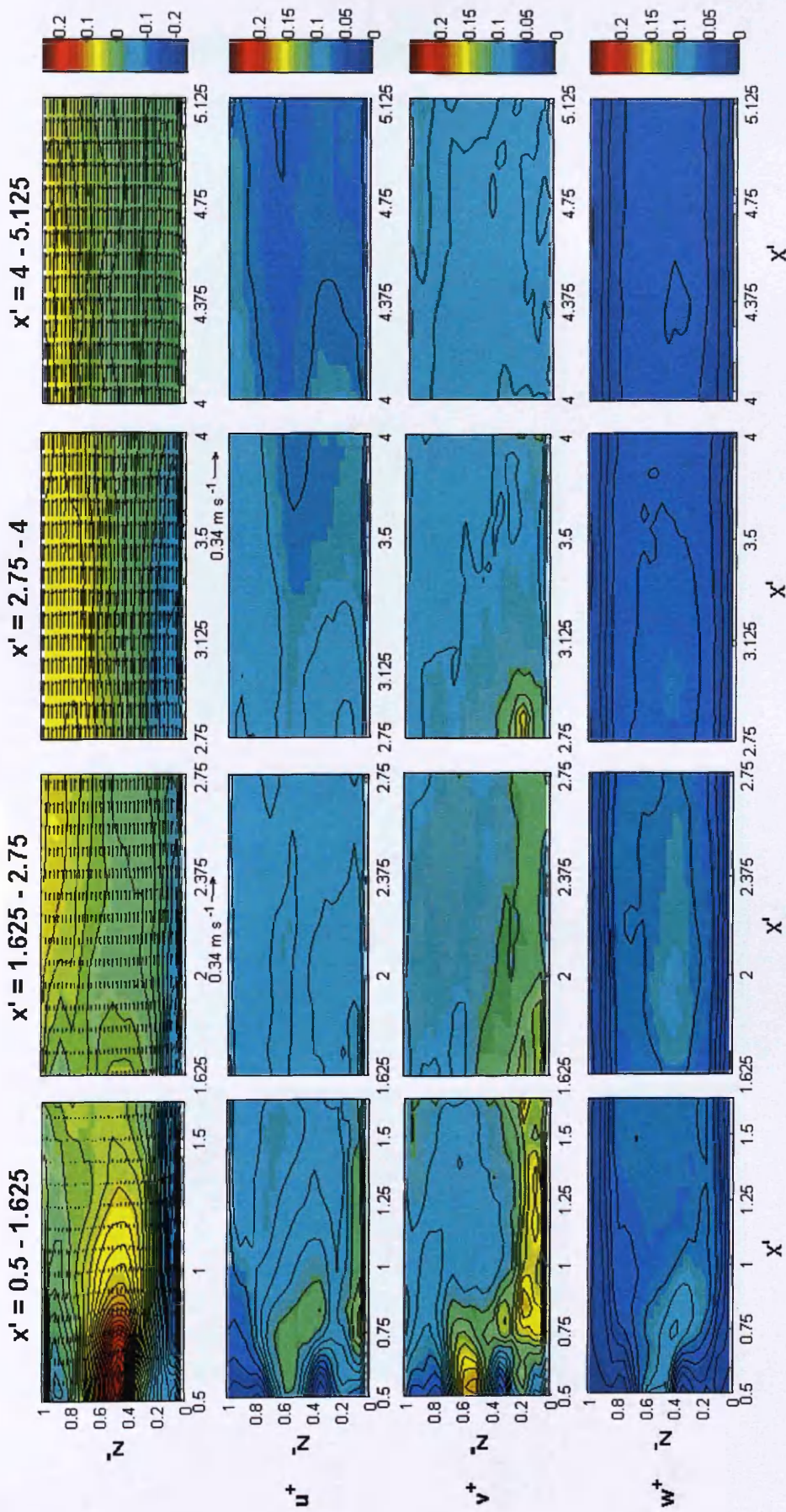
Figure 5-25. Turbulence intensities u^+, (2nd row) v^+ (3rd row), w^+ (bottom row) and mean flow (top row) for the live-bed test helical strake cylinder along the $y' = 0$ (centreline) plane.
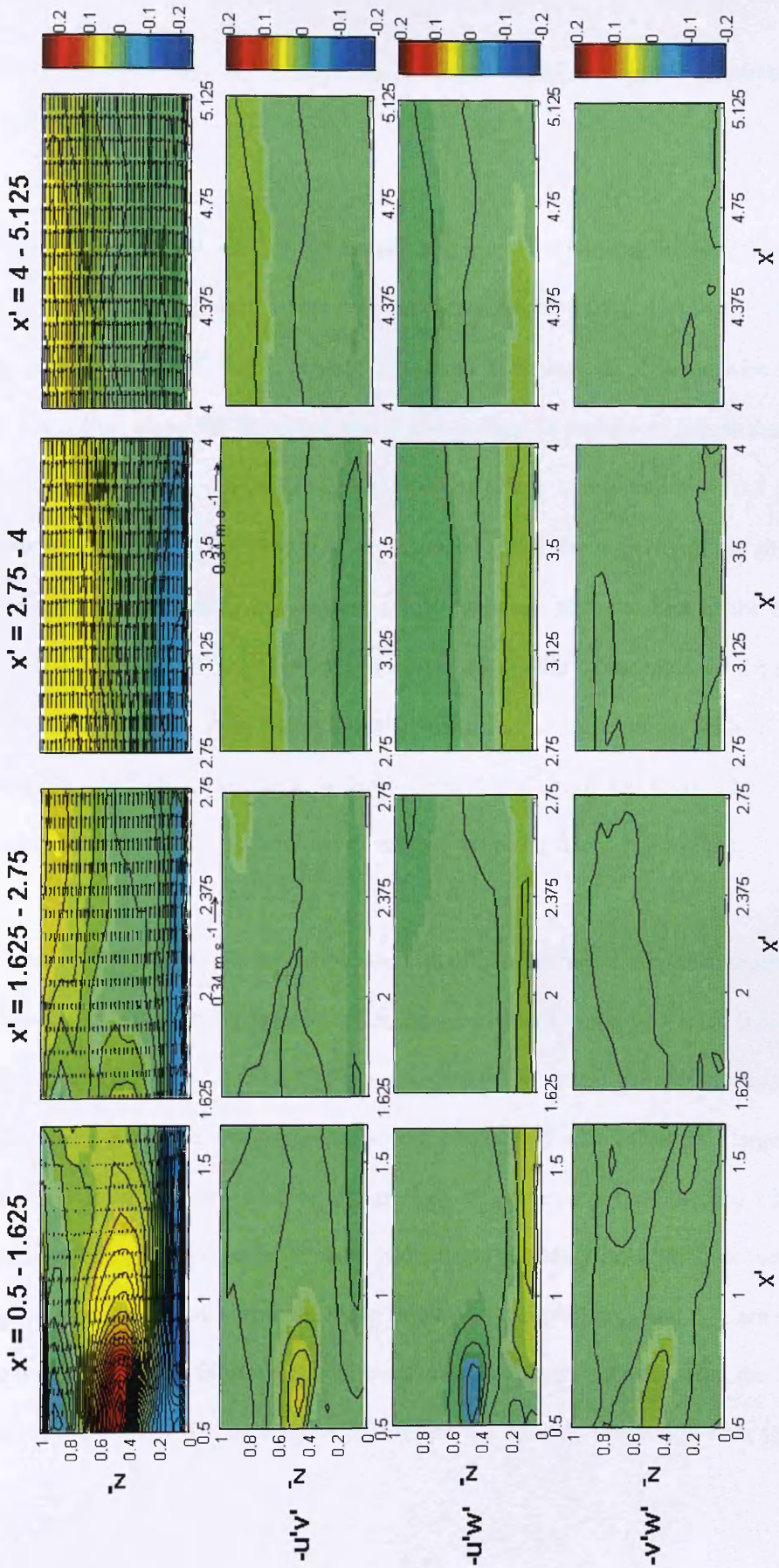
Figure 5-26. Reynolds Stress contours – uv, (2nd row) – uw (3rd row), – vw (bottom row) and mean flow (top row) for the live-bed test helical strake cylinder along the $y' = 0$ (centreline) plane.

5.4.6.4 Live-bed Test, Off - Centreline Slices (y' = 0.25, 0.5 and 0.75), Helical Strake

Cylinder

Figure 5-27 presents the TI distributions and the corresponding vector maps for $x' =$ 0.5 - 1.625 for the helical strake cylinder along the $y' = 0.25$. The distribution of TI again shows $v^+ > u^+ > w^+$. Large u^+ is located in the regions of streamwise shear. v^+ is larger than along the centreline and is also located in regions of lateral shear. w^+ is generally enhanced across the middle of the slice. Along the $y' = 0.5$ plane TI distributions are $u^+ \approx v^+ > w^+$. u^+ is enhanced across the majority of the slice due to the streamwise shear in this region. v^+ is enhanced near the bed in the region of greatest lateral shear. w^+ is enhanced across the middle of the slice. In the $y' = 0.75$ plane the flow field is still significantly influenced by the cylinder with u^+ greatest near the surface where there is large streamwise shear. However, the values of turbulence intensity are much lower than they are along the $y' = 0.5$ plane.

Figures 5-28 present the Reynolds stress distributions and the corresponding vector maps for $x' = 0.5 - 1.625$ for the helical strake cylinder in the $y' = 0.25, 0.5$ and 0.75 planes. In the $y' = 0.25$ plane τ_{uw} is the largest of the three Reynolds stresses and has a tendency to become positive near the bed, particularly where there is a large amount of shear in the streamwise flow. τ_{uv} is close to zero except near the bed where it is negative due to the presence of some streamwise boundary layer shear in this region. τ_{vw} is essentially zero across the slice. In the $y' = 0.5$ plane τ_{uv} and τ_{uw} are the most coherent with both forming two distinct zones of larger stresses near the bed and between $z' = 0.4 - 0.8$. In the $y' = 0.75$ plane τ_{vw} is again essentially zero across the

slice. Values of τ_{uv} and τ_{uw} are lower than those in the $y' = 0.5$ plane, but still remain non-zero across the middle of the slice.
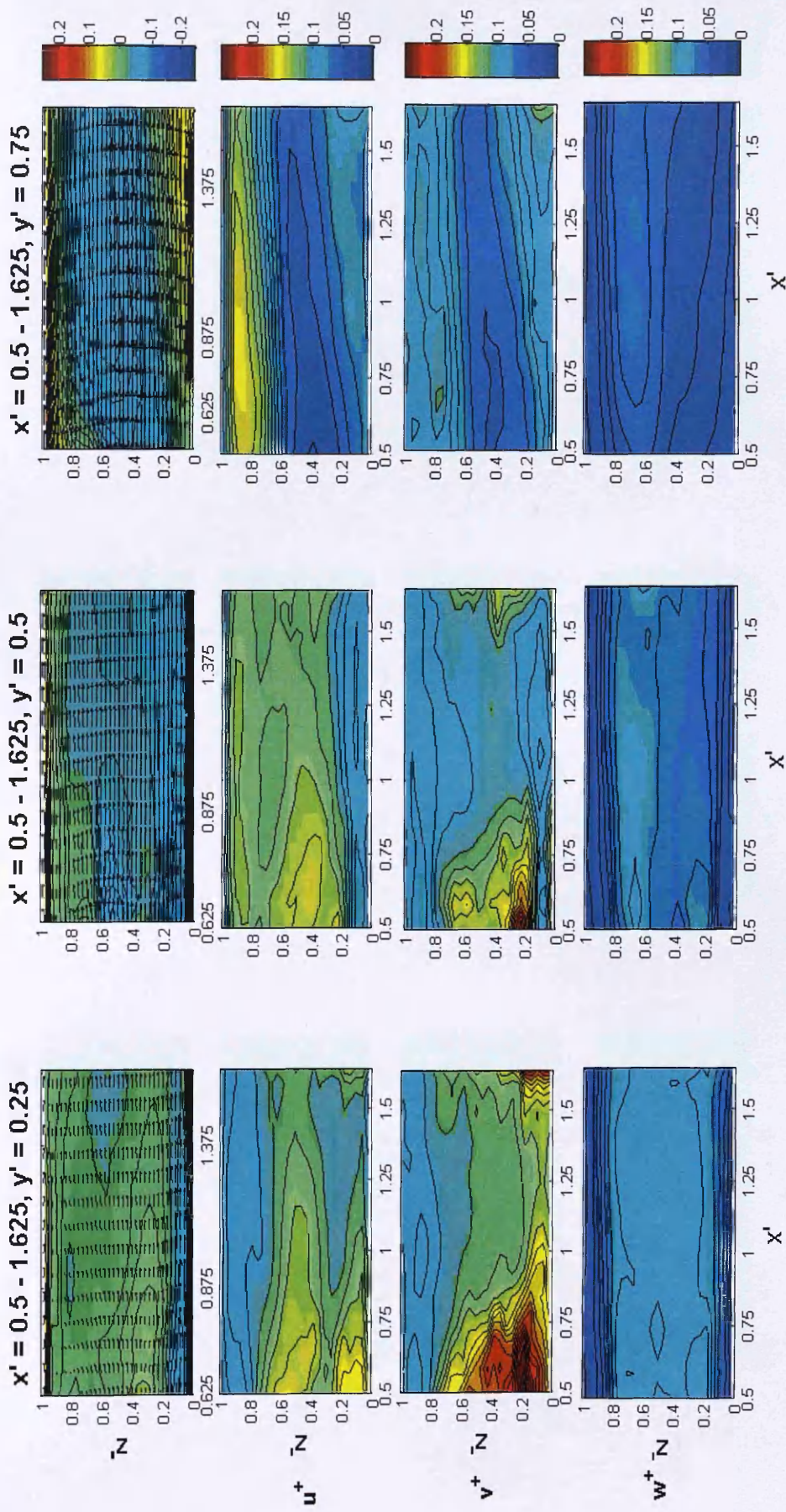
Figure 5-27. Turbulence intensities u^+, (2nd row) v^+ (3rd row), w^+ (bottom row) and mean flow (top row) for the live-bed test helical cylinder along the $y' = 0.25$, 0.5 and 0.75 planes.
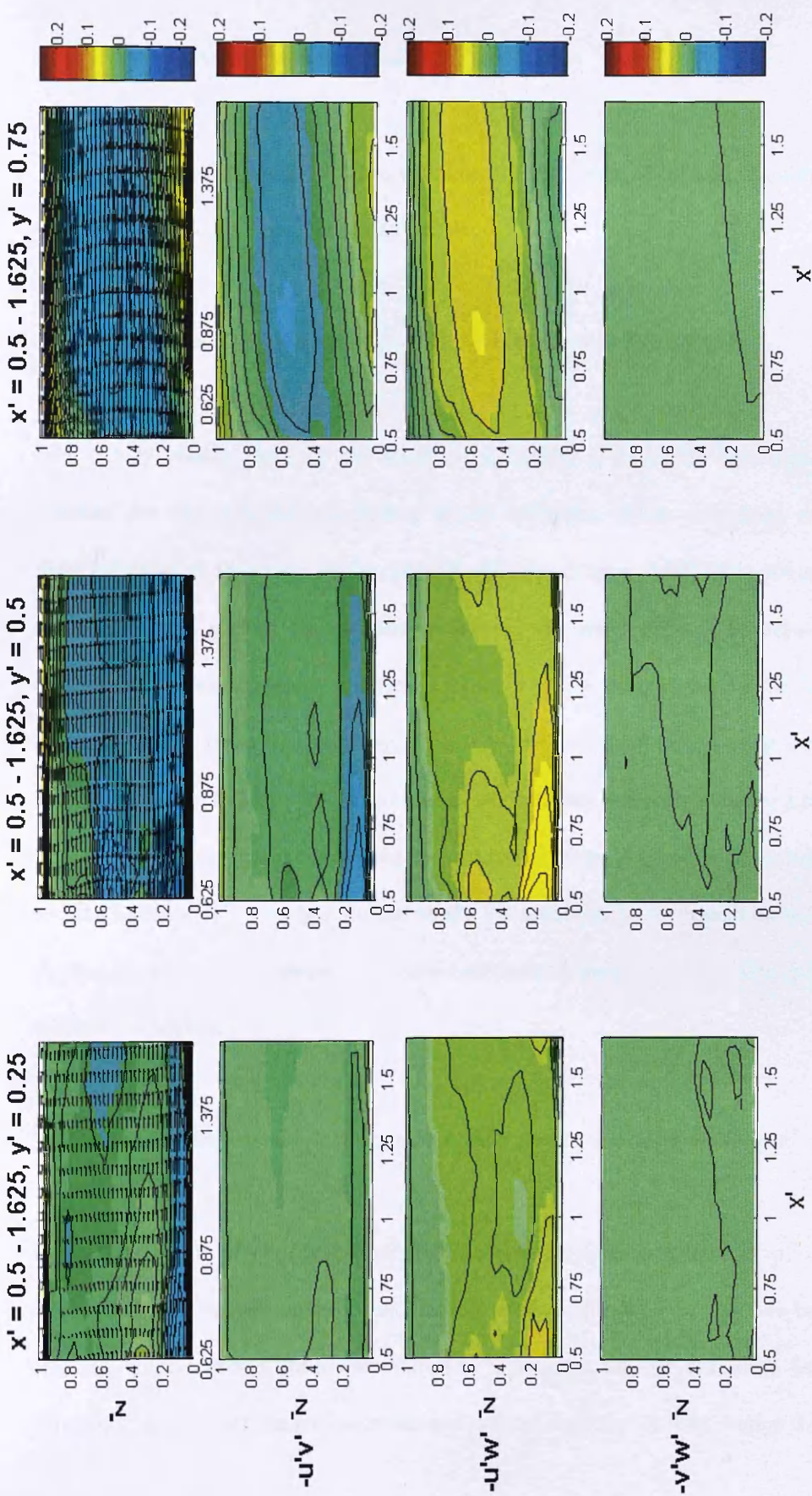
Figure 5-28. Reynolds Stress contours – uv, (2nd row) – uw (3rd row), – vw (bottom row) and mean flow (top row) for the live-bed test helical strake cylinder along the $y' = 0.25$, 0.5 and 0.75 planes.

5.4.7 Upstream Amplification of Bed Shear Stress

As for the smooth cylinder in §3.5, estimates of bed shear stress amplification using the TKE method (§3.5) are presented below.

5.4.7.1 Upstream Amplification of Bed Shear Amplification Distributions

Figure 5-29 shows plots of bed shear amplification α estimates upstream of the cylinder for the collared and helical strake cylinders. When compared with the distribution of α upstream of the smooth cylinder (Figure 3-30) the off-centreline values of α are similar for all three cylinders. The main differences between the collared and helical collared cylinders is found along the centreline. For the live-bed, the centreline increase in α between $x' = -0.3 - 0.133$ clearly visible upstream of the smooth cylinder is clearly suppressed near the collared and helical strake cylinders. This suppression of α is present along the centreline of the live-bed collar cylinder test and the live-bed and transition helical strake cylinder test. In the transition collar test the amplification of bed shear stress is not suppressed, as the lowest collar is situated at the water surface.

5.4.7.2 Near-cylinder Amplification of Bed Shear Amplification Distributions

Figure 5-30 shows plots of bed shear amplification α estimates in the near-pile region of the cylinder for the collared and helical strake cylinders. In the live-bed, the collared cylinder shows the lowest values of α between the two cylinders, ($\alpha < 10$) which is less than both the helical strake and smooth cylinder ($\alpha < 14$, Figure 3-31). In

the transition, the collared cylinder has no effect on the value of α as it is situated at the water surface.
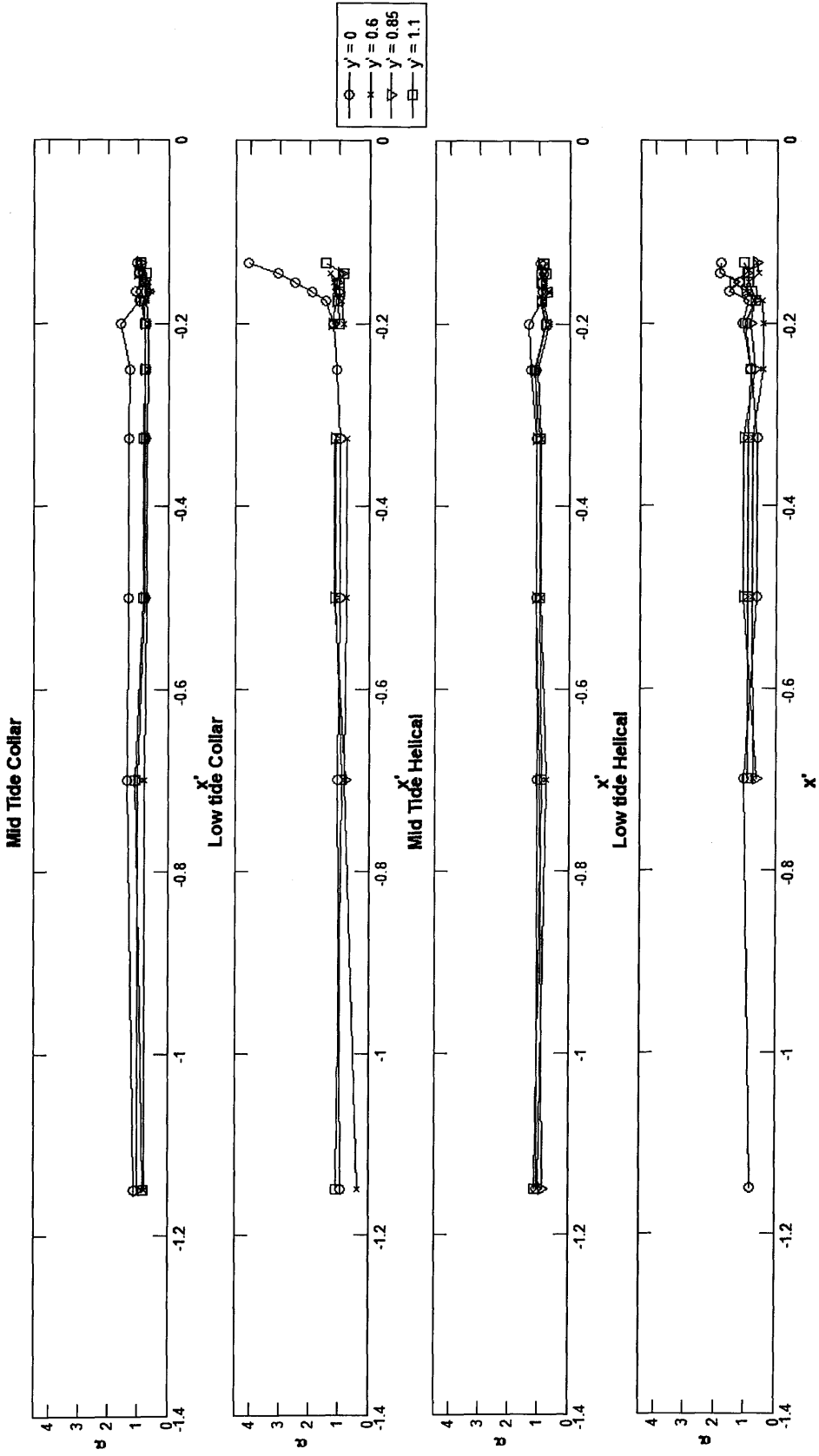
Figure 5-29. Upstream estimates of α for each test.

5-57
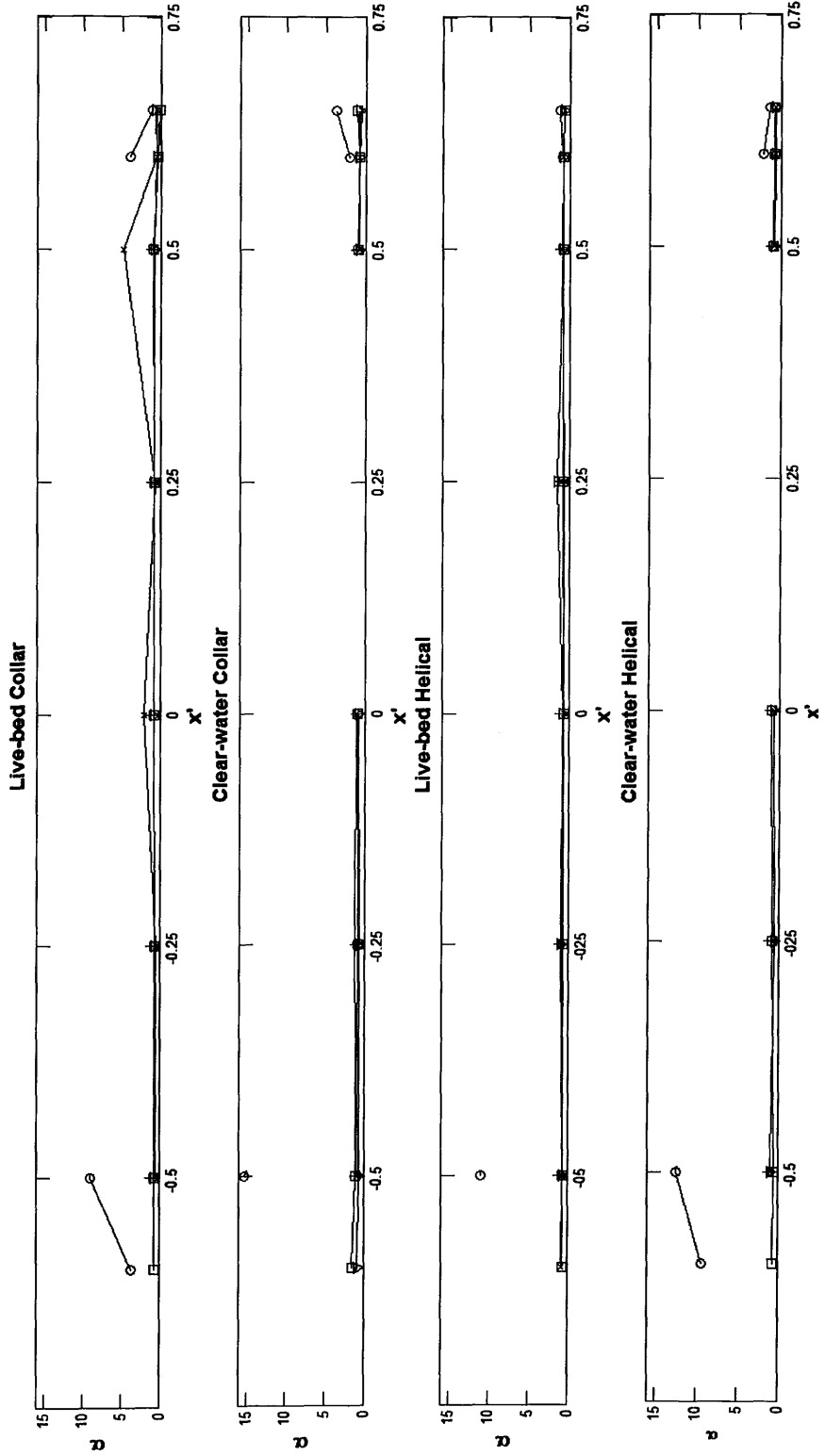
Figure 5-30. Near-cylinder estimates of α for each test.

5.4.7.3 Downstream Amplification of Bed Shear Amplification Distributions

Figure 5-31 shows plots of downstream α for the collared cylinder at live-bed and transition conditions while Figure 5-32 presents the corresponding plots for the helical strake cylinder. Along the centreline, α behaves similarly in both these tests as it does downstream of the smooth cylinder; being < 1 at $x' = 0.5$ before rising to a peak which in both cases occurs between $x' = 0.75$ and 0.875 before reducing with increasing distance downstream. The peak value reached in both cases ($\alpha = 1.8$ at $y' = 0.25$ $x' = 0.5$ and $\alpha = 4.6$ at $y' = 0.25$ $x' = 0.5$ for the collared cylinder live-bed and transition tests, and $\alpha = 2.8$ at $y' = 0.25$ $x' = 0.5$ and 5.6 at $y' = 0.625$ $x' = 0.5$ for the helical strake cylinder live-bed and transition tests) is similar (slightly less in places) to those downstream of the smooth cylinder. Off-centreline the distribution of α for both the collared and helical strake cylinder is much the same as for the smooth cylinder.

In the transition test, the distribution of α is much the same for the helical and collared cylinder as it is for the smooth cylinder (Figure 3-32). The main difference is along the $y' = 0.5$ plane where α, particularly for the collared cylinder, is enhanced further upstream and decreases with increasing distance downstream. This enhancement of α is also seen in the smooth cylinder, but along the $y' = 0.75$ plane (Figure 3-32).
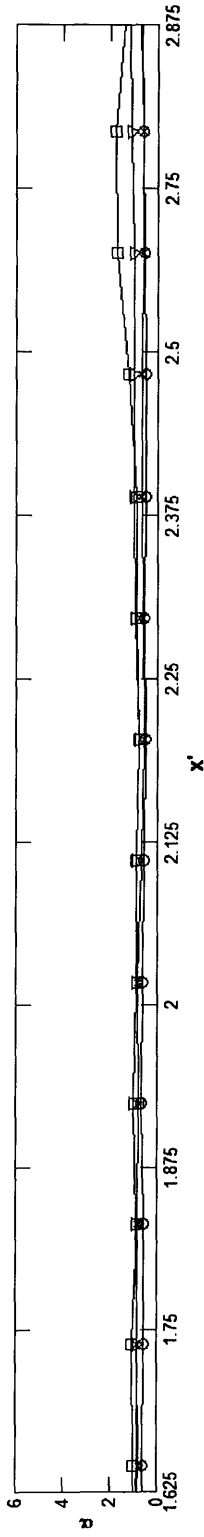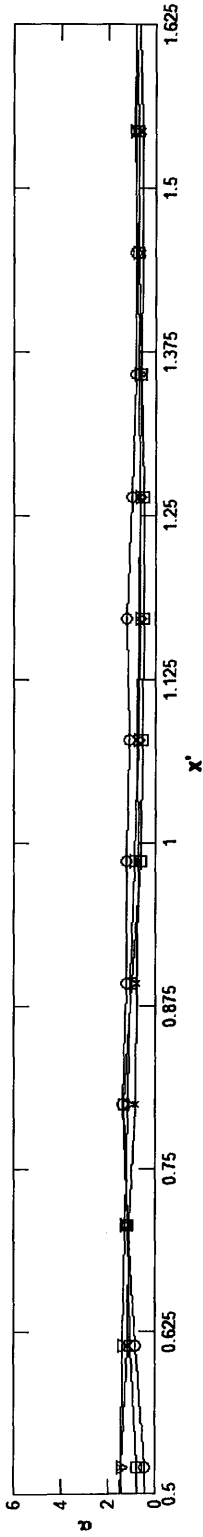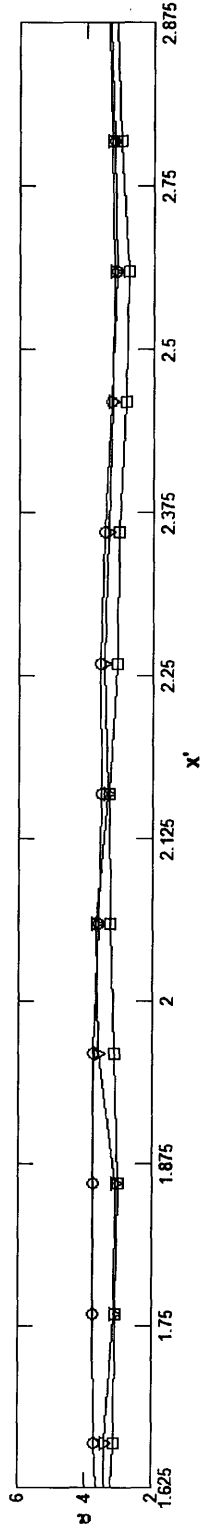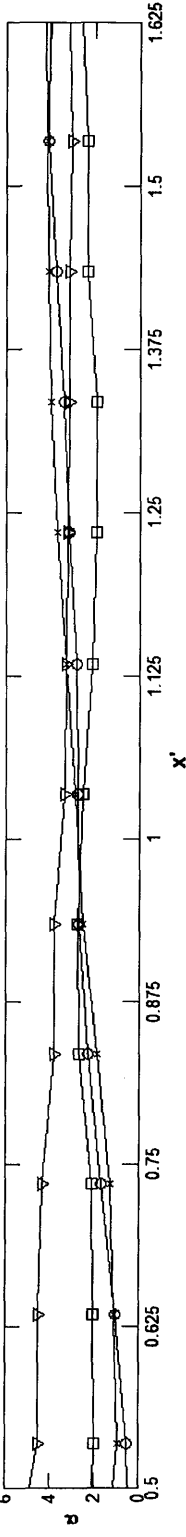
Figure 5-31. Downstream estimates of α for each test collared cylinder.
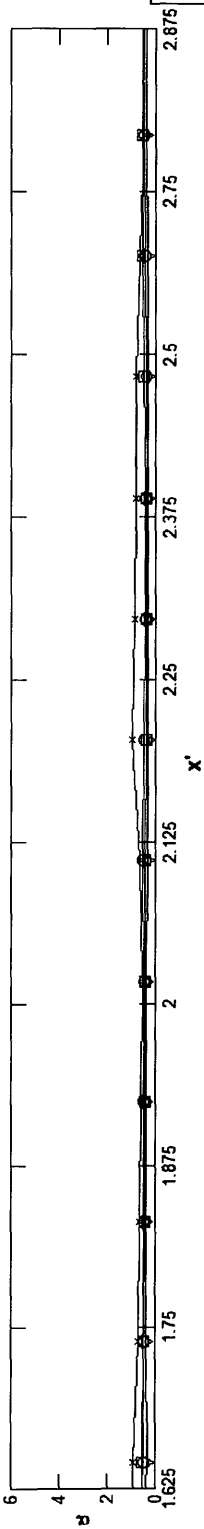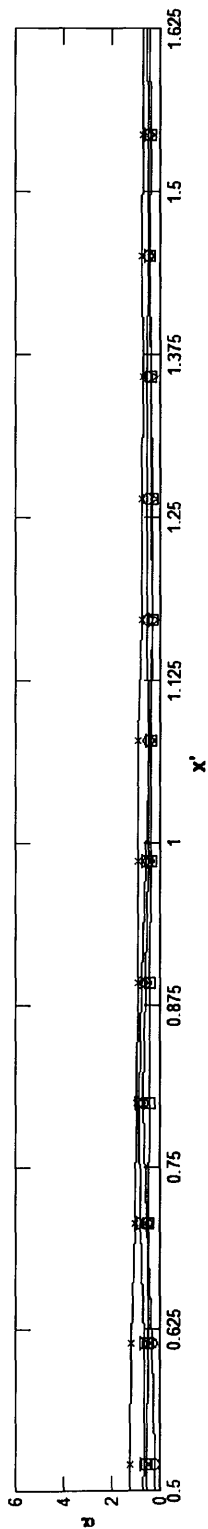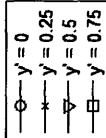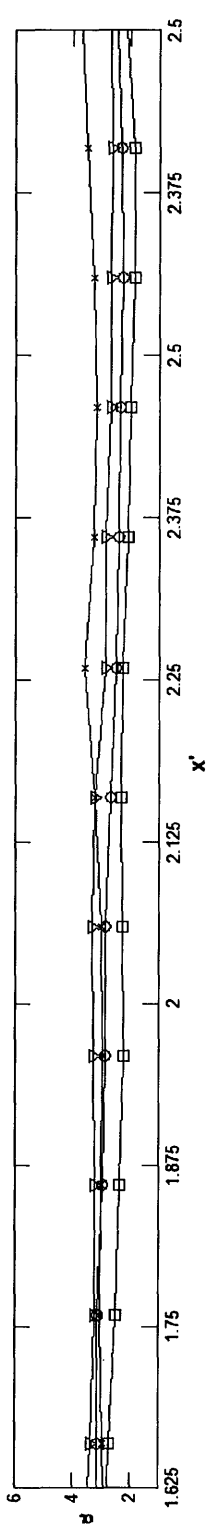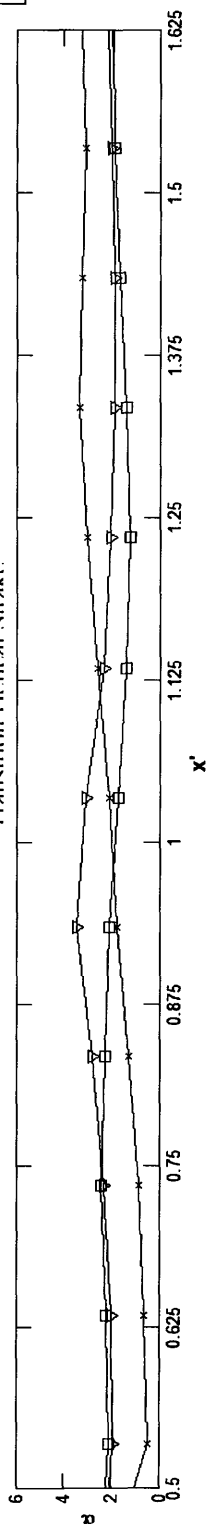
Figure 5-32. Downstream estimates of α for each test helical strake cylinder.

5.5 Quadrant Analysis of Flow Velocity Fluctuations

Quadrant analysis is a tool often employed to detect coherent turbulent structures known as 'burst events'. In these events, upward motion of fluid from the bed (positive w) causes anomalously slow downstream flow (negative u) away from the bed (ejections) and downward vertical motions of fluid (negative w) transport anomalously fast downstream flow (positive u) towards the bed (sweeps). These phenomena are thought to be important modes of sediment re-suspension and transport. The method is applied to the current data in order to determine what differences, if any, there may be in the potential for sediment re-suspension via these phenomena in the downstream flows behind the smooth, collared and helical strake cylinders.

Figure 5-33 shows a quadrant plot of the u and w time series centreline velocity components downstream of the helical strake cylinder at $x' = 0.575$, 1 and 1.5 which were recorded at $z' = 0.02$ (i.e, 0.5 cm above the bed) for the live-bed test. The data was collected using the Nortek 10 MHz Vectrino ADV as described in §2.1.2.3. As can be seen from the distribution within the quadrant plots, there is no clear evidence of preferential occurrence of sweeps and ejections (i.e., the distributions is approximately even in all four quadrants). This plot is also typical of the smooth and collared cylinders.
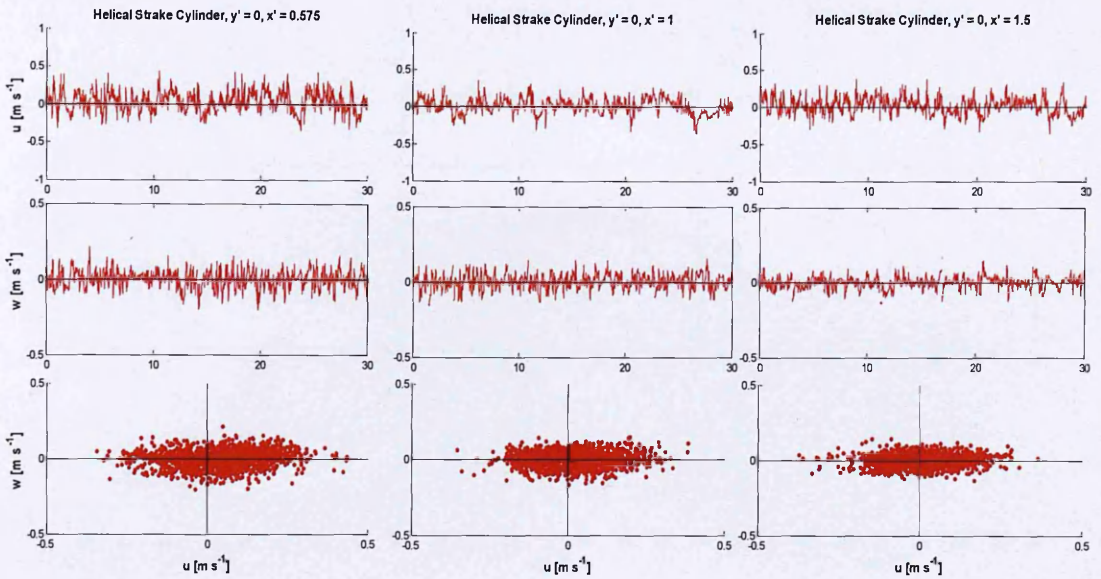
Figure 5-33. Quadrant plot of streamwise u' and vertical w' velocity fluctuations.

Figure 5-34 shows a quadrant plot of the u and w time series centreline, $y' = 0.5$, and $y' = 1$ velocity components downstream of the collared cylinder at $x' = 0.575$ which were recorded at $z' = 0.02$ (i.e, 0.5 cm above the bed) for the live-bed test. The data was collected using the Nortek 10 MHz Vectrino ADV as described in §3.1.2.3. Here again, there is little evidence of any trend towards burst events. This plot is also typical of those for the helical strake and smooth cylinders.
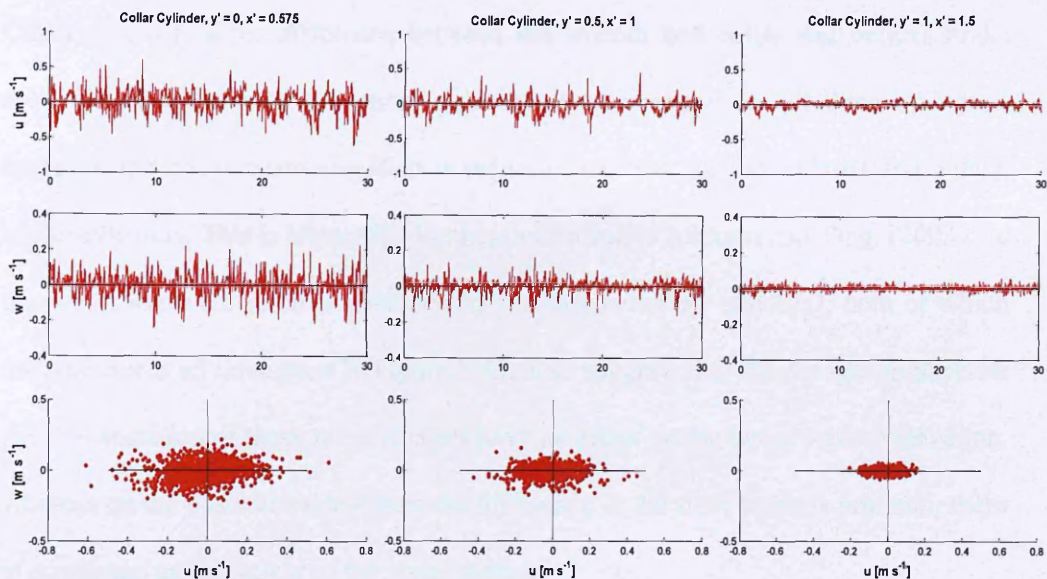
Figure 5-34. Quadrant plot of streamwise u' and vertical w' velocity fluctuations at $x' = 0.5$

and $y' = 0, 0.5$ and 1.

5.6 Water Surface Elevation around the Smooth, Helical Strake and Collared Cylinders

Centreline profiles of water elevation were recorded using an array of pressure sensors in the set-up described in §2.1.2.4. Figure 5-35 shows the change in elevation between the upstream and downstream side of each of the three cylinders. The change in water depth δh, $\delta h = h_{upstream}/h_{downstream}$ where between the upstream and downstream sides of the cylinder has been normalised with cylinder diameter D. In all three cases the water surface is greater on the upstream side than it is on the downstream side. This is the expected result and is evidently caused by the surface roller at the front face of the cylinder (§1.3.7). For the helical and collared cylinder the difference $\delta h/D$

is approximately 0.07 where as for the smooth cylinder it is approximately 0.04. Clearly there is some difference between the smooth and collar and helical strake cylinders. The upstream elevation is essentially unchanged for all three cylinders, however, the downstream elevation is reduced by 0.6cm for the collared and helical strake cylinders. This is interesting because according to Johnson and Ting, (2003) the change in water elevation is governed by the parameters Fr and h/D, both of which are constant in all three plots in Figure 5-35. This suggests that the changes in the flow field downstream of these two cylinders have an effect on the water surface elevation, whereas on the upstream side where the difference in the flow fields is minimal, there is no change on the height of the water surface.
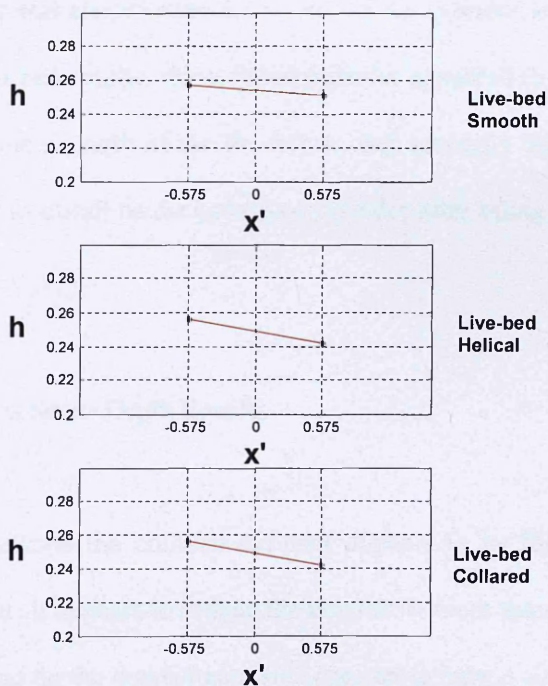
Figure 5-35. The change in water surface elevation on the upstream and downstream

centreline

5.7 Mobile Bed

In this section the variable reversing scour development data from the collared cylinder will be discussed and compared with the smooth cylinder time-series scour development and depth as presented in §4.3.2

5.7.1 Experimental Set-up

The mobile bed tests around the collared and helical strake cylinder were performed in the same flume as the mobile bed tests described in §4. The experimental set-up is described in §2-3 and the procedure and data collection was the same as in §2.3.2. Due to time constraints, only the collared cylinder was chosen for mobile bed tests. The collared cylinder was chosen over the helical strake cylinder for various reasons. Firstly, from the rigid bed results, the collared cylinder appeared to provide a slightly greater reduction in the strength of the downflow, and secondly because it is argued that collars are easier to install on the prototype cylinder after piling. This is discussed further in §5.8.2.1

5.7.2 URS Time Series Scour Depth Results

The results above indicate the collared cylinder appears to be the most promising design to reduce scour; it appears to reduce the downflow more than the helical strake cylinder (§5.3.1.3), and on the downstream side appears to have a similar effect on the reduction of vortex shedding as the helical strake cylinder. It is also likely easier to install on the prototype than the helical strake. To assess this further, the collared

cylinder was included in the mobile bed experiment as described in §2.3. The URS results are presented below for time-steps 1-3 (Figure 5-36), 4-6 (Figure 5-37), 7-9 (Figure 5-38) and 10-12 (Figure 5-39). The probe locations are as described in Figure 2-17. In each figure the initial scour depth present at the start of the time-step is presented by the black crosses on the solid line and the end scour depth by the red crosses on the solid line. Time-series depth readings taken at 5, 10, 15, 20 and 25 minutes are presented. As explained in §4.2, large amounts of suspended sediment in the downstream side of the cylinder during all time-steps prevented time series measurements during the test, and therefore, only the start and end depth still water depth readings are taken from the downstream probes.

In the first half-cycle (Figure 5-36) during time-step one (TS1) the greatest amount of scour occurs on the lateral planes. On both lateral planes the depth of scour reached at the end of TS1 is lower than for the smooth cylinder (2.4 and 1.7 cm for the smooth and collared cylinder on the 90 and 270° planes respectively). The main difference with the smooth cylinder, however, is that the deepest scour depth on the 90° plane is found at $x' = 0.825$ as opposed to $x' = 0.325$ for the smooth cylinder. As for the smooth cylinder, most scour in the half-cycle occurs in the live-bed TS2 with the greatest depth achieved of 4.25 cm at $x' = 0.325$ along the centreline B plane. This depth is less than the depth reached at the same position for the smooth cylinder (5.2 cm). In fact the depth around the collared cylinder is consistently lower than it is around the smooth cylinder until the second half cycle, as will be discussed later (Table 5-2). The deepest scour on the 90° plane is now located at $x' = 0.325$. There is very little change in scour depth during TS3.
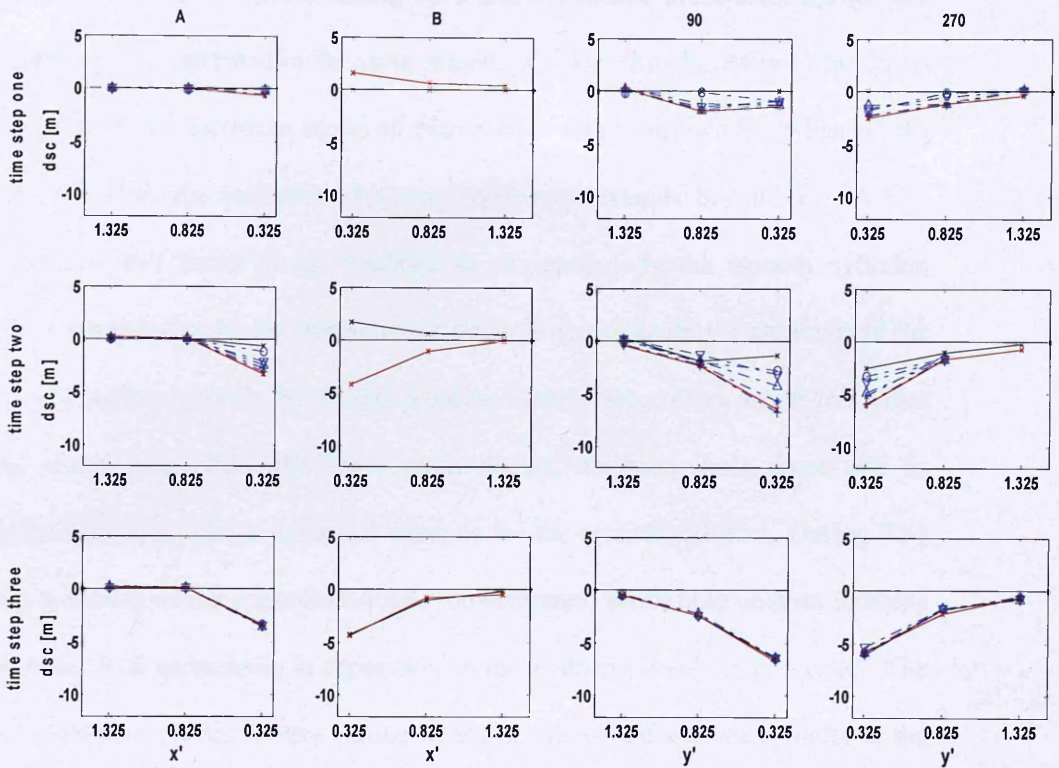
Figure 5-36. URS time series scour development between time steps 1 - 3. Time-series depth readings at 5, 10, 15, 20 and 25 minutes are represented by the circles, down-triangles, up-triangles, stars, and plus signs respectively on solid blue lines.

	1	2	3	4	5	6	7	8	9	10	11	12
Probe 1	0.144	0.6094	0.4965	0.8384	1.933	2.0099	1.8	1.477	1.3892	1.0615	0.3385	0.041
Probe 4	0.9336	0.3021	0.797	0.5577	2.4553	1.6365	1.3348	0.3275	-0.2343	-0.9153	0.291	-0.026
Probe 7	-0.2438	0.9445	1.1238	1.1233	1.9855	1.5932	1.6215	0.246	0.41	0.4399	0.8359	0.9857
Probe 10	0.7447	-0.332	0.3145	0.1603	0.0511	-0.7813	0.4898	-1.6275	-1.1128	-1.0041	0.8116	0.5238

Table 5-2. Difference in scour between the collar and smooth cylinders for each probe and each time-step. A positive value indicates the amount less of scour in cm recorded at the collared cylinder than the smooth cylinder.

During TS4 which is the first time-step with reversed flow, there is very little change in scour depth. The lack of scour during TS 3 and 4 was also present for the smooth cylinder and can be attributed to the same reasons; the low flow intensity of the clear-water (§4.3.2). Scour increases along all planes once more during TS5, when on the upstream A side of the centreline the scour hole now extends beyond $x' = 0.875$. Scour depth is still lower at all positions in comparison to the smooth cylinder, particularly along the centreline where scour depth is approximately 2 cm lower at the $x' = 0.325$ position on both the A and B sides. Clearly the collars are at this point reducing scour. Apart from the lower scour depths, the scour hole shape and its relative time-development is much the same as for the smooth cylinder. During TS6 there is a widening of the centreline A side (downstream) scour hole with an increase in depth along with an increase in deposition on the upstream B side at $x' = 1.325$. The resulting centreline profile is very similar to the profile of the smooth cylinder at the same time-step, only with a significant reduction in depth. The lateral profile remains asymmetrical, however, indicating that the rate of scour is slower than it was for the smooth cylinder (where during TS5 the lateral scour hole profile became effectively symmetrical). In fact the lateral scour hole profile for the collared cylinder only becomes approximately symmetrical during TS8 (the live-bed for the second positive half-cycle). Furthermore, the scour hole is wider for the collared cylinder in the lateral direction, indicating that although there is some reduction of scour depth, the flow field may cause a wider and shallower scour hole. TS6 shows a small increase in scour depth similar to that observed during TS6 for the smooth cylinder.
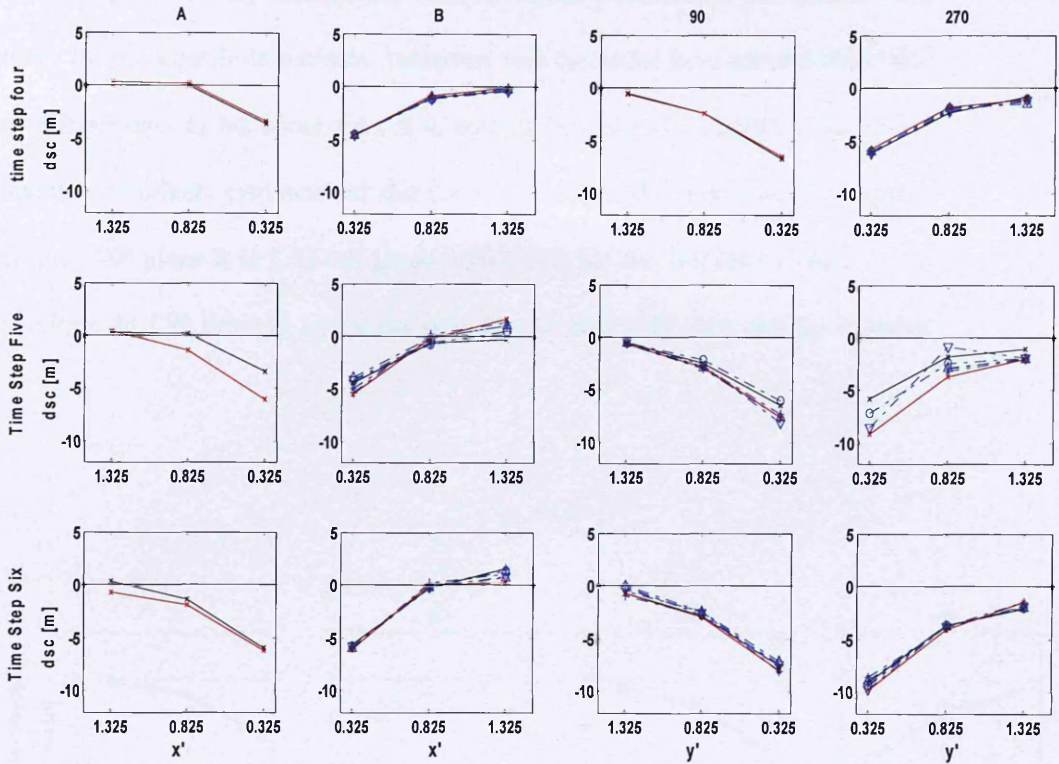
Figure 5-37. URS time series scour development between time steps four to six. Symbols as in

Fig 5-36.

During TS7 (which marks the beginning of the second and final cycle) the scour hole

continues to widen. The increase in depth, however, is only marginal and scour depth

remains lower than for the corresponding positions for the smooth cylinder, though

the difference is now less than at the end of TS5 (1.8 and 1.6 cm lower than the

smooth cylinder on the A and B plane respectively, Table 5-2). Laterally the scour

hole is still asymmetrical but the difference in scour to the smooth cylinder has also

reduced, (being 1.3 and 0.5 cm on the 90 and 270° planes respectively). In TS8 the

scour depth along the centreline increases quite significantly relative to the smooth

cylinder. The difference in depth is reduced to 1.4 cm on the A side and 0.25 cm on

the downstream B side. The collar is clearly no longer having a significant reducing

effect on the depth of scour, which is now similar to the smooth cylinder (Table 5-2). Asymmetry in the scour hole remains, however, and the scour hole around the collar cylinder still appears to be wider than it is around the smooth cylinder. The lateral planes are now relatively symmetrical and the depth on the 90° plane is 0.33 cm lower while on the 270° plane it is 1.63 cm *greater* than it is for the smooth cylinder at the same positions. In TS9 there is, as for the smooth cylinder, very little change in scour depth.
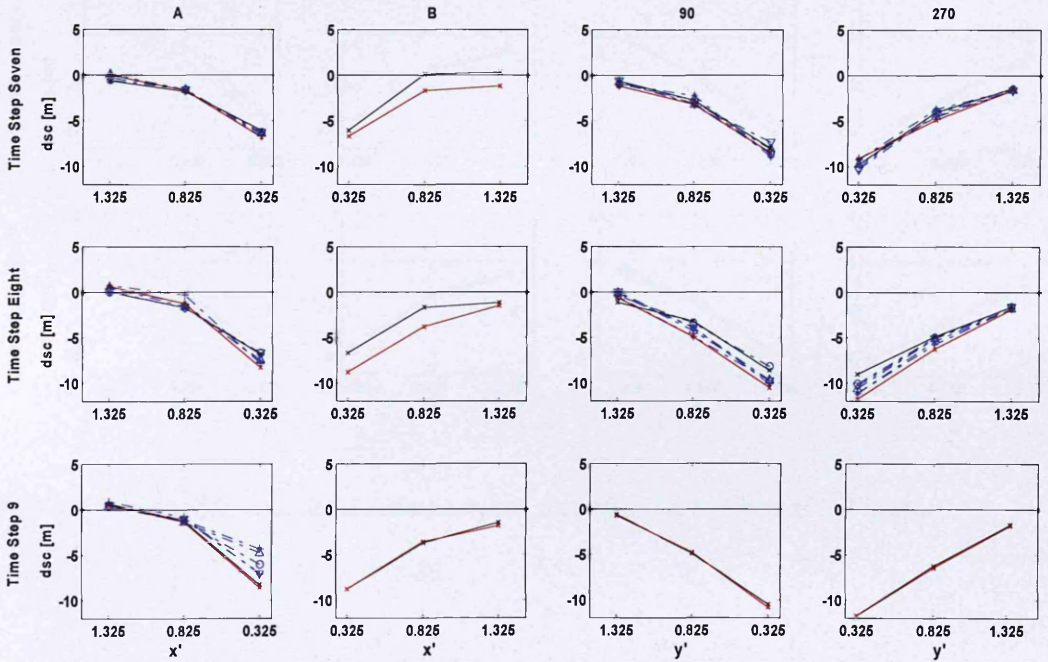
Figure 5-38. URS time series scour development between time steps 7 to 9. Symbols as in Figure 5-36.

In the final half-cycle (TS10-12), there is a marginal increase in scour depth and a steepening of the scour hole slopes. There is essentially no increase in the width of the

scour hole along all planes. At the end of the half-cycle the scour hole is very similar in depth to the smooth cylinder scour hole. The main differences are in its width and profile; it is wider and the slope is not as steep as it is for the smooth cylinder's scour hole (Figure 4-9).
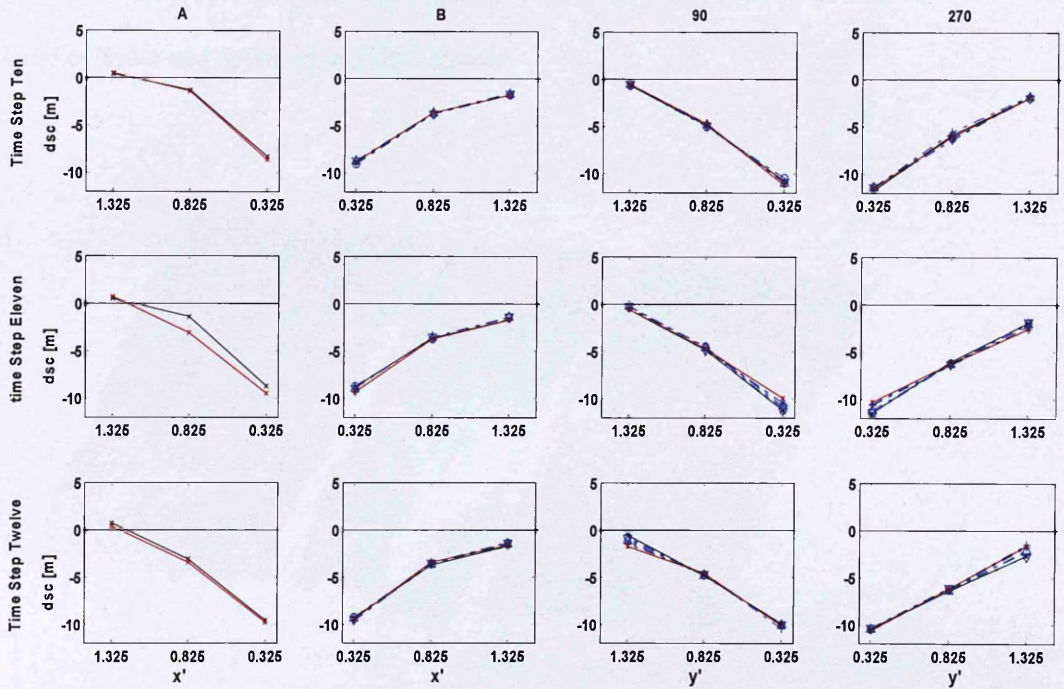
Figure 5-39. URS time series scour development between time 10 to 12. Symbols as in Figure 5-36.

During all time steps it was observed that sediment was deposited on the lower collar on the downstream side. Clearly suspended sediment was caught in the downstream vortex observed in §5.4.1.1. Though the deposition of sediment could not be quantified in this experiment, and it appeared to have negligible effect on the scour depth attained, visual observations demonstrated that it was significant. Its affect on the integrity of the collar is would need to be investigated further.

5-72

5.7.3 End of Test Laser Profiling

As for the smooth cylinder tests, an end of test laser bed profile was made for the collared cylinder (Figure 5-40) and this is compared with the smooth cylinder scour hole (Figure 5-41). The morphologies of both the scour holes are quite similar. The main observable difference is the lower bed level on the up and downstream side of the collared cylinder and apparent smaller ripples.
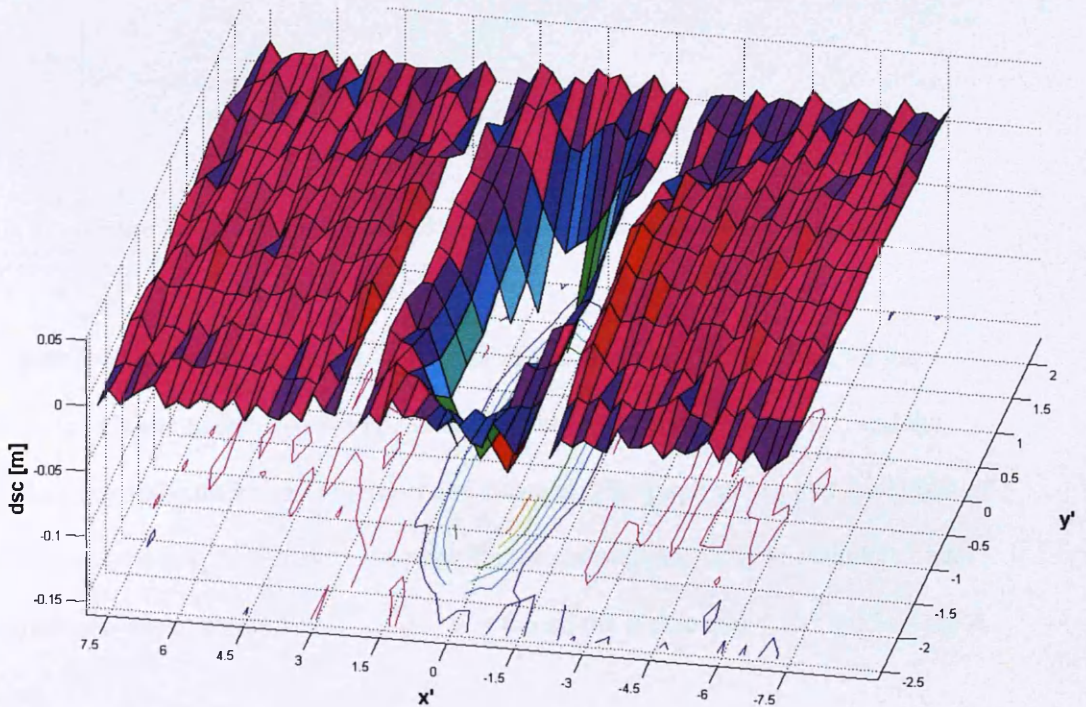
Figure 5-40. End of test laser bed profile of the collared cylinder's scour hole.
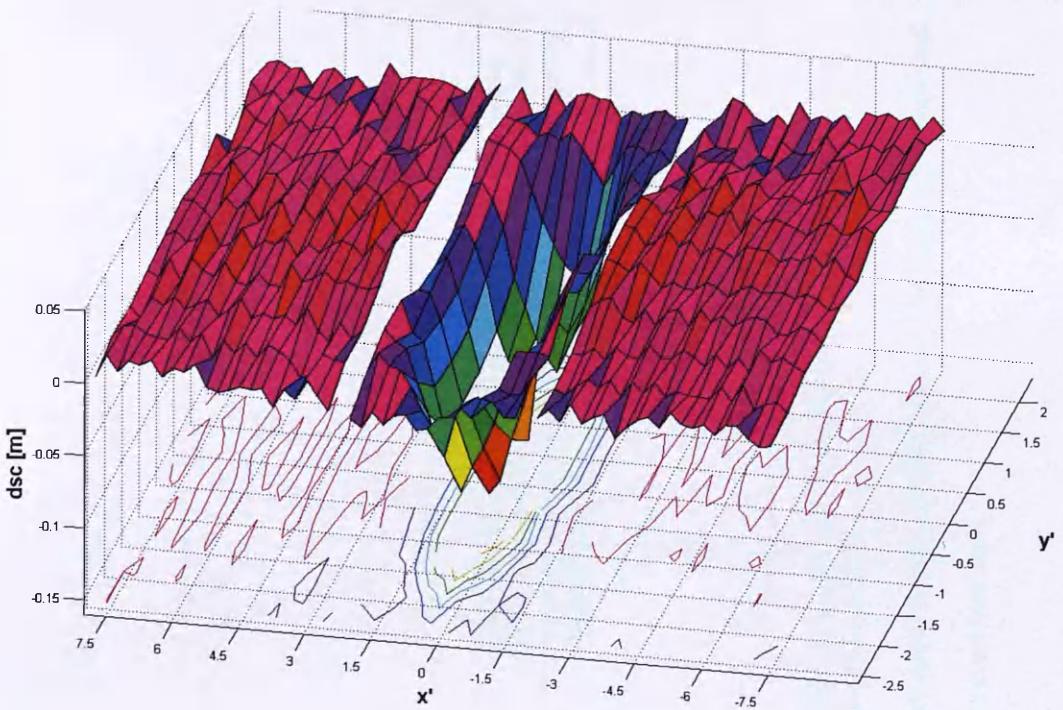
Figure 5-41. End of test laser bed profile of the smooth cylinder's scour hole.

Figure 5-42 shows a comparison of the end of test centreline bed profiles for the smooth cylinder under both unidirectional and variable reversing currents, and the collared cylinder under variable reversing currents. The graph shows that the length of the scour hole is approximately the same for the collared and smooth cylinders under variable reversing current flow being $< x' = 0.3$ on the B side and $< x' = 0.25$ on the A side.
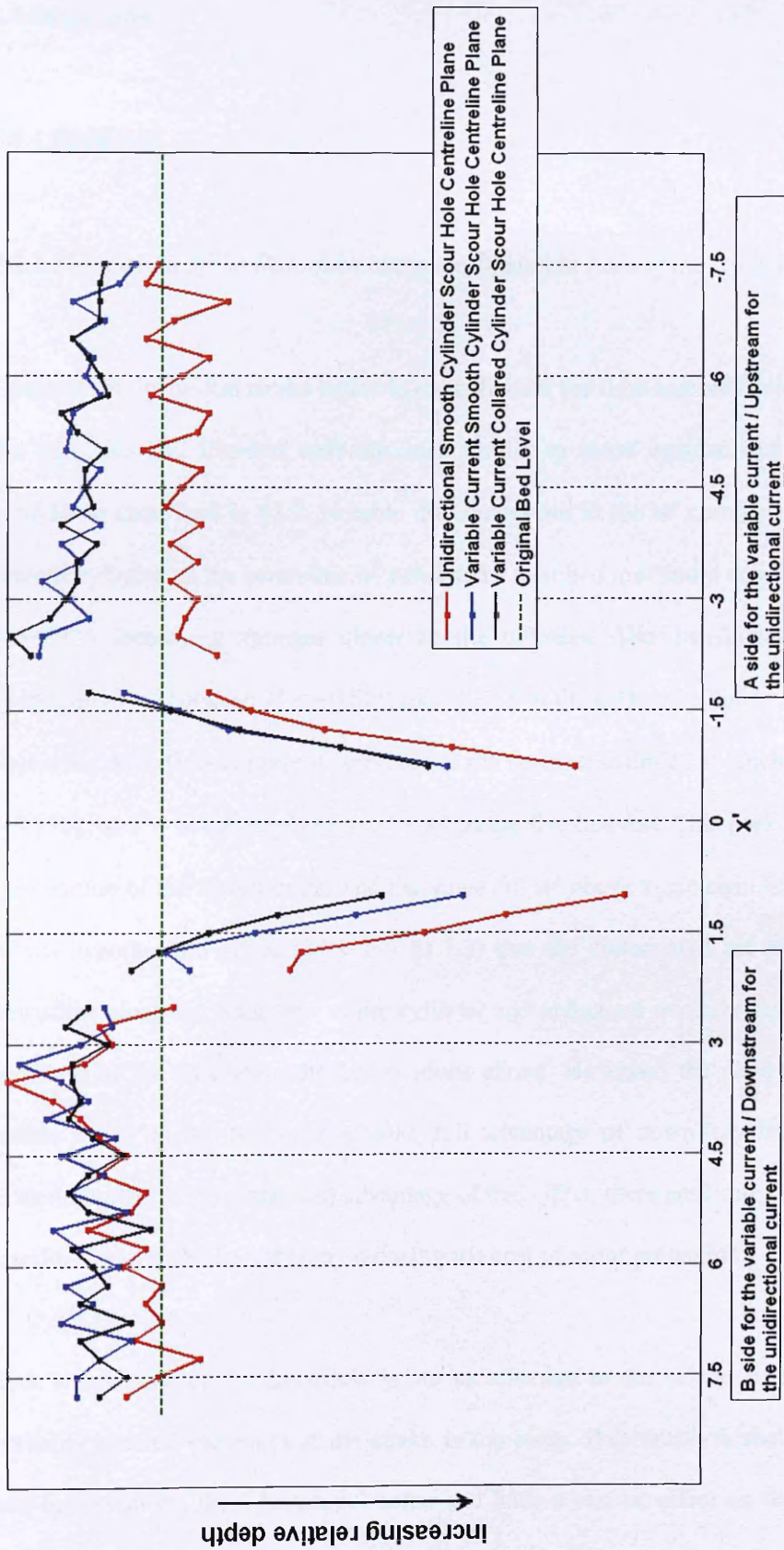
Figure 5-42. End of test laser bed profile of the centreline for the smooth and collared cylinder under variable currents (blue and black data respectively) and for the smooth cylinder under a unidirectional current (red data).

5.8 Discussion

5.8.1 Rigid Bed

5.8.1.1 Reduction of the Downflow along the Upstream Face of the Cylinder

Upstream of the helical strake and collared cylinders the flow and turbulence fields for the transition and live-bed tests are very similar to those upstream of the smooth cylinder as described in §3.2. Notable differences are in the w' component. Near the smooth cylinder on the centreline w' exhibited a near bed maximum downstream of x' = −0.825, becoming stronger closer to the cylinder. The distribution along the centreline of w' between x' = −0.825 and −0.665 in the collared cylinder (Figure 5-4) shows the downflow is present upstream of the collared cylinder. It reaches a peak of ≈ 0.15U_∞ at z' = 0.4 as opposed to z' = 0.1 in the live-bed test. This peak is located at the position of the lowest collar and the values of w' above it are significantly lower. It was hypothesised above (§5.1 and §1.7.3) that the collars will act to disrupt the downflow along the front face of the cylinder and reduce its overall strength and this seems to be the case from the observations above. However, the need to place the collars closer to the bed level to take full advantage of downflow interruption is evident. Furthermore to take full advantage of this effect, there need only be one collar installed close to the bed, thereby reducing the cost of scour protection.

Such a reduction of the downflow is not as effective in the helical strake cylinder, probably because the angle of the strake is too steep. Presumably a shallower angle will behave more like a horizontal collar and have a similar effect on the downflow

(e.g., Dey et al., 2006). However, the shallower the angle, the longer the strake becomes around the cylinder and the greater the cost of installation.

5.8.1.2 The Downstream Flow Field

From the time-averaged and time-series PIV flow velocity maps presented in Figures 5-16, 5-17 and 5-20, a detailed comparison of the flow field between the collared, helical strake and smooth cylinders was given.

In the collared cylinder wake the streamwise flow is characterised by a large, horizontal-axis vortex between the collars at $z' = 0.4$ and 0.8. The lateral flow here is strongly negative while above and below the lateral flow is positive indicating that the vortex is three-dimensional and wraps around the cylinder's surface. Below the lower collar at $z/h = 0.4$ the flow is streamwise and strongly positive. Much of the above description may be applied to the helical cylinder wake. Both the flow and turbulence fields are very different to those downstream of the smooth cylinder (§3.4).

5.8.1.3 Suppression of Vortex Shedding

Figures 5-43 shows 100 seconds of time-series spanwise v velocity data for the live-bed tests downstream of the smooth, helical strake and collared cylinders. This data was collected along the centreline using a Nortek 10 MHz Vectrino ADV at $z' = 0.02$ (0.5 cm above the bed) and $x' = 0.5$ (§2.1.2.3 describes the deployment). For the smooth cylinder, fluctuations in the v component take place in a quasi-cyclical manner, switching from between positive to negative v between approximately every

1 and 1.5 seconds. This fluctuation pattern suggests relatively steady vortex shedding behind the smooth cylinder. Such quasi-cyclical fluctuations are much harder to identify in the time series data behind the helical strake and collared cylinders (Figure 5-43). In both cases, fluctuations between positive and negative v are present but these do not occur in a definable manner. There is, however, evidence of changes in the shedding pattern with regions of marked difference in the helical strake time-series (for example between 70 and 100 seconds).
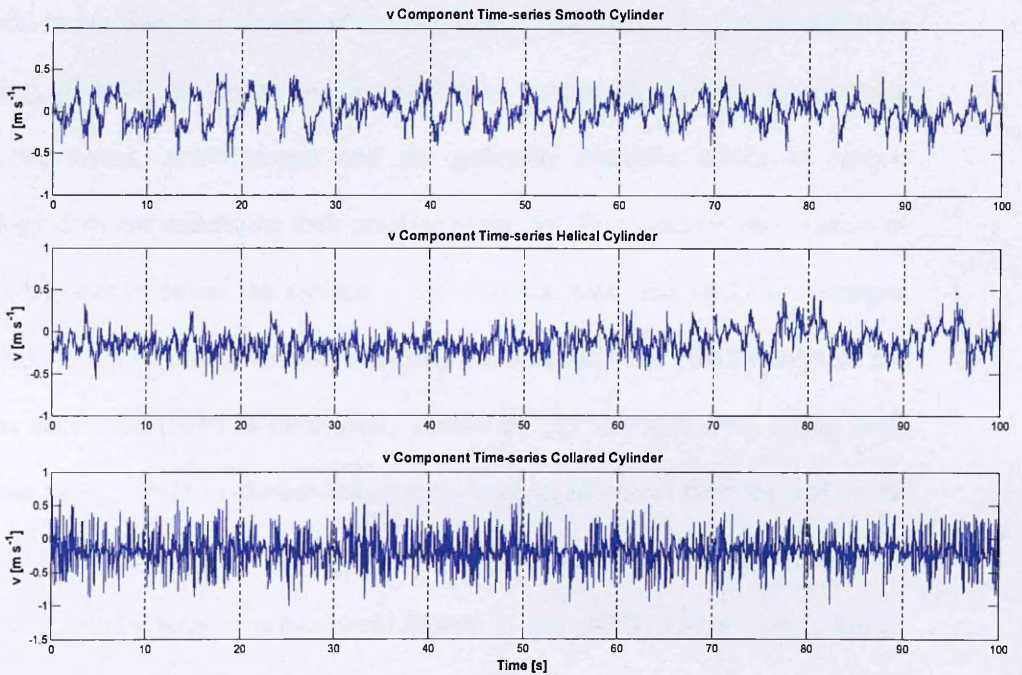
Figure 5-43. 100 seconds of time series cross-stream v component ([m s^{-1}]) at $x' = 0.5$, $z' = 0.4$ downstream of the smooth, helical strake and the collared cylinders.

5.8.2.1 Reduction of Scour by the Collared Cylinder.

Often in the literature on flow modification around bridge piers, the positioning of the collar is recommended to be just below the bed surface (e.g., Dey et al., 2006). The collar then prevents scour continuing below its location by providing a physical barrier between the downflow and horseshoe vortex and the sediment. The collar generally needs to have a radius which is greater than D to be most effective (e.g., Kumar et al., 1999), which may be less practical in a marine deployment. This may be impractical in the marine environment to install and maintain as it requires installation after piling, probably by divers and would require continuous monitoring to ensure passing bed forms, storm events and the generally dynamic nature of seabed morphology does not undermine their position at the bed. Furthermore, the location of a collar very near or below the surface would interfere with, and likely be damaged by, any rip rap scour protection that may also be installed. The effectiveness of the collar has only been tested in clear-water conditions (for example, Dey et al., 2006 and Kumar et al., 1999). A further uncertainty in its deployment near the bed is the possible interaction of passing bed forms with the collar and the consequent effects on its ability to reduce scour. Furthermore, Kumar et al., (1999) found that although collars that are installed at the bed reduce upstream and lateral scour to, in some cases zero (for a collar of $4D$), the amount of scour in the downstream side increases greatly – this may well be due to the large and strong horizontal axis vortex identified in §5.4. They attribute this to the lack of sediment deposition in the wake due to the absence of upstream and lateral scour, however, the results shown in §5.5.4 suggest that this may also be due to active scouring by the strong downward orientated streamwise flow below the horizontal axis vortex, which would be located next to the bed in the case of

a collar located at the bed. It should be noted that their deployment involved a single collar, and so it is not certain whether the same flow field observed in §5.4.4 will apply. It was for the above reasons it was chosen to install the collars at positions above the bed with the idea that this would be less of an engineering challenge, and may yield the greatest reduction of scour. However, as the mobile bed results presented in §5.7.1.2 show, the amount of scour at the end of the mobile bed test for the collared cylinder was essentially the same as it was for the smooth cylinder. This is a surprising result at first sight, however, there are indications that the collar may work better if positioned closer to the bed while keeping in mind the limitations in the proximity to the bed mentioned above.

As Table 5-2 above shows, the scour depth around the collared cylinder was consistently lower than it was for the same position and time around the smooth cylinder throughout the majority of the first half-cycle. The difference is regularly between 1 and 2 cm less than the smooth cylinder (i.e., between 15 - 25 % less depth than the smooth cylinder in places). The difference reduces quite rapidly during the second half-cycle. This is probably because the scour hole has become deep enough to reduce the ability of the collar to interrupt the downflow by the extra length of cylinder exposed. Furthermore and perhaps more importantly, as the scour hole grows in size, so does the horseshoe vortex (§1.3.2 and Melville, 1975) and the positioning of the collar above the bed level will not interact with the horseshoe vortex, which will form from separated flow coming off the scour holes' upstream lip allowing it to scour unimpeded.

5.8.2.2 Recommendations for the Reduction of Scour around the Cylinder

The above described deployment of collars around the cylinder is clearly not the most efficient one. The data suggests that a single wider collar positioned closer to the bed will have more effect. The optimum location and width of the collar requires further investigation and must take into account the following: 1) ease of installation and monitoring, 2) the effect it may have on the cylinder design, installation and routing of cables, 3) its interaction with any additional passive scour protection such as rip-rap and 4) the effect of live-bed conditions on its stability, and ability to reduce scour.

One solution may be to install the collar on the bed thereby armouring the bed and preventing any scour from taking place. In order for this to work the collar width must be greater than the scour hole width which, from the results shown in Figure 5-42, is similar to that of the smooth cylinder scour hole and, therefore $\sim 3D$ radius around the cylinder (see also §4.3.3). Identifying the optimum radius, thickness, and weight of such a free standing collar would require further research.

5.9 Summary

This chapter has presented results of detailed flow and turbulence measurements around two flow modifying cylinders which were designed to reduce the amount of scour that may occur. These included a helical strake and a collared cylinder. In addition to these tests a mobile bed test in which the collared cylinder was subject to

variable reversing currents was conducted and the time-development of scour was recorded.

The results showed that upstream of the two modified cylinders, the flow and turbulence fields were essentially similar to those upstream of the smooth cylinder. There was some evidence of a reduction in the strength of the downflow along the front face of the cylinder, particularly for the collared cylinder. The near-cylinder flow and turbulence fields were also essentially the same as for the smooth cylinder. Downstream of the modified cylinders the PIV vector maps described a very different flow field to that behind the smooth cylinder. The flow field is characterised by a large vortex with a horizontal axis of rotation that wraps around the cylinder. The rotation of the vortex is anti-clockwise and is highly three dimensional with a strong lateral flow just below its axis of rotation bounded by strong lateral flows above and below it in the opposing direction. It is located between the upper and lower collars and strakes.

In the mobile bed tests, no reduction of scour was found at the end of the test. However, the collar was effective in reducing scour significantly during the 1st half-cycle in particular. The effect of the collar became less as the scour hole developed. Positioning a single collar closer to the bed is suggested in order to yield better scour reduction.

6. Conclusions

Offshore wind turbines consist of a blade-driven turbine placed on top of a long circular cylindrical monopile that is pile-driven into the sea-bed. When a monopile is placed in the ocean, its presence causes changes in the tidal flow and turbulence field around it. These changes involve local increases in velocity, turbulence and shear stress which can lead to the formation of a scour hole around the monopile's base. Scour has a detrimental effect on monopile stability and longevity and as a result scour protection is often installed on the bed around the monopile. Such protection often involves the placement of heavier material on the bed which protects the lighter sediment below it from being transported away. These protection measures rely on accurate scour depth prediction and are themselves subject to damage which can, in turn, result in their failure to prevent scour, cause damage to the monopile, and damage any attached cabling.

On review of the literature, three research themes related to tidal flow around cylinders requiring further research were identified: 1) the flow field and mechanism of scour; 2) the evolution and depth of scour; and 3) methods of reduction of scour by flow modification. This thesis has addressed these three themes through a series of laboratory experiments involving scaled models of three offshore wind turbine monopile designs: a regular, smooth, cylindrical cylinder, and two flow-modifying

cylinder designs - one with collars and another with a helical strake. The main findings and conclusions for each theme are summarised below.

6.1 The Flow and Turbulence Field around the Cylinder

In a set of rigid bed experiments the flow and turbulence fields around the cylinder under three different flow velocity-depth configurations that were related to tidal flow were studied in detail. Using Particle Image Velocimetry (PIV) and Acoustic Doppler Velocimetry (ADV) an extensive velocity and turbulence data-set was collected. The analysis of this data-set provides an extensive and valuable addition to the knowledge of the flow and turbulence field around the cylinder that is currently available in the literature.

While the flow and turbulence fields share similar features between all three flow velocity-depth configurations, variation in the flow field around the model cylinder was significant enough to imply that the full understanding and accurate prediction of scour under tidal currents in the prototype must take the time-varying nature of the flow and turbulence field into account. Such variation included changes in the near-wake length, location of lateral flow separation, near-wake shape, stagnation zone and the magnitude of flow velocity and turbulence. As the current understanding of the flow field and therefore the basis of scour prediction in tidal currents is based on unidirectional steady flow derived predictor equations, these findings represent a significant challenge to the current status quo.

6.2 The Evolution and Depth of Scour in Tidal Currents

In order to assess the time-development of scour under tidal currents, a series of mobile bed tests were conducted. Scour time-development around the smooth cylinder was monitored over two 'tidal' cycles where flow velocity, depth and direction was varied systematically. In these tests scour was allowed to develop over four half-cycles with each half-cycle employing opposite flow direction from the previous. Each half-cycle consisted of three time-steps where the flow velocity and depth was varied between transition, live-bed and clear-water flow intensity conditions which are representative of scaled tidal flow. The main conclusions are summarised below.

During the first cycle the scour hole shape developed asymmetrically in a similar manner to unidirectional scour. Asymmetry gave way to symmetry during the second cycle. At the end of the variable reversing current test, deposition of sediment was found on both sides of the scour hole. This implies that the reversal of flow direction does not significantly remove sediment from the depositional mound that was previously downstream of the scour hole. The time-development of scour under variable reversing currents was found to be slower than it is for unidirectional currents. However, contrary to the literature, this was found to be due to the variation in the scour rate between each current stage rather than due to infilling of the scour hole which, though present, appeared to be less significant. The variable reversing current scour data was compared with unidirectional scour data, scour data from equal reversing currents, and theoretical predictions. The results implied that equilibrium scour depth under variable reversing currents is lower than it is under unidirectional

currents or equal reversing 'square' tidal currents. The findings above have implications for the installation of scour protection at off-shore wind turbine monopile's, which relies on accurate predictions of scour time development and depth. Currently these predictions are gained from empirically derived predictor equations of scour in unidirectional currents and as such may overestimate scour depth leading to overly conservative protection measures and unnecessary expenditure. Treating tidal flow as a unidirectional current also simplifies the processes that take place which are highlighted as being important in the above experiments. These include the changes in flow intensity, flow direction, scour hole shape and movement of bed forms.

6.3 Methods of Reduction of Scour by Flow-Modification

In order to assess the potential of reducing scour using flow-modifying cylinder designs, a series of rigid bed tests were conducted to analyse the changes in the time-variable flow and turbulence fields around a cylinder with circular collars attached to its circumference, and a second with a helical strake attached to its circumference. A summary of the main findings are given below.

The majority of the upstream and near-cylinder flow and turbulence fields for the flow modifying cylinder showed little difference from the smooth cylinder flow fields. The main difference was an interruption of the downflow along the leading edge.In both

the collared and helical strake cylinders it was found that the downflow strength was reduced just above the collar and helical strake but reformed again below it.

On the downstream side the flow and turbulence fields of the collared, helical strake and smooth cylinders were markedly different. Both flow-modifying cylinders were dominated by a horizontal axis vortex which wrapped around the cylinder in a similar manner to the horseshoe vortex.

The scour development in variable reversing currents was recorded over two 'tidal' cycles as in §5.2 around the collared cylinder in the same way as it was for the smooth cylinder in §6.2 and §4. The depth of scour around the collared cylinder was lower than it was for the smooth cylinder during the first cycle. During the second cycle the scour depth increased, finishing at the same depth as the smooth cylinder. The collars effect on scour reduction reduced when the scour hole increased in depth.

6.4 Recommendations for the Prediction and Mitigation of Scour around Offshore Wind Turbines in Tidal Currents, and Areas for Further Research

The following section makes some recommendations for the prediction and mitigation of scour around offshore wind turbines in tidal currents which are drawn from the analysis of the data presented in this thesis.

Currently, the prediction of scour around cylinders in tidal currents is made using equations that are based on the development of scour in unidirectional steady current flow. The rigid bed results suggest that in the prototype the flow and turbulence field will change significantly relative to the conditions of the tidal flow at that moment. The mobile bed tests highlighted these differences may also create a time-variable scour rate under a tidal current. Time-variable flow depth, intensity and direction are not accounted for if scour is predicted using unidirectional prediction methods. The model results also suggest that the scour depth under tidal currents may be lower than they are under unidirectional currents which would result in over compensation in the design limits of the cylinder and any scour protection installed, therefore leading to an unnecessary expenditure of resources. Further research which specifically compares the equilibrium depth of tidal scour against unidirectional scour is required to confirm this. Such research may also include the interaction of waves and their effect on scour.

It is hoped that the detail provided in the rigid bed tests will provide an extensive and valuable data set which will aid the calibration of numerical models, and increase the general understanding of the flow field.

The flow modifying cylinders resulted in the formation of a large horizontal vortex which acted to deposit sediment on the collar. This, over time, may cause damage to the collar and cylinder and should be investigated further. The effectiveness of the collars in reducing the downflow is dependent on their height above the bed. It is suggested that they should be placed as close to the bed as possible. However, their positioning next to or under the bed raises issues with the interaction of the changing

sea-bed morphology on their effectiveness and integrity. A free standing collar of large radius placed on the bed may be a viable solution. Further research is required to assess this. The angle of the helical strake angle should be reduced to a shallower angle as this will be more effective at blocking the downflow. Any reduction of strake angle may have an effect on the suppression of wake vortex shedding. However, as the results showed shedding to be suppressed downstream similarly in the collared and helical cylinder cases, further investigation of the effectiveness of the strake on vortex shedding, and whether this has a significant benefit on the reduction of scour, is needed.

A further problem associated with the monopile-sediment interface is that of liquefaction of the sediment around the monopile base. Liquefaction could possibly occur due to the monopile vibration induced by the rotation of the blades. Liquefaction has not been investigated in this thesis but will none the less play a role in the development of the scour hole. Further research would assess firstly whether liquefaction is a significant issue, and what the combined effect of monopile vibrations and tidal currents may have on the scour hole. Furthermore, to provide a complete picture of scour around the monopile in the marine tidal environment, the affect of wave-induced currents at shallower depths in particular would also need to be considered.

7. References

Adrian, R. J.. (1991) Particle Imaging Techniques for Experimental Fluid Mechanics. *Annual Review of Fluid Mechanics*, **23,** 261-304.

Ahmed, F., and Rajaratnam, N., (1998) Flow around Bridge Piers. *Journal of Hydraulic Engineering*, **124,** 288 - 300.

Anatec et al., (2008) Environmental Impact Assessment for the Rhyll Flats Offshore Wind farm, *nPower.*

Baker, C. J., (1979) The Laminar Horseshoe Vortex. *Journal of Fluid Mechanics*, **95,** 347 - 367.

Ballast N. and Oud, J. C., (2002) Foundation Design Monopile - Comparison Extra Steel Consumption Versus Scour Protection - 3.6 and 6 MW Wind Turbines. DOWEC. Nieuwegein.

Baker, R. E., (1986) Local Scour at Bridge Piers in Non-Uniform Sediment. University of Auckland.

British Oceanographic Data Centre, Online Data Base https://www.bodc.ac.uk/data/

Breusers, H. N. C., and Raudkivi, A. J., (1991) *Scouring*, Rotterdam, Balkema.

Breusers, H. N. C., Nicollet, G., and Shen, H. W., (1977) Local Scour around Cylindrical Piers. *Journal of Hydraulic Research*, **15,** 211 – 252.

Brown, E., Colling, A., Park, D., Phillips, J., Rothery, D., and Wright, J., (2005) Waves, Tides and Shallow-Water Processes, Milton Keynes, Butterworth Heinemann.

Chiew, Y. M., (1984) Local Scour at Bridge Piers. Auckland, Auckland University.

Chiew, Y. M., and Lim, S. Y., (2003) Protection of Bridge Piers using a Sacrificial Sill. *Water and Maritime Engineering* **156,** 53-62.

Dahlberg, R., (1983) Observations of Scour around Offshore Structures. *Canadian Geotechnical Journal*, **20,** 617 - 628.

Dargahi, B., (1987) Flow Field and Local Scouring around a Cylinder. Stockholm, Sweden, Royal Institute of Technology.

Dargahi, B., (1989) The Turbulent Flow Field around a Circular Cylinder. *Experiments in Fluids*, **8,** 1 - 12.

De Vos, L., (2008) Optimisation of Scour Protection Design for Monopiles and Quantification of Wave Run-Up: Engineering the Influence of an Offshore Wind Turbine on Local Flow Conditions. Ghent, University of Ghent.

Dey, S., and Raikar, R. V., (2007) Characteristics of Horseshoe Vortex in Developing Scour Holes at Piers. *Journal of Hydraulic Engineering*, **133,** 399 - 413.

Dey, S., Sumer, B. M., and Fredsoe, J., (2006) Control of Scour at Vertical Circular Piles under Waves and Current. *Journal of Hydraulic Engineering*, **132,** 270-279.

Dijk., V., (1980) Experiences of Scour in the North Sea. Proceedings of One Day Soc. For Underwater Technology Seminar on Scour Prevention Techniques Around Offshore Structures.

Escarameia, M., (1998) Laboratory Investigation of Scour around Large Structures in Tidal Waters. *3rd International Conference on Hydro-Science and – Engineering* Brandenburg University of Technology at Cottbus, Berlin, Germany, ICHE.

ESS (2003) Scour Analysis: Proposed Offshore Wind Park, Nantucket Sound, Massachusetts. Sandwich.

Ettema, R., (1980) Scour at Bridge Piers. University of Auckland.

Ettema, R., Melville, B. W., and Barkdoll, B., (1998a) Scale Effect in Pier-Scour Experiments. *Journal of Hydraulic Engineering*, **124,** 639 - 642.

Ettema, R., Mostafa, E. A., Melville, B. W., and Yassin, A. A., (1998b) On Local Scour at Skewed Piers. *Journal of Hydraulic Engineering*, **124,** 756 - 760.

Ettema, R., Kirkil, G., and Muste, M., (2006) Similitude of Large-Scale Turbulence in Experiments on Local Scour at Cylinders. *Journal of Hydraulic Engineering*, **132,** 33-40.

Fredsoe, J., and Deigaard, R., (1992) Mechanics of Coastal Sediment Transport, Singapore; New Jersey, World Scientific.

Frigaard, P., and De Vos, L., (2006) Offshore Wind Turbines Situated in Areas with

    Strong Currents: Laboratory Tests, Offshore Wind Turbines Situated in areas

    with Strong Currents. IN JENSEN, M. S. (Ed.). Esbjerg, Offshore Centre

    Denmark.

Gerrard, J. H., (1966) The Mechanics of the Formation Region of Vortices Behind

    Bluff Bodies. *Journal of Fluid Mechanics*, **25,** 401-413.

Gerrard, J. H., (1978) The Wakes of Cylindrical Bluff Bodies at Low Reynolds

    Number. *Phil. Transactions of the Royal Soc. London*, Series A, **288,** 351-382.

Goring, D. G., and Nikora, V. I., (2002) Despiking Acoustic Doppler Velocimeter

    Data. *Journal of Hydraulic Engineering*, **128,** 117-126.

Gothel, O., and Zielke, W., (2006) Numerical Modelling of Scour at Offshore

    Wind Turbines.

Graf, W. H., and Istiarto, I., (2002) Flow Pattern in the Scour Hole around a Cylinder.

    Journal of Hydraulic Research, **40,** 13 - 20.

Graf, W. H., and Yulistiyanto, B., (1999) Experiments on Flow around a Cylinder; the

    Velocity and Vorticity Fields. *Journal of Hydraulic Research*, **36,** 637 - 654.

Gupta, A. K., (1987) Hydrodynamic Modification of the Horseshoe Vortex at a

    Vertical Pier Junction with Ground. *Physics of Fluids*, **30,** 1213-1215.

Harris, J. M., Whitehouse, R. J. S., and Benson, T., (2010) The Time Evolution of

Scour around Offshore Wind Turbines. *Maritime Engineering*, **163,** 3-17.

HEC 18, (1993) Evaluating Scour at Bridges.

US Department of Transportation, Report No FHwA-IP-90-017. Federal
Highway Administration (FHwa), Washington, D.C.

Henderson, F. M., (1966) Open Channel Flow, New York, The Macmillan Company.

Hjorth, P., (1975) Studies on the Nature of Local Scour. Lund Institute of Technology.

Hoffmans, G. J., and Verheij, H.G., (1997) Scour Manual, Rotterdam, Balkema.

Hung, C. S., (1968) 'A Preliminary Study on the Resistance of Cylinders in Open
Channel Flow' Colorado State University.

Hughes, S. A., (1993) Physical Models and Laboratory Techniques in Coastal
Engineering, Singapore, River Edge, NJ.

Jain, S. C., and Fischer, E. E., (1979) Scour Around Circular Bridge Piers at High
Froude Numbers. Washington DC, Federal Highway Administration.

Jensen, M. S., Larsen, B. J., De Vos, L., Christiansen, E. D., Hansen, E, A., Solberg,
T., Hjertager, B. H., and Bove, S., (2006) Offshore Wind Turbines Situated in
Areas with Strong Currents. IN JENSEN, M. S. (Ed.). Esbjerg, Offshore
Centre Denmark.

Johnson, A., (1995) Comparison of Pier-Scour Equations Using Field Data. *Journal of
Hydraulic Engineering*, **121,** 626 - 629.

Johnson, K. R., and Ting, F. C. K., (2003) Measurements of Water Surface Profile and Velocity Field at a Circular Pier. *Journal of Engineering Mechanics*, **129,** 502 - 513.

Kim, S.-C., Friedrichs, C. T., Maa, J. P.-Y., and Wright, L. D., (2000) Estimating Bottom Stress in Tidal Boundary Layer from Acoustic Doppler Velocimeter Data. *Journal of Hydraulic Engineering*, **126,** 399-406.

Kobayashi, T., (1994) Experimental Study on Developing Process of Local Scour around a Vertical Cylinder. 23rd International Conference on Coastal Engineering. Kobe Japan.

Kumar, V., Ranga Raju, K. G., and Vittal, N., (1999) Reduction of Local Scour around Bridge Piers using Slots and Collars. *Journal of Hydraulic Engineering*, **125,** 1302 - 1305.

Lagasse, P. F., Zevenbergen, L. W., Schall, J. D., and Clopper, P. E., (2001) Bridge Scour and Stream Instability Countermeasures. HEC23 FHWA NHI 01-003, Federal Highway Administration, U.S. Dept. of Transportation. Washington, D.C.

Laursen, E. M., and Toch, A., (1956) Scour Around Bridge Piers and Abutments. Iowa Highway Research Board.

Louwersheimer, W. F., Verhagen, H.J., and Olthof, J., (2006) Scour around an Offshore Wind Turbine.

Margheritini, L., Martinelli, L., Lamberti, A., and Frigaard, P., (2006) Scour Around Monopile Foundation for Offshore Wind Turbine in the Presence of Steady and Tidal Currents. *Proceedings of the International Conference on Coastal Engineering, 2006.*

Melville, B. W., (1975) Local Scour at Bridge Sites. Auckland, Auckland University.

Melville, B. W., (1997) Pier and Abutment Scour - an Intergrated Approach. *Journal of Hydraulic Engineering*, **123,** 125-136.

Melville, B. W., and Coleman, S. E., (2000) Bridge Scour, Colorado, Water Resources Publications.

Melville, B. W., and Chiew, Y. M., (1999) Time Scale for local Scour at Bridge Piers. *Journal of Hydraulic Engineering*, **125,** 59-65.

Melville, B. W., and Raudkivi, R. J., (1977) Flow Characteristics in Local Scour at Bridge Piers. *Journal of Hydraulic Research*, **15,** 373 - 380.

Melville, B. W., and Sutherland, A. J., (1988) 'Design Method for Local Scour at Bridge Piers. *Journal of Hydraulic Engineering*, **114,** 1210 - 1226.

Mohamed, Y. A., Noor, M. J. M. M., Ghazali, A. H., and Haut, B. B. K., (2005) Validation of Some Bridge Pier Formulae Using Field and Laboratory Data. *American Journal of Environmental Sciences*, **1,** 119 - 125.

Mori, N., (2004) Func_despike_phasespace. 2.00 ed. MATLAB Function.

Neill, C. R., (1964) River-bed Scour, A Review for Engineers. Ottawa, Canadian Good Roads Association.

Niedoroda, A. W., and Dalton, C., (1982) A Review of the Fluid Mechanics of Scour. *Ocean Engineering*, **9,** 59 - 70.

Nielsen, P., (1994) Coastal Bottom Boundary Layers and Sediment Transport, Singapore, World Scientific.

Npower (2008) Personal Communication.

Oliveto, G., and Hager, W. H., (2002) Temporal Evolution of Clear-water Pier and Abutment Scour. *Journal of Hydraulic Engineering*, **128,** 811 -822.

Odgaard, A. J., and Wang, Y., (1987) Scour Prevention at Bridge Piers. IN RAGAN, R. M. (Ed.) *Proc., Nat. Conf. on Hydraulic Engineering.* New York, ASCE.

Raudkivi, A. J., (1986) Functional Trends of Scour at Bridge Piers. *Journal of Hydraulic Engineering*, **112,** 1 - 13.

Raudkivi, A. J., and Sutherland, A. J., (1981) Scour at Bridge Crossings. Road Resources Unit Bulletin 54,Wellington, New Zealand

Raffel, M., Willert, C., And Kompenhans, J., (1998) Particle Image Velocimetry, a Practical Guide, Berlin / Heidelberg, Springer-Verslag

Raudkivi, A. J., and Ettema, R., (1983) Clear-water Scour at Cylindrical Piers. *Journal of Hydraulic Engineering*, **109,** 339 - 350.

Roulund, A., Sumer, B. M., Fredsoe, J., and Michelsen, J., (2005) Numerical and

Experimental Investigation of Flow and Scour around a Circular Pile. *Journal of Fluid Mechanics*, **534,** 351-401.

Roshko, A., (1961) Experiments on the Flow Past a Circular Cylinder at Very High

Reynolds Number. *Journal of Fluid Mechanics*, **10,** 345-356.

Roulund, A., Sumer, B. M., Fredsoe, J., and Michelsen, J., (2005) Numerical and

Experimental Investigation of Flow and Scour around a Circular Pile. *Journal of Fluid Mechanics*, **534,** 351-401.

Sahin, B., and Ozturk, N. A., (2009) Behaviour of Flow at Junction of Cylinder and

Base Plate in Deep Water. *Measurement*, **42,** 225-240.

Saito, E., Sato, S., and Shibayama, T., (1990) Local Scour Around a Large Circular

Cylinder Due to Wave Action. Coastal Engineering, 1795-1804.

Sarker, A. M., (1998) Flow Measurement around Scoured Bridge Piers using

Acoustic-Doppler Velocimeter (ADV). *Flow Measurement and Instrumentation*, **9,** 217-227.

Schewe, G., (1983) On the Force Fluctuations Acting on a Circular Cylinder at Very

High Reynolds Number. *Journal of Fluid Mechanics*, **133,** 265-285.

Shen, H. W., Schneider, V. R., and Karaki, S. S., (1966) Mechanics of Local Scour.

US department of Commerce, National Bureau of Standards, Institute of

Applied Technology.

Shen, H. W., Schneider, V. R., and Karaki, S. S., (1969) Local Scour Around Bridge Piers. JHD Proc. ASCE, **95,** 1919 - 1940.

Sheppard, M. D., Odeh, M., and Glasser, T., (2004) Large Scale Clear-Water Local Pier Scour Experiments. *Journal of Hydraulic Engineering*, **130,** 957-963.

Shields, A., (1936) Anwendung der Aehnlichkeitsmechanik und Turbulenzforchung Auf die Geschiebebewegung. *Mitt Preuss Versuchsanstalt fur Wasserbau und Schiffbau*, **26**.

Soulsby, R. L., (1986) Coastal and Estuarine Sediment Dynamics. IN DYER, R. K. (Ed.) *Coastal and Estuarine Sediment Dynamics* New York, Wiley-Interscience.

Soulsby, R. L., (1997) Dynamics of Marine Sands, Thomas Telford.

Soulsby, R. L., and Whitehouse, R. J. S., (1997) Threshold of Sediment Motion in Coastal environments. *Pacific Coasts and Ports 1997*. New Zealand.

Sumer, B. M., and Fredsoe, J., (1997) Scour around a Large Vertical Circular Cylinder in Waves. 16th International Conference on Offshore Mechanics and Arctic Engineering. Yokohama, Japan.

Sumer, B. M., and Fredsoe, J., (1999) Wave Scour around Structures, World Scientific.

Sumer, B. M., and Fredsoe, J., (2001b) Scour around a Pile in Combined Waves and

Current. *Journal of Hydraulic Engineering,* **127,** 403 - 411.

Sumer, B. M., and Fredsoe, J., (2002a) Hydrodynamics around Cylindrical Structures (Revised Edition), World Scientific.

Sumer, B. M., and Fredsoe, J., (2002b) The Mechanics of Scour in the Marine Environment, Singapore, World Scientific.

Sumer, B. M., Fredsoe, J., and Christiansen (1992a) Scour around Vertical Pile in Waves. *Journal of Waterway, Port, Coastal, and Ocean Engineering,* **117,** 15 - 31.

Sumer, B. M., Christiansen, N., and Fredsoe, J., (1992b) Time Scale of Scour around Vertical Pile. 2nd International Offshore and Polar Engineering Conference. San Fransisco, The International Society of Offshore an Polar Engineers.

Sumer, B. M., Christiansen, N., and Fredsoe, J., (1997) Horseshoe Vortex and Vortex Shedding around a Vertical Wall-mounted Cylinder Exposed to Waves. *Journal of Fluid Mechanics,* **332,** 41-70.

Sumer, B. M., and Fredsoe, J., (2001a) Wave Scour around a Large Vertical Circular Cylinder. ASCE *Journal of Waterway, Port, Coastal and Ocean Engineering,* **127,** 125 - 134.

Sumer, B. M., and Fredsoe, J., (2001b) Scour around Pile in Combined Waves and Current. *Journal of Hydraulic Engineering,* 127, 403 - 411.

Sumer, B. M., Whitehouse, R. R. S., and Torum, A., (2001) Scour around Coastal

Structures: a Summary of Recent Research. *Coastal Engineering*, **44,** 153-19.

Sybert, J. H., (1963) Foundation Scour and Remedial Measures for Offshore

Platforms. SPE-AIME First Conference on Drilling and Rock Mechanics.

Austin, Texas.

Testik, F. Y., Voropayev, S. I., and Fernando, H. J. S., (2005) Flow around a Short

Horizontal Bottom Cylinder under Steady and Oscillatory Flows. *Physics of

Fluids,* **17.**

Tritton, D. J., (1990) Physical Fluid Dynamics, New York, Oxford University Press.

Van Oord, A. C. Z., (2003) Scour Protection for 6 MW OWEC with Monopile

Foundation in North Sea. Gorinchem.

Watson, T. N., (1979) Scour in the North Sea. Journal of Petroleum Technology, 26.

Wahl, T. L., (2002) WinADV - Version 2.027. Denver, Colorado, Water Resources

Research Laboratory, Bureau of Reclamation, D-8560

Whitehouse, R. J. S., (1998) Scour at Marine Structures, London, Thomas Telford.

Whitehouse, R. J. S., (2004) Marine Scour at Large Foundations. Second International

Conference on Scour and Erosion. Singapore, Meritus Mandarin.

Williamson, C. H. K., (1989) Oblique and Parallel modes of Vortex Shedding in the

Wake of a Circular Cylinder at Low Reynolds Number. *Journal of Fluid

Mechanics,* **206,** 579-627.

Zaaijer, M. B., and Van Der Tempel, J., (2004) Scour Protection: a Necessity or a

Waste of Money? 43rd IEA Topical Expert Meeting - Critical Issues

Regarding Offshore Technology and Deployment. Skaerbaek, Denmark.

Zdravkovich, M. M., (1997) Flow around Circular Cylinders, Volume 1, Oxford,

Oxford University Press.

Appendix A1 Schematic Diagram of the Monopile

Figure A1-1 shows a schematic diagram of a prototype monopile with cabling running down the side and to the bed via a J-tube. J-tubes, which are designed to be supported by the monopile and the material on the bed, may become exposed if scour occurs. This can result in damage from wave and current forcing (e.g., De Vos, 2008).
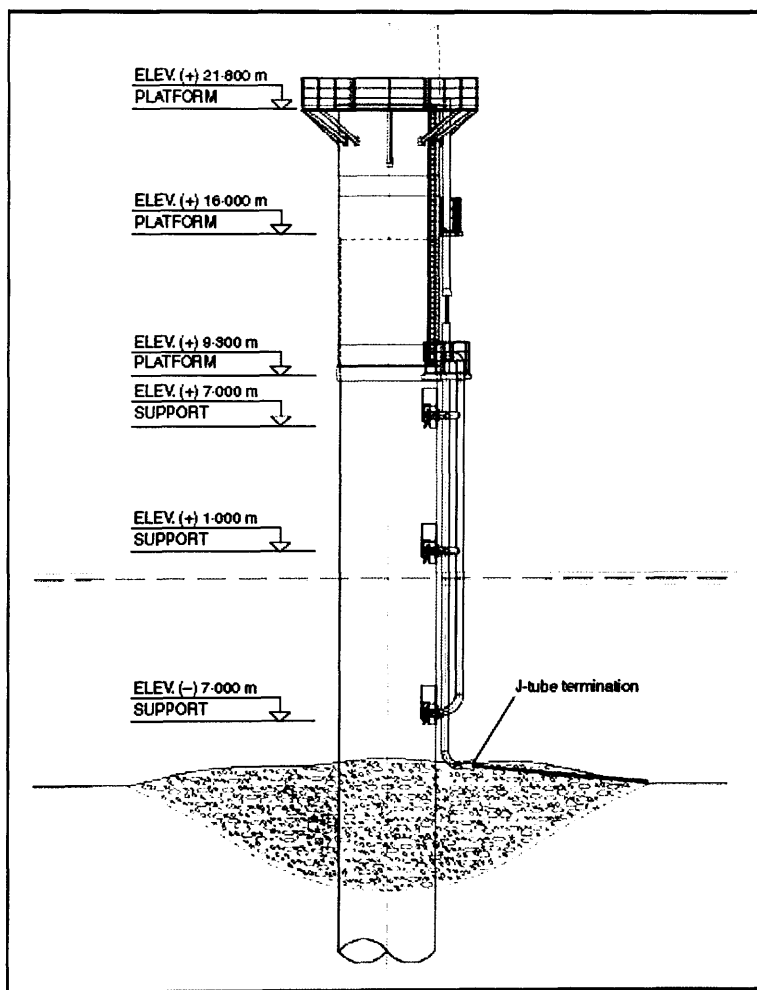
Figure A1-1. Schematic diagram of a monopile from NPower, (2008).

Appendix A2 ADV and Vectrino Specifications

A2.1 Nortek 3D 10 MHz ADV

Four Nortek 10 MHz Acoustic Doppler Velocimeters (ADV) were deployed in the flume to measure 3D flow velocity. Three of the ADVs were down-looking, and the fourth was side-looking. They have a maximum sampling rate of 100 Hz and in this deployment operated at 50 Hz. The ADVs measure velocity accurate to within +/- 1 mm s^{-1}.

A2.2. Nortek 3D 10 MHz ADV Post Processing

All data collected using the ADVs was processed using the WinADV program (Wahl, 2002). Data where the signal-to-noise ratio (SNR) was < 5, while the correlation was < 70 were removed. The data is filtered using the phase space threshold despiking method of Goring and Nikora, (2002) as modified by Wahl, (2002).

A2.3. Nortek 3D 10 MHz Vectrino

In the downstream side of the monopile, a 10 MHz Vectrino was deployed. The Vectrino is the latest version of the ADV includes the following improvements on the

earlier model (above): a 200 Hz maximum sampling frequency which reduces noise, smaller probe size to reduce flow interference on the sampling volume, fourth transducer for improved turbulence measurements and redundancy, and a minimised electronics package to improve portability. This particular model has a detached transducer head which is linked to the processor module via a flexible water proof cable, enabling extra flexibility in sampling and reduced interference on the flow as the processor module remains out of the water.

Figure A2-1 shows the Nortek 10 MHz Vectrino ADV Specifications Sheet as provided by Nortek. Velocity measurements are accurate to within +/- 0.5% of the measured velocity +/- 1 mm s^{-1}.

A2.4 Nortek 3D 10 MHz Vectrino Post Processing

The raw Vectrino data was despiked using the phase space method developed by Goring and Nikora, (2002) using a Matlab subroutine developed by Mori, (2004).

Specifications

Water Velocity Measurements

Range	±0.01, 0.1, 0.3, 1, 2, 4 m/s*) (user selectable)
Accuracy	±0.5% of measured value
±1 mm/s	
Sampling rate (output)	1–25 Hz
	1–200 Hz (Vectrino' firmware)

*) The velocity range is not the same in the horizontal and vertical direction. Please refer to the configuration software.

Sampling Volume

Distance from probe	0.05 m
Diameter	6 mm
Height (user selectable)	3–15 mm

Echo Intensity

Acoustic frequency	10 MHz
Resolution	Linear scale
Dynamic range	25 dB

Sensors

Temperature	Thermistor embedded in probe
• Range	−4°C to 40°C
• Accuracy/Resolution	1°C/0.1°C
• Time response	5 min

Data Communication

I/O	RS 232. The software supports
most	commercially available
USB–RS 232	converters.
Baud rate	300–115 200
User control	Handled via Vectrino Win32® software, ActiveX® function calls,
or	direct commands.
Analog outputs	3 channels standard, one for
each	velocity component.
Output range is	0–5 V, scaling is user
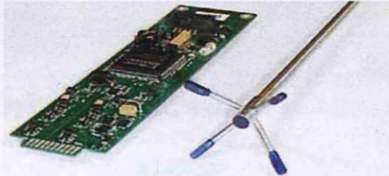
The Vectrino consists of two basic elements: the probe attached to a clyndrical housing and the processor inside the housing. From here the processed data is sent over a serial line or analog signals can be sent to an A/D converter.

selectable.	
Synchronization	SynchIn and SynchOut

Multi Unit Operation

Software	CollectV™ software
I/O	RS 232–USB support for devices with 1, 2, 4, and 8 serial ports.

Software ("Vectrino")

Operating system	Windows®2000, Windows®XP
Functions	Instrument configuration, data collection, data storage. Probe test modes.

Power

DC Input	12–48 VDC
Peak current	2.5 A at 12 VDC (user selectable)
Max. consumption, 200 Hz	1.5 W

Connectors

Bulkhead	IP68 connector or MCBH-12-FS, bronze (Impulse) – see also
options	below.
Cable	IP68 or PMCIL-12-MP – see also options below.

Materials

Standard model	Delrin® housing. Stainles steel
(316)	probe and screws.

Environmental

Operating temperature	−5°C to 45°C
Storage temperature −15°C to 60°C	
Shock and vibration IEC 721-3-2	

Dimensions

See drawing below

Options

- Standard or Vectrino' firmware (upgrade to Vectrino' firmware is also available as retrofit)
- 4-beam down-looking probe or side-looking probe. Fixed stem or flexible cable
- 12-pin IP68 waterproof connector (1h at 20m) or Impulse 12-pin underwater connector
- 10, 20, 30 or 50m cable with choice of IP68 or Impulse underwater connector
- RS232–USB converter (one-to-one, four-to-one or eight-to-one)
- Combined transportation and storage case
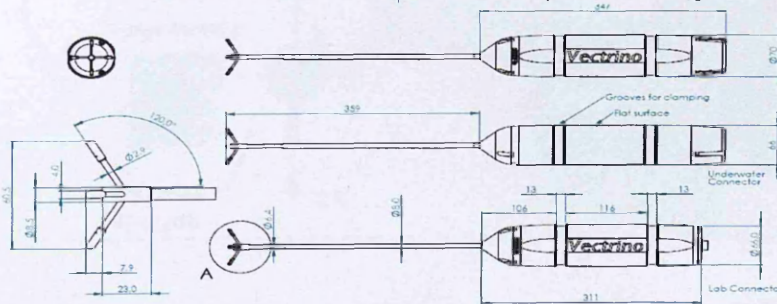
Figure A2-1. Specifications sheet of the Nortek 10 MHz Vectrino.

Appendix A3 Particle Image Velocimetry Specifications, Set-up and Error (PIV)

In this section further details on the set-up and application of the PIV in the tests is given. Figure A3-1 is a schematic outlining the PIV systems operation.
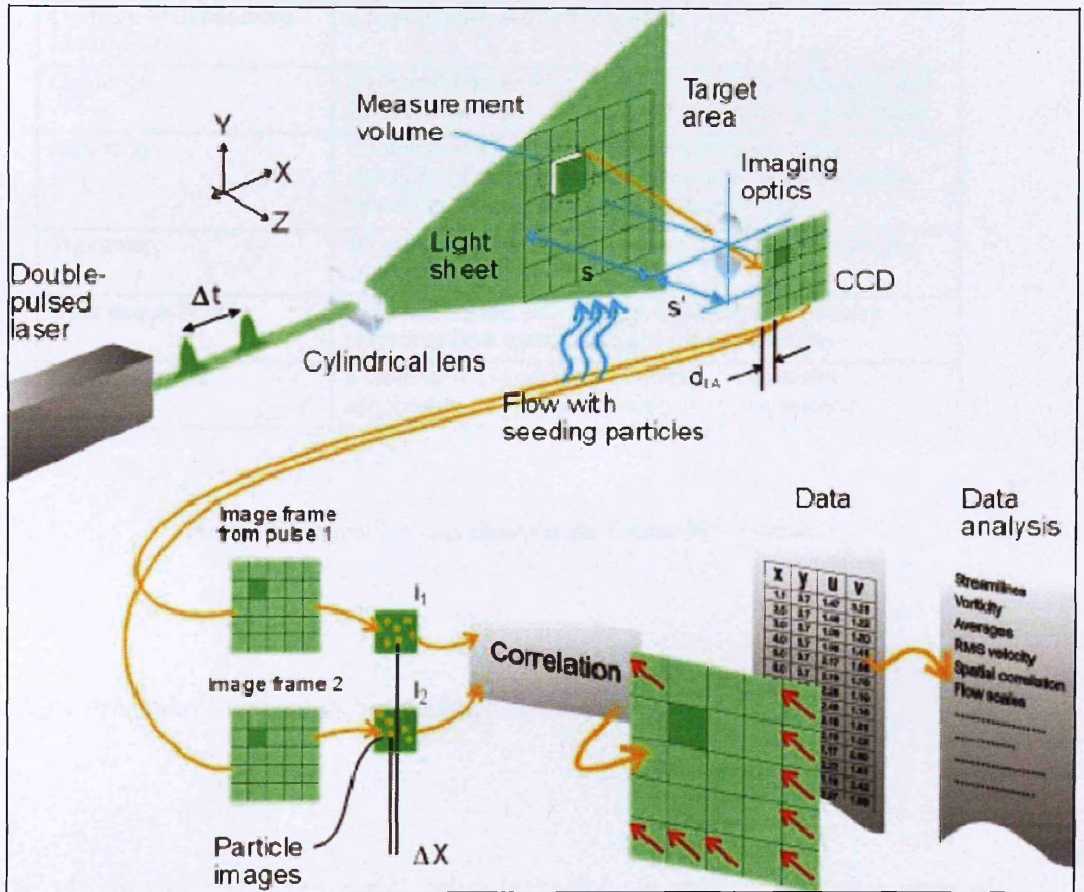
Figure A3-1 Schematic diagram of PIV operation, after Raffel et al., (1998)

A3.1 Specifications

Table A3-1 describes the specifications of the Dantec PIV system used in the flume.

Laser light source:	Nd:Yag (New Wave Solo PIV): 120mJ with 15Hz repetition rate.
Light sheet dimensions for 3D PIV:	0.5m by 0.5m at 2m from optics.
Cameras:	2 x Kodak/Roper 1k x 1k pixels with 8 bit resolution and 15Hz frame rate in cross-correlation (dual frame) mode.
Mounting:	Cameras and light sheet delivery mounted in a streamlined submersible housing with remote control focussing, schiemplflug adapter and F-stop.
Traverse:	3D automated traverse (x-range = 1020mm, y-range = 1140mm, z-range = 720mm).
Data acquisition:	Fully automated with at least 4 minutes continuous recording time (using 32Gbyte LIFO memory).
External inputs	8 channel A-D converter. Software for external synchronisation to measure periodic phenomena.

Table A3-1. Specifications sheet for the Dantec PIV System

A3.2 Principle of Operation, Set-up and Calibration

The PIV system uses stereoscopic camera technology to produce 3D vector maps of slices of flow. Figure A3-2 is a schematic diagram of its set-up, and Figure A3-3 shows two images of the PIV system in the flume. It is calibrated using a specially designed calibration plate which allows the camera and software to adjust to its known dimensions, (Figure A3-3). In Figure A3-4 camera A and B image the same area of the flow behind the cylinder herby known as a flow 'slice' from different angles.
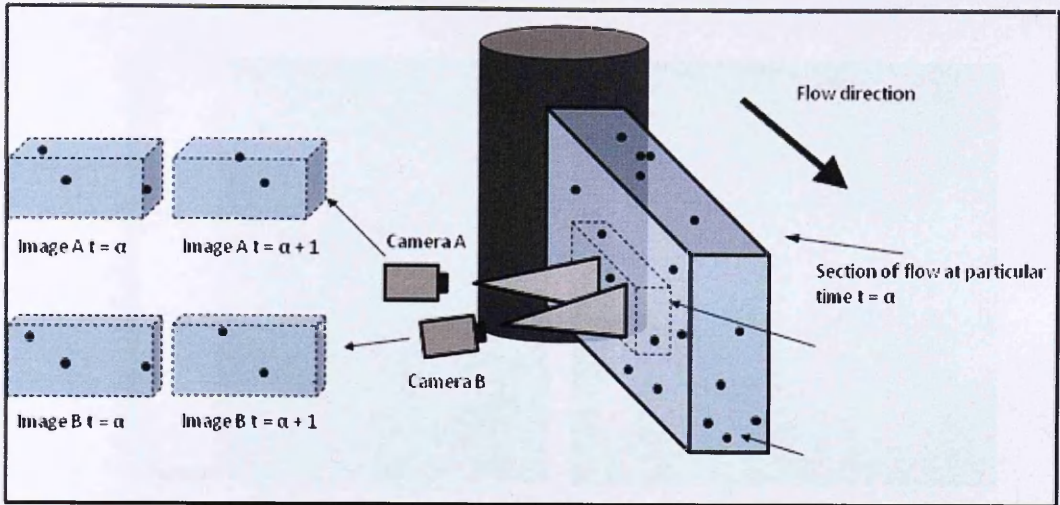
Figure A3-2. Schematic diagram showing the set-up and operation of the PIV system.
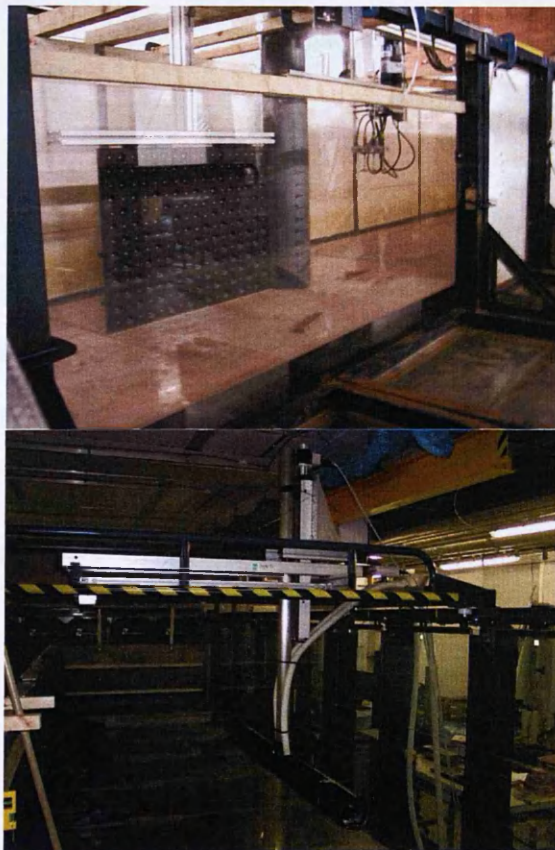
Figure A3-3. Left, image of the downstream side of the flume showing the calibration plate from outside the flume through the Perspex viewing window, and right, the two CCD cameras of the PIV system which image the flow through the Perspex viewing window.
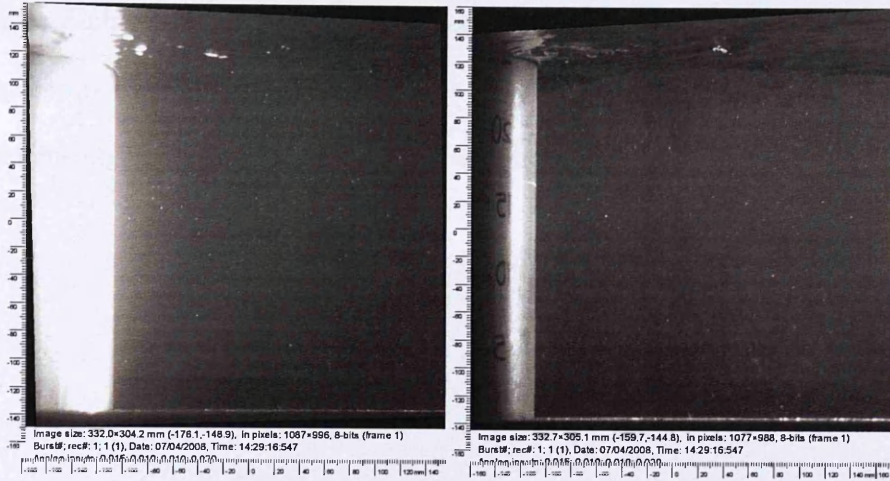
Figure A3-4. The raw A and B image of the same slice of flow field at the same instant in time. Note the position of the cylinder to the left and the reflection of seeding particles in the water column.

The position of seeding particles in such image pairs as the one in Figure A3-4 are compared with those in the next pair of images taken of the flow field. In this deployment a pair of images is capture 15 times a second over two minutes. This gives 1800 pairs each of which are compared with the next pair at the next instant in time and a 3D vector map is produced. From 1800 raw image pairs, 900 3D time-series vector maps are produced which are then averaged into one 3D time-averaged vector map.

A3.3   Error and Repeatability

In the experience of the collaborators in these tests, the calculation of error for this deployment is not necessary as it is a complex undertaking and calculations of error in

previous deployments of the PIV system at The Deep show error to be very small. Repeatability was tested by re-taking vector maps at several locations. These repeated measurements showed essentially identical flow fields.

Appendix A4 Ultrasonic Ranging System and Laser Profiler Specifications, Set-up and Error

A4.1. Ultrasonic Ranging System

In order to obtain time series data on the scour development around the cylinder, a Seatek 5 MHz Ultrasonic Ranging System (URS) was deployed. The system was custom built and calibrated by the manufacturer for this particular deployment. The system is composed of 12 transducers and comes with an electronics package including an electronics box capable of RS232 communications input and Serial port output to PC. The transducers operate at 5 MHz with a half beam angle of 0.9 degrees and a diameter of 1 cm. The closest measurement range is 3 cm and the furthest is 110 cm. The transducers emit and detect ultrasonic signals from which the return time is converted into a distance to transducer.

The 'CrossTalk' software package provides a PC interface from which the system can be controlled. Figure A4-1 is a screenshot of the 'Define Aquisition' interface of the CrossTalk software. From Figure A4-1: the number of bursts defines the frequency of scans over the defined sample rate; the blanking distance defines the lower cut-off of distance to target and is set to reduce the occurrence of false readings; the number pings to process per return describes the frequency of readings taken at each transducer per burst, it will take an average of 20 readings with the 3 highest and 3

lowest readings removed. The maximum resolution of the system is 0.1 mm with an error of +/- 0.2 mm.

```
┌─────────────────────────────────────────────────────────────────────┐
│  Define acquisition              Blanking, Range, and Threshold       │
│     Transducers                   Blanking (2 to 100 cm)      [5  ]    │
│        Select transducers to run                                      │
│                                   Maximum range (9 to 100 cm) [100 ]   │
│     Starting transducer (1:32)  [1   ]                                 │
│                                   Threshold (1 to 5000 mV)    [1500]   │
│     Ending transducer (1:64)    [32  ]                                 │
│                                   Number of pings to process per return│
│     Transducer increment (1-64) [1]                     (1 to 20)  [1  ]│
│                                                                       │
│                                   Water Temp. used to calc. speed of sound│
│     Number of bursts            [200    ]  Centigrade (5 to 80 C)  [20  ]│
│                                                                       │
│     Sample rate                   Begining analog channel       [1]    │
│     × 0.01 seconds (1 sec = 100) [100 ]  Number of analog channels [4] │
│                                                                       │
│                                   ┌─────┐  ┌────────┐  ┌──────┐        │
│                                   │ Ok  │  │ Cancel │  │ Help │        │
│                                   └─────┘  └────────┘  └──────┘        │
└─────────────────────────────────────────────────────────────────────┘
```

Figure A4-1. Screenshot of the Define Acquisition user interface.

Figure A4-2 shows images of the transducers and their set-up in the flume. The transducers were situated at 10 cm radial intervals at 90° intervals around the cylinder circumference starting along the centreline. The nearest transducer to the cylinder was situated at 6.5 mm from the surface. This was the closest position possible in the set-up. The transducers were fitted into specially cut Perspex rods which were attached to a height adjustable rig. The cables were run up to the top of the cylinder and then out of the flume.

Figure A4-2. Images of the URS set up; (top left) the transducers holders; (top right) top view showing transducers at 0, 90 and 270° with cabling running up the cylinder; (bottom row) images of the flume from either end.

A4.2. Leica Disto Laser Profiler

In order to produce profiles of the scour hole and surrounding bed on both sides of the cylinder, a laser distance measurer was attached to a specially designed rig. To allow profiles to be made the top of the cylinder was detached (Figure A4-3). The laser distance measurer (which is accurate to within +/- 1.5 mm) was mounted on a specially made rig which allowed variation of measurement location up and

downstream and either side of the cylinder (Figure A4-4). The rig itself was suspended from the flume walls and did not touch the sediment surface.

Figure A4-3 The fixed base of the cylinder with the top end removed.

Figure A4-4. (Left) the rig within the flume and (right) the sliding mount with the Disto laser attached.

Appendix A5 No-Cylinder ADV Control Tests

In order to determine the value of U_∞ for each of the tidal stages a series of control tests were performed at the different tidal parameters while there was no cylinder in the flume.

A5.1   No-Cylinder Upstream Velocity Control Tests

Figures A5-1, A5-2 and A5-3 show the u, v and w velocity profiles for the transition, live-bed and clear-water tests along the centreline and the $y' = 1.1$ planes. Table A5-1 shows the depth averaged velocities for each test from the centreline profile at $x' = 0.665$.
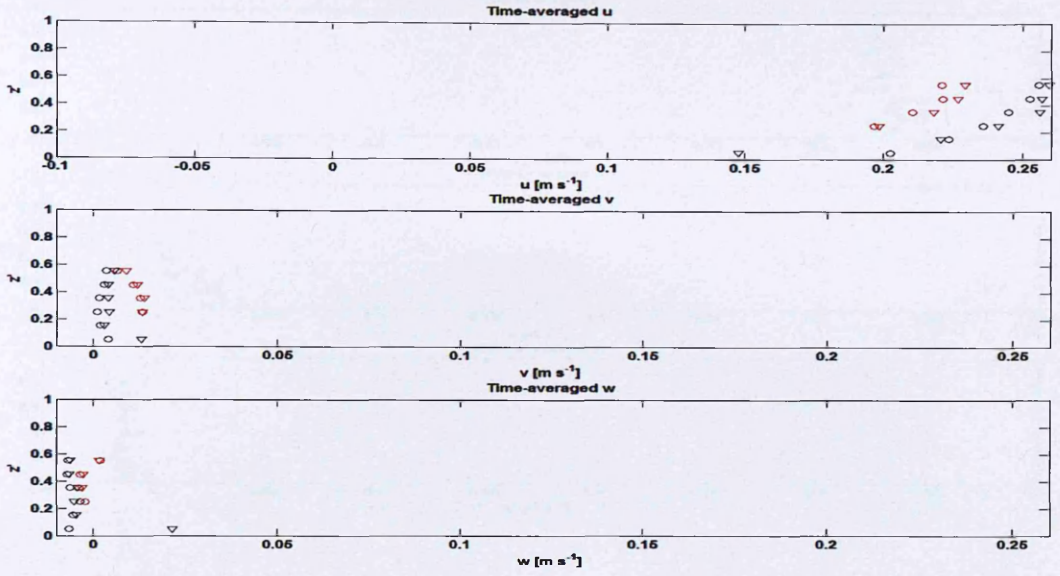
Figure A5-1. Time-averaged u, v and w velocity profiles taken upstream along the centreline at $x' = 5.75$ and 0.665 (black circles and down triangles respectively) and along the $y' = 1.1$ plane at $x' = 5.75$ and 0.665 (red circles and down triangles respectively) for the transition test parameters.
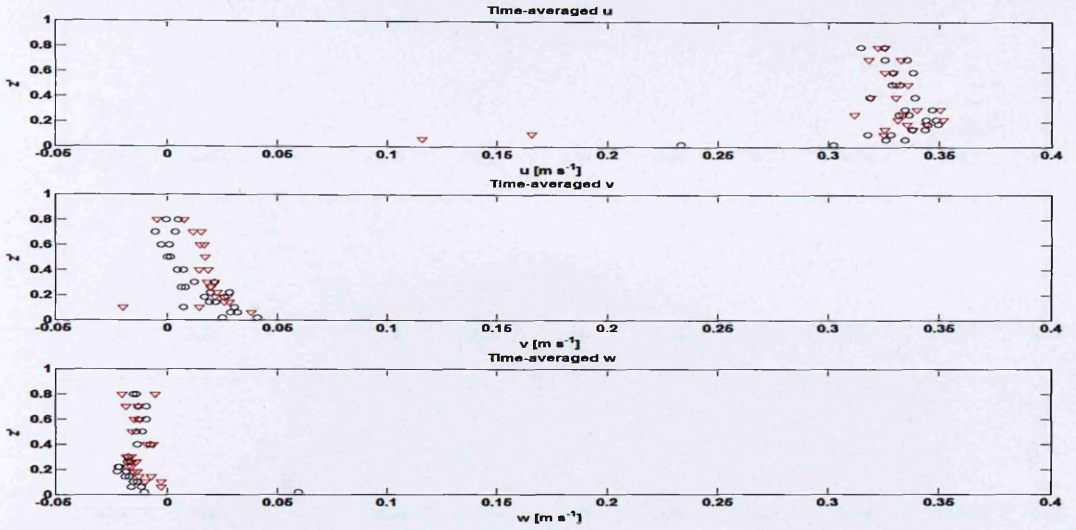
Figure A5-2. Time-averaged u, v and w velocity profiles taken upstream along the centreline at $x' = 5.75$ and 0.665 (black circles and down triangles respectively) and along the $y' = 1.1$ plane at $x' = 5.75$ and 0.665 (red circles and down triangles respectively) for the live-bed test parameters.
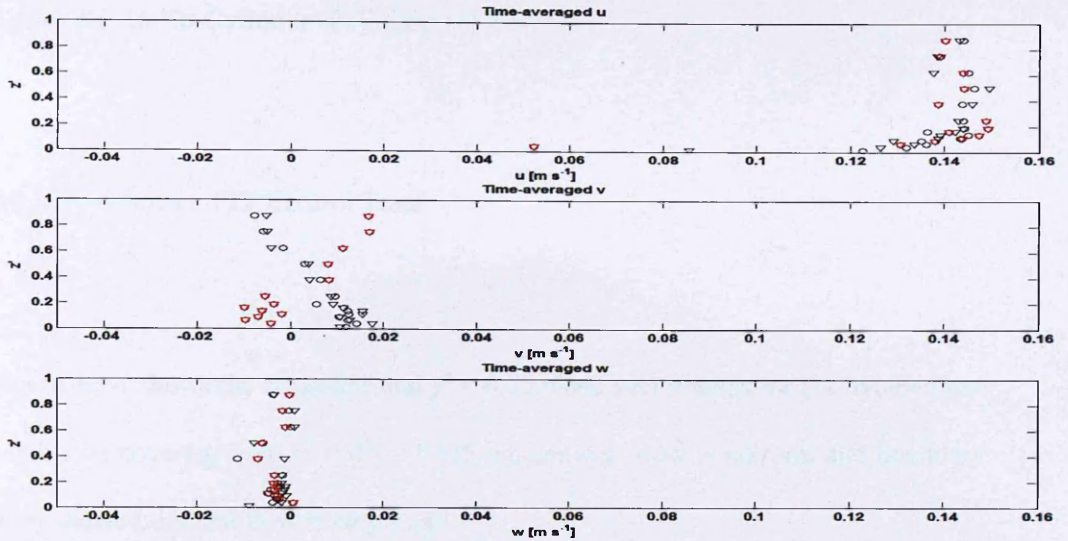
Figure A5-3. Time-averaged u, v and w velocity profiles taken upstream along the centreline at $x' = 5.75$ and 0.665 (black circles and down triangles respectively) and along the $y' = 1.1$ plane at $x' = 5.75$ and 0.665 (red circles and down triangles respectively) for the clear-water test parameters.

	Depth Averaged Velocities		
	Live-bed	Transition	Clear-water
u [m s^{-1}]	0.3398	0.2124	0.138
v [m s^{-1}]	0.0132	0.0083	0.0113
w [m s^{-1}]	-0.0127	-0.0019	-0.0036

Table A5-1. Depth averaged velocities calculated for each test with an error of +/- 0.1 mm s^{-1}.

As Table A5-1 and Figures A5-1, A5-2 and A5-3 show, the flow is essentially one-dimensional streamwise boundary layer sheared flow. Hence the velocity data in the experiments is normalised with the depth averaged velocity given in Table A5-1.

Appendix A6 No-Cylinder PIV Control Tests

A6.1 No-Cylinder PIV Control Tests

Figure A6-1 shows the centreline and $y' = 0.75$ plane vector maps for the live-bed test conditions covering from $x' = 0.5 - 1.625$. Streamwise flow is uniform and boundary layer sheared. Lateral flow is very small.
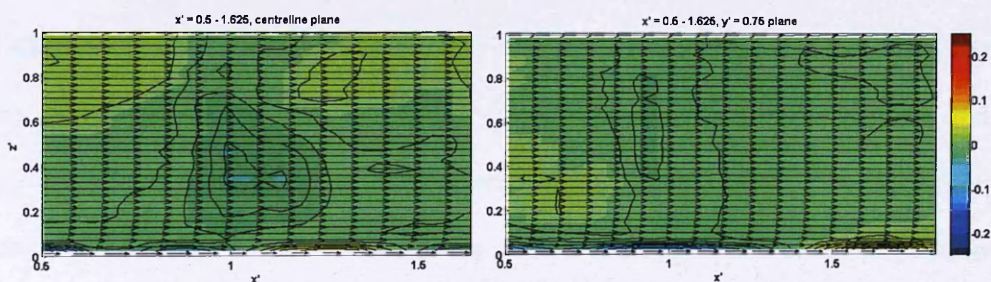
Figure A6-1. Velocity maps for the live-bed test along the centreline (left) and the $y' = 0.75$ plane (right)

Figure A6-2 shows the centreline and $y' = 0.75$ plane vector maps for the transition test conditions covering from $x' = 0.5 - 1.625$. Streamwise flow is uniform and boundary layer sheared. Lateral flow is very small. Near the bed there are some areas of increased lateral component, however, these are ignored as near-bed reflections of the laser decrease the ability of the PIV software to resolve velocity correctly.
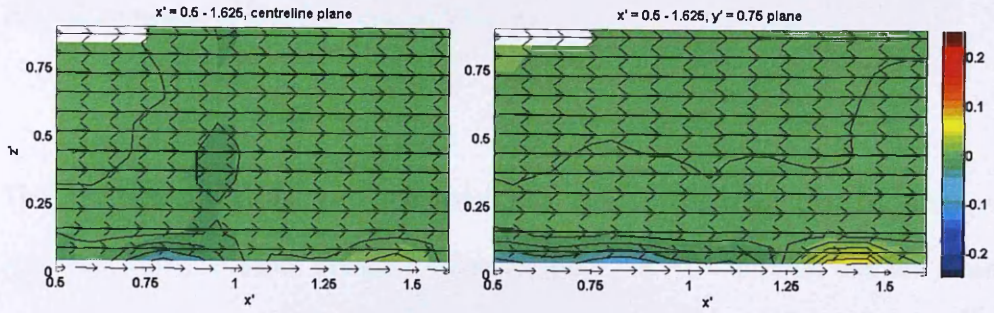
Figure A6-2. Velocity maps for the transition test along the centreline (left) and the $y' = 0.75$

plane (right)

Figure A6-3 shows the centreline and $y' = 0.75$ plane vector maps for the clear-water test conditions covering from $x' = 0.5 - 1.625$. Streamwise flow is uniform and boundary layer sheared. Lateral flow shows a distinct divide between negative flow near the bed and positive flow towards the surface. The distribution of lateral flows in these vector maps indicates the presence of a secondary flow in the flume, which is discussed in §3.2.1.2.
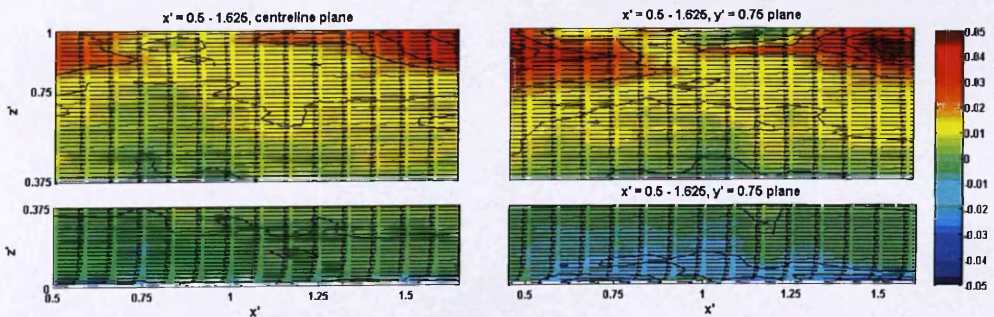
Figure A6-3. Velocity maps for the transition test along the centreline (left) and the $y' = 0.75$

plane (right)

A6.2 Comparison of Depth Averaged Velocity

The PIV velocity maps were compared with the ADV control profiles given in Appendix A5. The depth averaged velocities from the ADV profiles and the mean depth averaged velocity of the individual profiles in the centreline vector maps are given in Table A6-1. The depth averaged velocities between the two instruments are very similar.

Depth Averaged Velocities			
	Live-bed	Transition	Clear-water
ADV u	0.3398	0.2124	0.138
PIV u	0.3407	0.2211	0.139

Table A6-1. Depth averaged velocities calculated for each test with no cylinder in the flume from ADV profiles at $x' = 0.665$ and along for the PIV between $x' = 0.5 - 1.5$ along the centreline.

Appendix A7 Full PIV Velocity Maps for the Transition, Live-bed and Clear-water Tests

A7.1. Transition Test

Figure A7-1 shows the full PIV velocity slices for the transition test. This includes data that was not shown in §3.4.1.3 as it was stated that the downstream slices from x' > 2.5 did not present any observable changes in the flow structure except the gradual re-establishment of downstream boundary layer sheared flow.

A7.2 Live-bed Test

Figure A7-2 shows the full PIV velocity slices for the live-bed test. The figure shows the slice covering x' = 3 - 4.25 which was not included in §3.4.1.2 the slice was excluded from that discussion due to it showing little change from the previous slice except that of a gradual establishment of downstream boundary layer sheared flow and the reduction of lateral v velocity.
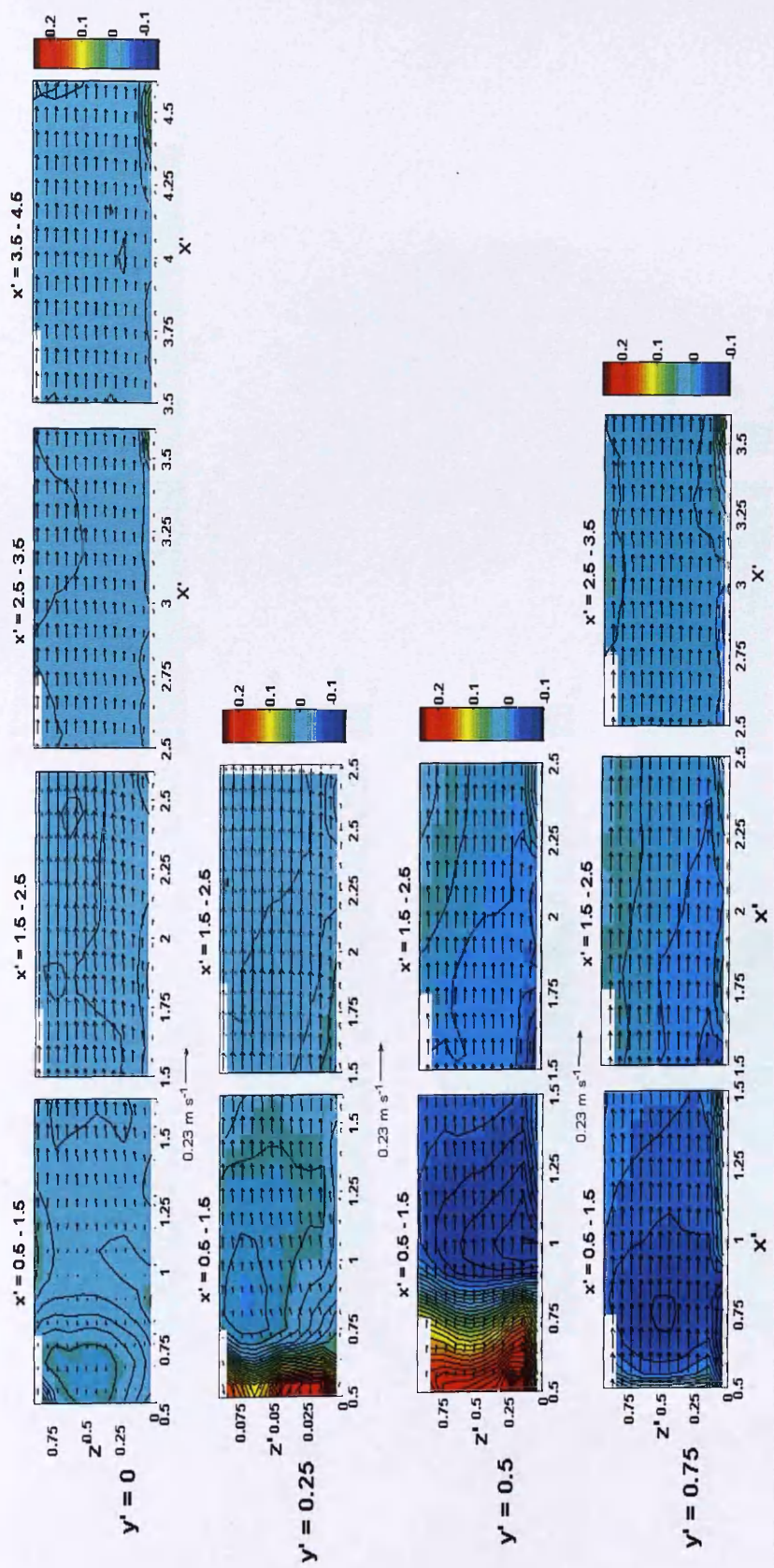
Figure A7.1. The full 3D PIV velocity slices for the transition test.
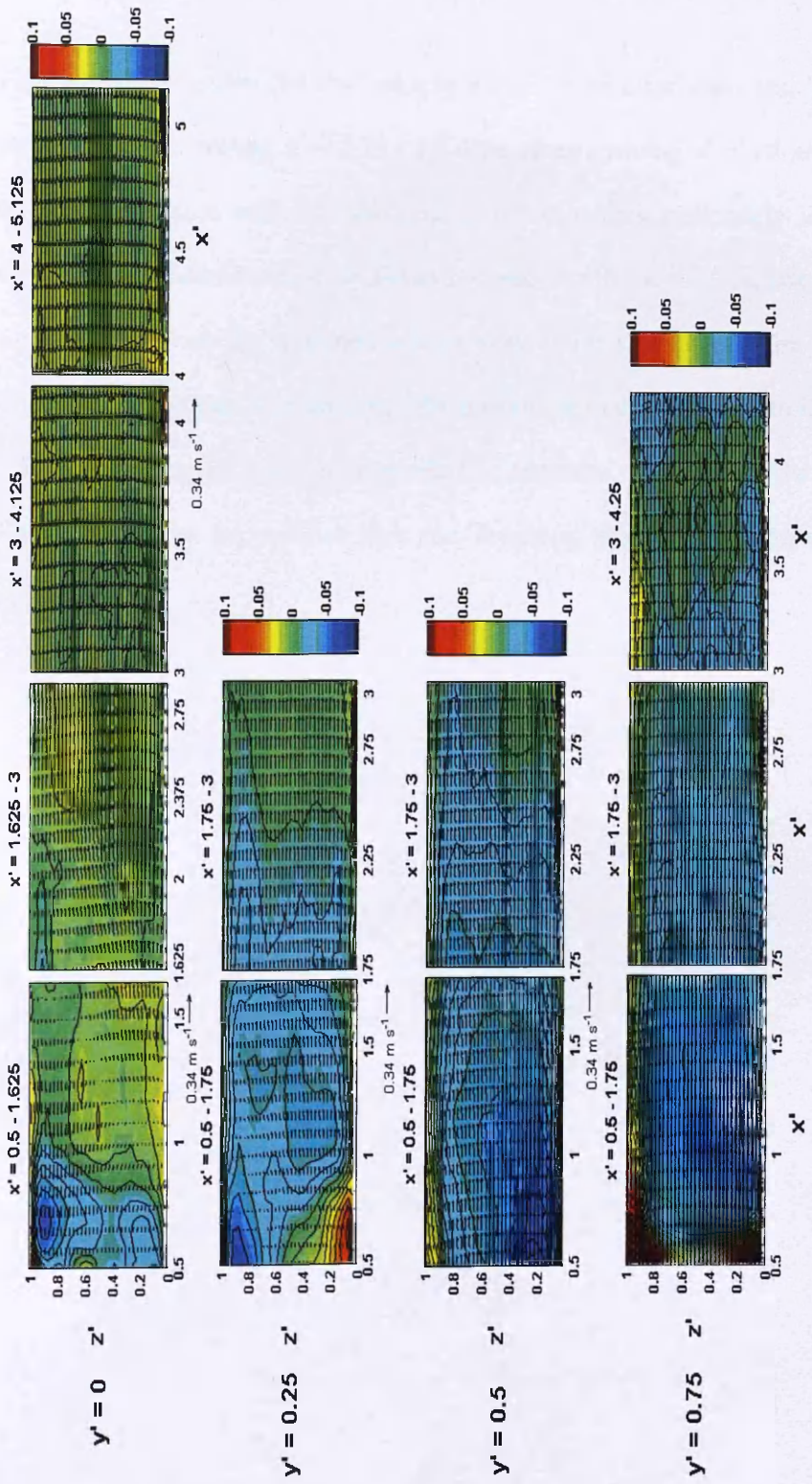
Figure A7.2. The full 3D PIV velocity slices for the live-bed test.

A7.3. Clear-water Test

Figure A7-3 shows the full PIV velocity slices for the clear-water test including the centreline slice covering $x' = 2.75 - 3.5$. The slices covering $x' > 3.5$ are not shown due to interference with the resolving of the velocities particularly in the lateral direction. This interference arose due to unexpected reflections of the laser off the tape used to make flush the joins between the flow dividers making up the flume walls. The effect of this can be observed on the downstream edge of the centreline $x' = 2.75 - 3.5$ slice where the lateral v component in particular, is distorted. The slice shows little change from the previous slice and, therefore, its exclusion from discussion is not significant.
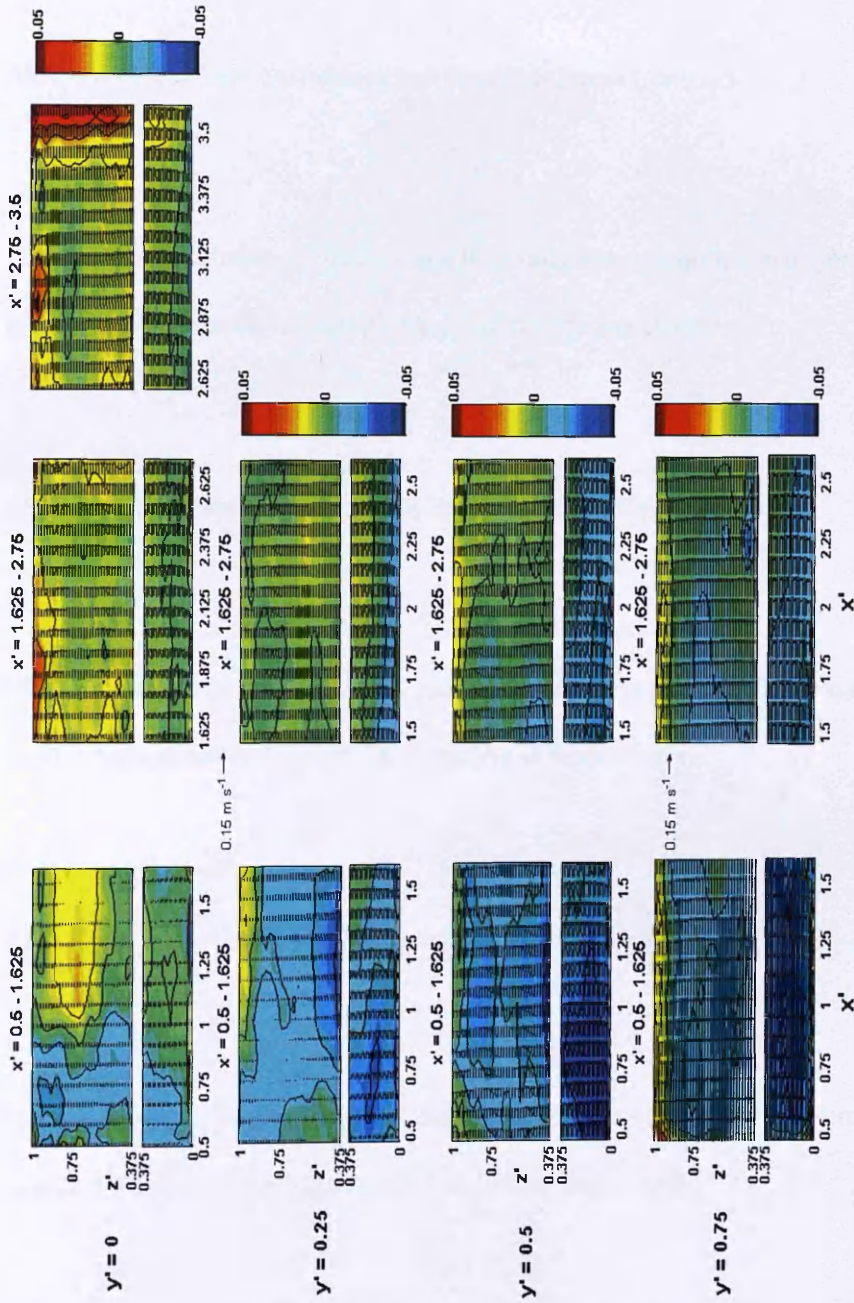
Figure A7.3. The full 3D PIV velocity slices for the clear-water test.

Appendix A8 Remaining PIV Turbulence and Reynolds Stress Contour Maps for Low, Mid and Clear-water Tests

A8.1. Transition Test Turbulence and Reynolds Stress Contours

The remaining turbulence intensity and Reynolds Stress contours that were not plotted in §43.4.3.3 are shown in Figures A8-1 and A8 -2 respectively.

A8.2. Live-bed Test Turbulence and Reynolds Stress Contours

The remaining turbulence intensity and Reynolds Stress contours that were not plotted in §3.4.3 are shown in Figures A8 -3 and A8 -4 respectively.

A8.3. Clear-water Test Turbulence and Reynolds Stress Contours

The remaining turbulence intensity and Reynolds Stress contours that were not plotted in §3.4.3.3 are shown in Figures A8-5 and A8-6 respectively.
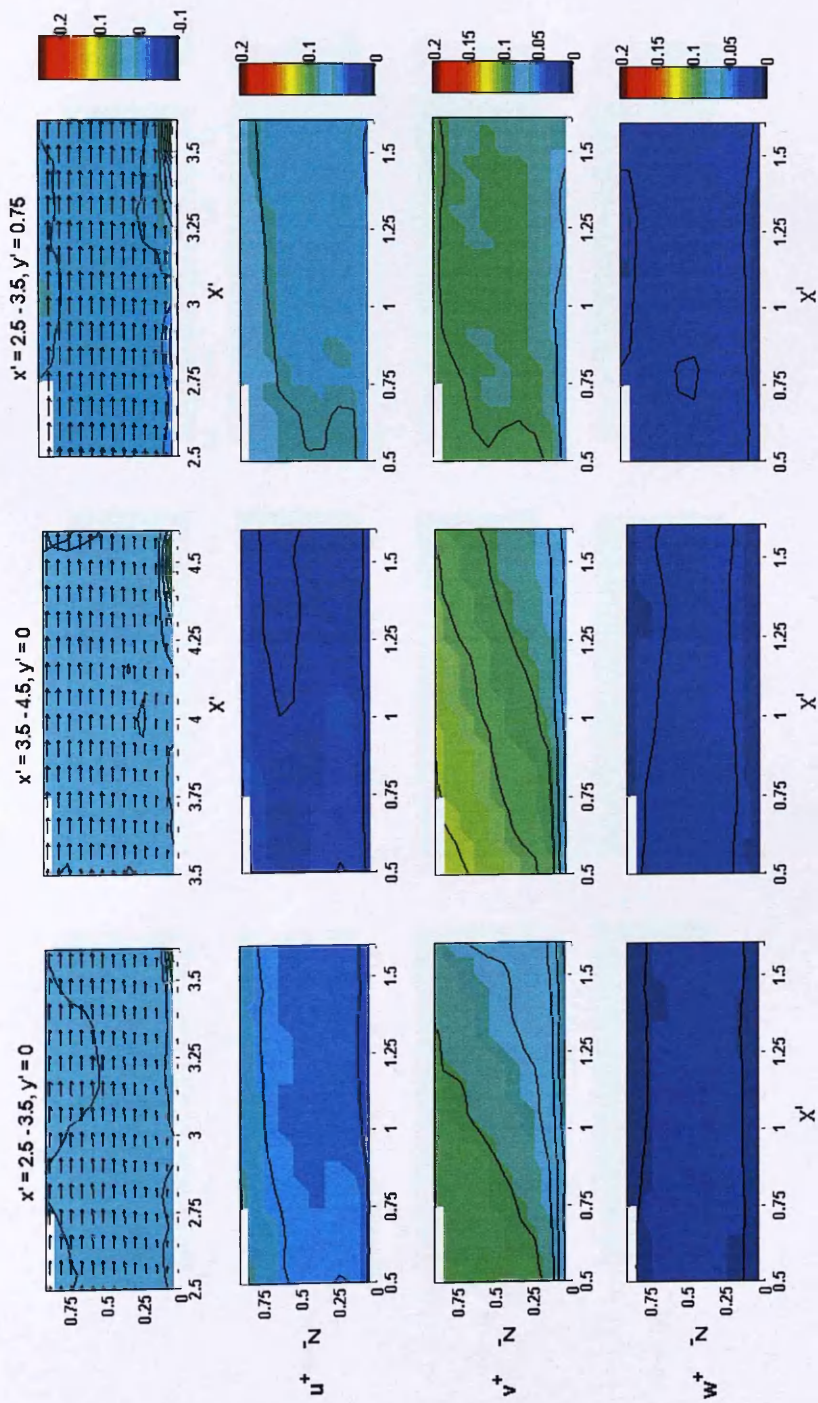
Figure A8-1. Remaining Turbulence intensity contours for the transition test PIV slices not shown in §3.4.3.3
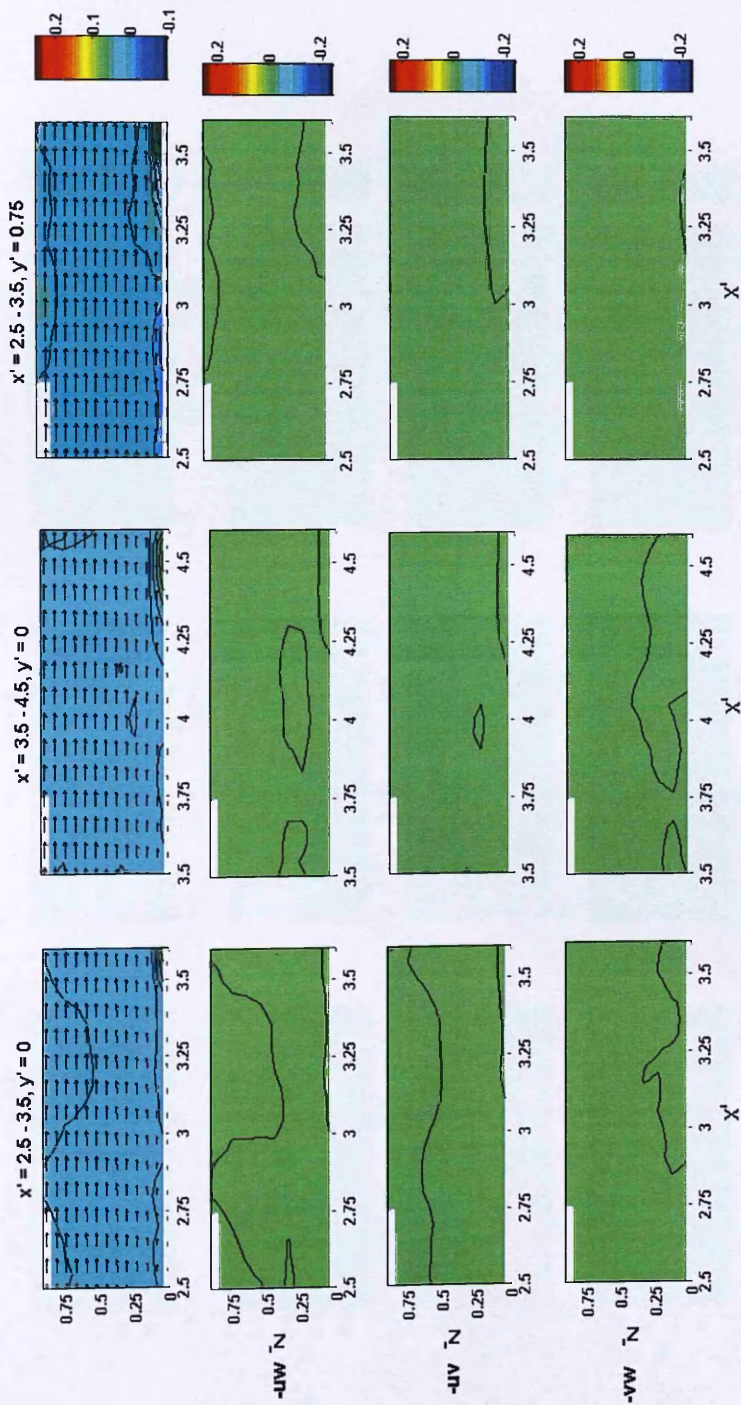
Figure A8-2. Remaining Reynolds Stress contours for the transition test PIV slices not shown in §3.4.3.3
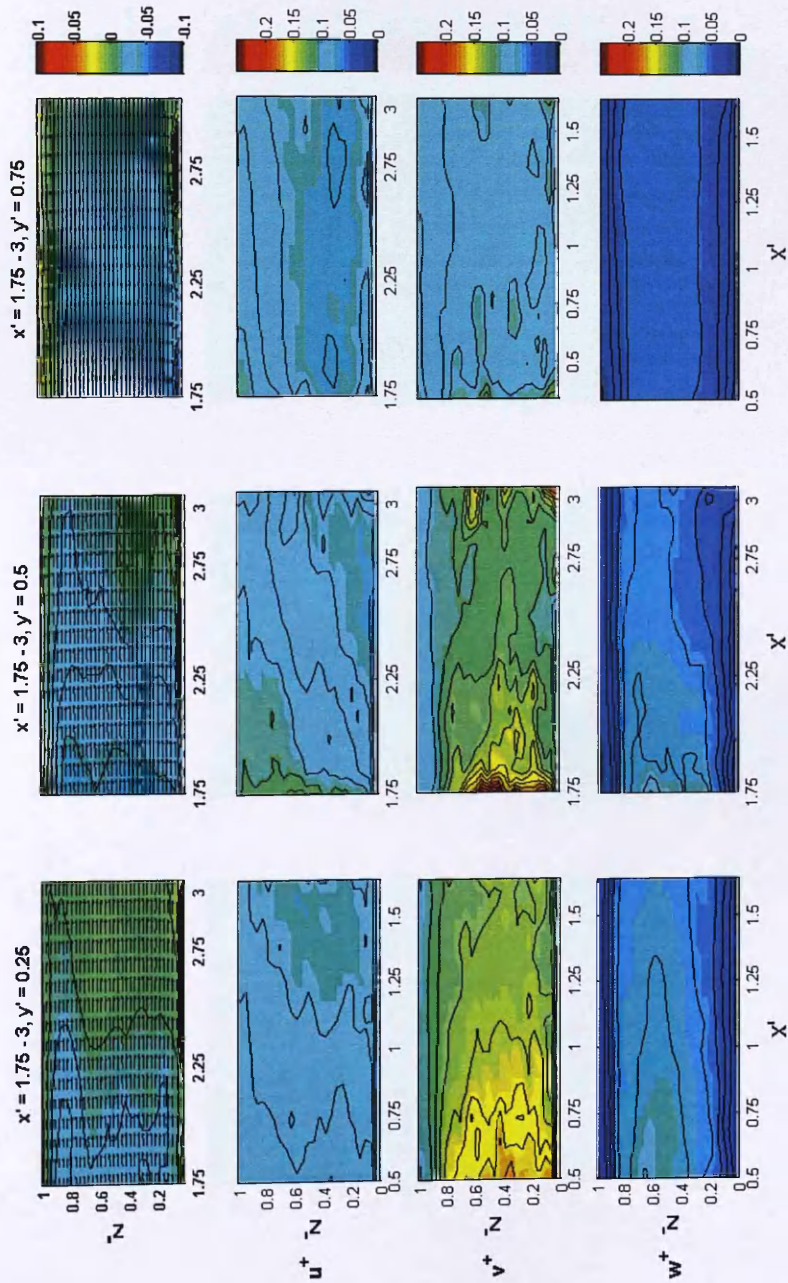
Figure A8-3. Remaining Reynolds Stress contours for the live-bed PIV slices not shown in §3.4.3
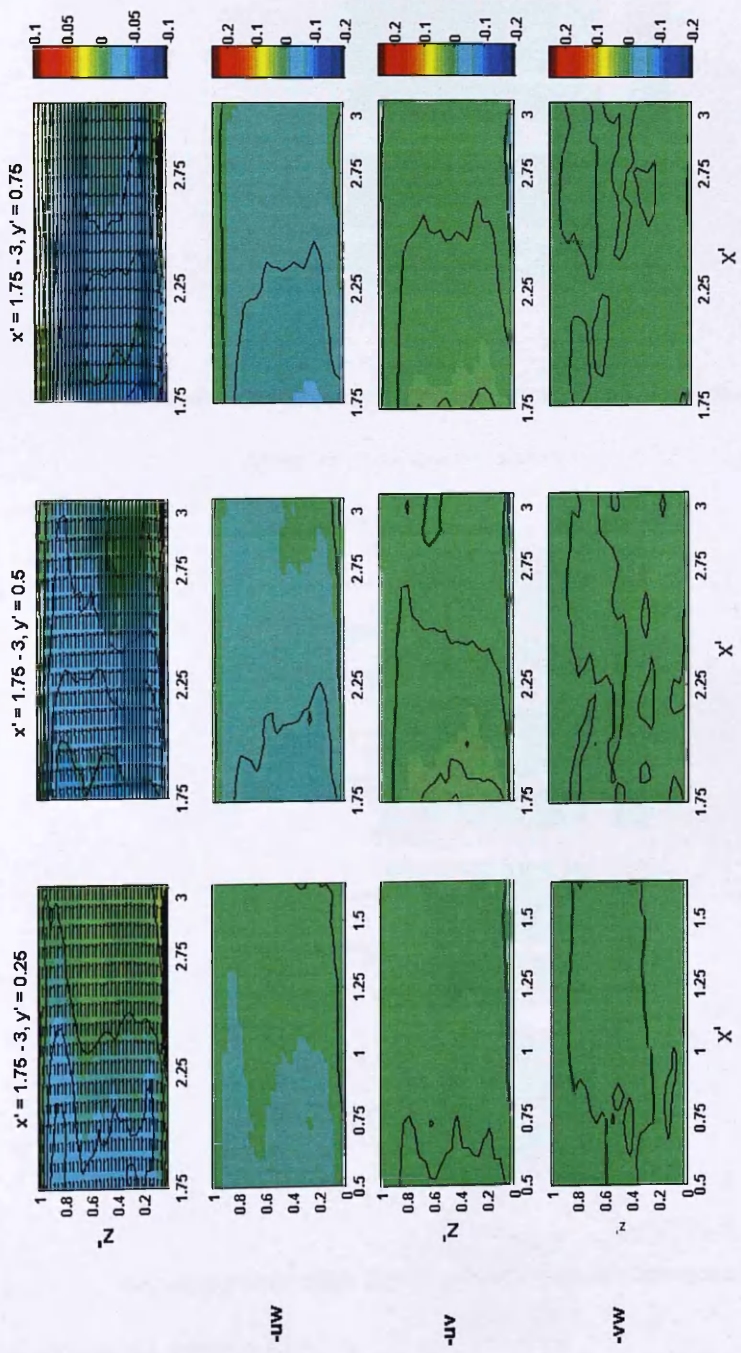
Figure A8-4. Remaining Reynolds Stress contours for the live-bed PIV slices not shown in §3.4.3
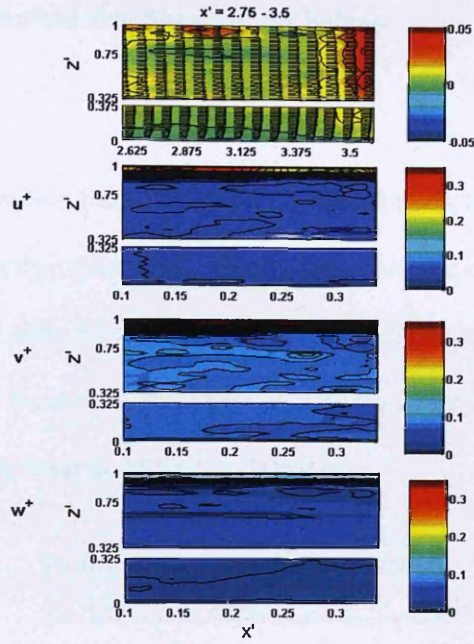
Figure A8-5. Remaining clear-water turbulence intensity contours between $x' = 2.75 - 3.5$, along the centreline not shown in §3.4.3.3.
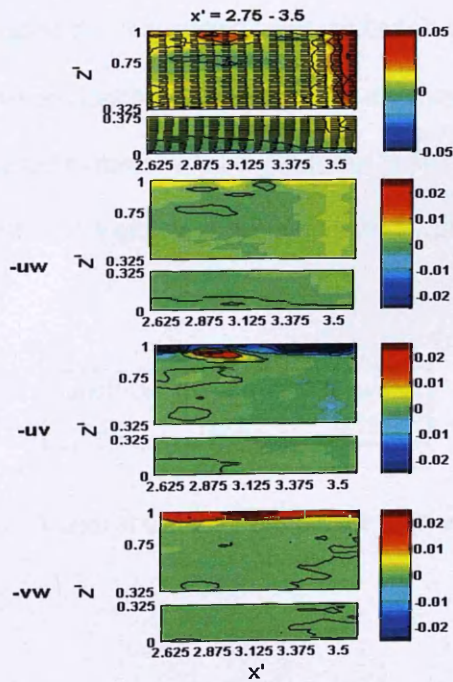
Figure A8-6. Remaining clear-water Reynolds Stress contours between $x' = 2.75 - 3.5$, along the centreline not shown in §3.4.3.3.

Appendix A9. Undisturbed Bed Shear Stress Values

The upstream values of bed shear stress were calculated using the TKE method described in §3.5 from the undisturbed velocity data along the centreline shown in Appendix A5. These values are shown in Table A9-1. Calculated values of upstream and near-cylinder bed shear stress were then normalised by the undisturbed values in Table A9-1 to give bed shear amplification factor α.

Transition	Live-bed	Clear-water
0.095	0.22	0.09

Table A9-1. Values of undisturbed bed shear stress in kg m^{-1} s^{-2}.

Downstream of the cylinder the undisturbed values of bed shear stress were calculated from the PIV data shown in Appendix A6. The values are shown in Table A9-2. The values are slightly different to those in Table A9-1, due most likely to experimental variation between the two types of data collection methods, and the time at which they were taken.

transition	live-bed	clear-water
0.06	0.24	0.13

Table A9-2. Values of undisturbed bed shear stress in kg m^{-1} s^{-2}.

Appendix A10 Boundary Layer Thickness Calculations

The thickness of the boundary layer ∂ was estimated from the logarithmic velocity profiles shown in Figure A10-1,
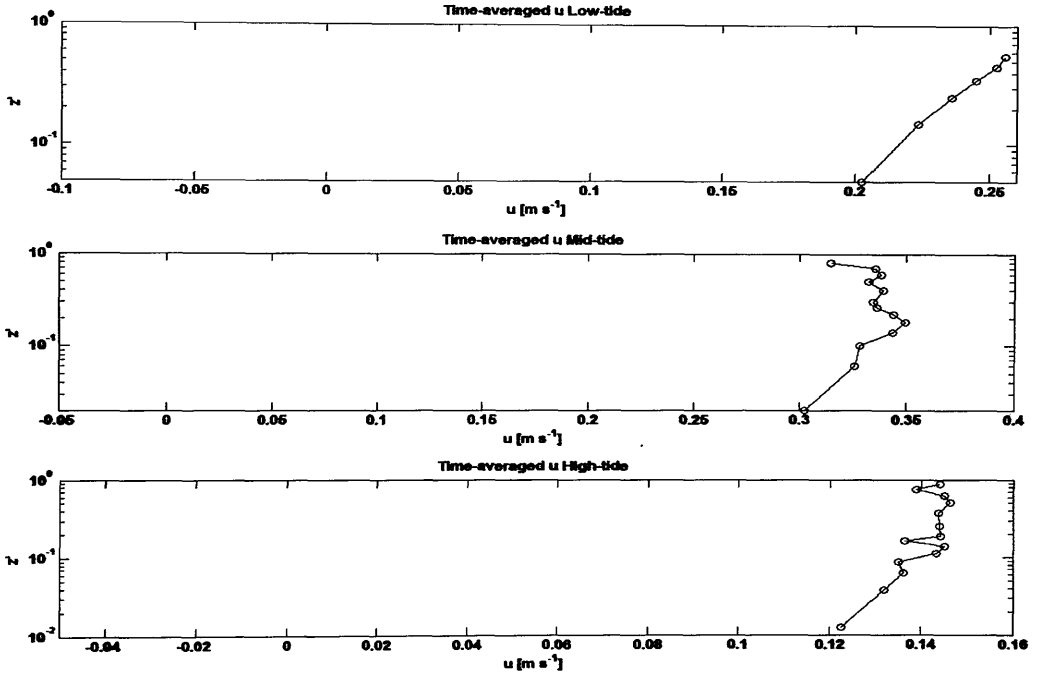
Figure A10-1. Logarithmic u velocity profiles taken in the no- cylinder control tests along the centreline at $x' = 0.665$.for the transition, live-bed and clear-water tests.

From the logarithmic plots of u given in Figure A10-1, the value of ∂ (defined as the point where the u ceases to increase logarithmically with increasing z, e.g., Brown et al., 2005) can be estimated (Table 10-1).

Time step	Approximate δ	Approximate δ/h
Clear-water	≈ 0.035	≈ 0.09
Live-bed	≈ 0.045	≈ 0.2
Transition	≈ 0.055	≈ 0.6

Table A10-1. Estimated values of ∂ from the observation of the logarithmic plots given in Figure A10-1.

Appendix A11 Prototype Tidal Data

In order to ensure scale that the scaling of parameters in the experiments could relate to real conditions, typical conditions found at various locations in the Irish sea Liverpool Bay area were analysed. The data is freely available online from the British Oceanographic Data Centre (BODC)) and was used to determine what typical tidal velocities, depths, ranges and time scales may be in the Liverpool Bay area. A number of data sets were used each of which contained readings are taken every ten minutes of the following information: start and end time, current velocity and water depth (Table A11-1).

Data Set	Start Date	Start Time	End Date	End Time	Peak Recorded u $cm\ s^{-1}$	Lowest Annual Tide Depth m
b0577561	21/05/1997	14:13:59	05/07/1997	08:43:59	56.3	22
b0592570	02/09/2001	13:59:59	11/09/2001	17:50:00	53.7	22
b0577573	06/07/1997	13:45:00	07/08/1997	08:15:00	52.6	21
b0577585	21/04/1997	14:05:00	21/05/1997	14:35:00	69.8	21
b0577597	21/04/1997	14:05:00	21/05/1997	14:35:00	58.9	21
b0577616	21/05/1997	16:36:00	08/06/1997	18:26:00	66.4	20
b0577628	06/07/1997	16:09:00	07/08/1997	07:29:00	72.3	20
b0577641	06/07/1997	16:03:59	07/08/1997	07:24:00	56.1	24
b0592521	02/09/2001	13:59:59	11/09/2001	17:50:00	50.3	24
b0592533	02/09/2001	13:54:59	06/09/2001	02:05:00	60.7	24

Table A11-1. Main details of the data sets used to define typical conditions in the Liverpool Bay area of the Irish Sea.

In order to define a typical range at which wind turbines may be found, depth data for individual turbines from the Rhyll Flats wind turbine farm are presented in Table A11-2.

nPower Rhyll Flats Turbine No	LAT Depth
1	11
2	11
3	11
4	11
5	10.5
6	10
7	9
8	12.5
9	12
10	11
11	10.5
12	10
13	9
14	9
15	8
16	8
17	8
18	6
19	11
20	10.5
21	9.5
22	9
23	9
24	8
25	8
26	6.5
27	6
28	6
29	7
30	4

Table A11-2. Individual turbine Lowest Annual Tide (LAT) depths for the Rhyll Flats Wind farm in Liverpool Bay

The tidal range was derived from sea floor pressure sensor data set b0033693 (BODC) by calculating the change in depth over several half cycles (Table 10-3).

cycle	ranges
1	4.3
2	7.2
3	8.4
4	3.7
5	8.2
6	6.5
average	6.4

Table A10-3. Tidal ranges calculated from pressure sensor data-set b0033693, (BODC).

The prototype data above was consulted in the scaling process in order to ensure that the model would be relevant to typical prototype conditions, though not be limited to a single prototype.

Appendix A12 Discussion of Change in Flow Depth between the Unidirectional Test and Live-bed Test Conditions

The mobile-bed experiment programme included a live-bed unidirectional test of one full cycle to allow comparison of the unidirectional scour depth and time-development with the variable reversing scour depth and development. Unfortunately difficulties were encountered in the application of the reverse flow pumps; actual discharge capacity was below the rated capacity resulting in a failure to provide live-bed discharge velocity as described in Table 2-2. Velocity was lowered to 0.31 m s^{-1} and the unidirectional test was run. Unfortunately pumping capacity fell further for unknown reasons meaning the variable reversing test had to have a reduce flow depth in the live-bed of 0.2 m as opposed to 0.25 m. Time constraints prevented a second, lower flow depth unidirectional live-bed test from being performed. Therefore the unidirectional test is presented under an increased flow depth and the validity of the comparison between it and the variable reversing tests is outlined here.

While the flow velocity ($u = 0.31$) and flow intensity ($u/U_c = 1.24$) parameters for the unidirectional test are the same as the live-bed time-step, the flow depth is increased by 5 cm to $h = 0.25$ m. This results in a flow depth to cylinder diameter ratio the ratio $D/h = 0.8$ as opposed to 1. Melville, (1997), from a plot of about 100 data from numerous literature identified that the effect of relative flow depth h/D on scour can be described by the parameter D/h which groups cylinder diameters into three categories; narrow ($D/h < 0.7$), intermediate ($0.7 < D/h < 5$) and wide ($D/h > 5$). For intermediate width diameters the influence of flow depth on scour

depth is only felt when the surface roller interacts with the horseshoe vortex. Hoffmans and Verheij, (1997) suggest that flow depth only has a direct effect on scour when the $D/h > 1$. This means that the main parameters influencing scour in these two tests are those relating to the flow (u/U_c and Froude number), though due to the decrease in flow depth is likely reduce the scour depth slightly as the surface roller is closer to the bed. The changes in maximum predicted scour depth calculated using Equations 1-25 (HEC-18, 1993) and 4-5 (Breusers et al., 1977) are given in Table A12-1.

	Eqn. 1-25	Eqn. 4-5
h = 0.2	0.21	0.23
h = 0.25	0.22	0.25
% difference	5	9

Table A12-1. Difference in predicted scour depth for the flow depth h = 0.2, and 0.25.

Figure A12-1 shows plots of the predicted time-development curve for the unidirectional test (circles), the live-bed time step (plus signs), the recorded unidirectional test time-series data (red crosses) and the maximum recorded scour depth at the end of the unidirectional test period (blue cross). Figure A12-2 shows that the predicted time development of scour is consistently higher (by ≈ 1 cm) for the unidirectional test due to the larger flow depth. The unidirectional time-series data shows a significantly smaller scour depth, due in part to the location of probe one, as discussed above (§4.3.1 and §4.3.2). The maximum scour depth recorded by the laser profiler at the end of the unidirectional test shows approximately a 1 cm reduction from the predicted curve. In fact the maximum scour depth recorded is similar to the predicted time-series curve for the live-bed. The conclusion from the equations'

predictions in Table A12-1 is that the scour depth increase due to the increased depth is < 10%, meaning that a comparison between the unidirectional test and the variable reversing test can be made within these limits.
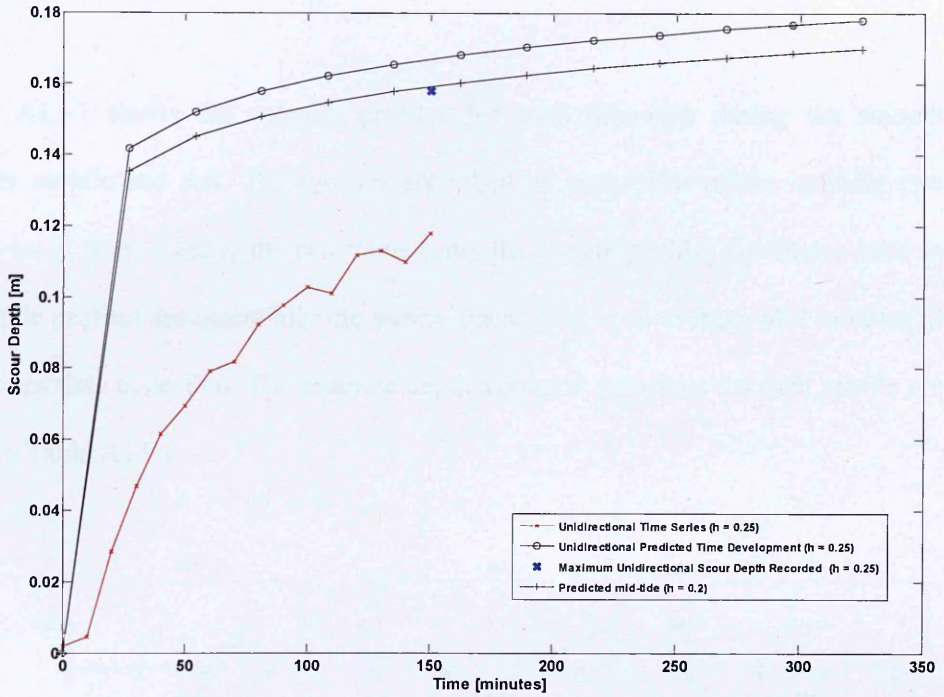
Figure A12-1. Time-development of the unidirectional scour depth upstream of the cylinder at $x' = 0.325$ and maximum scour depth recorded at $x = -0.75$ and $y = -0.5$, along with the time development curve prediction from Melville and Chiew, (1999).

Appendix A.13. Mobile Bed Velocity Profiles

A13.1 Smooth Cylinder Test

Figure A13-1 shows the velocity profiles for each time-step during the smooth cylinder mobile bed test. The profiles are taken on both sides of the cylinder two metres away from it along the centreline (only the A side profiles are shown here as the B side profiles are essentially the same). Each point is an average of 2 minutes of time series data collection. The absolute depth averaged velocities for each profile are given in Table A13-1.
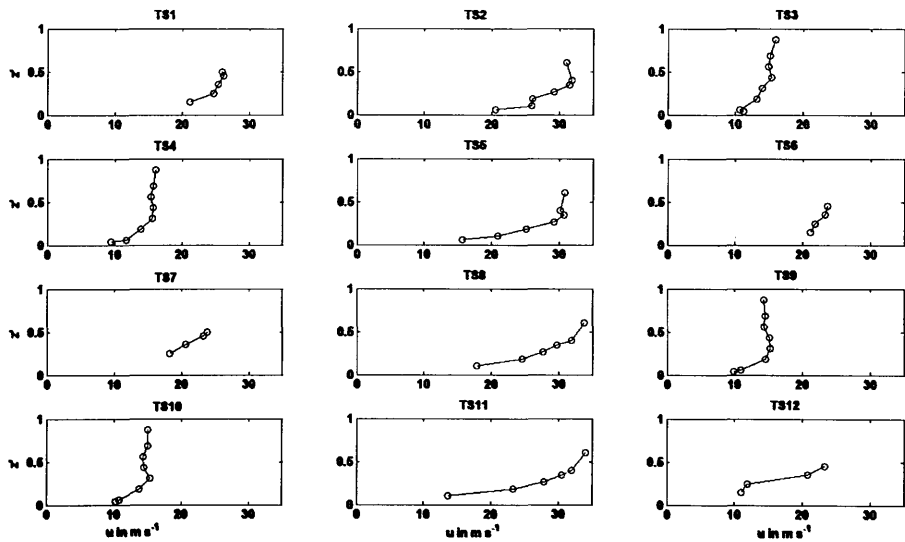
Figure A13-1. Velocity profiles for each time-step of the smooth monopile mobile bed test.

Depth Averaged Absolute Velocity	
Time step	cm s^{-1}
TS1	23.2
TS2	30.6
TS3	14.7
TS4	15.2
TS5	30
TS6	21.6
TS7	21
TS8	30.4
TS9	14
TS10	13.9
TS11	31
TS12	22

Table A13-1. Depth-averaged velocities for each time-step of the smooth cylinder mobile bed test from the velocity profiles shown in Figure A13-1.

A13.2 Collared Cylinder Test

Figure A13-2 shows the velocity profiles for each time-step during the collared cylinder mobile bed test. The profiles are taken on both sides of the cylinder two metres away from it along the centreline (only the A side profiles are shown here as the B side profiles are essentially the same). Each point is an average of 2 minutes of time series data collection. The absolute depth averaged velocities for each profile are given in Table A13-2.
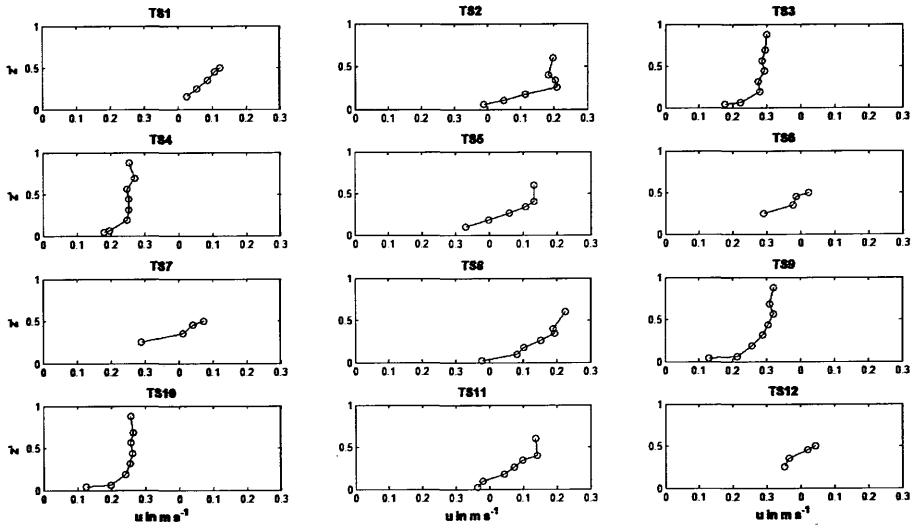
Figure A13-2. Velocity profiles for each time-step of the collared cylinder mobile bed test.

Depth Averaged Absolute Velocity	
Time step	cm s^{-1}
TS1	21.9
TS2	29.2
TS3	14.1
TS4	14.2
TS5	24.3
TS6	21.3
TS7	22.1
TS8	29.3
TS9	15.8
TS10	13.8
TS11	29.4
TS12	19.5

Table A13.3, Absolute depth average velocities for each time step from the velocity profiles shown in Figure A13-3